

Measurement of the inclusive $t\bar{t}$ cross section and search for additional scalars in $t\bar{t}$ final states at the CMS experiment

Dissertation

zur Erlangung des Doktorgrades
an der Fakultät für Mathematik, Informatik und Naturwissenschaften
Fachbereich Physik
der Universität Hamburg

von

Laurids Jeppe

Hamburg
2025

Gutachter der Dissertation:	Prof. Dr. Christian Schwanenberger Dr. Alexander Grohsjean
Zusammensetzung der Prüfungskomission:	Prof. Dr. Christian Schwanenberger Dr. Alexander Grohsjean TBD TBD TBD
Vorsitzender der Prüfungskommission:	TBD
Datum der Disputation:	TBD
Vorsitzender Fach-Promotionsausschuss Physik:	Prof. Dr. Wolfgang J. Parak
Leiter des Fachbereichs Physik:	Prof. Dr. Markus Drescher
Leiter der Fakultät MIN:	Prof. Dr.-Ing. Norbert Ritter

Contents

1	Introduction	6
2	Theoretical framework	8
2.1	Standard Model	8
2.1.1	Top quark	9
2.1.2	Higgs mechanism	10
2.2	The $p p \rightarrow t\bar{t}$ process	11
2.2.1	Spin state of the $t\bar{t}$ system	13
2.2.2	Spin density matrix	15
2.2.3	Bound state effects in $t\bar{t}$	18
2.3	Beyond the Standard Model	21
2.3.1	Heavy scalars in $t\bar{t}$ production	22
2.3.2	Two-Higgs Doublet Model	24
2.3.3	Axion-Like Particles	25
3	Monte Carlo event generation	28
3.1	Matrix Element generators	28
3.2	Parton showers and matching	30
3.3	Multi-parton interactions	31
3.4	Hadronization	32
3.5	Pileup	33
3.6	Detector and trigger simulation	33
4	Experimental methods	34
4.1	The Large Hadron Collider	34
4.2	The CMS experiment	35
4.3	Object reconstruction	38
4.4	Statistical interpretation	39
5	Measurement of the inclusive $t\bar{t}$ cross section at $\sqrt{s} = 13.6$ TeV	45
5.1	Introduction	45
5.2	Datasets and event selection	46
5.2.1	Datasets	46
5.2.2	Object definition	47
5.2.3	Channel definition	48

5.3	Corrections	49
5.3.1	Experimental corrections	50
5.3.2	Data-driven background estimation	53
5.4	Control distributions	60
5.5	Systematic uncertainties	60
5.6	Fit results	68
5.6.1	Statistical checks	70
5.6.2	Top quark mass dependence	70
5.7	Summary and Outlook	71
6	Simulation of on- and off-shell $t\bar{t}$ production with <code>bb4l</code>	74
6.1	Introduction	74
6.2	The Monte Carlo generator <code>bb4l</code>	74
6.3	Other $t\bar{t}$ Monte Carlo generators	75
6.3.1	<code>hvq</code>	76
6.3.2	<code>ST_wtch</code>	76
6.3.3	<code>ttb_NLO_dec</code>	76
6.4	Technical setup	77
6.4.1	Parton shower matching	77
6.4.2	Same-flavor leptons	78
6.5	Results	78
6.5.1	Comparison between generators	78
6.5.2	Comparison of FSR matching settings	84
6.5.3	Recoil in top decay	86
6.6	Summary and Outlook	88
7	Search for heavy scalar or pseudoscalar bosons in $t\bar{t}$ final states	89
7.1	Introduction	89
7.2	Analysis setup	90
7.2.1	Datasets	90
7.2.2	Object definition	93
7.2.3	Event selection	93
7.2.4	Experimental corrections	94
7.2.5	Reconstruction of the $t\bar{t}$ system	96
7.2.6	Sensitive observables	99
7.3	Higher-order corrections in $t\bar{t}$	100
7.3.1	NNLO QCD corrections	101
7.3.2	NLO EW corrections	101
7.4	Matrix element reweighting for A/H signals	103
7.4.1	Principle of the method	103
7.4.2	Combination of multiple origin samples	105
7.4.3	Validation	106

7.5	Systematic uncertainties	106
7.5.1	Theory uncertainties	106
7.5.2	Experimental uncertainties	109
7.5.3	Uncertainty smoothing	110
7.5.4	Differences between MC generators	111
7.6	Pre-fit distributions	113
7.7	Interpretation of the excess	119
7.7.1	Extraction of $t\bar{t}$ bound state effects	119
7.7.2	Parity of the excess	119
7.7.3	Checks of the result	119
7.7.4	Interpretation in terms of A and H	126
7.8	Limits on A/H bosons	127
7.9	Combination with the $\ell+$ jets channels	129
7.9.1	Analysis strategy in the $\ell+$ jets channel	129
7.9.2	A/H limits	135
7.9.3	Simultaneous A+H exclusion contours	135
7.10	Comparison to other results	142
7.10.1	ATLAS $A/H \rightarrow t\bar{t}$ search	142
7.10.2	Other $t\bar{t}$ measurements	143
7.11	Summary and Outlook	144
8	Investigation of Axion-Like Particles decaying to $t\bar{t}$	146
8.1	Introduction	146
8.2	Translation of experimental limits	146
8.3	Phenomenological setup	148
8.4	Comparison of ALP and A	150
8.5	Projected limits for ALPs	152
8.6	Summary and Outlook	154
9	Summary and Conclusions	156
A	Bibliography	157

¹ 1 Introduction

² It has always been the goal of high-energy physics to decipher the fundamental rules
³ of nature. The most recent triumph in this journey was undoubtably the discovery of
⁴ the Higgs boson at the ATLAS and CMS experiments of the Large Hadron Collider
⁵ (LHC) in 2012 [1–3], thus completing the Standard Model of particle physics (SM).
⁶ Since then, the SM has been measured with ever-growing precision in the hope
⁷ of finding and characterizing possible deviations from its predictions, and searches
⁸ for new phyiscs beyond the Standard Model (BSM) have been performed in many
⁹ possible phase spaces and for many SM extensions. So far, no significant discrepancy
¹⁰ has been found.

¹¹ One promising avenue for searches for new physics is the top quark, which is
¹² the most massive fundamental particle in the SM. It is thus relevant for possible
¹³ new particles with Yukawa couplings, i.e. couplings proportional to the particle
¹⁴ mass, such as extended Higgs sectors. It is also of interest within the context of
¹⁵ the SM: as the only colored particle that decays before hadronizing, it allows for
¹⁶ measurements of spin properties, and poses challenges for its precision modeling in
¹⁷ quantum chromodynamics (QCD).

¹⁸ In this thesis, different aspects of top quark pair ($t\bar{t}$) production in proton-proton
¹⁹ collisions at the LHC are studied. It has been performed as part of the Compact
²⁰ Muon Solenoid (CMS) experiment [4], which is one of the two large general-purpose
²¹ LHC experiments. The first topic is a measurement of the inclusive $t\bar{t}$ production
²² cross section, performed at a center-of-mass energy of $\sqrt{s} = 13.6$ TeV [5]. This world-
²³ record energy was reached by the LHC for the first time in 2022 at the start of LHC
²⁴ Run 3, after three years of shutdown and technical upgrades. The measurement
²⁵ performed here uses only 1.21 fb^{-1} of data, taken directly at the start of Run 3 in
²⁶ July and August 2022, to achieve a precision on the $t\bar{t}$ cross section comparable with
²⁷ previous LHC measurements. This was made possible by designing a strategy aimed
²⁸ at estimating needed experimental corrections directly as part of the measurement.
²⁹ In addition to confirming the SM at a new energy, the result was the first public
³⁰ result of LHC Run 3 and showed the high quality of the then-fresh collision data.

³¹ Second, the modeling of $t\bar{t}$ production in off-shell regions of phase space as well
³² as the interference between $t\bar{t}$ and tW production at CMS is studied [6]. This is
³³ done using the Monte Carlo (MC) event generator **bb41** [7], which computes the full
³⁴ $pp \rightarrow b\bar{b}\ell^+\ell^-\nu_\ell\bar{\nu}_\ell$ matrix element for the dilepton decay channel of $t\bar{t}$, thus naturally
³⁵ including off-shell and interference effects. **bb41** is validated for the first time in
³⁶ the CMS simulation setup, and compared to other MC generators for $t\bar{t}$ production,

³⁷ preparing its use in future precision $t\bar{t}$ measurements at CMS.

³⁸ Finally, a search for new spin-0 states decaying to $t\bar{t}$ is performed, using the
³⁹ full CMS Run 2 dataset with a luminosity of 138 fb^{-1} [8, 9]. The dilepton decay
⁴⁰ channel of $t\bar{t}$ is considered, and besides the invariant $t\bar{t}$ mass ($m_{t\bar{t}}$), spin correlation
⁴¹ observables constructed from the leptons and top quarks are used to distinguish
⁴² different spin states of the $t\bar{t}$ system, giving sensitivity to the \mathcal{CP} structure of possible
⁴³ new states. Excitingly, a statistically significant excess is observed in the data
⁴⁴ compared to the standard SM predictions, which is located at low $m_{t\bar{t}}$ values and
⁴⁵ prefers pseudoscalar spin states. The excess is interpreted to be consistent with a
⁴⁶ pseudoscalar $t\bar{t}$ (quasi-)bound state, which is expected to exist in the SM according
⁴⁷ to non-relativistic QCD calculations, though its modeling remains a challenge. This
⁴⁸ constitutes the first time such a $t\bar{t}$ bound state is experimentally observed.

⁴⁹ Alternatively, the results are interpreted in terms of generic additional pseu-
⁵⁰ doscalar or scalar bosons, as expected e.g. in a Two-Higgs-Doublet Model. The
⁵¹ interference of these new bosons decaying to $t\bar{t}$ and SM $t\bar{t}$ production is taken into
⁵² account, leading to complex signatures in the $m_{t\bar{t}}$ spectrum. In addition to an inter-
⁵³ pretation of the same low- $m_{t\bar{t}}$ excess, exclusion regions are derived for the presence
⁵⁴ of either one or two such new bosons in terms of their couplings to the top quark.
⁵⁵ For this purpose, the analysis of the dilepton decay channel of $t\bar{t}$ is further combined
⁵⁶ with a separate analysis of the lepton+jets decay channel.

⁵⁷ As a third interpretation, heavy Axion-Like Particles (ALPs) decaying to $t\bar{t}$ are
⁵⁸ considered for the first time [10]. After explicitly translating the experimental results
⁵⁹ for generic pseudoscalars to ALPs in the limiting case of no explicit gluon couplings,
⁶⁰ the general case is studied in simulated events. Sensitivity estimates for heavy
⁶¹ ALPs coupling to top quarks, and for the possibility to distinguish them from other
⁶² pseudoscalars, are derived for the currently available luminosity as well as future
⁶³ projections.

⁶⁴ The thesis is organized as follows. In Chapters 2 to 4, the framework used for
⁶⁵ the analyses is outlined. In particular, Chapter 2 describes aspects of the SM and
⁶⁶ BSM theories relevant for this work, Chapter 3 briefly discusses the machinery of
⁶⁷ Monte Carlo generators as used for all relevant studies, and Chapter 4 describes the
⁶⁸ LHC and the CMS detector as well as object reconstruction and statistical inference
⁶⁹ techniques. Following that, Chapters 5 to 8 each discuss one of the experimental
⁷⁰ or phenomenological results that comprise this work: the inclusive $t\bar{t}$ cross section
⁷¹ measurement in Chapter 5, the study of off-shell $t\bar{t}$ production and $t\bar{t}/tW$ inter-
⁷² ference in Chapter 6, the search for spin-0 states in $t\bar{t}$, including its interpretation
⁷³ as a $t\bar{t}$ bound state, in Chapter 7, and the investigation of ALPs decaying to $t\bar{t}$
⁷⁴ in Chapter 8. Chapters 5 and 6 fully consist of work done as part of this thesis,
⁷⁵ while in Chapters 7 and 8 the major contributions from this thesis are summarized
⁷⁶ at the beginning of the chapters. Finally, a short summary and outlook is given in
⁷⁷ Chapter 9.

⁷⁸ 2 Theoretical framework

⁷⁹ This chapter gives an outline of the theoretical concepts and models used in this
⁸⁰ thesis. It is split into two parts: First, the Standard Model of elementary particle
⁸¹ physics is discussed, with a heavy emphasis on the top quark. Secondly, several
⁸² hypothesized extensions of the Standard Model, relevant for the searches presented
⁸³ in Chapters 7 and 8, are briefly introduced and compared.

⁸⁴ 2.1 Standard Model

⁸⁵ The Standard Model of elementary particle physics, often simply called the Stan-
⁸⁶ dard Model or SM, is, at the time of writing, the most successful theory describing
⁸⁷ the fundamental particles making up our universe. It is the result of a steady pro-
⁸⁸ gression of increasingly complex models, starting with the introduction of quantum
⁸⁹ mechanics in the early 20th century and ending - for now - with the discovery of the
⁹⁰ Higgs boson at the LHC in 2012. The model has been extensively tested at many
⁹¹ different experiments, most importantly the large collider experiments like LEP, the
⁹² Tevatron, and the LHC. So far, it has survived all these tests with excellence.

⁹³ The SM is formulated as a relativistic quantum field theory (QFT). That is, its
⁹⁴ most fundamental objects are fields acting on four-dimensional spacetime which,
⁹⁵ after a quantization procedure, yield physically observable particles as fundamental
⁹⁶ excitations. By the usual counting scheme, there exist seventeen different such fields,
⁹⁷ which can be classified into different groups, as schematically shown in Fig. 2.1.

⁹⁸ The first group consists of the twelve fermions, which have spin $\frac{1}{2}$ and make up
⁹⁹ all visible matter. They are further split into the leptons, consisting of three elec-
¹⁰⁰ trically charged leptons - electron, muon, and tau lepton - and three corresponding
¹⁰¹ electrically neutral neutrinos, as well as the quarks, of which there are six differ-
¹⁰² ent flavors, called up, down, strange, charm, bottom, and top. The quarks have
¹⁰³ fractional electric charge, and in addition carry color charge as their defining prop-
¹⁰⁴ erty. Of note is that the fermions are also split into three generations, with each
¹⁰⁵ generation consisting of a charged lepton, a neutrino, and two quarks. The only fun-
¹⁰⁶ damental differences between the particles of different generations are their masses,
¹⁰⁷ though the resulting physically observable properties, such as the lifetime, might be
¹⁰⁸ dramatically different.

¹⁰⁹ The second group of particles are the bosons, which have integer spin. Here,
¹¹⁰ the four gauge bosons with spin 1 act as the force carriers of the four fundamental
¹¹¹ interactions described by the SM: the photon, for the electromagnetic interaction

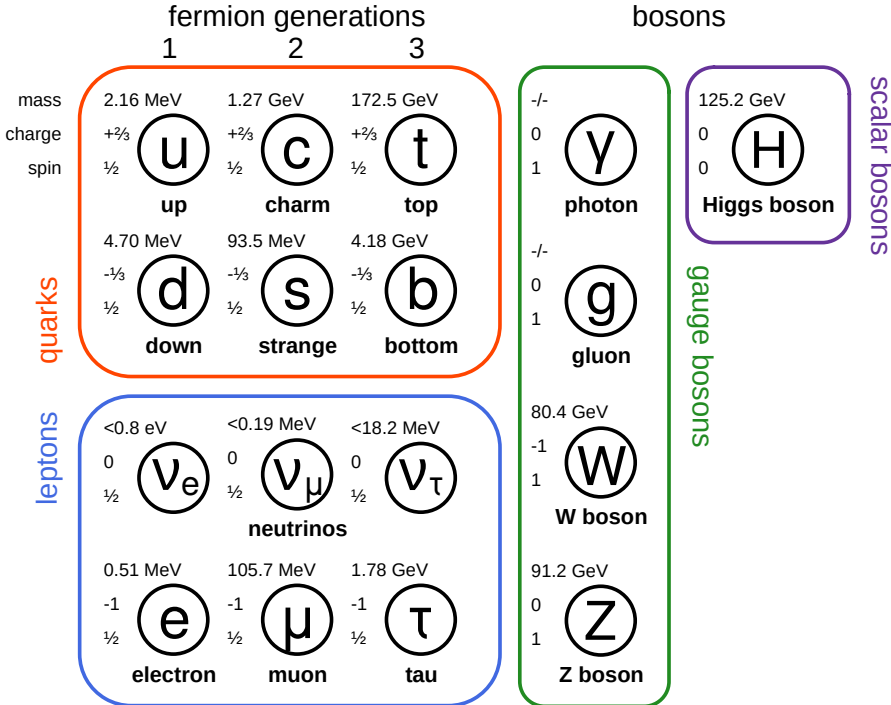


Figure 2.1: **The Standard Model.** A schematic depiction of the particle content of the SM, showing the seventeen fundamental particles, split into six quarks, six leptons, four gauge bosons, and the Higgs boson. The masses, electromagnetic charges, and spin of the particles is given next to the labels. Mass information is taken from Ref. [11].

with coupling strength α_{elm} ; the W and Z bosons, for the weak interaction with coupling strength α_W ; and the gluon, for the strong interaction with coupling strength α_S . At high enough energies, the electromagnetic and weak interaction unify into the electroweak interaction (coupling strength α_{EW}). The last and final particle is the Higgs boson, which has spin 0. Its most important role in the SM is to give mass to the fermions, as well as the W and Z bosons, through the so-called Higgs mechanism [12, 13], which is briefly outlined in Sec. 2.1.2.

2.1.1 Top quark

All results presented as part of this thesis focus on one particular fundamental particle: the top quark. As such, it will be described in further detail in this section.

The top quark was first discovered in 1995 at the Tevatron by the CDF and D0 experiments [14, 15]. With a rest mass of $m_t \approx 172.5 \text{ GeV}$, the top quark is the most massive known fundamental particle, and as a result it has unique properties compared to the other quarks: Its extremely short lifetime of $\sim 5 \times 10^{-25} \text{ s}$ is lower

than the typical time needed for a quark to hadronize under the strong interaction, making it the only bare quark - that is, the only quark which, via its decay products, is observable outside of hadrons. Among others, a consequence of this is that it fully preserves spin information during its decay, while such information is typically lost for other quarks during hadronization. More details on this are found in Sec. 2.2.2.

A second extraordinary property of the top quark that follows from its high mass is its large Yukawa coupling to the SM Higgs boson, which is of order one. As a result, the Higgs boson couples preferentially to the top quark of all SM particles, and the study of both the SM Higgs boson and hypothetical additional Higgs bosons (see Sec. 2.3) is tightly connected to the top quark.

In the SM, the top quark decays to a bottom quark and a W boson with a branching ratio (BR) of almost 100% (to the degree that all other decays are commonly neglected). The W boson, in turn, can decay either to a charged lepton (e , μ or τ) and the corresponding neutrino with a BR of $\sim 32.6\%$, or to a pair of quarks (one up- and one down-type) with a BR of $\sim 67.4\%$. This results in different final states for top production processes, which are discussed more in Sec. 2.2.

2.1.2 Higgs mechanism

The Higgs boson is the most recently discovered particle of the SM. Its existence was confirmed in 2012 at the LHC by the ATLAS and CMS collaborations [1–3], firmly establishing the SM in its current form as the accepted description of elementary particle physics. While this work does not focus on the SM Higgs boson as it does on the top quark, a short discussion of its role in the SM - the so-called Higgs mechanism - is relevant for possible SM extensions to additional Higgs bosons, which are searched for in Chapters 7 and 8.

In the SM Lagrangian, the Higgs boson appears as a complex doublet ϕ in the form

$$\mathcal{L}_{\text{SM}} \subset (D_\mu \phi)^\dagger D^\mu \phi + V(\phi) \quad (2.1)$$

where D_μ is the covariant derivative, containing the minimal coupling to the gauge fields, and the Higgs potential $V(\phi)$ is

$$V(\phi) = \mu^2 \phi^\dagger \phi - \lambda (\phi^\dagger \phi)^2. \quad (2.2)$$

Here, μ^2 and λ are free parameters of the model. If both parameters are positive, this potential (known as the “Mexican hat potential”) has a minimum at a non-zero value of

$$|\phi| = \frac{\mu}{\sqrt{2\lambda}} \equiv \frac{v}{\sqrt{2}} \quad (2.3)$$

with the vacuum expectation value $v = \mu/\sqrt{\lambda}$. On the other hand, the minimum -

158 corresponding to the vacuum state - is degenerate with respect to the three phases
159 (i.e. the $SU(2)$ symmetry) of the complex doublet.

160 In the Higgs mechanism, this symmetry is now spontaneously broken in the transi-
161 tion from the high-energy state of the early universe (where the minimum is at
162 $|\phi| = 0$) to the low-energy state observed today. The physical particles after sym-
163 metry breaking are then described by fluctuations around the new vacuum state.
164 If the Higgs field were to be considered on its own, this would lead to one massive
165 (corresponding to fluctuations in the $|\phi|$ direction) and three massless degrees of
166 freedom (corresponding to the phases).

167 However, the interaction with the electroweak gauge fields encoded within D_μ
168 leads to the massless degrees of freedom being absorbed into the gauge fields. This
169 turns three of the four massless spin-1 gauge fields of the electroweak Lagrangian
170 (with two degrees of freedom each) into massive fields instead (which have an ad-
171 ditional longitudinal polarization, and thus three degrees of freedom). These three
172 massive gauge fields are identified with the W and Z bosons, while the remaining
173 massless field is identified with the photon. Finally, the leftover massive degree of
174 freedom from the Higgs doublet ϕ is identified with the spin-0 boson observed at
175 the LHC.

176 The resulting masses of the Z, W and Higgs bosons can be predicted as a function
177 of μ^2 , λ and the electroweak couplings and thus used to test the Higgs mechanism.
178 In addition to the electroweak bosons, the Higgs mechanism can also give masses to
179 fermions (charged leptons and quarks) by including a Yukawa interaction term in the
180 Lagrangian. This results in couplings between the SM Higgs boson and the different
181 fermions that are proportional to the respective fermion mass, leading to the largest
182 coupling to the top quark. In possible extensions of the SM, this proportionality
183 might be modified, making Yukawa coupling measurements attractive as tests of the
184 SM.

185 2.2 The $pp \rightarrow t\bar{t}$ process

186 In proton-proton collisions at the LHC, the dominant production mode of top quarks
187 is the production of a top-antitop quark pair ($t\bar{t}$). The different parts of this thesis all
188 focus on this process in different ways, and so this chapter gives a detailed overview
189 of relevant effects.

190 At LO in QCD, there are three diagrams (up to permutations of initial and final
191 states) contributing to $t\bar{t}$ production, which can be seen in Fig. 2.2. They differ in
192 their initial states: the first two diagrams are induced by gluon fusion, while the
193 last one is induced by quark fusion (mostly from $u\bar{u}$ and $d\bar{d}$). The fraction of these
194 is determined by the corresponding parton densities; at a center-of-mass energy of
195 $\sqrt{s} \geq 13$ TeV, gluon fusion dominates with a fraction of roughly 90%.

196 At NLO in QCD, many more diagrams become relevant, including those induced

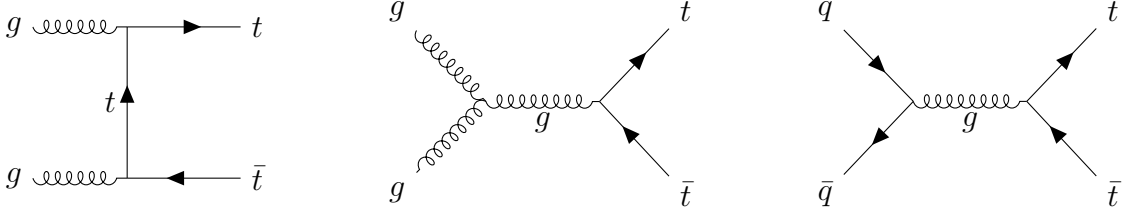


Figure 2.2: **Feynman diagrams for $pp \rightarrow t\bar{t}$.** The three diagrams (up to permutations) that contribute to the $pp \rightarrow t\bar{t}$ process at LO in QCD.

by the fusion of one quark and one gluon, while radiating a real quark. Similarly, real emissions of gluons can take place in gg or $q\bar{q}$ fusion diagrams. These effects change the kinematic properties of the produced top quarks, leading to NLO corrections for predicted distributions.

After production, both the top quark and antiquark in the $t\bar{t}$ pair decay into a W boson and a b (anti)quark each. This leads to three different decay channels of the $t\bar{t}$ pair depending on the decays of the two W bosons, which are classified according to their number of leptons: The dilepton channel, with final state $b\bar{b}\ell^+\ell^-\nu\bar{\nu}$; the lepton+jets channel, with final state $b\bar{b}\ell\nu q\bar{q}$; and the all-hadronic channel, with final state $b\bar{b}qq\bar{q}\bar{q}$. Here, q stands in for any light quark (u, d, s or c).

The three channels differ greatly in their experimental challenges: The dilepton channel has the lowest branching ratio of $\sim 10.6\%$, which is further reduced to $\sim 5.1\%$ when excluding τ leptons due to then being experimentally hard to reconstruct. It also suffers from the fact that the two produced neutrinos escape the detector unobserved and are only measured as missing transverse momentum, losing both information in the forward direction as well as the ability to disentangle the two neutrinos. On the other hand, the final state of two opposite-sign charged leptons, two b jets, and missing transverse momentum does not have many other contributing processes in the SM, leading to very pure selections (particularly when the two leptons are an electron and a muon). All results in this thesis make use of this channel prominently.

By contrast, the lepton+jets channel has a large BR of $\sim 43.9\%$ ($\sim 30.3\%$ when excluding τ leptons), leading to high data statistics, and allows for easier interpretation of the missing transverse momentum due to only one neutrino. However, it can suffer from contamination by W+jets and multijet QCD background (the latter with non-prompt or fake leptons), from issues with combinatorics (i.e. the assignment of experimentally measured jets to the decay products) and from hadronic jet uncertainties, which can be large. This decay channel is employed for the result in Chapter 5 as well as in the combination in Chapter 7.

Finally, the all-hadronic channel, with a similar BR of $\sim 45.4\%$, is typically difficult to isolate from the background of QCD multijet production, and in addition suffers even more strongly from combinatorics and jet uncertainties than the

Term symbol	Spin multiplicity	\mathcal{P}	\mathcal{C}
1S_0	singlet	-1	+1
3P_0	triplet	+1	+1
3S_1	triplet	-1	-1
1P_1	singlet	+1	-1
3P_1	triplet	+1	+1
3D_1	triplet	-1	-1

Table 2.1: **Spin states of $t\bar{t}$.** Overview of the possible angular momentum states of the $t\bar{t}$ system with $J \leq 1$, including the spin multiplicity, the parity \mathcal{P} and the charge-parity \mathcal{C} .

229 lepton+jets channel. As a result, it is in many cases the least precise of the three
 230 channels, and is not studied further in this work.

231 2.2.1 Spin state of the $t\bar{t}$ system

232 As fermions with spin $\frac{1}{2}$, top quarks have two possible spin states. As a result, the
 233 relative spins of the $t\bar{t}$ system can be either aligned, leading to a total vector state
 234 with spin $S = 1$, or anti-aligned, leading to a scalar state with spin $S = 0$. Further-
 235 more, the $t\bar{t}$ system as a whole can have orbital angular momentum L , where L is a
 236 non-negative integer. In analogy to atomic orbitals, the total angular momentum is
 237 then $\vec{J} = \vec{L} + \vec{S}$, and for any chosen basis the set of quantum numbers $\{S, L, J, J_z\}$
 238 consists of conserved quantities. The angular momentum state is commonly written
 239 using a term symbol $^{2S+1}L_J$, where $2S + 1$ denotes the multiplicity of the spin state,
 240 and the orbital angular momentum L is written using spectroscopic notation (S for
 241 $L = 0$, P for $L = 1$, D for $L = 2$ etc). An overview of the lowest possible states
 242 ($J \leq 1$) is given in Tab. 2.1, including also the parities and charge-parities \mathcal{P} and
 243 \mathcal{C} , which can be inferred from the intrinsic parities of top and antitop as well as the
 244 orbital angular momentum. In proton-proton collisions, a mixture of all these states
 245 is produced, with the ratio depending on the production mode (gg , $q\bar{q}$ or gq) as well
 246 as the energy.

247 In practice, the spins of the top (anti)quarks cannot be observed directly, and
 248 instead must be inferred from their decay products. The way in which the spin
 249 information is passed to the decay products is determined by the maximally parity-
 250 violating nature of the weak interaction together with conservation of angular mo-
 251 mentum. This is illustrated in Fig. 2.3 for the leptonic decay of the top (anti)quark:
 252 Since the b quark is light compared to the top quark and will thus be ultra-
 253 relativistic, as a fermion its helicity is determined by its chirality. As a result,
 254 for the decay $t \rightarrow W^+b$ the b quark - left-handed due to the weak interaction - has
 255 negative helicity (spin opposite to its direction of flight), leading to two possibilities

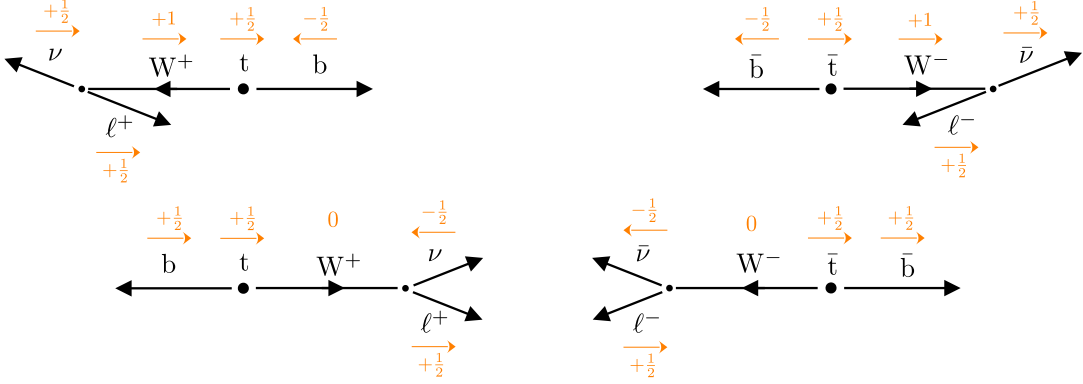


Figure 2.3: **Helicity in top decays.** Sketch of the allowed helicity configurations in a top quark (left) and antiquark decay (right) in the rest frame of the quark, involving either a transversely (top, $S_z = 1$) or longitudinally polarized W boson (bottom, $S_z = 0$). The z axis corresponds to the spin of the top (anti)quark, and the orange arrows and numbers illustrate the spin in the z direction of the respective particles. It can be seen that, due to conservation of angular momentum and the parity-violating nature of the weak interaction, the ℓ^+ is preferred to be emitted in the direction of the t spin, while the ℓ^- is preferred to be emitted opposite to the direction of the \bar{t} spin.

for the W boson through conservation of angular momentum: transversely polarized (spin 1, top left in Fig. 2.3) or longitudinally polarized (spin 0, bottom left in Fig. 2.3).

Since the decay of the W^+ into $\ell^+\nu$ is again mediated by the weak interaction, and both decay products are nearly massless, the helicities of ℓ^+ and ν must be positive and negative, respectively. Applying again conservation of angular momentum, one finds from the sketch that in both cases, the charged lepton is emitted preferably in the direction of the top quark spin.

Repeating the same line of arguments for the decay of the antitop (Fig. 2.3 on the right), one finds that the opposite holds there: the charged lepton is emitted preferably opposite to the antitop spin. As a result, the direction of flight of the charged lepton in the center-of-mass system of its parent (anti)top can be used as a proxy for the (anti)top spin (or, equivalently, its polarization). It should be noted that this property of the top quark is unique among the quarks of the SM, since all other quarks hadronize via the helicity-ignorant strong interaction, losing all information about the spin.

Returning to the full $t\bar{t}$ system, and applying the above observation to both top and antitop, one can now define observables to probe the $t\bar{t}$ spin state, or equivalently, the spin correlation between t and \bar{t} . A simple such variable is the azimuthal difference $\Delta\phi_{\ell\ell}$ between the two leptons in a dileptonic decay. Assuming

276 that the top and antitop are emitted back-to-back, a state with the top and antitop
 277 spins aligned (i.e. $S = 1$) will cause the two leptons to be emitted preferably in
 278 opposite directions, leading to large $\Delta\phi_{\ell\ell}$, while anti-aligned spins ($S = 0$) will
 279 lead preferably to parallel leptons and thus small $\Delta\phi_{\ell\ell}$. While this variable has
 280 the advantage of being easy to define and experimentally clean to measure, it is
 281 suboptimal in that it is also strongly affected by the kinematics of the $\text{t}\bar{\text{t}}$ production,
 282 including higher-order corrections in QCD. Thus, it is afflicted with large modeling
 283 uncertainties.

284 A more powerful variable can be defined by employing suitable reference systems
 285 as follows: the lepton and antilepton are first Lorentz boosted into the center-of-
 286 mass frame of the $\text{t}\bar{\text{t}}$ system, and then further boosted into the center-of-mass frame
 287 of their parent (anti)tops. Then, a correlation variable c_{hel} is defined as the scalar
 288 product of their direction unit vectors in these reference frames¹:

$$c_{\text{hel}} = \hat{\ell}_t^+ \cdot \hat{\ell}_{\bar{t}}^- \quad (2.4)$$

289 It can be shown that, irrespective of the mode of production of the $\text{t}\bar{\text{t}}$ system and
 290 inclusive in the rest of the phase space, the distribution of this observable always
 291 follows a straight line [17], i.e.

$$\frac{1}{\sigma} \frac{d\sigma}{dc_{\text{hel}}} = \frac{1}{2} (1 - D c_{\text{hel}}) \quad (2.5)$$

292 The slope D depends on the spin and angular momentum of the produced $\text{t}\bar{\text{t}}$ state.
 293 At LO in QCD, it can be shown that $D = -1$ for pure singlet states (anti-aligned
 294 spins, e.g. ${}^1\text{S}_0$, ${}^1\text{P}_1$) and $D = +\frac{1}{3}$ for pure triplet states (aligned spins, e.g. ${}^3\text{S}_1$,
 295 ${}^3\text{P}_0$) [18]. Higher-order corrections in QCD can slightly reduce these slopes through
 296 emissions of real gluons in the decay, which weaken the correlations, but these effects
 297 are on the order of 0.2% at NLO for leptons [19, 20].

298 In practice, any observed ensemble of $\text{t}\bar{\text{t}}$ pairs will be a mixture of the different spin
 299 states depending on the production mechanism and underlying theory, which can
 300 be probed by measuring the slope D . As will be discussed in Sec. 2.3, extensions
 301 of the SM can change the predicted slope, making measurements of D attractive
 302 tests for new physics. The value of D has been measured e.g. in Refs. [21–23], as
 303 well as more recently as a proxy variable in the context of measurements of quantum
 304 entanglement in $\text{t}\bar{\text{t}}$ production [24, 25].

305 2.2.2 Spin density matrix

306 A more detailed way to quantify the spin properties of the $\text{t}\bar{\text{t}}$ system, respective
 307 to an arbitrary spin basis, is the production spin density matrix \mathbf{R} , which (when

¹In this work, the naming convention from Ref. [16] is followed for c_{hel} . In e.g. Ref. [17], this variable is instead called $\cos\varphi$.

2 Theoretical framework

308 averaged over initial spins and colors, and summed over final colors) can be written
309 as [18, 26]

$$\mathbf{R} = A \mathbb{1} \otimes \mathbb{1} + B_i^1 \sigma_i \otimes \mathbb{1} + B_i^2 \mathbb{1} \otimes \sigma_i + C_{ij} \sigma_i \otimes \sigma_j. \quad (2.6)$$

310 Here, $\mathbb{1}$ is the two-dimensional identity matrix, σ_i with $i = 1, 2, 3$ are the Pauli
311 matrices, and the first and second components of the tensor product refer to the
312 spin of the top quark and antiquark, respectively. The scalar coefficient A describes
313 the overall amplitude (i.e. the cross section) of $t\bar{t}$ production, the vectors \vec{B}^1 and
314 \vec{B}^2 describe the polarization of the top quark and antiquark, and the matrix \mathbf{C}
315 describes the correlation between their spins. All of them are, in general, functions
316 of the partonic center-of-mass energy and the scattering angle of the top quark
317 relative to the incoming partons.

318 As explained in Sec. 2.2.1, in a dileptonic decay the spin information is transferred
319 almost completely to the charged leptons. Defining the lepton directions of flight in
320 their parent frames $\hat{\ell}_t^+$ and $\hat{\ell}_{\bar{t}}^-$ as in Eq. (2.4), the resulting differential cross section
321 in terms of the lepton angles is [26]

$$\frac{1}{\sigma} \frac{d\sigma}{d\Omega} = 1 + \vec{B}^1 \cdot \hat{\ell}_t^+ + \vec{B}^2 \cdot \hat{\ell}_{\bar{t}}^- + (\hat{\ell}_t^+)^T \mathbf{C} \hat{\ell}_{\bar{t}}^- \quad (2.7)$$

322 By integrating out the remaining angles, it can be shown from this that irrespec-
323 tive of the chosen basis the slope D as defined in Eq. (2.5) can be recovered from
324 the matrix \mathbf{C} as [17, 27]

$$D = -\frac{1}{3} \text{Tr} [\mathbf{C}] \quad (2.8)$$

325 As discussed in Sec. 2.2.1, D is maximally negative for pure singlet states, and thus
326 is ideal for separating those in a mixed ensemble. One can define similar separating
327 observables for other states using the spin density matrix by choosing a suitable spin
328 basis. In this work, the so-called helicity basis proposed in Ref. [28] is used. The
329 three axes of this basis, denoted \hat{k} , \hat{r} and \hat{n} , are defined as follows: \hat{k} is simply the
330 direction of flight of the top quark in the center-of-mass frame of the $t\bar{t}$ system, such
331 that the top quark spin with respect to \hat{k} is equal to the helicity. The second axis,
332 \hat{r} , is orthogonal to \hat{k} in the scattering plane of the $pp \rightarrow t\bar{t}$ process. Finally, the
333 third axis \hat{n} is orthogonal on both \hat{k} and \hat{r} , oriented such that the $\{\hat{k}, \hat{r}, \hat{n}\}$ system
334 is left-handed. If \hat{p} denotes the beam axis and θ_t^* the top scattering angle, the latter
335 two axes are given by

$$\hat{r} = \frac{\hat{p} - \cos \theta_t^* \hat{k}}{|\hat{p} - \cos \theta_t^* \hat{k}|} \quad \text{and} \quad \hat{n} = \hat{r} \times \hat{k} = \frac{\hat{p} \times \hat{k}}{|\hat{p} \times \hat{k}|}. \quad (2.9)$$

336 This coordinate system is visualized in Fig. 2.4. It is used, among others, in
337 Refs. [22, 23] to measure both the polarizations \vec{B}^1 and \vec{B}^2 and spin correlation

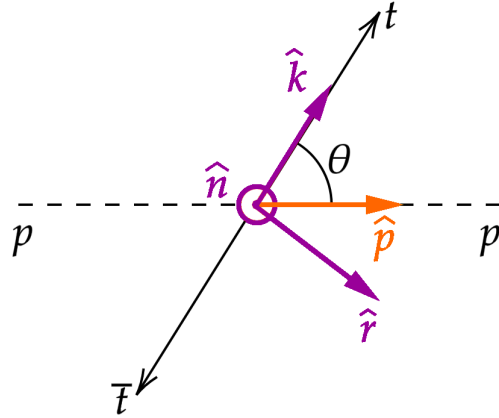


Figure 2.4: **Helicity basis.** Sketch of the helicity basis used to define the top and antitop quark spins. The unit vectors \hat{k} , \hat{r} and \hat{n} define the right-handed basis, while the beam axis is given by \hat{p} and the top quark scattering angle by θ . This figure is taken from Ref. [18].

³³⁸ coefficients C_{ij} ($i, j = k, r, n$). In this work, only the spin correlation is considered.
³³⁹ Particularly, in addition to c_{hel} , the following observable is defined:

$$c_{\text{han}} = (\hat{\ell}_t^+)_k (\hat{\ell}_{\bar{t}}^-)_k - (\hat{\ell}_t^+)_r (\hat{\ell}_{\bar{t}}^-)_r - (\hat{\ell}_t^+)_n (\hat{\ell}_{\bar{t}}^-)_n \quad (2.10)$$

³⁴⁰ where $(\hat{\ell})_i$, $i = k, r, n$ refers to the i -th component of the respective vector in the
³⁴¹ $\{k, r, n\}$ basis. This observable, like c_{hel} , has the advantage of always being linear
³⁴² in the absence of phase space cuts, i.e.

$$\frac{1}{\sigma} \frac{d\sigma}{dc_{\text{han}}} = \frac{1}{2} (1 + D^{(k)} c_{\text{han}}) \quad (2.11)$$

³⁴³ where [18]

$$D^{(k)} = -\frac{1}{3} (C_{kk} - C_{rr} - C_{nn}). \quad (2.12)$$

³⁴⁴ From Eq. (2.12), it can be seen that the slope $D^{(k)}$ is maximal when the top and
³⁴⁵ antitop spins are anti-correlated along the top direction of flight ($C_{kk} = -1$) and
³⁴⁶ correlated along the orthogonal directions ($C_{rr} = C_{nn} = +1$). The (unpolarized)
³⁴⁷ state described by these correlations can be shown to be a pure triplet state ($S =$
³⁴⁸ 1) [18].

349 2.2.3 Bound state effects in $t\bar{t}$

350 When predicting distributions of observables for hard scattering processes such as
 351 $t\bar{t}$ production, one usually employs perturbative calculations at a fixed order in the
 352 strong coupling constant α_S , possibly matched to a parton shower (see Chapter 3).
 353 However, at low energy scales (or equivalently, long distances) the strong interaction
 354 becomes non-perturbative, leading to effects that can not be captured in the usual
 355 perturbative expansion irrespective of the order in α_S .

356 In the $pp \rightarrow t\bar{t}$ process, such effects might play a role in the vicinity of the $t\bar{t}$ pro-
 357 duction threshold, i.e. for $m_{t\bar{t}} \sim 2m_t$, where the relative velocities of the produced
 358 top quarks become small. In particular, one possible class of non-perturbative ef-
 359 fects are $t\bar{t}$ bound states (“toponium”). Such states (also called quarkonia) are
 360 well-known in $c\bar{c}$ and $b\bar{b}$ production, where they lead to composite particles such as
 361 J/ψ , η_c or Υ . When translating this knowledge to $t\bar{t}$, however, there is a signifi-
 362 cant difference: due to the large top quark mass, the lifetime of the top quark is
 363 expected to be shorter than the (formal) lifetime of any possible $t\bar{t}$ bound state. As
 364 a result, the state would in the majority of cases not decay e.g. to photons, gluons
 365 or hadrons like the lighter quarkonia, but instead disassociate by one of the con-
 366 stituent top quarks decaying normally to Wb . This phenomenon, sometimes called
 367 a “quasi-bound state” or a “virtual bound state”, would lead to a possible peak in
 368 the $m_{WWb\bar{b}}$ spectrum slightly below the $t\bar{t}$ threshold.

369 Calculations of the $m_{WWb\bar{b}}$ spectrum at the $t\bar{t}$ threshold including the effects
 370 from a possible bound state have been performed independently in Refs. [29–33].
 371 All of these calculations work in the framework of non-relativistic QCD (NRQCD),
 372 which treats the slowly moving ($v \ll c$) top (anti)quarks as non-relativistic particles.
 373 This approach can be seen as a low-energy effective field theory (EFT) of the SM
 374 where high-energy modes have been integrated out. The result is a non-relativistic
 375 Schrödinger equation for the wavefunction of the $t\bar{t}$ system, with the interaction
 376 between the top quarks described by the low-energy limit of the QCD Coulomb
 377 potential, representing the exchange of soft gluons. At LO, it is given by [30]

$$V_{\text{QCD}}^{[1,8]}(q) = -\frac{4\pi\alpha_S C^{[1,8]}}{q^2}, \quad (2.13)$$

378 where the color factor is $C^{[1]} = 4/3$ for color-singlet and $C^{[8]} = -1/6$ for color-octet
 379 states. As a result, only $t\bar{t}$ systems in a color-singlet state feel an attractive force
 380 and can possibly form a bound state, while color-octet states are instead repulsed.
 381 At the LHC, $t\bar{t}$ bound states can thus at LO be produced only from gg initial states,
 382 since $q\bar{q}$ systems are always color-octets. From this, the spin state of the produced
 383 bound state can be inferred: Since both of the top quarks have low velocity, states
 384 with orbital angular momentum $L \neq 0$ will be strongly suppressed (beyond NLO in
 385 NRQCD [30]). Since the gg initial state in $t\bar{t}$ production always has spin $S = 0$ (and
 386 thus total angular momentum $J = 0$), the resulting $t\bar{t}$ system must be in the ${}^1S_0^{[1]}$

³⁸⁷ state. At NLO in QCD, also $^3S_1^{[1]}$ states can be produced; however, the contribution
³⁸⁸ is very small (less than 0.1% of the total cross section [30]).

³⁸⁹ Refs. [30–33] agree that the binding energy of the $t\bar{t}$ bound state, defined as the
³⁹⁰ difference of the peak position in the $m_{WWb\bar{b}}$ spectrum to $2m_t$, is around -2 GeV ,
³⁹¹ resulting in a “mass” of 343 GeV for the $t\bar{t}$ bound state for a top mass of 172.5 GeV .
³⁹² The exact lineshape of the peak is less well known. However, the experimental
³⁹³ resolution of $m_{WWb\bar{b}}$ is expected to be much larger than the bound state width of
³⁹⁴ order $\sim 2\Gamma_t$ (see Sec. 7.2.5), making the details of the spectrum irrelevant to an
³⁹⁵ experimental search.

³⁹⁶ The existing NRQCD calculations predict only certain differential distributions
³⁹⁷ and cannot be directly compared to experimental data on a per-event level. Because
³⁹⁸ of this, a simplified model for the $t\bar{t}$ bound state is introduced following Refs. [18,
³⁹⁹ 34–36]. Instead of a first-principles calculation, the bound state effects are modeled
⁴⁰⁰ as an additional state spin-0 state η_t , which is added to the conventional perturbative
⁴⁰¹ QCD (pQCD) calculation of $t\bar{t}$. η_t is defined to couple directly to gluons and top
⁴⁰² quarks via the Lagrangian

$$\mathcal{L}_{\eta_t} = -\frac{1}{4}g_{gg\eta_t}\eta_t G_{\mu\nu}^a \tilde{G}^{a\mu\nu} - ig_{t\bar{t}\eta_t}\eta_t \bar{t}\gamma_5 t \quad (2.14)$$

⁴⁰³ where $G_{\mu\nu}^a$ is the gluon field strength tensor, $\tilde{G}_{\mu\nu}^a$ its dual, and $g_{gg\eta_t}$ as well as $g_{t\bar{t}\eta_t}$
⁴⁰⁴ are arbitrary coupling strengths. The resulting model has three free parameters: the
⁴⁰⁵ binding energy $E_b = m(\eta_t) - 2m_t$, the total width $\Gamma(\eta_t)$ and the production cross
⁴⁰⁶ section $\sigma(\eta_t)$ (the latter determining the couplings $g_{gg\eta_t}$ and $g_{t\bar{t}\eta_t}$). In Ref. [35], they
⁴⁰⁷ are determined by fitting them to the NRQCD calculation from Ref. [31], yielding

$$E_b = -2\text{ GeV} \implies m(\eta_t) = 343\text{ GeV}, \quad \Gamma(\eta_t) = 7\text{ GeV}, \quad \sigma(\eta_t) = 6.43\text{ pb} \quad (2.15)$$

⁴⁰⁸ In the generation of events, the top quarks are allowed to be fully off-shell by
⁴⁰⁹ calculating the full amplitude $pp \rightarrow \eta_t \rightarrow W^+W^-b\bar{b}$, thus making sure that the
⁴¹⁰ phase-space region $m_{WWb\bar{b}} < 2m_t$ is populated. Furthermore, Ref. [35] recommends
⁴¹¹ that the contribution of η_t should be restricted to the region $|m_{WWb\bar{b}} - m_{\eta_t}| \leq 6\text{ GeV}$
⁴¹² so that the bulk of the $t\bar{t}$ phase space, in which the pQCD calculation is expected
⁴¹³ to be accurate while the NRQCD calculation misses relativistic corrections, is not
⁴¹⁴ affected.

⁴¹⁵ However, Refs. [34, 36] recommend instead

$$E_b = -2\text{ GeV} \implies m(\eta_t) = 343\text{ GeV}, \quad \Gamma(\eta_t) = 2\Gamma_t = 2.8\text{ GeV}. \quad (2.16)$$

⁴¹⁶ and no cut on $|m_{WWb\bar{b}} - m(\eta_t)|$.

⁴¹⁷ The resulting $m_{WWb\bar{b}}$ distribution for the combination of pQCD $t\bar{t}$ and η_t is shown

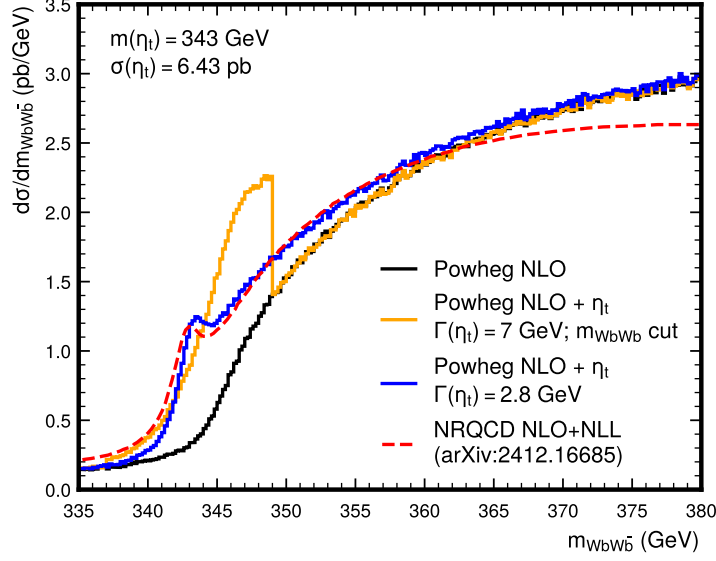


Figure 2.5: **Lineshape of η_t .** The $m_{WbWb\bar{b}}$ distribution close to the $t\bar{t}$ threshold, as predicted by the η_t model stacked on top of a pQCD $t\bar{t}$ prediction from Powheg hvq (see Sec. 3.1). For the orange line, the η_t width is chosen to be 7 GeV, and a cut on $|m_{WbWb\bar{b}} - m(\eta_t)|$ is applied (Eq. (2.15)), while for the blue line, the width is chosen as 2.8 GeV, and no further cuts are made (Eq. (2.16)). Both models are compared to an NRQCD prediction from Ref. [33].

in Fig. 2.5 at the level of hard scattering for both parametrizations, and compared to an NRQCD prediction from Ref. [33]. At the level of hard scattering, the lower width of $\Gamma(\eta_t) = 2\Gamma_t$ agrees much better with the predicted NRQCD spectrum and avoids an unphysical discontinuity due to the $m_{WbWb\bar{b}}$ cutoff. Thus, this parametrization will be used in this work wherever possible, i.e. in Secs. 7.7 and 7.8, though the parametrization of Eq. (2.15) is retained for the sake of consistency with other results in Sec. 7.9. For more details, see these sections.

In the final stages of this work, a more involved model for $t\bar{t}$ bound states was published in Ref. [37]. There, instead of simulating an additional pseudoscalar state η_t , the bound state effects are included in leading-order color-singlet $t\bar{t}$ production by directly reweighting produced events with the ratio of Green's functions. This model is in principle fully predictive, i.e. it does not require fitting parameters to external calculations. However, it could not be validated in time for inclusion in the results of Chapter 7, and it is also unclear on how to match it to the $t\bar{t}$ continuum. Because of this, it is not further considered here and its investigation left for future work.

While NRQCD predicts any possible $t\bar{t}$ bound state contribution to be dominated

435 by the ${}^1S_0^{[1]}$ state, with contributions from excited states strongly suppressed, ex-
 436 perimentally it will still be useful to compare this spin state to other possibilities.
 437 To this end, a second toy model, denoted χ_t , is defined in analogy to η_t by the
 438 interaction Lagrangian

$$\mathcal{L}_{\chi_t} = -\frac{1}{4}g_{gg\chi_t}\chi_t G_{\mu\nu}^a \tilde{G}^{a\mu\nu} - g_{t\bar{t}\chi_t}\chi_t \bar{t}t \quad (2.17)$$

439 where $g_{gg\chi_t}$ and $g_{t\bar{t}\chi_t}$ are again arbitrary couplings. This Lagrangian contains a \mathcal{CP} -
 440 even coupling to the top quark, compared to the \mathcal{CP} -odd coupling in Eq. (2.14). It
 441 thus produces $t\bar{t}$ systems in the ${}^3P_0^{[1]}$ state, which is the only other possible state with
 442 $J = 0$ (cf. Tab. 2.1). The free parameters of this model are again cross section, mass,
 443 and width; they are set here to the same values as for η_t in all cases. In Sec. 7.7.2,
 444 it will be used in conjunction with η_t to probe the spin state of the observed excess.
 445 Other possible states, such as the vector state ${}^3S_1^{[0]}$, are not considered here and
 446 instead left for future work.

447 2.3 Beyond the Standard Model

448 The Standard Model, greatly successful as it is at describing the results of collider
 449 experiments so far, is nonetheless known to be incomplete. In fact, there exist
 450 several experimental results which can not be explained by SM predictions, such
 451 as the observation of dark matter in many astrophysical contexts or the observed
 452 masses of the neutrinos.

453 In addition, the SM is plagued by several theoretical challenges that will likely not
 454 be overcome without major modifications to the theory. Chief among these is the
 455 unification of the forces of the SM - the electroweak and strong interactions - with
 456 gravity as described by General Relativity, which is not included in the SM at all.
 457 Doing so has proven extremely challenging, and no fully consistent unified theory
 458 of all forces is known yet. Further open questions are, for example, the hierarchy
 459 problem or the strong \mathcal{CP} problem.

460 In order to solve these problems in a satisfactory manner, the SM will have to be
 461 extended with new physics contributions, which in most cases results in additional
 462 as of yet undiscovered particles. There is a multitude of such Beyond the Standard
 463 Model (BSM) extensions, each attacking different parts of the problems, and one of
 464 the major tasks of particle physics is to explore which parts of the parameter space
 465 of these models can be probed with the current experiments.

466 This work, in particular, aims to probe models predicting new, heavy spin-0 states
 467 coupling strongly to the top quark. Such states can be searched for in the $pp \rightarrow t\bar{t}$
 468 process, as outlined in a generic fashion in Sec. 2.3.1. Following that, two explicit
 469 realizations of such models are discussed, namely the Two-Higgs Doublet Model
 470 (2HDM) (Sec. 2.3.2) and Axion-Like Particle (ALP) models (Sec. 2.3.3).

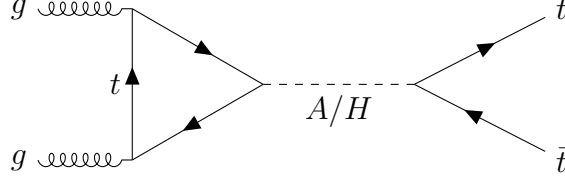


Figure 2.6: **Feynman diagram for $gg \rightarrow A/H \rightarrow t\bar{t}$.** Only the leading-order gluon fusion diagram is shown, with a top quark running in the loop.

471 2.3.1 Heavy scalars in $t\bar{t}$ production

472 Consider an unspecified BSM extension predicting (possibly among others) a massive
 473 spin-0 state Φ coupling to top quarks via a Yukawa interaction. In the absence of
 474 couplings to other particles, the Lagrangian of such a state can be written as [18]

$$\mathcal{L}_\Phi = \frac{1}{2}(\partial_\mu \Phi)(\partial^\mu \Phi) + \frac{m_\Phi^2}{2}\Phi^2 + g_{\Phi\bar{t}t} \frac{m_t}{v} \bar{t}\Phi (\cos \alpha + i\gamma_5 \sin \alpha) t. \quad (2.18)$$

475 where m_Φ is the mass of the new state and $g_{\Phi\bar{t}t}$ is a coupling modifier, scaled to
 476 the SM Higgs-top Yukawa coupling with the SM Higgs vacuum expectation value v .
 477 The phase α is a free parameter determining the \mathcal{CP} structure of the $\Phi\bar{t}t$ coupling:
 478 For $\alpha = 0$, the coupling is purely \mathcal{CP} -even or scalar, while for $\alpha = \pi/2$, the coupling
 479 is purely \mathcal{CP} -odd or pseudoscalar. Intermediate values for α will cause \mathcal{CP} -mixed
 480 couplings, which in general will result in \mathcal{CP} violation in processes involving top
 481 quarks. Possible experimental indicators of such \mathcal{CP} violation in $pp \rightarrow t\bar{t}$ are e.g.
 482 discussed in Ref. [27].

483 In the scope of this work, only the limiting \mathcal{CP} -conserving cases of Φ are consid-
 484 ered. For convenience, the pure pseudoscalar case will in the following be called A ,
 485 while the pure scalar case will be called H .

486 Similar to the SM Higgs boson, the most important production channel of either
 487 state at the LHC will be through loop-induced gluon fusion, followed by associated
 488 production with either $t\bar{t}$ or a single top quark. Only the former is considered here;
 489 experimental searches for the latter case can be found e.g. in Ref. [38]. Furthermore,
 490 the decay of the new state will depend on its mass: For low masses, the particle
 491 will decay either through loop-induced couplings to e.g. gg or $\gamma\gamma$ or, if present,
 492 through couplings to other SM or BSM particles than the top quark. For masses
 493 of $m_{A/H} > 2m_t$, however, the decay to $t\bar{t}$ is kinematically allowed and will in many
 494 cases be dominant due to the large Yukawa coupling. In this case, the process
 495 $gg \rightarrow A/H \rightarrow t\bar{t}$ will lead to the same final state as SM $t\bar{t}$ production, as illustrated
 496 in Fig. 2.6. This process will be considered in more detail in the rest of this chapter,
 497 and one of the main results of this thesis is an experimental search for such a
 498 signature (Chapter 7).

499 Fig. 2.7 shows the predicted differential cross sections of this model, in form of the

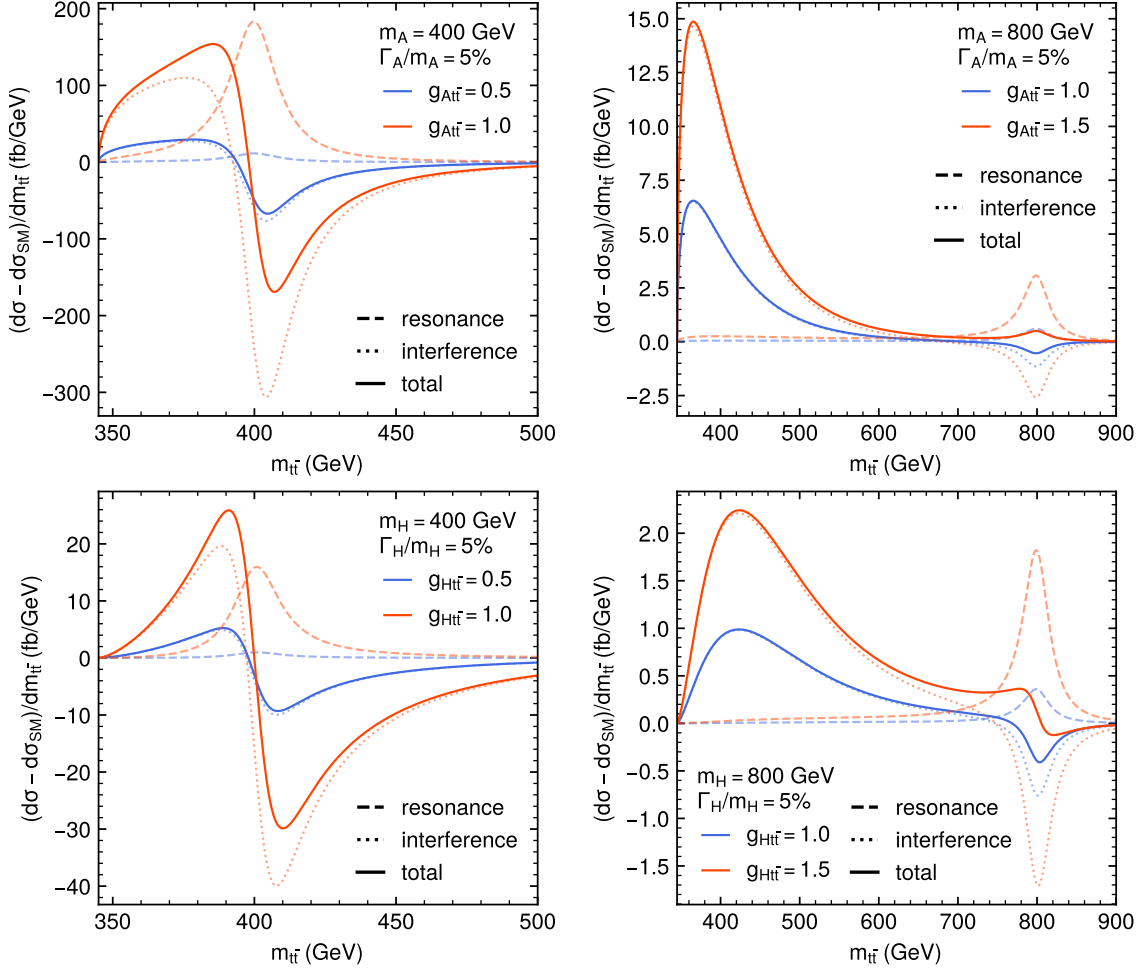


Figure 2.7: **Differential cross sections for $A/H \rightarrow t\bar{t}$.** The hadronic differential cross section as a function of the invariant $t\bar{t}$ mass, with the SM prediction subtracted, for A (top) and H (bottom) as well as $m_{A/H} = 400$ GeV (left) and $m_{A/H} = 800$ GeV (right). Different values of the coupling modifiers are shown in different colors. The resonance and interference components as well as their sum are shown as dashed, dotted and solid lines, respectively. They are calculated using formulas from Ref. [39] and using the NNPDF3.1 PDF set [40].

difference to the SM, for different masses and couplings in terms of $m_{t\bar{t}}$, the invariant mass of the $t\bar{t}$ pair, at the level of the hard scattering and at LO in QCD. It can be seen that the total effect of A and H is a very distinct peak-dip structure around the A/H mass. This is because the $gg \rightarrow A/H \rightarrow t\bar{t}$ production channel interferes with SM $gg \rightarrow t\bar{t}$ production, which leads to deficits in certain regions of phase space due to destructive interference. For high A/H masses, there is an additional broad peak

506 at low masses of $m_{t\bar{t}}$. This originates in the gluon PDF, which is steeply falling for
 507 rising partonic center-of-mass energy and thus compensates the suppression by the
 508 off-shell A/H at low $m_{t\bar{t}}$ for the A/H-SM interference.

509 A further consequence of the interference is that the differential cross section
 510 scales non-linearly with the coupling modifiers $g_{A t\bar{t}}$ and $g_{H t\bar{t}}$. The dependence (for
 511 arbitrary observables) can be parameterized as

$$d\sigma = d\sigma^{\text{SM}} + g_{A/H t\bar{t}}^2 d\sigma^{\text{int}} + g_{A/H t\bar{t}}^4 d\sigma^{\text{res}} \quad (2.19)$$

512 where the superscripts “SM”, “int” and “res” refer to the SM, SM-A/H interference,
 513 and resonant A/H contributions, respectively.

514 In addition to the $m_{t\bar{t}}$ spectrum, an A/H contribution is also expected to modify
 515 the spin state of the $t\bar{t}$ system. As a single particle, an intermediate A/H resonance
 516 has neither spin nor orbital angular momentum. Due to conservation of angular
 517 momentum, this implies that the $t\bar{t}$ system will be produced in a state with $J = 0$,
 518 which leaves only the 1S_0 and 3P_0 states (compare Tab. 2.1).

519 Furthermore, the spin-0 intermediate state has positive intrinsic parity and is
 520 charge-neutral. This implies that for H, whose interaction with the top quark is
 521 separately \mathcal{C} - and \mathcal{P} -conserving, the $t\bar{t}$ system will have quantum numbers of $\mathcal{C} = +1$
 522 and $\mathcal{P} = +1$, which is true for the 3P_0 state. For A, on the other hand, the
 523 interaction is maximally \mathcal{P} -violating, leading to quantum numbers of $\mathcal{C} = +1$ and
 524 $\mathcal{P} = -1$, which matches the 1S_0 state. As a result, the process $gg \rightarrow A \rightarrow t\bar{t}$ will
 525 always produce a spin singlet state, while $gg \rightarrow H \rightarrow t\bar{t}$ will produce a spin triplet
 526 state.

527 As explained in Secs. 2.2.1 and 2.2.2, the observable c_{hel} has maximal slope D for
 528 spin-singlet states, making it a good discriminator between A and the SM. For H,
 529 it can be shown that the produced triplet state instead maximizes the slope $D^{(k)}$ of
 530 the observable c_{han} , as defined in Eq. (2.10) [18]. Consequently, both c_{hel} and c_{han}
 531 will be used in the experimental search for such states presented in Chapter 7.

532 2.3.2 Two-Higgs Doublet Model

533 A common class of models predicting additional scalars as discussed in Sec. 2.3.1
 534 are Two-Higgs-Doublet Models (2HDMs) [41, 42]. In these models, there are two
 535 complex Higgs doublets with eight degrees of freedom in total (as opposed to a
 536 single doublet in the SM), which after electroweak symmetry breaking results in five
 537 physical states (compare Sec. 2.1.2). Such a structure for the Higgs sector arises,
 538 for example, in many supersymmetric models [43] or axion models [44].

539 In general, 2HDMs can include \mathcal{CP} -violating interactions (similar to Sec. 2.3.1)
 540 as well as flavor-changing neutral currents (FCNCs). Both of these phenomena are
 541 experimentally well constrained, and so it makes sense to restrict oneself to \mathcal{CP} -
 542 and flavor-conserving limits. Doing so leads to definite quantum numbers of the

543 five physical scalar states of the 2HDM: two neutral scalar (\mathcal{CP} -even) states h and
 544 H , a neutral pseudoscalar (\mathcal{CP} -odd) state A , and two charged states H^+ and H^- .
 545 Usually, the state h is identified with the SM Higgs boson at a mass of 125 GeV.
 546 Then, the two other neutral states H and A - if massive enough - could play the
 547 role of additional Higgs bosons decaying to $t\bar{t}$ as discussed in Sec. 2.3.1.

548 Depending on the nature of the discrete symmetry that is used to impose flavor
 549 conservation, there can be different types of 2HDMs, which differ in the structure of
 550 the couplings to the SM. No particular 2HDM type is assumed in this work, and the
 551 results of Chapter 7 are instead presented in terms of the generic model of Sec. 2.3.1.

552 2.3.3 Axion-Like Particles

553 Another very generic class of BSM scalars relevant to the $pp \rightarrow t\bar{t}$ process are
 554 axions and Axion-Like Particles (ALPs), denoted here as a . Axions were originally
 555 conceived as solutions to the strong \mathcal{CP} problem [45–48], which is a result of the
 556 non-trivial vacuum structure of QCD: when deriving the effective QCD Lagrangian,
 557 the presence of certain classes of topological solutions to the classical Yang-Mills
 558 equations leads to an additional \mathcal{CP} -violating term [49]

$$\mathcal{L}^{QCD} \supset \theta \frac{\alpha_S}{8\pi} G_{\mu\nu} \tilde{G}^{\mu\nu}, \quad (2.20)$$

559 where $G_{\mu\nu}$ is the gluon field strength and $\tilde{G}_{\mu\nu}$ its dual. The coefficient θ of this
 560 term is a free parameter in the range $[0, 2\pi]$, with no particular value preferred from
 561 first principles. However, experimentally, no \mathcal{CP} violation in pure QCD has been
 562 observed, and θ is strongly bounded at $|\theta| \leq 10^{-10}$ (the strongest bounds coming
 563 from measurements of the electromagnetic dipole moment of the neutron). The
 564 strong \mathcal{CP} problem thus consists of explaining why the \mathcal{CP} -violating $G_{\mu\nu} \tilde{G}^{\mu\nu}$ term
 565 vanishes.

566 The most prominent way to solve the strong \mathcal{CP} problem is by introducing a new
 567 real scalar field a , the axion field, with a Lagrangian [49]

$$\mathcal{L}^{ax} = \frac{1}{2} \partial_\mu a \partial^\mu a + \frac{\alpha_S}{8\pi} \frac{a}{f_a} G_{\mu\nu} \tilde{G}^{\mu\nu} + \text{interaction terms} \quad (2.21)$$

568 where f_a is called the axion scale, and all other interaction terms with SM fields are
 569 required to be invariant under a shift $a \rightarrow a + \kappa f_a$ with arbitrary κ . It can be shown
 570 that this Lagrangian, when added to the SM QCD Lagrangian including the term
 571 in Eq. (2.20), leads to a global minimum at $a/f_a + \theta = 0$, so that after a field shift
 572 the \mathcal{CP} -violating term is absorbed in the axion-gluon coupling and no \mathcal{CP} violation
 573 is expected in QCD alone. This is known as the Peccei-Quinn mechanism.

574 In Eq. (2.21), the axion-gluon interaction term has dimension 5 and is thus non-
 575 renormalizable, with the cutoff scale given by f_a . The axion must thus be necessarily
 576 be seen as an low-energy EFT description of different physics at the higher scale

2 Theoretical framework

577 f_a . Many different UV-complete models including axions exist [49–53], which lead
578 to different interaction terms with other SM particles such as photons, electroweak
579 bosons or massive fermions.

580 In this work, a focus is placed upon models which predict couplings to SM
581 fermions, particularly the top quark, and the EFT Lagrangian is parametrized in a
582 model-independent approach as [54]

$$\begin{aligned} \mathcal{L}^{\text{ALP}} = & \frac{1}{2} \partial_\mu a \partial^\mu a + \frac{m_a}{2} a^2 - \frac{a}{f_a} c_G \frac{a}{f_a} G_{\mu\nu} \tilde{G}^{\mu\nu} - \frac{a}{f_a} c_B \frac{a}{f_a} B_{\mu\nu} \tilde{B}^{\mu\nu} \\ & - \frac{a}{f_a} c_W \frac{a}{f_a} W_{\mu\nu} \tilde{W}^{\mu\nu} - \frac{\partial^\mu a}{f_a} \sum_f c_f \bar{\Psi}_f \gamma_\mu \Psi_f, \end{aligned} \quad (2.22)$$

583 where the index f runs over the SM fermions, Ψ_f are the fermion fields, $B_{\mu\nu}$ and
584 $W_{\mu\nu}$ are the EW boson fields before symmetry breaking, and the free parameters
585 are the scale f_a , the mass m_a , and the couplings to gluons c_G , to EW bosons c_B
586 and c_W and to fermions c_f (where no flavor mixing was assumed). This Lagrangian,
587 depending on the choice of the free parameters, might or might not correspond to
588 a UV-complete model and solve the strong \mathcal{CP} problem. Because of this, the field
589 a is here called an Axion-Like Particle. Even when it does not correspond to a true
590 axion, it might be a physically well-motivated extension of the SM, e.g. as a dark
591 matter candidate or mediator.

592 In the ALP-fermion interaction term in Eq. (2.22), the shift symmetry of a is
593 directly manifest since it only depends on the derivative of a . However, by employing
594 the equations of motion for a as well as the Higgs mechanism, one can rewrite
595 Eq. (2.22) with a Yukawa-like interaction instead. Dropping the EW bosons and
596 fermions other than the top quark leads to

$$\mathcal{L}^{\text{ALP}} = \frac{1}{2} \partial_\mu a \partial^\mu a + \frac{m_a}{2} a^2 - \frac{a}{f_a} c_{\tilde{G}} \frac{a}{f_a} G_{\mu\nu} \tilde{G}^{\mu\nu} + i c_t m_t \frac{a}{f_a} \bar{t} \gamma^5 t. \quad (2.23)$$

597 Performing this basis change includes an additional ALP-gluon coupling term (in
598 general dependent on the other SM couplings), which was absorbed by redefining
599 the Wilson coefficient from c_G to $c_{\tilde{G}}$. This basis will be used in the remainder of
600 this work.

601 It can be seen by comparing Eq. (2.23) to Eq. (2.18) that the ALP-top coupling
602 has the exact same structure as the generic \mathcal{CP} -odd boson introduced in Sec. 2.3.1.
603 Thus, if the ALP is heavy enough to be produced at the LHC and decay to $t\bar{t}$, it
604 can be searched for in $t\bar{t}$ final states similarly to the generic pseudoscalar A . Such
605 heavy ALP masses can be reached naturally and serve as solutions to the strong \mathcal{CP}
606 problem e.g. in UV models containing extra non-abelian gauge groups, resulting in
607 containing forces with large containment scales [55–58].

608 If, in addition, the ALP couplings also satisfy $c_{\tilde{G}} = 0$, the two Lagrangians in

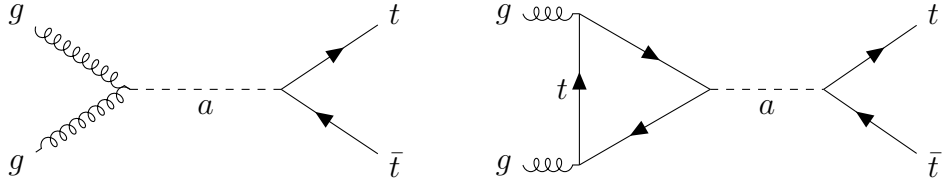


Figure 2.8: **Feynman diagrams for $gg \rightarrow a \rightarrow t\bar{t}$.** The left diagram corresponds to the gluon-ALP contact interaction and scales with $c_{\tilde{G}}c_t$, while the right diagram shows the top quark loop and scales with c_t^2 .

609 Eqs. (2.18) and (2.23) are identical, and all conclusions drawn on A can be directly
 610 transferred to the ALP. On the other hand, if $c_{\tilde{G}} \neq 0$, an additional production
 611 diagram involving a gluon contact interaction becomes available, as depicted in
 612 Fig. 2.8. A phenomenological study characterizing both cases in detail forms the
 613 core of Chapter 8 of this work.

614 3 Monte Carlo event generation

615 In order to test the Standard Model or extract any of its parameters at the LHC, one
616 requires a prediction which can be compared to the experimental data recorded by
617 the detectors in the form of collision events. This is, in general, a very complex task
618 consisting of many different subprocesses and physical scales. The generation starts
619 with the hard parton scattering, then continues with the emission of additional
620 radiation, underlying event effects, hadronization, and pileup, and ends with the
621 simulation of the different subdetectors and triggers. Many of these processes are not
622 only probabilistic, but intractable through direct analytical or numeric integration
623 due to the large phase space and the complexity of the problems involved.

624 Instead, the Monte Carlo (MC) method is used for this purpose. Here, it amounts
625 to randomly sampling an event from the phase space of the starting distribution - in
626 this case, the hard scattering - and then passing it through a chain of simulation tools
627 for the remaining steps until one arrives at an event that is directly comparable to
628 events recorded experimentally. This method is advantageous in that the numerical
629 error in an arbitrary region of phase space always scales with $1/\sqrt{N}$, where N is
630 the total number of events produced, independently of the dimensionality of the
631 problem. Thus, getting a numerically accurate prediction is mostly a matter of
632 producing a sufficient number of MC events.

633 In this chapter, the different tools used in the CMS simulation chain are discussed.
634 A focus is laid on the hard scattering or matrix element generators (Sec. 3.1) as well
635 as the parton showering (Sec. 3.2) since these are the focus of the studies presented
636 in Chapter 6, while underlying event effects (Sec. 3.3), hadronization (Sec. 3.4),
637 pileup (Sec. 3.5), as well as the detector and trigger simulation (Sec. 3.6) are only
638 briefly touched upon.

639 3.1 Matrix Element generators

640 At the LHC, protons are collided with large center-of-mass energies of multiple
641 TeV. Because protons are not fundamental particles, but bound states of QCD
642 which cannot be perturbatively described from first principles, providing accurate
643 predictions for proton-proton collisions is generally a very challenging task. For the
644 specific case of hard scattering processes, i.e. processes in which the particles in
645 the final state X have large transverse momenta, one can employ the factorization
646 theorem of QCD [59]:

$$\sigma(pp \rightarrow X) = \int_0^1 dx_1 \int_0^1 dx_2 \sum_{a,b} f_a(x_1, \mu_F) f_b(x_2, \mu_F) \hat{\sigma}(a(x_1 P) + b(x_2 P) \rightarrow X) \quad (3.1)$$

647 where P is the incoming momentum of the protons, assumed to be purely longitudinal
 648 and thus $P = \sqrt{s}/2$, and the sum runs over all possible combinations a, b of
 649 initial state partons (quarks and gluons). This formula factorizes the total hadronic
 650 cross section into two parts: The partonic cross section $\hat{\sigma}(a + b \rightarrow X)$ describes the
 651 scattering of two partons at high energies, and can be computed perturbatively in
 652 α_S due to asymptotic freedom of QCD. The functions $f_a(x, \mu_F)$ on the other hand
 653 are the parton distribution functions (PDFs) and describe the probability of finding
 654 a parton of type a with momentum fraction $p_a/P = x$ in the proton structure.
 655 Since they probe low momentum scales where α_S is large, they cannot be computed
 656 perturbatively and instead need to be measured experimentally. In addition to x ,
 657 they also depend on the factorization scale μ_F , which is the energy scale defining
 658 the separation between hard (perturbative) and soft (non-perturbative) QCD. It is
 659 typically set to be equal to the characteristic energy of the incoming partons, e.g.
 660 half the partonic invariant mass. In contrast to the dependence on x , the dependence
 661 on μ_F is a prediction of QCD and follows from the DGLAP equations [60,
 662 61].

663 The partonic cross section can further be written differentially as [59]

$$d\hat{\sigma}(ab \rightarrow X) = \frac{1}{2\hat{s}} \left(\prod_f \frac{d^3 p_f}{(2\pi)^3} \frac{1}{2E_f} \right) |\mathcal{M}(ab \rightarrow X)|^2 (2\pi)^4 \delta^{(4)} \left(\sum_f p_f \right) \quad (3.2)$$

664 where $\hat{s} = x_1 x_2 s$ is the partonic center-of-mass energy squared, the term in the
 665 brackets refers to the integral over the final state phase space and depends only
 666 on the number and masses of the final state particles f , the δ function encodes
 667 momentum conservation, and only the scattering matrix element \mathcal{M} depends on the
 668 physics of the process considered.

669 Events are now generated by drawing randomly from the full kinematically allowed
 670 final state phase space, as well as from the PDFs characterizing the initial state, and
 671 keeping them with a probability proportional to the corresponding hadronic cross
 672 section according to Eq. (3.1). The partonic cross section here might be known ana-
 673 lytically for simple processes, or might need to be integrated numerically for complex
 674 processes (especially at NLO or higher). The PDFs, based on fits to experimental
 675 data, are usually tabulated and interpolated; in this work, the NNPDF 3.1 PDF set
 676 is most commonly used for this purpose [40]. In practice, codes usually employ an
 677 adaptive sampling algorithm to enhance the fraction of events that pass and thus

678 speed up the calculation, see e.g. Ref. [62].

679 ME generators exist at LO, NLO, and (approximate) NNLO in QCD, all of which
 680 are used at different points in this work. For NLO and NNLO processes, care must
 681 be taken to cancel ultraviolet (UV) as well as infrared (IR) divergences that often
 682 appear in the integration of the matrix element. The former is done in the framework
 683 of renormalization, which usually introduces a dependence on an additional scale,
 684 the renormalization scale μ_R . Similar to μ_F , it is typically set to the energy scale
 685 of the process, and, since the dependence is expected to vanish at infinite order in
 686 QCD, variations of μ_R and μ_F are often used to asses the size of uncertainties due
 687 to missing higher orders [63].

688 IR divergences, on the other hand, arise when the momenta of massless particles
 689 in loop diagrams, such as gluons or light quarks, approach zero. They need to
 690 be canceled with corresponding divergent diagrams containing the emission of a
 691 real particle, which occur when the emission is soft or collinear with respect to the
 692 emitter. As a result, NLO calculations for the final state X will always need to also
 693 take into account the final state $X + j$, where j can be a gluon or light quark [64].

694 In this work, two different ME generators are used. The first is MG5_AMC@NLO,
 695 a general-purpose ME generator that can work both at LO and NLO [65]. It features
 696 fully automated computation of arbitrary processes in the SM or BSM, where new
 697 BSM models can be specified in the Universal FeynRules Output (UFO) format [66].
 698 It is used in this work for both SM and BSM processes.

699 The second ME generator used is POWHEG (short for Positive Weighted Hardest
 700 Emission Generator), which is a generic framework for NLO and approximate NNLO
 701 generators [67–69]. In contrast to MG5_AMC@NLO, it is not automated, and re-
 702 quires the manual implementation of each process. Many processes are publicly
 703 available as part of the POWHEG Box collection, and several are used in this work.
 704 Importantly, $pp \rightarrow t\bar{t}$ is generated at NLO with the POWHEG Box process `hvq` [70]
 705 in Chapters 5, 7 and 8. POWHEG has the advantage that it generates (almost) only
 706 events with positive weights, while the subtraction procedure in MG5_AMC@NLO
 707 leads to a significant fraction of negative weights at NLO, possibly leading to nu-
 708 matical instability in certain regions of phase space.

709 3.2 Parton showers and matching

710 The output of ME generators are events whose final states typically involve quarks
 711 and gluons with high momenta. Formally, such computations are accurate to some
 712 fixed order in α_S at which the calculation was performed, and all further emissions
 713 of gluons, as well as splittings of gluons into quark-antiquark-pairs, is suppressed
 714 by additional powers of α_S . However, one finds that, again due to IR singularities,
 715 such emissions and splittings are in fact proportional to $\alpha_S \log(\hat{s}/\Lambda_{QCD}^2)$, where
 716 $\Lambda_{QCD} \approx 250$ MeV is the scale at which QCD becomes nonperturbative. This term

717 is of order 1 and thus leads to large corrections [59, 61].

718 A way to incorporate these corrections is by using parton showers. The idea of a
719 parton shower is to successively generate all real emissions and splittings down to
720 the scale of Λ_{QCD} , where every splitting happens with a probability proportional to
721 α_S and the corresponding logarithm. To do this, one needs to define an ordering
722 variable which determines in which order the splittings are performed. Two common
723 choices are the transverse momentum of the emission (p_T -ordered shower) or the
724 emission angle respective to the emitting particle (angular-ordered shower). The
725 result of either choice is an effective resummation of the logarithms associated to
726 each emission, which is why parton showers are said to be leading-log (LL) accurate
727 for certain observables.

728 The main parton shower used in this work is a p_T -ordered dipole shower, included
729 as part of the PYTHIA multi-purpose event generator [71, 72]. It is mostly used
730 by matching it to the ME generators described in Sec. 3.1. This is usually trivial
731 at LO: the parton shower simply starts from the final state as given by the ME
732 generator. At NLO or higher, however, the additional emissions in the final state of
733 the ME generator that need to be inherently included to regularize IR singularities
734 would lead to double-counting if the parton shower is run in a naive way. To prevent
735 this, the most common strategy in PYTHIA is to start both initial state and final
736 state parton showers at the scale of the ME-level emission (sometimes called “wimpy
737 shower”).

738 This approach assumes that the scale definitions in the ME generator and the
739 parton shower are identical, which in general will not always be the case. In par-
740 ticular, for the important case of POWHEG matched to PYTHIA, used in this work
741 for the simulation of $pp \rightarrow t\bar{t}$, there is a mismatch in the scales which might lead to
742 double-counting. A more refined approach here is to use a vetoed shower: the shower
743 is started at the kinematically allowed limits and evolved downwards as usual, or-
744 dered by the scale as defined by PYTHIA. For the first emission the scale is then
745 recomputed according to the POWHEG definition, and it is vetoed and reshowered
746 if this scale is higher than the one in the ME.

747 More complicated procedures have to be invoked in the case that the ME contains
748 more than one real emission. This case is studied in detail for the ME generator **bb41**
749 in Chapter 6. Furthermore, besides PYTHIA, multi-purpose generator HERWIG [73,
750 74] is considered in parts of Chapter 7, and briefly described there.

751 3.3 Multi-parton interactions

752 In addition to the hard scattering, additional soft QCD interactions might occur
753 in a scattering event between the other partons in the two colliding protons. This
754 is referred to as multi-parton interactions (MPI) or underlying event (UE). It is
755 handled by PYTHIA based on heuristic models, interleaved with the parton shower.

756 In general, MPI parameters need to be tuned to experimental data. This was done
 757 by the PYTHIA authors, such as the different versions of the Monash tune [75], and
 758 building on top of this by the CMS collaboration in the form of the CP tune family,
 759 most recently the CP5 tune [76]. Both tunes are based on a large dataset of e^+e^- ,
 760 ep , $p\bar{p}$, and pp collision data from many different experiments. The CP5 tune will
 761 be used in all parts of this work.

762 3.4 Hadronization

763 The result of the MPI-interleaved parton shower consists of a collection of bare
 764 quarks and gluons at energies of $\mathcal{O}(\Lambda_{\text{QCD}})$, at which QCD becomes non-perturbative.
 765 The hadronization of these quarks and gluons into hadrons as well as their subse-
 766 quent decays thus need to be described heuristically.

767 For most of this work, this is done using the Lund string fragmentation model [77,
 768 78], again implemented in PYTHIA. In this model, the strong force between a quark
 769 and an antiquark of opposite color is modeled as a string in space-time, standing in
 770 for e.g. a three-dimensional flux tube. The energy stored in the string is proportional
 771 to its length, consistent with the long-distance behavior of QCD observed e.g. in
 772 lattice QCD. Hard gluons can be accommodated in this model as kinks in the string,
 773 i.e. for a $q\bar{q}g$ state, the q and \bar{q} are connected through the gluon instead of directly.

774 As the quarks move apart, the energy stored in the string increases, until it is large
 775 enough that the string fragments by creating an additional $q\bar{q}$ pair from the vacuum.
 776 If the energy in the resulting strings is still large enough, the procedure repeats.
 777 Otherwise, the low-mass $q\bar{q}$ pair is considered a meson, based on the flavors of its
 778 constituents. In its purest form, this model has only two free parameters (usually
 779 denoted a and b) which parametrize the distribution of the momentum fraction
 780 of the $q\bar{q}$ pair in each fragmentation. However, in order to correctly describe e.g.
 781 flavor composition and p_T spectra of jets, many more parameters usually have to be
 782 introduced. For more detail on string fragmentation in PYTHIA, see e.g. Ref. [72].
 783 Similar to MPI, hadronization parameters need to be tuned to data, and are also
 784 included in the Monash and CP5 tunes.

785 One shortcoming of the default MPI and hadronization models are that both
 786 work in the leading color (LC) approximation, i.e. in the limit of a large number
 787 of QCD colors ($N_c \rightarrow \infty$). This simplifies the models greatly because the chance
 788 of two unrelated color lines sharing the same color becomes infinitesimally small.
 789 Corrections to this approximation are typically of order $1/N_c^2 = 1/9$, and can be done
 790 via color reconnection (CR), for which different models exist, see e.g. Refs. [79, 80].
 791 The difference between different models is often considered a source of uncertainty
 792 in measurements, such as in Secs. 5.5 and 7.5.

793 Finally, decays of produced unstable hadrons, including possible decay chains,
 794 are also handled by PYTHIA. Branching ratios are taken from experimental mea-

795 surements where available, and predicted from heuristic models where not, see e.g.
796 Ref. [72].

797 3.5 Pileup

798 At the currently achieved instantaneous luminosities, the proton bunches colliding at
799 the LHC contain more than 10^{11} protons on average. Because of this large number, it
800 is expected that a single collision event contains interactions between more than one
801 pair of protons from the two colliding bunches. This is known as pileup. It differs
802 from MPI, in which the different interactions are between multiple partons in the
803 same proton and are thus correlated from a QFT perspective, while different pileup
804 interactions are in principle independent from each other. In Run 2, the average
805 number of pileup interactions per bunch crossing ranged from 23-32 depending on
806 the era of datataking [81], while it is 40 or higher in Run 3.

807 In simulation, pileup interactions are considered by mixing the generated hard
808 interaction process with a dedicated sample of purely soft-QCD interactions, also
809 generated in PYTHIA. The probability distribution of the number of pileup interac-
810 tions is an input to this procedure, and is typically corrected after the generation
811 is finished by reweighting in a suitable variable. In Sec. 5.3.1, an experimental ap-
812 proach to this problem is taken by correcting experimentally accessible pileup-related
813 parameters directly to data. In Sec. 7.2.4, on the other hand, the distribution of
814 the true number of interactions is instead reweighted based on a theory prediction
815 given the total inelastic cross section [82].

816 3.6 Detector and trigger simulation

817 After the simulation of the interaction processes, the resulting collection of particles
818 produced in an event is propagated to a full physics-based detector simulation using
819 the program GEANT4 [83]. Based on the output of this simulation, the two tiers of
820 trigger systems are similarly simulated using in-house tools. The result is a set of
821 detector information from all subdetectors as well as the outputs of different triggers,
822 similar to true experimental data, and so it can be passed to the different object
823 reconstruction algorithms (cf. Sec. 4.3) in the same way as the data. Events are then
824 analyzed by comparing the reconstructed objects and quantities between data and
825 simulation, ensuring a one-to-one comparison. Possible residual differences between
826 data and simulation are often corrected for by applying calibration factors measured
827 using well-known processes. The details of such calibrations will be explained in
828 Chapters 5 and 7 where relevant.

829 **4 Experimental methods**

830 **4.1 The Large Hadron Collider**

831 At the time of writing, the Large Hadron Collider [84] is the largest and most
832 powerful particle accelerator in the world. Located underground at the border of
833 France and Switzerland close to Geneva, it consists of two circular beamlines of
834 roughly 27 km circumference, in which proton bunches are accelerated and collided.
835 Superconducting magnets, cooled with liquid helium at around 4 K temperatures,
836 generate magnetic fields of over 8 T to keep the protons on their circular orbit,
837 and similarly superconducting electromagnetic radio-frequency cavities accelerate
838 the protons to beam energies up to 7 TeV. When operating as designed, around
839 2800 proton bunches per beam containing 3×10^{14} protons total are present in the
840 beamline simultaneously, revolving with a frequency of about 11.245 kHz. From
841 this, peak instantaneous luminosities of about $20 \text{ kHz} \mu\text{b}^{-1}$ can be reliably reached.
842 Alternatively, the LHC can also collide heavy ions, such as lead or oxygen, instead
843 of protons.

844 There are four large experiments making use of the colliding beams at the LHC,
845 located at the four interaction points. The two larger of these are ATLAS [85]
846 and CMS [4], both of which are general-purpose experiments intended to study
847 all aspects of the Standard Model in proton-proton collisions. The work of thesis
848 was performed as part of the CMS collaboration, and so the CMS experiment is
849 described in Sec. 4.2 in more detail. The two smaller experiments, on the other
850 hand, are specialized for certain tasks, namely the study of B physics and exotic
851 hadrons for LHCb [86] and the study of heavy-ion collisions for ALICE [87].

852 The data taken at the LHC so far can be divided into three Runs. Run 1 lasted
853 from 2010–2012, during which the LHC operated at center-of-mass energies of 7 and
854 8 TeV, significantly below the original target values, and yielded a total integrated
855 luminosity of about 29 fb^{-1} . It is this data that led to the original discovery of the
856 Higgs boson. Following this, after two years of pause, Run 2 resumed in 2015 with
857 a center-of-mass energy of 13 TeV and lasting to 2018. Around 140 fb^{-1} of data was
858 collected during this time. This complete dataset, save for the small contribution
859 from 2015, is analyzed in Chapter 7 of this thesis.

860 Finally, Run 3 of the LHC started in 2022 after another three years of pause, and
861 is planned to last until 2026 at the time of writing. The center-of-mass energy was
862 again increased slightly to 13.6 TeV, and in the years 2022–2024 around 196 fb^{-1}
863 have been recorded, already surpassing Run 2. In Chapter 5 of this thesis, the very

864 first data of Run 3, corresponding to 1.21 fb^{-1} taken in July and August 2022 at
865 CMS, are analyzed in the context of a $t\bar{t}$ cross section measurement.

866 In the future, it is planned to upgrade the LHC to be able to run at higher
867 instantaneous luminosities as well as a further increased energy of 14 TeV [88]. The
868 CMS detector will similarly be upgraded to replace aging components and deal
869 with the increased pileup conditions [89, 90], and a total integrated luminosity of
870 around 3 ab^{-1} is expected to be collected. In Chapter 8, among others, sensitivity
871 projections for this luminosity are made for Axion-Like Particles decaying to $t\bar{t}$.

872 4.2 The CMS experiment

873 The Compact Muon Solenoid experiment [4, 90], located at Interaction Point 5 of
874 the LHC close to Cessy, France, is a general-purpose particle detector targeting a
875 broad range of SM and BSM phenomena. Its main feature is a superconducting
876 solenoid magnet creating a strong magentic field of 3.8 T. CMS is a hermetic detec-
877 tor, covering almost the full solid angle in space, and is split into a *barrel*, covering
878 pseudorapidities of $|\eta| \lesssim 1.5$, and two forward *endcaps*, covering high $|\eta|$ values. It
879 consists of several subdetectors, which are geared towards different particle types
880 and properties.

881 **Subdetectors** The innermost part of CMS is the *tracker*, which is a silicon detec-
882 tor comprised of several layers of silicon pixel and strip sensors [92, 93]. These record
883 interactions with particles (“tracker hits”) shooting outwards from the interaction
884 point in the center in three-dimensionsial space. Through reconstruction of the par-
885 ticle tracks and fits of the curvature due to the magenetic field, the tracker thus
886 allows for the measurement of particle momenta. Furthermore, extrapolating the
887 tracks back to their origin allows for the determination of the point of interaction,
888 and thus for discrimination between particles arising from different proton-proton
889 interactions. Due to the presence of the beampipe, the tracker covers only pseu-
890 dorapidities of $|\eta| < 2.5$, enabling high precision momentum determination in this
891 range only.

892 The second-to-innermost subdetector is the *electromagnetic calorimeter* (ECAL),
893 which is intended to measure the energy of electrons and photons [94, 95]. It consists
894 of transparent lead tungstate cells, in which incoming electrons or photons create
895 electromagnetic showers leading to avalanches of electron-positron pairs and photon
896 radiation. These are then recorded by photodiodes, and the energy of the incoming
897 particle can be reconstructed from the amount of measured photons. Pseudorapididi-
898 ties of $|\eta| < 1.48$ and $1.65 > |\eta| < 3$ are covered for the barrel and the endcaps,
899 respectively. The majority electrons and photons are fully stopped in the ECAL
900 and do not interact with the further subdetectors.

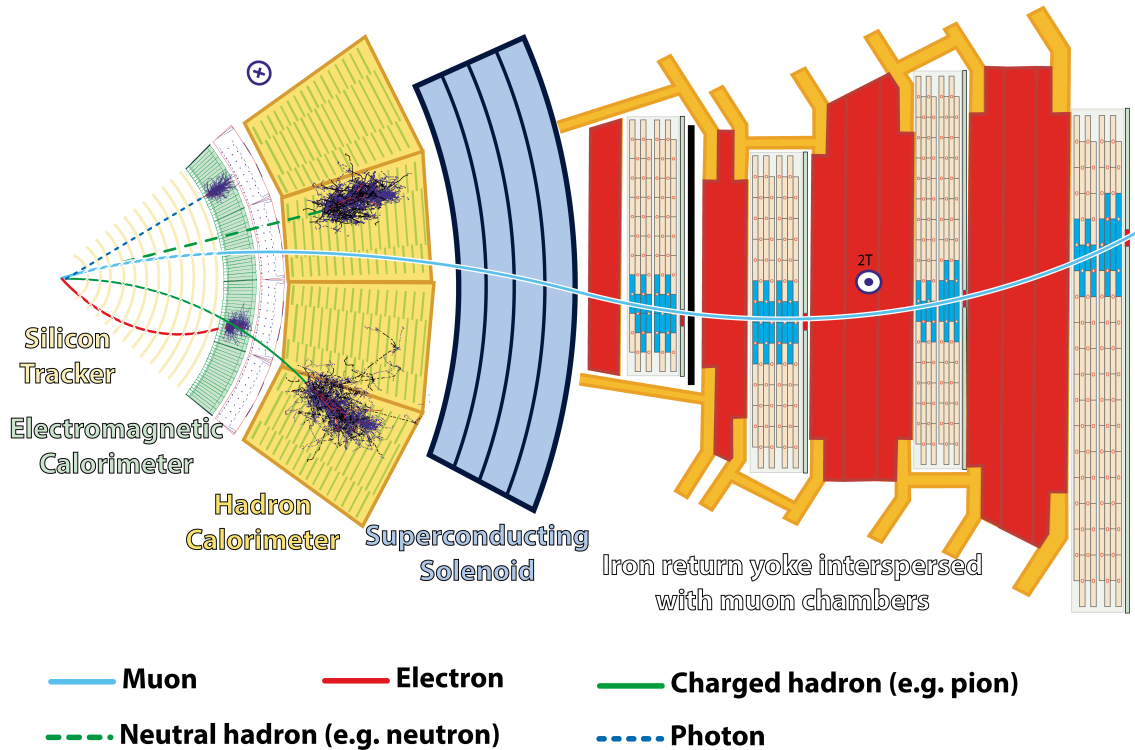


Figure 4.1: **The CMS detector.** A cross section view of the different CMS subdetectors, with the trajectories of example particles and their interactions. This figure is taken from Ref. [91].

Following the ECAL, and similar in functionality, the *hadronic calorimeter* (HCAL) measures the energy of charged or neutral hadrons [96, 97]. It consists of interleaved absorber plates, which initiate hadronic showers through the strong interaction with the nuclei of the material, and scintillators, which transmute the hadronic showers into photons to be detected by photodetectors. The HCAL covers $|\eta| < 1.4$ and $1.4 < |\eta| < 3$ for the barrel and endcaps, respectively, and additionally features a forward section ranging up to $|\eta| < 5$, though the latter is not used anywhere in this work.

Surrounding the HCAL lies the superconducting solenoid, followed by the final subdetector: the *muon chambers* [98, 99]. They are interspersed with four layers of the iron return yoke of the magnet, which confines the magnetic field. Since muons interact only sparsely with matter, they escape the calorimeters and the solenoid unhindered, and are detected in four muon subsystems working in accord at different pseudorapidities: the drift tubes ($|\eta| < 1.2$), cathode strip chambers ($0.9 < |\eta| < 2.4$), resistive plate chambers ($|\eta| < 1.9$) and gas electron multipliers ($1.6 < |\eta| < 2.4$). All of them are gas detectors, which are sensitive to the ionization of a gas when a muon passes through it, and record hits of the muon trajectory, thus allowing for a momentum measurement similar to the tracker.

Trigger system Besides the different subdetectors, a crucial part of the CMS experiment is the *trigger system* [100]. It is necessary due to the large number of bunch crossings at the LHC, which, if they were all recorded, would produce event rates on the order of GHz, far in excess of the computational bandwidth and storage capacities available. To combat this, only events which are of physical interest should be recorded. It is the task of the trigger system to determine what these events should be.

The trigger system is split into two parts. The first is the low-level or level-one trigger (L1T) [101], which is a hardware trigger consisting of custom electronics and whose inputs are directly the output signals of several of the subdetectors. It is designed to trigger on signatures consistent with specific objects, such as electrons, muons or hadronic jets, with significant energy. Since it needs to take a decision for every collision event, it only has a time interval of around $4\,\mu\text{s}$ to do so, requiring purpose-build low-latency electronics. Its target is a output event rate of 100 kHz, which can be adjusted by prescaling certain trigger paths so that only a fraction of passing events is recorded.

The second part of the trigger system is the high-level trigger (HLT) [102, 103]. It is a software trigger, running on a GPU-accelerated server farm directly in the CMS service cavern, on which a dedicated, speed-optimized version of the standard CMS object reconstruction algorithm is executed for each event passing the L1T. Specific triggers are then implemented as decisions based on these reconstructed trigger objects, allowing large freedom in selecting events based on the desired physics

941 program. Typical triggers require, for example, the presence of different numbers or
942 combinations of electrons, muons, photons, hadronic jets or missing transverse mo-
943 mentum. The transverse momentum thresholds and further requirements on these
944 objects need to be adjusted so that the total trigger rate is reduced to an average
945 of around 400 Hz. Only these events are then saved to hard drives, and kept for
946 further analysis.

947 4.3 Object reconstruction

948 In order to interpret the physics behind a collision event, the outputs of the sub-
949 detectors have to be translated into physics objects which can be mapped to the
950 underlying physical particles. At CMS, this is done with a single unifying method,
951 the Particle Flow (PF) algorithm [104], which is designed to combine the informa-
952 tion from the several subdetectors to build physics objects (called PF candidates)
953 as appropriate. The physics objects relevant to this work are listed in the following.

954 *Charged particle tracks* are obtained from the tracker by fitting recorded tracker
955 hits using a χ^2 minimization, and their momentum and charge are estimated from
956 their curvature as described above [92]. By extrapolating the tracks back to their
957 origin, the position of vertices in space can also be determined.

958 From the tracks, the *primary vertices* (PVs) can be determined, which are the
959 locations of the proton-proton interactions that caused the tracks in the first place.
960 By contrast, secondary vertices arise from the decays of particles with long enough
961 lifetime that they move a significant distance from the PV. PVs are determined by
962 a likelihood fit to all tracks of sufficient quality [92]. In each event, the PV whose
963 tracks show the largest p_T sum is designated the hard-scattering PV, assumed to
964 correspond to the physical process of interest, while further PVs are due to soft-QCD
965 pileup interactions. The number of PVs per event is thus a good measure of the
966 amount of pileup.

967 The other main ingredient besides tracks and vertices are *calorimeter clusters*
968 from either the ECAL or the HCAL. A clustering algorithm is required here because
969 particles typically deposit their energy in more than one calorimeter crystal.

970 By matching the positions of calorimeter clusters and charged particle tracks, *elec-*
971 *trons* (for the ECAL) and *charged hadrons* (for the HCAL) can be constructed. The
972 combined measurements of the momentum (from the curvature) and the deposited
973 energy (from the calorimeter) allows for the reconstruction of the mass, and thus the
974 identification of the particle. For electrons, the effect of bremsstrahlung originating
975 in the tracker volume has to be considered, usually resulting in multiple calorimeter
976 clusters per electron (called a supercluster) which need to be combined together.
977 Isolation criteria on the clusters are also required to veto electrons that are part of
978 a hadronic jet. By contrast, calorimeter clusters which do not have charged tracks
979 are assigned to *photons* (for the ECAL) or *neutral hadrons* (for the HCAL). CMS

980 furthermore employs algorithms to remove hadrons that are believed to originate
981 from pileup instead of the hard-scattering vertex. In Run 2, the Charged Hadron
982 Subtraction (CHS) method [104] was used for this purpose, while in Run 3, the
983 better performing PUPPI method [81, 105] was used instead.

984 *Muons* do not interact with the calorimeter, and are instead built by directly
985 combining charged tracks with hits in the muon chambers. In this work, muons are
986 only considered if they match to hits in both subdetectors.

987 From these definitions, further high-level objects can be build. The first are
988 *hadronic jets*, which are clustered from all other PF candidates using the anti- k_T
989 algorithm with a distance parameter of $\Delta R = 0.4$ [106] (referred to as AK4 jets).
990 This algorithm is infrared- and collinear-safe, i.e. it is not strongly sensitive to
991 soft nonperturbative QCD effects [61], and has the advantage that the resulting
992 jets are approximately circular in the φ - η plane. Since leptons or photons can be
993 created from electroweak decays of hadrons, these also need to be included in the jet
994 clustering; to ensure that they are not double-counted, leptons and photons that are
995 included in jets are removed from further consideration through isolation criteria.

996 Hadronic jets can further be *b tagged*, that is, identified as originating from a B
997 hadron. Since the strong interaction is flavor-conserving, the decay of B hadrons
998 to hadrons of other flavors has to be mediated by the flavor-mixing in the weak
999 interaction, leading to comparatively long lifetimes. B hadrons can thus be identified
1000 through secondary vertices corresponding to the B hadron decay, which can be
1001 displaced from the PV by several millimeters. In practice, machine learning-based
1002 classifiers like the DEEPJET algorithm [107] are used, which take more properties
1003 of the jet into account besides the displacement of the secondary vertex.

1004 Finally, the *missing transverse momentum* \vec{p}_T^{miss} can be calculated as the negative
1005 of the vectorial sum of all transverse momenta in the event [108]. Since the initial
1006 state of a collision at the LHC has negligible transverse momentum, \vec{p}_T^{miss} represents
1007 the total transverse momentum of the particles that left the detector unobserved.
1008 In the SM, this is the case for neutrinos, but it could also be BSM particles such as
1009 e.g. dark matter candidates.

1010 4.4 Statistical interpretation

1011 In experimental particle physics, results are typically extracted by comparing detector-
1012 level predictions, for example obtained using MC simulation, to the observed data
1013 for suitably chosen observables. The measured data here are necessarily afflicted
1014 by statistical uncertainties, both due to the inherent randomness of quantum me-
1015 chanics and the probabilistic behaviour of the detector. They should thus be seen
1016 as a sample drawn from a random distribution, and in order to extract underlying
1017 parameters of any model, statistical methods are required.

1018 In this work, all statistical interpretation is performed in the framework of *binned*

4 Experimental methods

1019 *profile maximum likelihood fits.* This method follows the Frequentist approach of
1020 considering physical properties that should be extracted to be fixed, if unknown,
1021 quantities, which enter the random distribution of the observed data as parameters.
1022 In order to estimate the desired properties, the observed datapoints are sorted into
1023 orthogonal bins according to one or more sensitive observables, and each bin is
1024 treated as an independent counting experiment where the observed number of events
1025 is given by a Poissonian distribution.

1026 **Likelihood definition** Denoting the set of physical properties to be estimated
1027 (the parameters of interest or POIs) collectively as $\vec{\mu}$, the likelihood of $\vec{\mu}$ for bin i ,
1028 given that N_i events were observed, is [109]

$$L_i(\vec{\mu}, \vec{\theta}) = \text{Pois}\left(N_i | n_i(\vec{\mu}, \vec{\theta})\right). \quad (4.1)$$

1029 Here, Pois refers to the Poissonian distribution, and $n_i(\vec{\mu}, \vec{\theta})$ is the mean expected
1030 number of events in bin i as predicted by the physics model under consideration.
1031 The set of parameters $\vec{\theta}$ are *nuisance parameters* (NPs), which encode the effects
1032 of different sources of systematic uncertainty affecting the measurement. The full
1033 likelihood of the measurement is now given as the product of all bins:

$$L(\vec{\mu}, \vec{\theta}) = \prod_i L_i(\vec{\mu}, \vec{\theta}) \cdot G(\vec{\theta}). \quad (4.2)$$

1034 The function $G(\vec{\theta})$ represents the *constraint terms* of the NPs, encoding any possi-
1035 ble prefit uncertainties on them. For example, an experimental source of uncertainty
1036 (e.g. a scale factor) f might be measured with a mean value of \hat{f} and standard de-
1037 viation σ_f . Then, the corresponding NP would be normalized as $\theta_f = (f - \hat{f})/\sigma_f$,
1038 and the constraint terms $G(\vec{\theta})$ would include a factor $\mathcal{N}(\theta_f | 0, 1)$, i.e. the standard
1039 normal distribution for θ_f . This way, the range $\theta_f = \pm 1$ corresponds to one standard
1040 deviation of the corresponding systematic uncertainty source.

1041 In practice, the functional form of the expectation n_i must be given by the physics
1042 model studied in the experiment. In this work, the events are modeled as a sum of
1043 signal and background processes. An important case is a linear signal, where the
1044 only POI is the *signal strength* μ and the expectation for bin i is

$$n_i(\mu, \vec{\theta}) = \mu s_i(\vec{\theta}) + b_i(\vec{\theta}). \quad (4.3)$$

1045 The functions s_i and b_i are the signal and background expectations, respectively,
1046 which both can be influenced by NPs.

1047 To extract a best-fit value of the POI (or multiple POIs), one now maximizes
1048 the full likelihood simultaneously over both the POIs $\vec{\mu}$ and the NPs $\vec{\theta}$, giving the
1049 *maximum likelihood estimator* for $\vec{\mu}$. In practice, usually the function $-2 \ln L$ is

1050 minimized instead to have numerically tractable quantities.

1051 **Confidence intervals** In the Frequentist approach to statistics, an uncertainty
 1052 can be assigned to the estimate in the form of *confidence intervals*. To do so, a *test*
 1053 *statistic* has to be defined, which usually takes the form of a *profile likelihood ratio*,
 1054 e.g. [109]

$$\lambda(\vec{\mu}) = -2 \ln \frac{\hat{L}(\vec{\mu})}{\max_{\vec{\mu}'} \hat{L}(\vec{\mu}')}, \quad \text{with} \quad \hat{L}(\vec{\mu}) = \max_{\vec{\theta}} L(\vec{\mu}, \vec{\theta}). \quad (4.4)$$

1055 $\hat{L}(\vec{\mu})$ is the profile likelihood, i.e. the likelihood maximized over the NPs, and the
 1056 ratio is taken between the probed POI values $\vec{\mu}$ and the best-fit values $\vec{\mu}'$. Small
 1057 values of $\lambda(\vec{\mu})$ now signalize good agreement with the data for the POI values $\vec{\mu}$.
 1058 The value of the test statistic λ depends on the observed data N_i , and can thus be
 1059 seen as a random variable with a probability density $f(\lambda|\vec{\mu})$, which again depends
 1060 on the POIs as parameters. Then, given an observed value of the test statistic λ^{obs} ,
 1061 a set of POIs $\vec{\mu}$ is excluded at confidence level (CL) α if

$$P(\lambda(\vec{\mu}) < \lambda^{\text{obs}}) = \int_0^{\lambda^{\text{obs}}} f(\lambda|\vec{\mu}) d\lambda > \alpha. \quad (4.5)$$

1062 The probability density $f(\lambda|\vec{\mu})$ can be evaluated numerically using toy datasets.
 1063 Alternatively, for simple signal models like the linear signal given in Eq. (4.3), it
 1064 can be analytically shown that λ is approximately χ^2 -distributed, with the degrees
 1065 of freedom equaling the number of POIs [110, 111].

1066 In particular, for the case of one POI μ with best-fit value $\hat{\mu}$, a two-sided confi-
 1067 dence interval at $\sim 68\%$ CL (corresponding to one standard deviation of the normal
 1068 distribution) is then simply given as [109]

$$\lambda(\hat{\mu} \pm \Delta\mu) = -2(\ln \hat{L}(\hat{\mu} \pm \Delta\mu) - \ln \hat{L}(\hat{\mu})) = 1. \quad (4.6)$$

1069 That is, the uncertainty corresponds to a change in negative profile log-likelihood
 1070 $-2 \ln \hat{L}$ by 1 with respect to the best-fit point.

1071 **Significance** The framework of confidence intervals can also be used to define the
 1072 *significance* of an observed signal. To do so, a hypothesis test is performed, with the
 1073 background-only case as the null hypothesis to be rejected. For an observed value
 1074 of the test statistic λ^{obs} (defined again by Eq. (4.4)), the probability to make this
 1075 observation under the background-only hypothesis (the *p-value*) is

$$p_0 = \int_0^{\lambda^{\text{obs}}} f(\lambda|\vec{\mu} = 0) d\lambda. \quad (4.7)$$

4 Experimental methods

To translate this into a significance, the p -value is compared to the area under the curve of a standard normal distribution: a significance of 2 standard deviations, giving $\approx 95\%$ probability under the normal distribution, corresponds to a p -value of 0.05. Similar to the case described above, the p -value can be obtained from analytical approximate distributions in the case of a simple linear signal.

Exclusion limits A different application of confidence intervals are *exclusion limits*, used in experiments where no or little signal was observed. Here, for a POI that is bounded from below (usually by zero, e.g. a signal strength), an upper limit μ^{up} is sought such that all values $\mu > \mu^{\text{up}}$ are excluded at a certain CL. At the LHC, the CL_s method [112, 113] is commonly used for this purpose. The test statistic is modified from Eq. (4.4) to be

$$q(\mu) = \begin{cases} \lambda(\mu), & \hat{\mu} \leq \mu \\ 0, & \hat{\mu} > \mu \end{cases} \quad (4.8)$$

where $\hat{\mu}$ again refers to the best-fit value of μ . The point of this modification is that a certain value of μ should not be seen as excluded if the data is more compatible with a higher μ value; thus, the test statistic is set to zero in this case.

Following that, for an observed test statistic q^{obs} , the CL_s value is defined as

$$\text{CL}_s(\mu) = \frac{p_{s+b}(\mu)}{1 - p_b} \quad (4.9)$$

with

$$p_{s+b}(\mu) = \int_0^{q^{\text{obs}}} f(q|\mu) dq \quad \text{and} \quad p_b = \int_0^{q^{\text{obs}}} f(q|\mu=0) dq. \quad (4.10)$$

p_{s+b} and p_b are the probabilities to observe a test statistic of q^{obs} under the signal+background and background-only hypotheses, respectively, defined similarly as in Eq. (4.7). The ratio of the two probabilities is used instead of p_{s+b} directly to prevent exclusion of small signals in the case that the data is not well compatible with neither the background-only or the signal+background hypothesis (particularly if the experiment is not very sensitive to a certain kind of signal and p_{s+b} and p_b are thus similar). The exclusion limit at CL α is then simply given by $\text{CL}_s(\mu^{\text{up}}) = 1 - \alpha$. A common choice, used in this work, is $\alpha = 95\%$ (corresponding to a p -value of 0.05).

Nuisance parameter diagnostics Real maximum likelihood fits used in analyses at the LHC are often very complex, with more NPs than there are bins. In such underconstrained fits, the behaviour of the different NPs - encoding the different sources of uncertainty - is often not intuitively clear a priori, and it is thus important to investigate their postfit behaviour to check whether the fit is healthy and

1105 numerically stable.

1106 To do so, first, the *pulls and constraints* of the NPs are defined as their best-
1107 fit values and profiled postfit uncertainties, similar as for the POIs above, relative
1108 to their prefit uncertainties. To have a NP pulled means that its best-fit value is
1109 different from the prefit expectation. Similarly, to have it constrained means that its
1110 estimated postfit uncertainty is smaller than the assumed prefit value. Both of these
1111 effects are not necessarily a sign of an unhealthy fit: If the observables considered in
1112 the fit are sensitive to a particular physical or experimental parameter as encoded
1113 by the NP in question, a constraint, and possibly a pull, are expected, and simply
1114 show the power of the fit to measure that particular parameter.

1115 If, on the other hand, a strong constraint or pull (beyond what is expected from
1116 statistical fluctuations) is seen in a NP to which no sensitivity is expected, it might
1117 be a sign of problems with the fit, such as spurious constraints from noisy inputs,
1118 missing degrees of freedom to describe the data, or too small prefit uncertainties.
1119 Whether this casts doubt on the result or not needs to be gauged on a case-by-case
1120 basis, and depends on the relevance of the NP in question.

1121 The relevance of individual NPs to the result can be quantified using *impacts*.
1122 The impact of a NP θ with best-fit value $\hat{\theta}$ and postfit uncertainty $\Delta\theta$ is defined by
1123 repeating the maximum likelihood fit at values of $\hat{\theta} \pm \Delta\theta$, with θ then held fixed in
1124 the maximization of Eq. (4.4). The shift in the resulting POI values with respect to
1125 the best-fit POI is the impact on that particular POI. In a fit with a single POI, the
1126 impacts can be used to rank the NPs and the systematic uncertainties they encode
1127 in order of importance to the fit result. In particular, NPs with very small impact
1128 can be considered irrelevant for the fit result. However, it should be kept in mind
1129 that this procedure does not fully account for possible correlations between the NPs.

1130 **Uncertainty breakdown** Related but not identical to the concept of impacts
1131 is an *uncertainty breakdown*, which can be used to quantify the contribution from
1132 different sources of uncertainty to the total postfit uncertainty on the POI. To do so,
1133 either a single NP or a group of NPs originating from the same source (e.g. all NPs
1134 corresponding to a certain correction) are frozen at their postfit values, and the fit
1135 is repeated with the POI and remaining parameters left untouched. The result will
1136 yield the same best-fit value for the POI, but with a possibly reduced uncertainty (as
1137 estimated from the likelihood). The uncertainty due to the frozen NP or NP group
1138 is then defined as the quadratic difference to the nominal uncertainty. This method
1139 does not account for correlations between different uncertainty sources (though it
1140 does consider correlations between the NPs in a certain group). As a result, the
1141 uncertainties obtained in this way will in general not sum up in quadrature to the
1142 original uncertainty.

1143 A further use of this method is to define the statistical component of the uncer-
1144 tainty on a POI: it is simply the remaining uncertainty when all considered NPs are

4 Experimental methods

1145 frozen to their postfit values simultaneously. Conversely, the quadratic difference
1146 between the total and the statistical uncertainty can be considered the systematic
1147 uncertainty.

1148 **Technical implementation** In this work, two different tools are used to imple-
1149 ment the methods described above. In Chapters 5 and 7, where experimental data
1150 is analyzed, the CMS general-purpose statistics tool `combine` is used [114]. In Chap-
1151 ter 8, on the other hand, the Python-based tool `pyhf` [115, 116] is employed for the
1152 purpose of calculating expected significances and limits.

1153 **5 Measurement of the inclusive $t\bar{t}$ cross**
1154 **section at $\sqrt{s} = 13.6$ TeV**

1155 **5.1 Introduction**

1156 In July 2022, the LHC officially resumed collecting data after a roughly three-year
1157 shutdown, thereby starting LHC Run 3. It did so at a new, unprecedented center-
1158 of-mass energy of $\sqrt{s} = 13.6$ TeV, inviting the experiments to measure energy-
1159 dependent physical observables at the new energy frontier.

1160 One important such observable is the inclusive $t\bar{t}$ production cross section. As
1161 mentioned in Chapter 2, the top quark has a special place in the standard model as
1162 the heaviest known elementary particle, as well as the only colored particle that does
1163 not hadronize due to its short lifetime. It is thus important for many BSM scenarios
1164 such as additional Higgs bosons, which might couple strongly to the top quark. As
1165 such, measurements of top quark-related observables at the highest possible energies
1166 are attractive tests of the SM. The inclusive $t\bar{t}$ cross section, as one of the simplest
1167 top quark observables, is well suited for a first measurement at the new center-of-
1168 mass energy.

1169 Simultaneously, restarting such a large experiment as CMS after a three-year
1170 shutdown poses many experimental challenges. Due to the change in energy, as well
1171 as physical changes in the accelerator and detector, most calibrations and correc-
1172 tions needed to describe the recorded data in simulation need to be re-derived and
1173 validated. An early measurement of the inclusive $t\bar{t}$ cross section is well suited to
1174 cross-check this: Because of the decay chain of the top quark, a top quark measure-
1175 ment involves many of the different objects reconstructed at CMS, enabling a check
1176 of a wide landscape of calibrations.

1177 The measurement described in this chapter was designed specifically with these
1178 motivations in mind, and as such exhibits several novel features. Firstly, it com-
1179 bines events from both the dilepton and $\ell+jets$ decay channels of $t\bar{t}$, categorized
1180 by lepton flavor content, combining the higher statistics of the $\ell+jets$ channel with
1181 the high purity of the $e\mu$ channel and allowing to constrain uncertainties on the
1182 lepton identification efficiency directly from the data. This is done using a simul-
1183 taneous maximum likelihood fit to the event yields in the different categories, with
1184 experimental and theoretical uncertainties treated as nuisance parameters.

1185 Secondly, the events are additionally categorized by their number of b-tagged jets,
1186 which similarly allows for an in-situ measurement of the b-tagging efficiencies. This

1187 averts needing to wait for external b-tagging calibrations, allowing for a measure-
1188 ment as early as possible.

1189 The results of this work were first presented as a Physics Analysis Summary in
1190 September 2022 [117], only two months after the start of datataking, as the first
1191 public physics result of LHC Run 3. It was later published in *JHEP* as Ref. [5],
1192 again representing the first published Run 3 result. A similar result by ATLAS was
1193 later published in Ref. [118].

1194 This chapter is structured as follows: In Sec. 5.2, the used datasets, object def-
1195 initions, and event selection criteria are described, followed by the derivation and
1196 application of needed corrections in Sec. 5.3, and the resulting data-MC agreement
1197 is shown in Sec. 5.4. The considered systematic uncertainties are listed in Sec. 5.5,
1198 and the fit results are presented in Sec. 5.6. The chapter is concluded by a short
1199 summary and outlook in Sec. 5.7.

1200 5.2 Datasets and event selection

1201 In this section, the choice of datasets for experimental data and for simulation, as
1202 well as the choice of triggers, is described. Following that, the object and event se-
1203 lection procedure is outlined and several event categories to be used in the likelihood
1204 fit are defined.

1205 5.2.1 Datasets

1206 **Experimental data** The measurement is performed on data recorded during the
1207 period between July 27th and August 02nd 2022 (part of Era C of year 2022), cor-
1208 responding to an integrated luminosity of 1.21 fb^{-1} . This amount of data is chosen
1209 as a balance between sensitivity and speed for the early measurement: It roughly
1210 corresponds to the point where data statistics no longer significantly limit the mea-
1211 surement uncertainty, while at the same time it is not required to study calibrations
1212 at different beam and detector conditions (e.g. average pileup, which changed during
1213 the different eras of 2022).

1214 Both single-lepton and dilepton triggers were used to select events used in this
1215 measurement during detector operation, identifying leptons in the range of $|\eta| < 2.5$.
1216 The p_T requirements of the triggers are summarized in Tab. 5.1.

1217 **Simulation** To compare the data with predictions, Monte Carlo (MC) simula-
1218 tion is used to simulate both the $t\bar{t}$ signal as well as most important background
1219 processes, specifically single-top quark production in the t -channel, associated tW
1220 production, $Z+jets$ production, $W+jets$ production, and diboson (WW , WZ and
1221 ZZ) production. The MC generator POWHEG v2 [67–69] is used to generate $t\bar{t}$,
1222 single-top, and tW events at next-to-leading order (NLO) in perturbative QCD,

Trigger	Lepton requirement
e+jets	$e(p_T > 32 \text{ GeV})$
μ +jets	$\mu(p_T > 27 \text{ GeV})$
ee	$e(p_T > 23 \text{ GeV})$ and $e(p_T > 12 \text{ GeV})$
$\mu\mu$	$\mu(p_T > 17 \text{ GeV})$ and $\mu(p_T > 8 \text{ GeV})$
e μ	$e(p_T > 23 \text{ GeV})$ and $\mu(p_T > 8 \text{ GeV})$ or $e(p_T > 12 \text{ GeV})$ and $\mu(p_T > 23 \text{ GeV})$

Table 5.1: **Trigger definitions** as used for the $t\bar{t}$ cross section measurement. The leptons are required to be isolated and in the pseudorapidity range $|\eta| < 2.5$.

1223 while the generators **MADGRAPH5_AMC@NLO** [65] and **PYTHIA 8** [71] are used
 1224 to generate Z+jets/W+jets and diboson events, respectively, at leading order (LO).
 1225 For t -channel single-top, **MADSPIN** is used to simulate the top decay.

1226 All of the generated events are interfaced to **PYTHIA 8** for parton showering and
 1227 hadronization, using the MLM prescription in the case of the samples produced
 1228 with **MADGRAPH**, and further processed in a full simulation of the CMS detector
 1229 as described in Chapter 3. The proton structure in the matrix element calculation is
 1230 described by the NNPDF3.1 parton distribution function (PDF) set at NNLO. Note
 1231 that another background contribution, from QCD events with fake or non-prompt
 1232 leptons, is not simulated, but estimated from data (see Sec. 5.3.2).

1233 Theoretical predictions, as well as the measured integrated luminosity, are used
 1234 to normalize the cross sections of the signal and background samples as follows: The
 1235 $t\bar{t}$ signal, is normalized to a cross section of $921^{+29}_{-37} \text{ pb}$ computed at NNLO+NLLL
 1236 in QCD [119], which is also used as a prediction for comparison with the SM. For
 1237 the other backgrounds, the following orders in QCD and methods or programs are
 1238 used: MCFM [120] (NNLO) for single-top, DYTurbo [121] (NNLO) for W+jets
 1239 and Z+jets, MATRIX [122] (NLO) for diboson, and an NNLO calculation from Ref.
 1240 [123] for tW.

1241 5.2.2 Object definition

1242 **Leptons** Electrons or muons are considered for the analysis if they have $p_T > 10$
 1243 GeV and $|\eta| < 2.4$. For electrons, the range $1.44 < |\eta| < 1.57$, corresponding to the
 1244 transition region between barrel and endcaps in the ECAL, is removed. Furthermore,
 1245 additional identification criteria (ID) are applied to remove non-prompt or fake (i.e.
 1246 wrongly reconstructed) leptons and enrich the selection with $t\bar{t}$ events.

1247 For electrons, the “tight” working point of the cut-based ID described in Ref. [95]
 1248 is applied, which includes information from both the details of the electromagnetic
 1249 shower in the ECAL and the track, as well as the matching between the two. It also

includes a requirement for the electron to be isolated from other particles such as hadrons, which is implemented in the form of the relative isolation variable I_{rel} . It is defined as the scalar p_T sum of all particles in a cone around the lepton in question, divided by the lepton p_T . Here, $\Delta R = \sqrt{(\Delta\eta)^2 + (\Delta\varphi)^2} < 0.3$ is used for the radius of the cone. Additional corrections accounting for pileup particles are applied.

For muons, a similar cut-based ID is used as described in Ref. [124], also at the tight working point. Here, criteria on the compatibility of tracks in the inner tracker, the muon detectors and the reconstructed primary vertex are employed. Again, a cut on I_{rel} is used, defined equivalently but with a cone size of $\Delta R < 0.4$.

Jets The anti- k_T algorithm [106] is used to cluster reconstructed particles into jets with a distance parameter of 0.4. In order for a jet to be considered, it is required to have $p_T > 30$ GeV and $|\eta| < 2.4$, and jets overlapping with any considered leptons (i.e. fulfilling the above criteria) are removed.

Tagging of b jets A special role is played by jets originating from the showering and hadronization of b quarks. Naively, two such jets are expected per $t\bar{t}$ event from the two top decays, although in practice one or both jets may fall out of acceptance of the detector or otherwise not get identified, and conversely additional b quarks may be produced by radiation at higher orders in QCD. Correctly tagging these jets as such can greatly improve signal purity by cutting away backgrounds such as Z+jets, W+jets and QCD multijet events.

Here, the DEEPJET algorithm is used to tag b jets, which is based on a deep neural network (DNN) classifier [107, 125]. A working point with an identification efficiency of more than 75% is used, with misidentification rates of around 17% for charm jets and around 1% for other jets (i.e. from light quarks or gluons).

5.2.3 Channel definition

Events are selected with either one or two leptons, corresponding respectively to the dilepton and $\ell+\text{jets}$ decay channels of $t\bar{t}$. They are categorized into lepton channels by their lepton flavor content, and additional requirements are applied for the different channels.

Dilepton channels Events with exactly two leptons, required to have opposite electric charge, are sorted into three dilepton channels ($e\mu$, ee , and $\mu\mu$). The presence of at least one jet is required, and in the same-flavor channels (ee and $\mu\mu$), at least one jet is required to be b tagged in order to reject Z+jets and QCD multijet background. In the much purer $e\mu$ channel, on the other hand, events without b tags are retained to later help constrain the b tagging efficiency in the fit to data.

1285 In order to reject even more Z+jets background, events in the same-flavor channels
 1286 with an invariant dilepton mass of $|m_{\ell\ell} - m_Z| < 15$ GeV, where m_Z is the Z boson
 1287 mass, are removed.

1288 **ℓ +jets channels** Events with exactly one lepton are sorted into the e+jets or
 1289 μ +jets channels based on their flavor. At least three jets are required, of which
 1290 at least one needs to be b tagged. Note that regardless of these selections, there
 1291 is still non-negligible background from QCD multijet events where the lepton is
 1292 non-prompt or fake, which will be estimated from data (see Sec. 5.3.2).

1293 **p_T requirement** In all channels, the considered leptons are required to have $p_T >$
 1294 35 GeV. This requirement is needed in the ℓ +jets channels in order to stay above the
 1295 single-lepton trigger p_T thresholds (compare Tab. 5.1). In this measurement, the
 1296 choice is made to apply the same p_T requirement also both leptons in the dilepton
 1297 channels to ensure consistency between the lepton definitions. This is done to help
 1298 constrain the lepton ID scale factors using the combination of lepton flavor channels,
 1299 which otherwise might not be accurate since the scale factors for different lepton
 1300 definitions might differ. It especially opens up the possibility to extract a result on
 1301 the cross section without any prior knowledge on the lepton ID efficiencies, which
 1302 was done in the first published version of this analysis [117].

1303 **b tag and jet categorization** In practice, the efficiency of the b tagging algo-
 1304 rithm used might be different between simulation and data, necessitating a correc-
 1305 tion to prevent bias. In this analysis, this efficiency is measured simultaneously
 1306 with the cross section directly in the data. To do so, the lepton flavor channels
 1307 are additionally split into categories based on the number (exactly 0, 1, or 2) of b
 1308 tagged jets. Since only the ep channel allows events with 0 b tags, this results in 11
 1309 categories total.

1310 In order to increase possible separation between $t\bar{t}$ signal and background, the
 1311 selected events are finally coarsely binned into the number of accepted jets for the
 1312 eventual fit, giving a total number of 40 bins.

1313 5.3 Corrections

1314 While the simulation used in CMS tries to model as many physics and detector
 1315 effects as possible, in practice it should always be expected that not all observables
 1316 agree with the experimental data perfectly. This is especially true for an early
 1317 analysis such as this, as the detector conditions might have changed significantly
 1318 during the long shutdown between LHC Runs 2 and 3, and the simulation had not
 1319 been recalibrated at the time of the measurement.

Because of this, the analysis setup is designed to either directly measure or cross-check as many required experimental calibration and correction factors as possible. This includes pileup corrections, efficiency scale factors for triggers, electrons, muons and b tags, as well as jet energy corrections, all of which are briefly described in this section.

In addition to these experimental corrections, background processes might also be imperfectly described by the simulation because of theoretical shortcomings. In this case, ways have to be found to correct them directly from the experimental data. Here, two such cases are relevant and will be presented in the latter half of this section: The $Z+jets$ background in the dilepton channels and in the presence of b tagged jets, for which the normalization is taken from data; and the QCD background in the $\ell+jets$ channels, which uses a fully data-driven estimation and foregoes simulation entirely.

5.3.1 Experimental corrections

Pileup reweighting The simulation samples used in this analysis were generated before the start of Run 3 datataking using a projected estimate of the average pileup. As a result, the pileup distribution in the simulation does not match the one observed in data, which could influence mostly jet-related variables such as the number of jets and the jet p_T .

Since at the time of the measurement, no theory-based calculation for the correct pileup distribution were available, an experimental approach was taken. Three experimental observables that are strongly correlated with pileup were identified:

- The number of well-reconstructed primary vertices per event n_{PV} ;
- The median p_T density in the calorimeter, calculated from calorimeter-only jets as $\rho^{\text{calo}} = \text{med}(p_T/A)$, where A is the jet area defined in the φ - η plane and the median is taken over all jets in the event;
- The median p_T density in the tracker ρ^{trk} , defined equivalently as ρ^{calo} , but for jets calculated only from tracker information.

A binned reweighting from simulation to data is derived for each observable based on the full data sample, and the average of the three weights is applied to the simulation, so that approximate agreement is achieved in all three variables. The distributions before and after reweighting can be seen in Fig. 5.1.

Trigger scale factors The trigger efficiency, i.e. the probability for an event falling into the selection phase space to be triggered by the low- and high-level triggers, needs to be corrected for in the simulation. In principle, both dilepton and single-lepton triggers are used for this measurement and should be considered for the

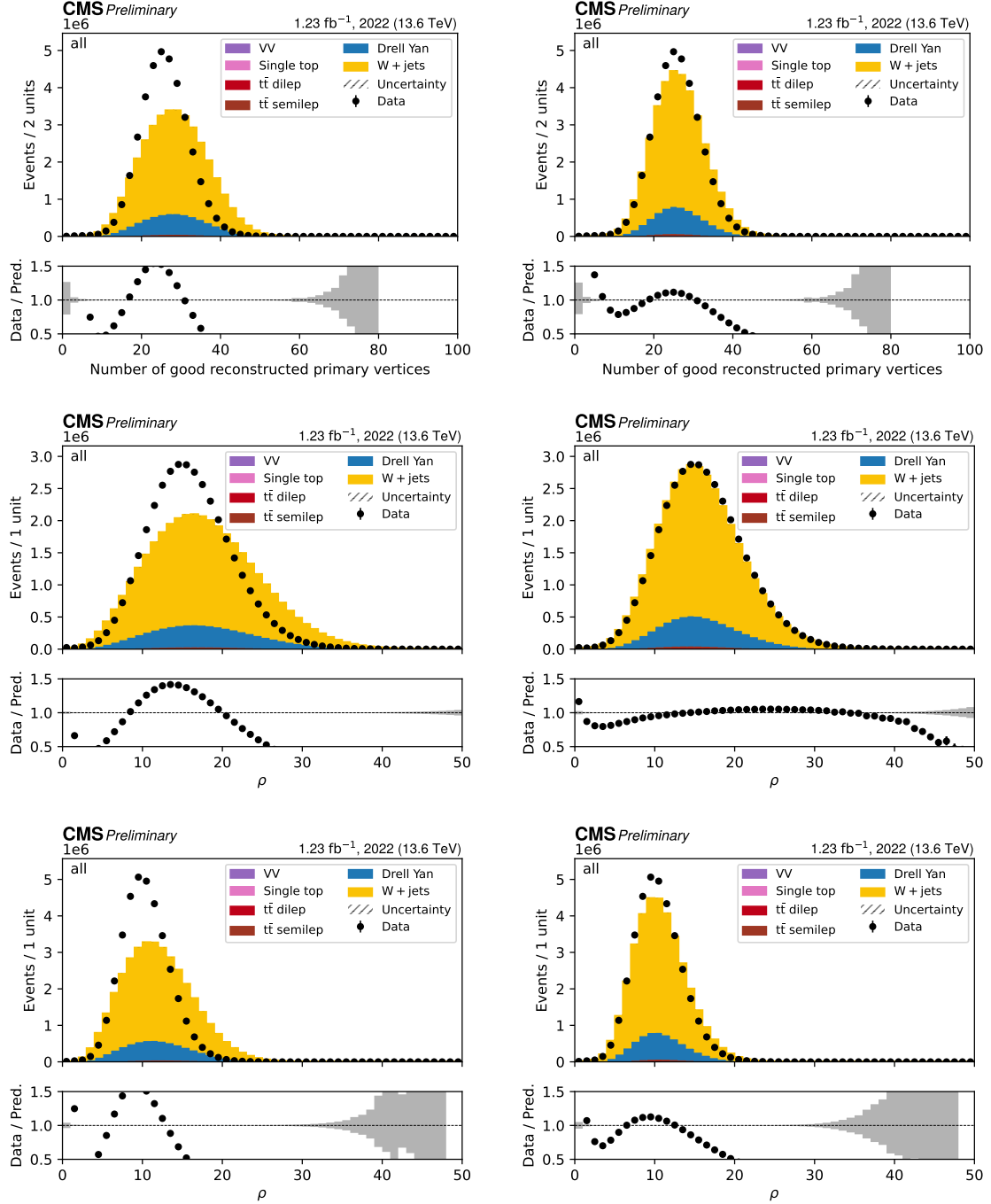


Figure 5.1: Pileup reweighting. Pileup-related distributions in MC and data in before (left) and after reweighting (right). From top to bottom: number of primary vertices as well as the mean energy densities ρ^{calo} (calculated using tracker input) and ρ^{trk} (calculated using calorimeter input).

TODO prettify plots

efficiency calculation. However, due to the high offline p_T requirements for the two leptons applied in all channels, the fraction of events that are triggered only by the dilepton triggers is very small, and can be neglected for the purpose of determining the scale factor. Thus, only the single-lepton triggers are considered in this section for simplicity.

The efficiency measurement is performed by the so-called tag-and-probe (T&P) method, using $Z \rightarrow e^+e^-$ and $Z \rightarrow \mu^+\mu^-$ events. They are selected using the same definitions presented above, including the lepton identification, except for requiring their invariant mass to fulfill $|m_{\ell\ell} - m_Z| < 20$ GeV. At least one of the leptons is required to pass the relevant single-lepton trigger and is then designated the tag, while the other lepton might or might not pass the trigger and is designated the probe. Assuming the probability for the two leptons to pass the trigger to be independent of each other, the trigger efficiency, given by probability of the probe to pass, can be written as

$$\epsilon_{\text{tr}} = \frac{N(\text{Probe passes})}{N(\text{Probe passes}) + \frac{1}{2}N(\text{Probe fails})} \quad (5.1)$$

where N is the observed event yield, and the combinatoric factor $\frac{1}{2}$ comes from the fact that either one or the other lepton can fail to pass the trigger.

The efficiency is measured in this way in coarse bins of lepton p_T and $|\eta|$, separately for muons and electrons, in both simulation and experimental data. It is then applied to simulation in the following way: For $\ell+\text{jets}$ events, a simple ratio $\epsilon_{\text{tr,data}}/\epsilon_{\text{tr,sim}}$ is applied to each simulation event as a scale factor, which is displayed in Fig. 5.2. For dilepton events, on the other hand, the fact that only one lepton needs to pass the single-lepton trigger needs to be taken into account. This leads to a per-event efficiency given by

$$\epsilon_{\text{tr},\ell\ell} = \epsilon_{\text{tr},\ell 1} + \epsilon_{\text{tr},\ell 2} - \epsilon_{\text{tr},\ell 1}\epsilon_{\text{tr},\ell 2} \quad (5.2)$$

where $\epsilon_{\text{tr},\ell 1}$ and $\epsilon_{\text{tr},\ell 2}$ are the efficiencies evaluated at the p_T and $|\eta|$ of the two leptons, respectively. Again, the ratio of this event efficiency in data and simulation is applied to the simulation.

Lepton scale factors Similarly to the triggers, the reconstruction and identification of leptons can exhibit different efficiencies between simulation and data, and thus require scale factors. The efficiencies are measured with a similar tag-and-probe method as for the triggers, and the simulation is corrected to the data. This is the standard approach commonly taken in CMS, detailed in Refs. [95, 124] for electrons and muons, respectively. The efficiency measurement was not performed as part of this thesis, but is still shown in Figs. 5.3 and 5.4 for reference. The muon scale factors are split into a reconstruction and an identification part, while these are combined for the electron scale factors.

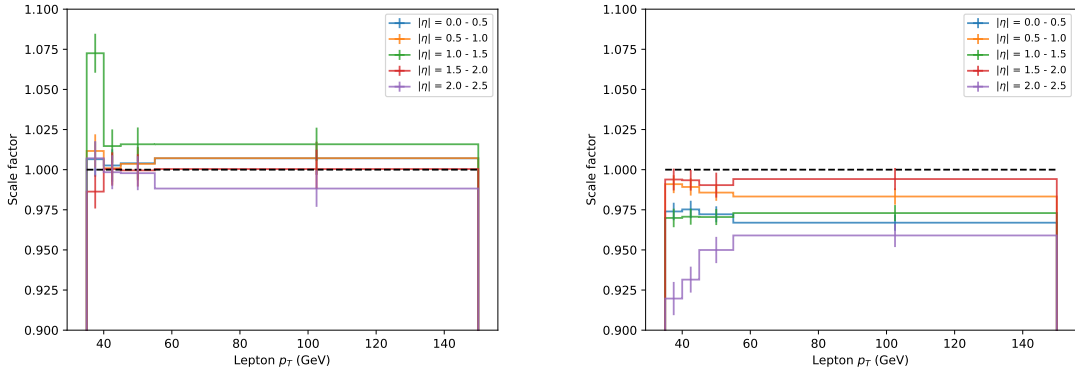


Figure 5.2: **Trigger scale factors.** Single-lepton trigger scale factors for electrons (left) and muons (right) as a function of lepton p_T and $|\eta|$, calculated using a tag-and-probe-method. The error bars designate both statistical and systematic uncertainties. **TODO prettify plots**

1391 **b tagging scale factors** The performance of b tagging algorithms, including
 1392 the DEEPJET algorithm used here, is also well-known to have differences between
 1393 simulation and data, and requires correction. This is especially true since the multi-
 1394 variate classifier underlying DEEPJET had at the time of the measurement not been
 1395 re-trained on Run 3 data, and the calibration from Run 2 was used instead.

1396 However, no external calibration of the b tagging was available at the timescale of
 1397 this work. Instead, the b tagging efficiency in data will be measured simultaneously
 1398 with the $t\bar{t}$ cross section in a single likelihood fit, which is described in more detail
 1399 in Sec. 5.5. No b tagging scale factors are applied at the level of object selection.

1400 **Jet energy corrections.** Another observable that often differs significantly be-
 1401 tween observed data and simulation is the measured energy response of the jets.
 1402 It is usually corrected by empirical methods, i.e. comparing simulation to data for
 1403 well-known resonances like the Z boson. The jet energy correction (JEC) is not
 1404 measured as part of this thesis, and instead centrally provided by CMS following
 1405 the methods of Ref. [126].

1406 5.3.2 Data-driven background estimation

1407 **QCD background** A significant background contribution in the $\ell + \text{jets}$ channels,
 1408 especially in the categories with only one b tag, is given by QCD multijet events
 1409 with one reconstructed lepton. The lepton in question might be non-prompt, e.g.
 1410 from radiated photons splitting into leptons or weakly decaying hadrons created
 1411 during hadronization, or it might be fake, i.e. a different particle (such as a photon
 1412 or pion in the case of electrons) misidentified as a lepton.

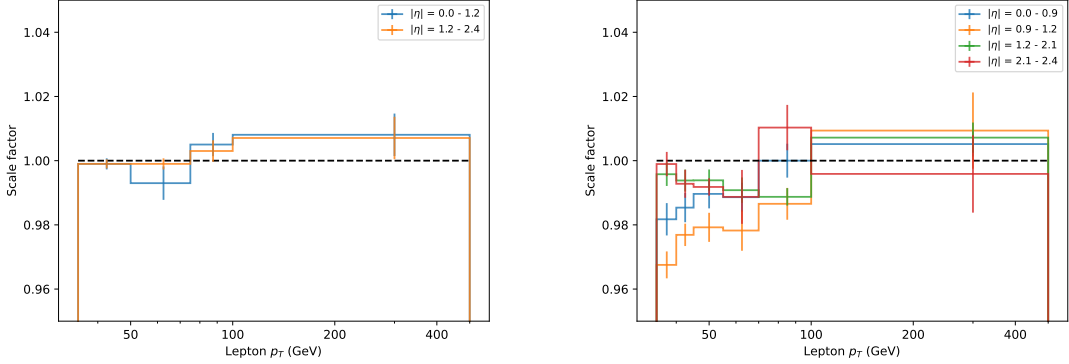


Figure 5.3: **Muon scale factors**, split into reconstruction (left) and identification (right) and shown as a function of lepton p_T and $|\eta|$, calculated using a tag-and-probe-method. The error bars designate both statistical and systematic uncertainties. **TODO** prettify plots

1413 It is often not practical to estimate this background using MC simulation as is done
 1414 for the other backgrounds in this analysis. The reason is that, due to the large cross
 1415 section of QCD multijet events at the LHC but low ratio of events with a fake or non-
 1416 prompt lepton, very large MC datasets are needed to achieve significant statistics
 1417 in the selected phase space, which would require excessive computing power. In
 1418 addition to that, especially fake leptons are not certain to be described well by the
 1419 simulation.

1420 Instead, a fully data-driven approach is taken to estimate the QCD background
 1421 in the $\ell + \text{jets}$ channels. For this, several control regions (CRs) orthogonal to the
 1422 signal region (SR) are defined. In the first CR, denoted “QCD CR”, the same
 1423 cuts as in the SR are applied, except that the requirement for the single lepton
 1424 to be isolated from other particles (I_{rel} , see Sec. 5.2.2) is inverted. It is expected
 1425 that QCD events that fall in either the QCD CR or the SR show similar shapes
 1426 in observable distributions, as long as said observables are uncorrelated with the
 1427 lepton isolation. Thus, the shape of the QCD background can be extracted from
 1428 the CR and applied in the SR. Figs. 5.5 and 5.6 show some control distributions in
 1429 the $\mu + \text{jets}$ and $e + \text{jets}$ channels, respectively, with the difference between data and
 1430 MC in this region considered QCD background.

1431 The normalization of the QCD background is fixed through the so-called *ABCD*
 1432 *method*, for which an additional CR (the “1-jet CR”) is defined. It again contains
 1433 events that pass the main selection, except for requiring exactly one jet (as opposed
 1434 to at least three jets in the SR or QCD CR). These events are enriched with QCD
 1435 events and contain negligible amounts of $t\bar{t}$ signal. They are used to measure the
 1436 ratio f_{fake} of QCD events that pass or fail the lepton isolation requirement, given by

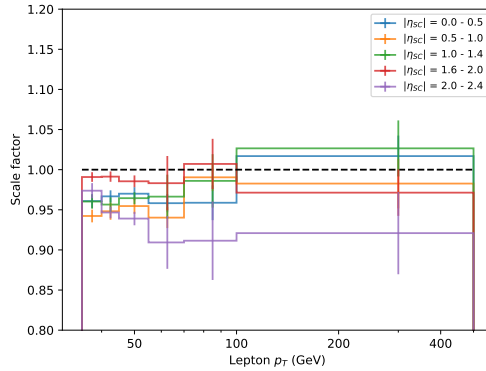


Figure 5.4: **Electron scale factors.** The combined electron scale factors as a function of lepton p_T and $|\eta|$, calculated using a tag-and-probe-method. The error bars designate both statistical and systematic uncertainties.
TODO prettify plots

$$f_{\text{fake}} = \frac{N_{1 \text{ jet}, \text{ pass}}^{\text{data}} - N_{1 \text{ jet}, \text{ pass}}^{\text{MC}}}{N_{1 \text{ jet}, \text{ fail}}^{\text{data}} - N_{1 \text{ jet}, \text{ fail}}^{\text{MC}}} \quad (5.3)$$

where $N_{1 \text{ jet}, \text{ pass}}$ and $N_{1 \text{ jet}, \text{ fail}}$ denote 1-jet-events that pass and fail the lepton isolation requirement, respectively; “data” refers to the experimental data, and “MC” refers to the sum of all non-QCD processes, which are estimated by MC simulation. Here, this ratio is measured in four coarse bins of lepton p_T and $|\eta|$ to accurately model lepton-related distributions; it can be seen in Fig. 5.7.

Naively, the full distribution of the QCD background in the SR for any observable can then be written as

$$N_{\text{SR}}^{\text{QCD}} = (N_{\text{CR}}^{\text{data}} - N_{\text{CR}}^{\text{MC}}) \times f_{\text{fake}} \quad (5.4)$$

where $N_{\text{CR}}^{\text{data}}$ and $N_{\text{CR}}^{\text{MC}}$ refer to the total data and non-QCD MC yields in the QCD CR.

In practice, this is complicated by the fact that a non-negligible amount of $t\bar{t}$ signal is present in the QCD CR, whose cross section, as the parameter of interest in the measurement, is not known *a priori*. To circumvent this problem, a modified method is introduced, which is agnostic about the prediction for the $t\bar{t}$ cross section. One sets for the SR

$$N_{\text{SR}}^{\text{data}} = N_{\text{SR}}^{t\bar{t}} + N_{\text{SR}}^{\text{MC,BG}} + N_{\text{SR}}^{\text{QCD}} \quad (5.5)$$

and similarly for the QCD CR

5 Measurement of the inclusive $t\bar{t}$ cross section at $\sqrt{s} = 13.6$ TeV

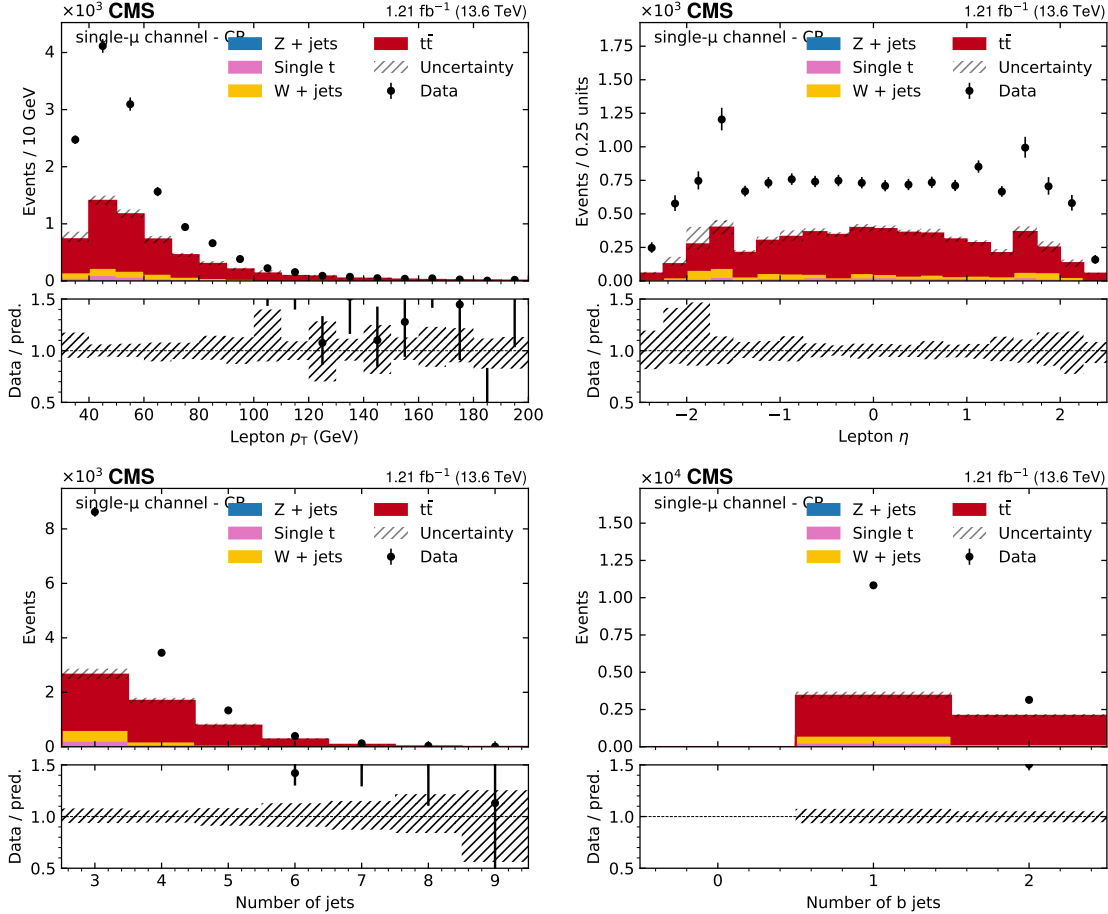


Figure 5.5: **QCD control region for $\mu+$ jets.** Distributions in the QCD CR for the $\mu+$ jets channel. From top left to bottom right: p_T of the lepton, η of the lepton, the number of jets, and the number of b-tagged jets. The uncertainty bands include MC statistical and systematic uncertainties. The difference between data and MC is considered QCD background. **TODO** prettify plots; also actually show the estimated QCD in green instead of as the difference between data and MC

$$N_{\text{CR}}^{\text{data}} = N_{\text{CR}}^{t\bar{t}} + N_{\text{CR}}^{\text{MC,BG}} + N_{\text{CR}}^{\text{QCD}}, \quad (5.6)$$

where N^{data} is the total data yield, $N^{t\bar{t}}$ is the $t\bar{t}$ signal contribution, $N^{\text{MC,BG}}$ is the contribution of non-QCD backgrounds as predicted by MC, and N^{QCD} is the QCD contribution. It is assumed that the ratio f_{sig} of signal events in the SR and QCD CR (but not necessarily the normalization) is correctly predicted by MC:

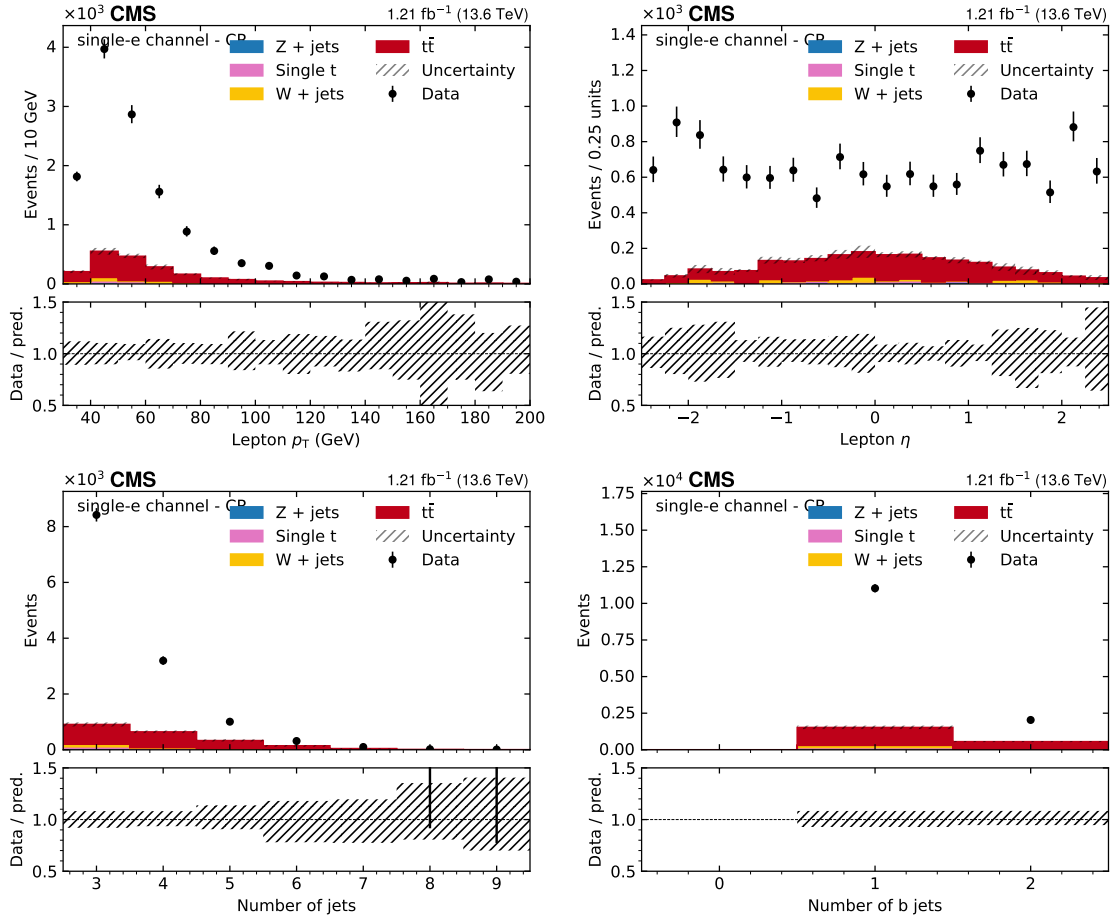


Figure 5.6: **QCD control region for e+jets.** Distributions in the QCD CR for the e+jets channel, same as in Fig. 5.5. **TODO** prettify plots

$$f_{\text{sig}} := \frac{N_{\text{CR}}^{\text{t}\bar{t}}}{N_{\text{SR}}^{\text{t}\bar{t}}} = \frac{N_{\text{CR}}^{\text{t}\bar{t}, \text{MC}}}{N_{\text{SR}}^{\text{t}\bar{t}, \text{MC}}} \quad (5.7)$$

Furthermore, one sets similar to Eq. (5.4)

$$N_{\text{SR}}^{\text{QCD}} = N_{\text{CR}}^{\text{QCD}} \times f_{\text{fake}} \quad (5.8)$$

where f_{fake} is still given by Eq. (5.3), which is unaffected since the $t\bar{t}$ signal contamination in the 1-jet CR is negligible.

Combining all these equations, one can first replace $N_{\text{CR}}^{\text{t}\bar{t}}$ in Eq. (5.6) by $f_{\text{sig}} N_{\text{SR}}^{\text{t}\bar{t}}$ according to Eq. (5.7), then eliminate $N_{\text{SR}}^{\text{t}\bar{t}}$ in favour of $N_{\text{SR}}^{\text{data}}$, i.e. the total data yield in the SR, and get

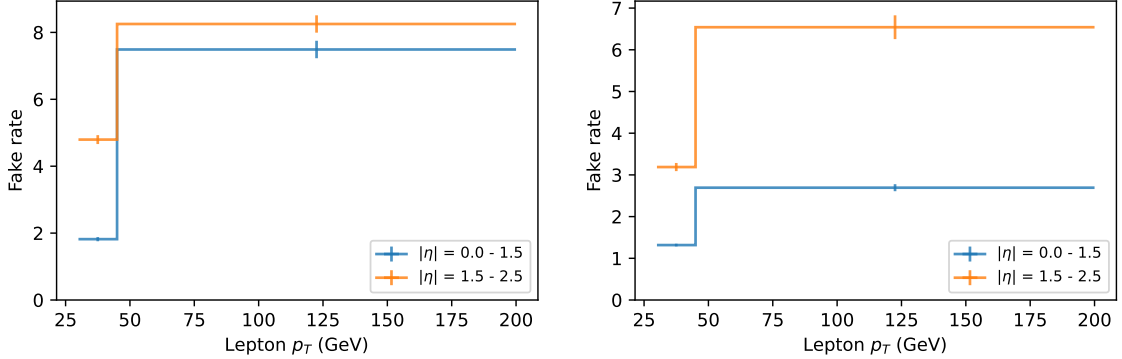


Figure 5.7: **QCD fake rate.** The fake rate for the QCD background estimated in the 1 jet bin for electrons (left) and muons (right) as a function of lepton p_T and $|\eta|$. The error bars designate statistical uncertainties only.

$$N_{\text{SR}}^{\text{QCD}} = f_{\text{fake}} \left(N_{\text{CR}}^{\text{data}} - N_{\text{CR}}^{\text{MC,BG}} - f_{\text{sig}} \left(N_{\text{SR}}^{\text{data}} - N_{\text{SR}}^{\text{MC,BG}} - N_{\text{SR}}^{\text{QCD}} \right) \right). \quad (5.9)$$

¹⁴⁶² Solving this equation for $N_{\text{SR}}^{\text{QCD}}$ finally yields the corrected QCD contribution in
¹⁴⁶³ the SR:

$$N_{\text{SR}}^{\text{QCD}} = \left(N_{\text{CR}}^{\text{data}} - N_{\text{CR}}^{\text{MC,BG}} - f_{\text{sig}}(N_{\text{SR}}^{\text{data}} - N_{\text{SR}}^{\text{MC,BG}}) \right) \times \frac{f_{\text{fake}}}{1 - f_{\text{sig}}f_{\text{fake}}} \quad (5.10)$$

¹⁴⁶⁴ The resulting QCD distributions from this method are further treated in the same
¹⁴⁶⁵ way as the MC backgrounds, and can be seen together with them in Figs. 5.8 to 5.10.

¹⁴⁶⁶ **Z+jets background** In contrast to the QCD background, the Z+jets background,
¹⁴⁶⁷ which is relevant mostly in the ee and $\mu\mu$ channels, can in general be well described
¹⁴⁶⁸ by MC simulation. However, in the phase space used in the analysis, there can
¹⁴⁶⁹ be problems related to the b tag requirement. For Z+jets events, b jets are only
¹⁴⁷⁰ generated at the matrix element level at higher orders in perturbative QCD, and
¹⁴⁷¹ might thus not be well modeled compared to observed data. This in turn could
¹⁴⁷² influence the acceptance of Z+jets events, leading to an incorrect normalization in
¹⁴⁷³ events with one or more b tags.

¹⁴⁷⁴ Here, a data-driven normalization is derived for Z+jets events with one or two b
¹⁴⁷⁵ tags in the dilepton channels, following Ref. [38]. This is important especially in the
¹⁴⁷⁶ same-flavor channels, where Z+jets is a dominant background.

¹⁴⁷⁷ The normalization is derived using a CR in which the cut on $m_{\ell\ell}$ is inverted, i.e.
¹⁴⁷⁸ in events with $|m_{\ell\ell} - m_Z| < 15$ GeV (“inside the Z window”), which are strongly

enriched in Z+jets contributions. It is assumed that the Z+jets contribution in the e μ channel (which stems mostly from $Z \rightarrow \tau\tau$ events) is negligible compared to the ee and $\mu\mu$ channels, and that all other backgrounds (including $t\bar{t}$) are approximately equal in the three dilepton channels up to combinatorics, in the sense that their differences are small compared to the Z+jets event yield. Then, said Z+jets yield in the Z window in the same-flavor channels can be estimated directly from data by subtracting the e μ channel – and with it, the other backgrounds – from the ee and $\mu\mu$ channels. This results in

$$N_{ee/\mu\mu}^{Z+jets} = N_{ee/\mu\mu, in}^{\text{data}} - \frac{1}{2} N_{e\mu, in}^{\text{data}} k_{ee/\mu\mu, in} \quad (5.11)$$

where $N_{\ell\ell, in}^{\text{data}}$ refers to the number of observed events inside the Z window for the respective channel, and $k_{ee} = k_{\mu\mu}^{-1} = \sqrt{N_{ee, in}^{\text{data}}/N_{\mu\mu, in}^{\text{data}}}$ is a efficiency factor to correct for the different acceptance of electrons and muons.

To translate this yield from the CR to the SR, the ratio $R_{in/out} = N_{in}^{Z+jets}/N_{out}^{Z+jets}$ (referring to *inside* and *outside* of the Z window) of event numbers between those two regions has to be estimated. This could in principle be done by directly using the MC simulation (as done in e.g. Refs. [16, 127]). However, since this ratio might by itself be mismodeled in MC, a more cautious approach is taken here. A second CR is defined from events with 0 b tags (which are not considered in the main measurement in the same-flavor channels) and used to construct to construct a more loose assumption:

$$\frac{R_{in/out}^{\text{data}}(\geq 1 \text{ b tag})}{R_{in/out}^{\text{MC}}(\geq 1 \text{ b tag})} = \frac{R_{in/out}^{\text{data}}(0 \text{ b tags})}{R_{in/out}^{\text{MC}}(0 \text{ b tags})} \quad (5.12)$$

This equation means that the *ratio of ratios* $R_{in/out}(\geq 1 \text{ b tag})/R_{in/out}(0 \text{ b tags})$ is assumed to be well described by MC. It can be solved for the Z+jets yield outside of the Z window in the same-flavor channels, yielding

$$\begin{aligned} N_{out}^{Z+jets} &= \frac{N_{in}^{Z+jets}}{R_{in/out}^{\text{data}}(\geq 1 \text{ b tag})} \\ &= \frac{R_{in/out}^{\text{MC}}(0 \text{ b tags})}{R_{in/out}^{\text{data}}(0 \text{ b tags})} \frac{N_{in}^{Z+jets}}{R_{in/out}^{\text{MC}}(\geq 1 \text{ b tag})} \end{aligned} \quad (5.13)$$

where N_{in}^{Z+jets} is given by Eq. (5.11). In practice, this yield is quoted as a scale factor compared to the nominal MC prediction. For the e μ channel (in which Z+jets is much less important), the scale factor is simply assumed to be the geometric mean of the ee and $\mu\mu$ scale factors.

The final scale factors can be seen in Tab. 5.2.

ee	e μ	$\mu\mu$
1.36 ± 0.04	1.32 ± 0.03	1.28 ± 0.03

Table 5.2: **Z+jets scale factors.** Ratio of the Z+jets event yields estimated in data using the method described in Sec. 5.3.2 to the prediction by the MC simulation. Uncertainties are statistical only.

5.4 Control distributions

The agreement between simulation and data in several control distributions is presented in Figs. 5.8 to 5.10. All corrections described in the previous section are applied in these figures. In addition, they are already scaled by the b tagging scale factors as will be measured in the likelihood fit (Sec. 5.6).

Good agreement between data and simulation within the full uncertainties is seen in all distributions.

5.5 Systematic uncertainties

In order to translate the distribution of observed and expected events into a result for the inclusive $t\bar{t}$ cross section while taking into account all relevant sources of systematic uncertainties, a binned profile maximum likelihood fit as described in Sec. 4.4 is performed using the tool `combine` [114]. The parameter of interest (POI) used for this fit is the signal strength $r = \sigma_{t\bar{t}}/\sigma_{t\bar{t}}^{\text{pred}}$, i.e. the inclusive $t\bar{t}$ cross section normalized to its theoretical prediction. A linear signal model is used as defined in Eq. (4.3), and the $t\bar{t}$ cross section is extracted using its maximum likelihood estimate and uncertainty.

This section describes the considered systematic uncertainties, which can be divided into experimental uncertainties, arising from incomplete knowledge of the details of the detector and resulting differences between data and simulation, and theoretical uncertainties, which concern imperfect modeling of the underlying physical processes in the different event generators.

All systematic uncertainties are included in the fit as nuisance parameters (NPs) as discussed in Sec. 4.4. In practice, NPs which encode shape effects on the considered observables are implemented using *template morphing*, i.e. a smooth polynomial interpolation between the nominal shape and the shapes encoding the variations by ± 1 standard deviations. NPs that encode only normalization effects are instead implemented as simple log-normal uncertainties. Both definitions can be found in detail in Ref. [114].

Special attention is given in this section to some experimental uncertainties which are important to this measurement. This includes the luminosity, which is the dominating uncertainty, as well as the b tagging uncertainties due to the special

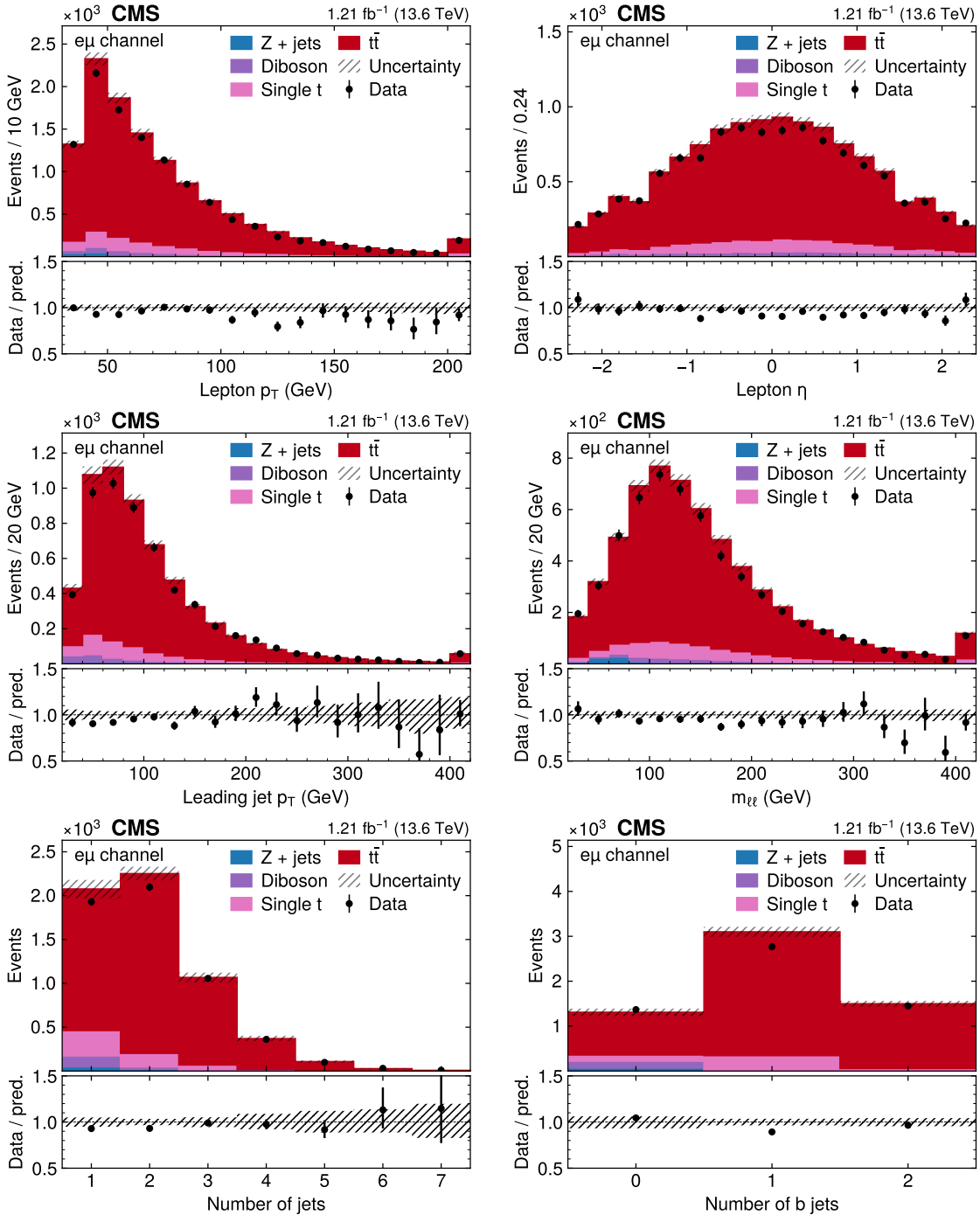


Figure 5.8: Control distributions in the $e\mu$ channel. Shown are (from top left to bottom right) the distributions of p_T of both leptons, $|\eta|$ of both leptons, p_T of the leading jet, the invariant lepton mass $m_{\ell\ell}$, the number of jets and the number of b jets. All figures show both data (black dots) and different simulated background processes (colored bars). For the latter, all corrections described in Sec. 5.3 as well as post-fit b tagging scale factors (Sec. 5.6) are applied, and the shaded area covers both statistical and systematic uncertainties.

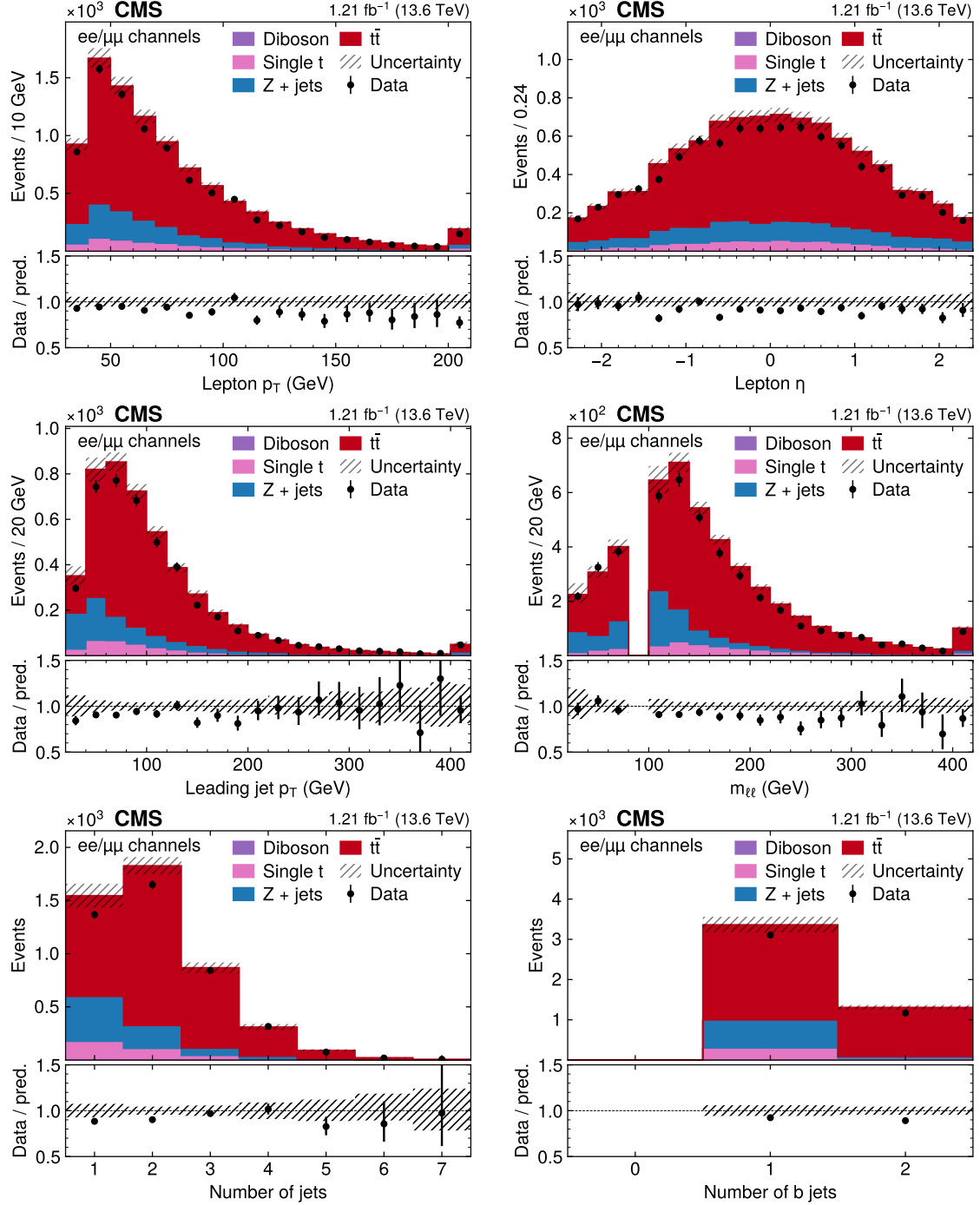


Figure 5.9: **Control distributions in the ee and $\mu\mu$ channels.** The distributions are shown in the same manner as in Fig. 5.8.

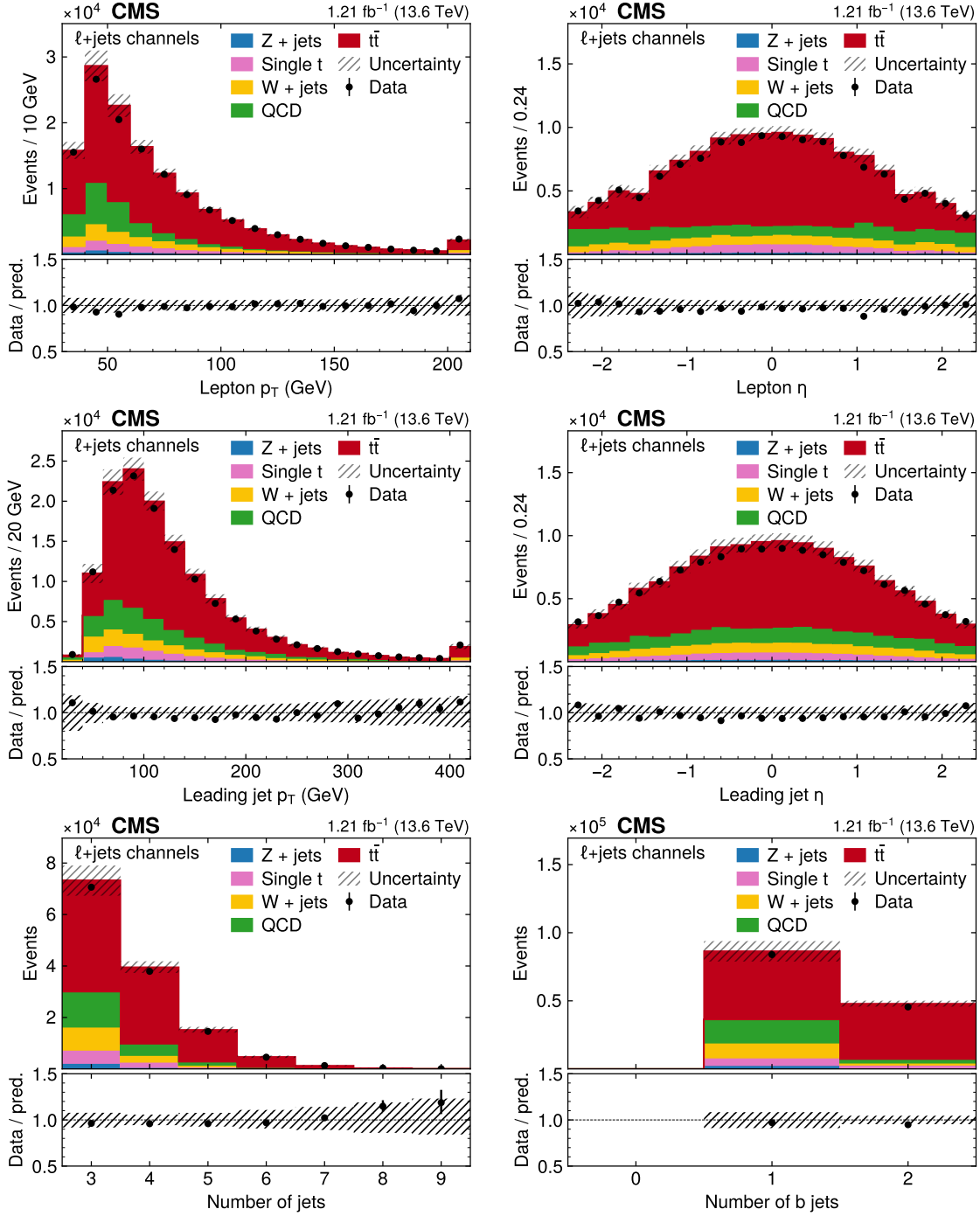


Figure 5.10: **Control distributions in the ℓ +jets channels.** The distributions are shown in the same manner as in Fig. 5.8, except for the center-right figure, which here shows $|\eta|$ of the leading jet.

1537 way they are treated in the fit.

1538 **Luminosity uncertainty** In order to translate event yields, as measured using
1539 histograms, into a result on any cross section, the total integrated luminosity is
1540 required as a calibration constant. It is immediately clear that any experimental
1541 error on the luminosity will be directly transferred to the total error on the mea-
1542 surement, and thus minimizing the luminosity uncertainty is crucial for any cross
1543 section measurement.

1544 For the dataset used in this analysis, the total luminosity uncertainty was eval-
1545 uated by CMS to be 2.3%. Of this number, 2.1% is due to the calibration of the
1546 integrated luminosity, using the methods presented in Ref. [82]. The largest con-
1547 tribution comes from factorization bias, which arises in the van der Meer method
1548 from the assumption that the transverse luminous area factorizes in the x and y
1549 coordinates, and from residual beam position deviations.

1550 The agreement in the absolute scale is checked by comparing different indepen-
1551 dently calibrated luminosity measurements, and the integrated luminosity measured
1552 with the hadronic forward (HF) calorimeter and the silicon pixel detector is found to
1553 agree at a level of better than 0.8%. Taking additional contributions due to residual
1554 differences in the time-stability and linearity between the luminosity detectors into
1555 account leads to the full figure of 2.3%. A cross-check of the integrated lumino-
1556 sity using the yield of reconstructed Z bosons decaying into pairs of muons [128],
1557 corrected for efficiencies and normalized to the fiducial cross section prediction cal-
1558 culated at NNLO with next-to-NNLL corrections applied, shows good agreement as
1559 well.¹

1560 In contrast to all other uncertainties described below, the uncertainty in the inte-
1561 grated luminosity is not included in the fit, but treated as an external uncertainty
1562 and added in quadrature afterwards, since it is expected to factorize completely from
1563 all other uncertainties. The impact of varying the normalization of the backgrounds
1564 estimated from simulation by the integrated luminosity uncertainty was found to be
1565 negligible.

1566 **b tagging uncertainty** As mentioned in Sec. 5.3.1, the efficiency for correctly
1567 identifying a jet originating from a b quark (b tagging) is expected to be different
1568 in data and simulation. At the time of this measurement, directly after the start of
1569 Run 3, no general-purpose b tagging studies had been available. Thus, the approach
1570 adopted here is to consider the b tagging efficiency in data to be completely unknown
1571 and measure it concurrently with the cross section in the likelihood fit.

1572 For this purpose, the probability for an event with n_{jet} selected jets to have n_{btag}
1573 correctly identified b jets, depending on the assumed b tagging efficiency ϵ_b , is

¹Since publication of this result, a more precise luminosity measurement for 2022 data has become available in Ref. [129].

5.5 Systematic uncertainties

1574 assumed to be a multinomial of the form

$$P(n_{\text{btag}}|n_{\text{jet}}) \propto \epsilon_b^{n_{\text{btag}}} (1 - \epsilon_b)^{n_{\text{no tag}}} \quad (5.14)$$

1575 Here, $n_{\text{no tag}}$ is the number of true b jets in the event which fall into the accep-
 1576 tance of the selection, but fail to be tagged by DEEPJET. It is estimated from MC
 1577 simulation.

1578 By taking the ratio of eq. 5.14 in data and simulation, one can derive a per-event
 1579 weight which corrects the number of b tags in MC:

$$w_b = \frac{(\epsilon_b^{\text{data}})^{n_{\text{btag}}} (1 - \epsilon_b^{\text{data}})^{n_{\text{no tag}}}}{(\epsilon_b^{\text{MC}})^{n_{\text{btag}}} (1 - \epsilon_b^{\text{MC}})^{n_{\text{no tag}}}} = (f_b)^{n_{\text{btag}}} \left(\frac{1 - f_b \epsilon_b^{\text{MC}}}{1 - \epsilon_b^{\text{MC}}} \right)^{n_{\text{no tag}}} \quad (5.15)$$

1580 Here, $f_b = \epsilon_b^{\text{data}} / \epsilon_b^{\text{MC}}$ is the unknown b tagging scale factor. It is left freely
 1581 floating in the likelihood fit. This is technically implemented by producing shape
 1582 templates from MC with f_b varied up and down by a fixed value and interpolating
 1583 inbetween. This shape template can be seen in Fig. 5.11, where it is evident that
 1584 the categorization in the number of b tags gives significant constraining power for
 1585 f_b . In the 1b categories, the shape with respect to the number of jets deviates
 1586 significantly from a flat variation proportional to f_b as naively expected. This is
 1587 because of out-of-acceptance jets, corresponding to the second factor in Eq. (5.15).

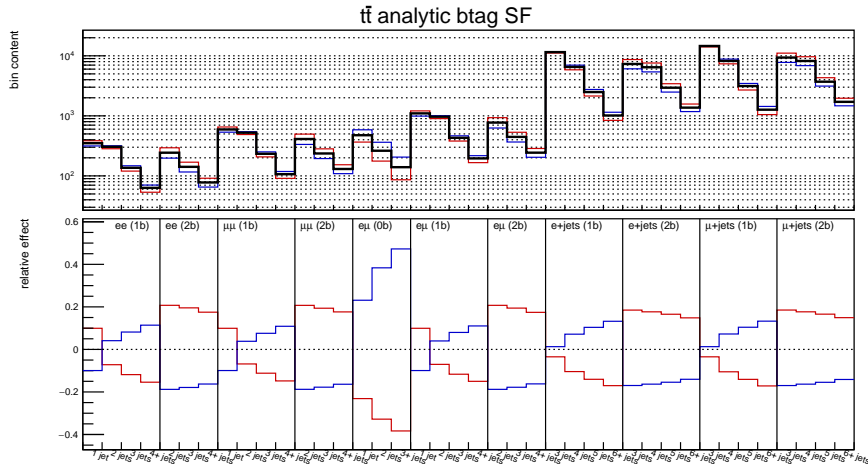


Figure 5.11: **b tagging scale factor variation.** The effect of varying the b tagging scale factor f_b in $t\bar{t}$ MC by an arbitrary value of ± 0.1 , shown for the number of jets in the 11 fit categories. **TODO** prettify figure

1588 Note that any dependence of ϵ_b on the jet kinematics factorizes out as long as
 1589 said dependency is the same in data and MC. Possible kinematic dependencies of
 1590 the ratio f_b are neglected; since no kinematic information is used in the fit, this is

1591 deemed acceptable.

1592 **Lepton identification uncertainty** The uncertainty assumed on the lepton iden-
1593 tification scale factors comes from two different sources: First, an inherent uncer-
1594 tainty originating in the tag-and-probe method (as described in Sec. 5.3.1) is con-
1595 sidered. It consists of statistical uncertainties from both data and simulation, a
1596 systematic uncertainty derived from a comparison with a different Z+jets simula-
1597 tion sample produced at NLO in QCD, and another systematic uncertainty due
1598 to the choice of fitting function. Together, they make up for an uncertainty of
1599 $\sim 0.8\%$ (0.5%) on the electron (muon) scale factors in the bulk of the phase space,
1600 and can rise up towards $\sim 5\%$ for high lepton p_T .

1601 Secondly, it is taken into account that the scale factor between data and simulation
1602 might be slightly different in the Z+jets selection used for the T&P method and the
1603 $t\bar{t}$ selection used for the measurement of the cross section. The most important rea-
1604 son for this is the requirement of (b tagged) jets in almost all considered categories,
1605 as well as the requirement for at least three jets in the lepton+jets channels.

1606 This effect has been studied at CMS in the past and the difference found to be
1607 less than 0.5% for muons and 1.0% for electrons. Taking a conservative approach,
1608 these values are used as an additional component in the respective uncertainties.

1609 **Pileup uncertainty** As described in Sec. 5.3.1, three different pileup-related vari-
1610 ables are employed to reweight the simulation to the observed data, and the average
1611 of the three weights is used as the nominal value. This method is repeated using
1612 only one of the variables - the number of good reconstructed vertices n_{PV} - and
1613 the difference in expected yields treated as an uncertainty. It should be noted that
1614 this difference was found to be larger than the more common method of estimat-
1615 ing pileup-related uncertainties, which consists of deriving a theoretical expectation
1616 for the number of interactions depending on the total inelastic proton-proton cross
1617 section, and varying this number by its experimental uncertainty.

1618 **Jet energy uncertainties** Uncertainties in the jet energy calibration are split
1619 into 26 different sources concerning different experimental and theoretical effects,
1620 following the standard CMS procedure outlined in Ref. [126]. 17 of these sources
1621 are found to be non-negligible and included in the fit. These sources include, among
1622 others, uncertainties due to jet p_T resolution and jet flavour composition, statistical
1623 uncertainties in the derivations of the energy corrections, and residual differences
1624 between data and simulation.

1625 **Trigger uncertainties** Since the trigger scale factors are derived using the tag-
1626 and-probe method in the same way as the lepton scale factors, similar uncertainties
1627 are applied, including the extrapolation uncertainties of 0.5% for muons and 1.0%

for electrons. The only difference is that in the dilepton channels the uncertainties need to be propagated according to Eq. (5.2). This has the effect of greatly reducing the impact of the trigger uncertainties in those channels compared to the lepton ID uncertainties, since the nominal per-event trigger efficiency is already very close to one.

Matrix element scale uncertainties The theoretical predictions of both signal and background are calculated using matrix elements at either LO or NLO in perturbative QCD, matched to a parton shower. Since this effectively means truncating the perturbative expansion of the scattering amplitude at a given power in the strong and electroweak coupling constants, the effect of higher-order terms is neglected in the calculation.

At the same time, the necessity of renormalization of divergent diagrams and factorization of non-perturbative contributions introduces non-physical parameters into the prediction in the form of the renormalization and factorization scales μ_R and μ_F (cf. Sec. 3.1). These parameters are usually set to typical energy scales of the considered process, and might also depend on the event kinematics (dynamic scales).

To estimate possible errors due to these missing terms as well as due to the choice of scales, the scales μ_R and μ_F are varied separately by a factor of 2 up and down, and the resulting change in simulation is taken as an uncertainty in the form of shape templates [130]. In order to not double-count uncertainties in the cross section prediction for the backgrounds (see below), but keep possible rate variations due to acceptance effects, the templates are normalized to the nominal cross section values before any selection cuts are applied. Different physical processes are considered to be uncorrelated since they are produced with different generators and at different orders.

PDF uncertainties The parton distribution functions (PDFs) used to evaluate the non-perturbative contribution of the proton-proton collision have systematic uncertainties attached. They are estimated by independently reweighting the simulation to 100 different replicas of the used NNPDF 3.1 PDF set and taking the envelope of the resulting changes, following the recommendations of the PDF4LHC working group [131]. Additionally, the effect of the choice of the strong coupling constant in the PDF is assessed using a similar reweighting, and attached as a separate nuisance parameter. Analogously to the matrix element uncertainties, the resulting variations are normalized before any selection cuts to keep acceptance and shape effects while not double-counting cross section changes.

Parton shower uncertainties Furthermore, the parton shower model used for the predictions is only accurate (at most) at leading-log (LL) as well as leading color

¹⁶⁶⁶ (LC) in QCD (cf. Sec. 3.2) and thus requires appropriate uncertainties. For this
¹⁶⁶⁷ purpose, the scales at which the strong coupling constant is evaluated are varied up
¹⁶⁶⁸ and down by a factor 2 separately for initial and final state radiation and for different
¹⁶⁶⁹ processes, and the resulting changes propagated to the fit as shape templates.

¹⁶⁷⁰ **ME/PS matching uncertainty** For the simulation of the $t\bar{t}$ signal, an additional
¹⁶⁷¹ uncertainty concerning the matching between matrix element simulation in POWHEG
¹⁶⁷² and parton showering in PYTHIA is considered. This is done by varying the h_{damp}
¹⁶⁷³ parameter in POWHEG controlling the amount of radiation generated at matrix
¹⁶⁷⁴ element level, following Ref. [132].

¹⁶⁷⁵ **Background cross section uncertainties** For the cross sections of the different
¹⁶⁷⁶ processes, log-normal rate uncertainties are assigned based on the process and order
¹⁶⁷⁷ at which it was calculated. Specifically, a 15 % uncertainty is used for the single- t
¹⁶⁷⁸ background since it is generated fully at NLO with a NNLO prediction for the
¹⁶⁷⁹ cross section, while uncertainties of 20 % and 30 % are used for Z+jets as well
¹⁶⁸⁰ as W+jets and Diboson, respectively, since these samples are only generated at
¹⁶⁸¹ LO. Additionally, for the fully data-driven QCD background, two separate nuisance
¹⁶⁸² parameters for the e+jets and μ +jets channels are defined, covering a conservative
¹⁶⁸³ uncertainty of 30 % each.

¹⁶⁸⁴ **Background statistical uncertainties** Finally, since the background in this
¹⁶⁸⁵ measurement is estimated either using MC simulation or data-driven methods, an
¹⁶⁸⁶ independent statistical uncertainty needs to be attached to each bin, reflecting the fi-
¹⁶⁸⁷ nite number of events it contains. This is done using the method given in Ref. [133].
¹⁶⁸⁸ For MC backgrounds, these uncertainties are minuscule; however, they are non-
¹⁶⁸⁹ negligible for the data-driven QCD background due to the limited data statistics
¹⁶⁹⁰ used there.

¹⁶⁹¹ 5.6 Fit results

¹⁶⁹² Performing the fit yields a $t\bar{t}$ signal strength of $r = 0.958 \pm 0.025$, where the un-
¹⁶⁹³ certainty includes statistical and all systematic contributions, except for the 2.1%
¹⁶⁹⁴ uncertainty on the luminosity. This corresponds to an inclusive $t\bar{t}$ cross section of

$$\sigma_{t\bar{t}} = 882 \pm 23 (\text{stat+syst}) \pm 20 (\text{lumi}) \text{ pb}$$

¹⁶⁹⁵ The result is in agreement within one standard deviation with the standard model
¹⁶⁹⁶ prediction of $\sigma_{t\bar{t}}^{\text{pred}} = 921^{+29}_{-37}$ pb.

¹⁶⁹⁷ Fig. 5.12 shows the agreement between data and simulation before and after the
¹⁶⁹⁸ fit. It can be immediately seen that the fit greatly reduces the uncertainty on the

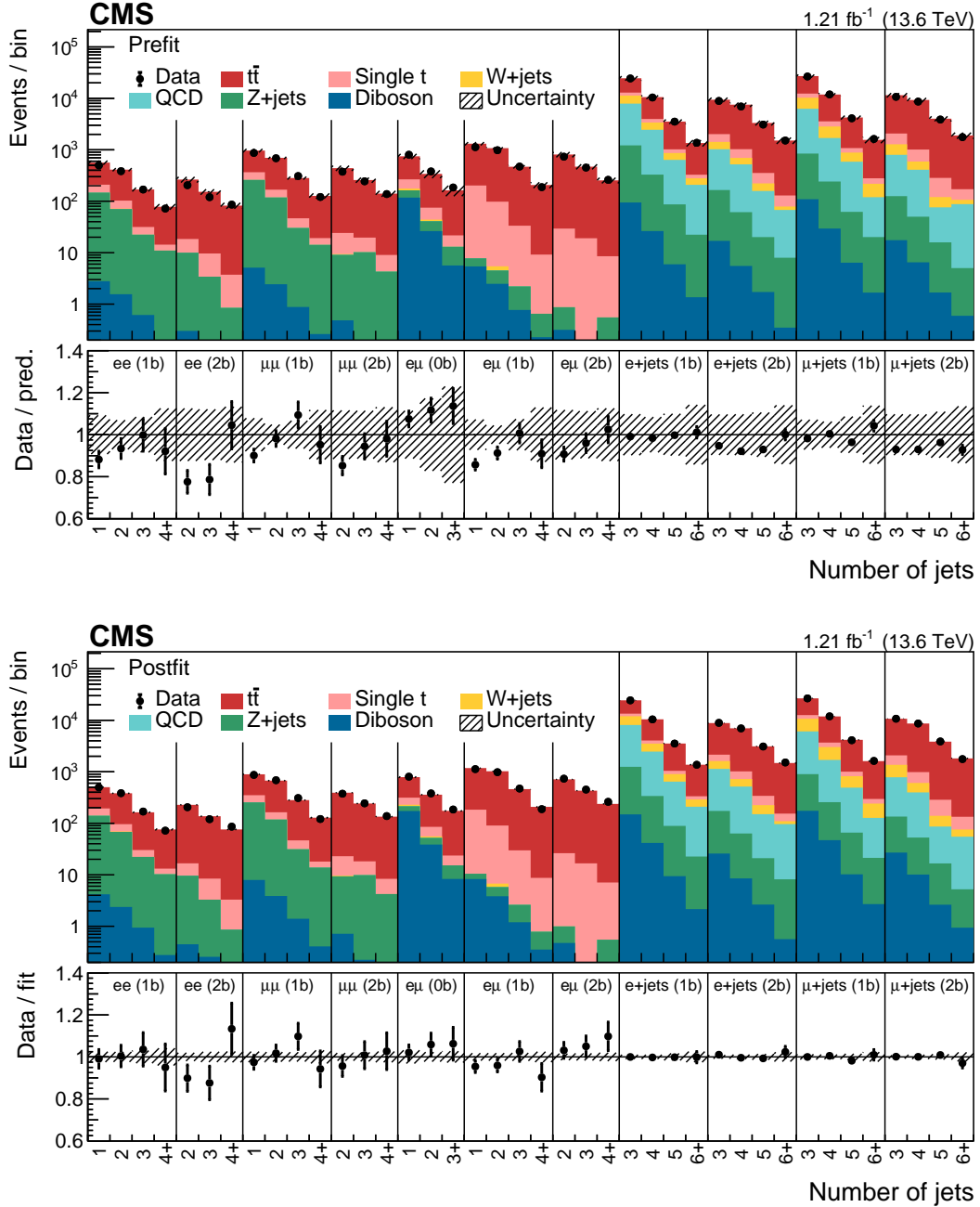


Figure 5.12: Comparison of data and simulation before and after the fit.

The distribution of the number of jets in the different fit categories is shown for data and simulation before (top) and after the likelihood fit (bottom). The fit greatly improves the agreement and strongly constrains the background uncertainties.

1699 prediction by constraining systematic uncertainties and simultaneously improves the
1700 agreement compared to the data.

1701 Of particular note here is the free-floating b tagging efficiency (compare sec. 5.5),
1702 whose effect can be directly read off from the categorization in the number of b jets:
1703 Before the fit (Fig. 5.12 top), the event yield for two or more b jets is overestimated in
1704 the simulation, while the yield for zero b jets is underestimated. This suggests that
1705 the b tagging efficiency is slightly lower in the data than assumed in the simulation.
1706 Indeed, the fit confirms this: the b tagging scale factor between data and simulation
1707 in the phase space of this measurement is measured to be $f_b = 0.980 \pm 0.009$. As a
1708 result, after the fit (Fig. 5.12 bottom), the event yields agree in all b jet categories.

1709 5.6.1 Statistical checks

1710 To better understand the sources of systematic uncertainty, as well as the contribu-
1711 tions of the different measurement channels, the fit is repeated twice, restricted
1712 to either the dilepton or the $\ell+jets$ channels. For both cases as well as the combi-
1713 nation, the contribution of different groups of nuisance parameters is calculated as
1714 explained in Sec. 4.4. The results can be found in Tab. 5.3, where it can be seen
1715 how the combination of channels helps to reduce the total uncertainty.

1716 Furthermore, the nuisance parameter pulls, constraints and impacts, as defined
1717 in Sec. 4.4, are shown in Fig. 5.13. One can see here especially how the electron
1718 identification scale factors, which are the leading impact, are constrained by the
1719 combination of channels, while the same is not true of the muon identification scale
1720 factors due to their lower pre-fit uncertainty.

1721 5.6.2 Top quark mass dependence

1722 An additional source of uncertainty that has not been considered so far is the choice
1723 of top quark mass in the $t\bar{t}$ MC simulation. It affects the selection efficiency indi-
1724 rectly via the p_T cuts on leptons and jets, with higher top quark mass values leading
1725 to harder spectra and thus to larger efficiencies.

1726 Contrary to other uncertainty sources, the top quark mass is not profiled in the
1727 likelihood fit. Instead, the dependence of the extracted $t\bar{t}$ cross section is explicitly
1728 quantified as a function of the top quark mass by shifting its value in simulation by
1729 ± 3 GeV from its default of $m_t = 172.5$ GeV. The extraction of $\sigma_{t\bar{t}}$ is then repeated
1730 and the dependence on m_t extracted through a simple linear fit.

1731 For an upwards shift of $\Delta m_t = 1$ GeV, the $t\bar{t}$ cross section is found to shift down-
1732 wards by 8.5 pb, and vice versa. If one takes the current experimental uncertainty of
1733 0.3 GeV [11] as an allowed range for m_t , this would lead to an additional uncertainty
1734 on $\sigma_{t\bar{t}}$ of 0.3%.

Source	Full measurement	dilepton only	$\ell+$ jets only
Lepton ID efficiencies	1.6	2.4	1.0
Trigger efficiency	0.4	0.0	0.5
JES	0.7	0.7	1.0
b tagging efficiency	1.0	0.4	1.8
Pileup reweighting	0.5	0.0	1.0
ME scale, $t\bar{t}$	0.5	0.4	0.6
ME scale, backgrounds	0.1	0.1	0.3
ME/PS matching	0.2	0.2	0.4
PS scales	0.4	0.9	0.6
PDF and α_S	0.3	0.4	0.4
Single t background	1.1	1.2	0.8
Z+jets background	0.3	0.1	0.0
W+jets background	0.0	0.0	0.1
Diboson background	0.4	0.4	0.0
QCD multijet background	0.3	0.0	0.5
Statistical uncertainty	0.5	1.2	0.5
Combined uncertainty	2.6	3.3	3.0
Integrated luminosity	2.3	2.3	2.3

Table 5.3: **Sources of systematic uncertainty.** The relative per-cent contribution of different groups of sources of systematic uncertainty for the full measurement as well as for restrictions to the dilepton and $\ell+$ jets channels only. They are calculated according to Sec. 4.4 and do not take correlations between the different groups into account.

1735 5.7 Summary and Outlook

1736 In this chapter, the inclusive $t\bar{t}$ cross section is measured for the first time at a center-
 1737 of-mass energy of $\sqrt{s} = 13.6$ TeV. Data corresponding to an integrated luminosity of
 1738 1.21 fb^{-1} from the beginning of LHC Run 3 are analyzed. Despite this comparatively
 1739 small amount of data, a total precision of ca. 3% with respect to the inclusive cross
 1740 section is achieved.

1741 Fig. 5.14 compares the result of this chapter to other inclusive $t\bar{t}$ cross section
 1742 measurements performed by CMS at other center-of-mass energies [134–141], as
 1743 well as to the SM prediction [142]. The precision is comparable to other measure-
 1744 ments at $\sqrt{s} = 7, 8$, and 13 TeV, some of them with significantly higher integrated
 1745 luminosities. All results are in agreement with the SM.

1746 This measurement was designed specifically for the earliest data of Run 3, and

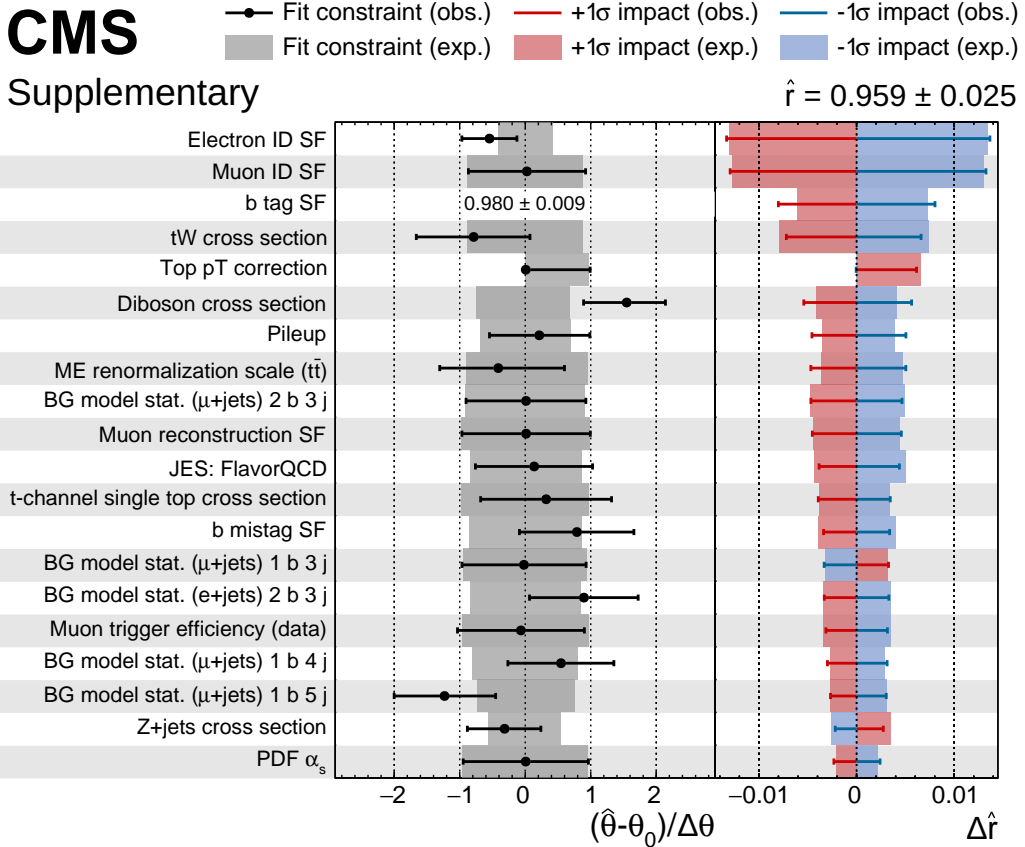


Figure 5.13: **Nuisance parameter pulls, constraints and impacts.** The expected and observed values are shown as shaded bands and error bars, respectively. Nuisance parameters are sorted by their observed impact on the signal strength r . For the b tagging scale factor, for which no pre-fit uncertainty is defined, the post-fit uncertainty is shown instead of the pull.

this is what allows it to reach comparatively high precision even though not all calibrations were available. In particular, b tagging and lepton efficiencies can be constrained in situ using the combination of dilepton and $\ell+jets$ channels as well as the categorization by number of b-tagged jets. No large inconsistencies for any of the considered physics objects were found. The measurement was made public in September of 2022 just two months after the start of Run 3 and constituted the first public result of LHC Run 3. At the time, it provided a valuable first proof that the data taken in Run 3 was of high quality and ready for physics.

The next step for this result would be to transfer the technique developed in this work to well-understood data and high integrated luminosities in order to achieve the highest precision possible for $\sigma_{t\bar{t}}$. Such a measurement will certainly be domi-

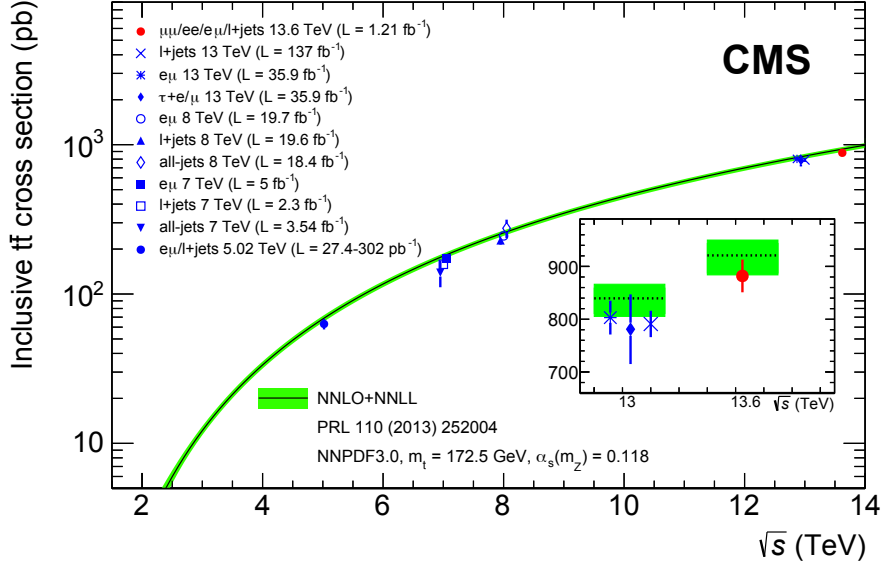


Figure 5.14: **Summary of $\sigma_{t\bar{t}}$ measurements.** An overview of inclusive $t\bar{t}$ cross section measurements at CMS at different center-of-mass energies [134–141] as well as comparison to the SM prediction [142]. This measurement is displayed as the red dot.

nated by systematic uncertainties, most importantly the luminosity and the lepton identification efficiencies (as already partly the case here). The channel combination method developed here could help reduce the latter of these through an in situ constraint, while the former is orthogonal to the analysis strategy and its reduction requires more precise luminosity measurements. It will likely also be necessary to study the different sources of uncertainty in more detail, and investigate whether some of them can be reduced through more careful calibrations.

Additionally, one could try to use such a high-precision $t\bar{t}$ cross section measurement to indirectly measure the top quark mass, one of the fundamental parameters of the Standard Model, by comparing the measured value to SM predictions for different top quark masses. For this purpose, it would be important to reduce the dependence on the top quark mass in simulation (c.f. Sec. 5.6.2), for example by reducing the p_T requirements on leptons and jets as much as experimentally feasible. All of this is, however, not part of this thesis and material for future work.

1772 6 Simulation of on- and off-shell $t\bar{t}$ 1773 production with **bb41**

1774 6.1 Introduction

1775 The accurate modeling of top quark production processes at the LHC is of crucial
1776 importance for precision measurement of top quark properties. In particular, the
1777 fact the top quark is an unstable resonance with a short lifetime presents challenges
1778 for correctly modeling its mass lineshape as used for top mass and width measure-
1779 ments [143–145]. Typically, the modeling is done with full NLO MC simulations
1780 matched to a parton shower (NLO+PS), and multiple such generators are available
1781 with different features and degrees of accuracy.

1782 In this chapter, the predictions of some of these generators from the POWHEG
1783 framework [67, 68] are compared to each other, as well as to unfolded data mea-
1784 sured in Ref. [146], for different variables relevant to top mass and/or width mea-
1785 surements. A particular focus is the generator **bb41** [7], which specifically improves
1786 the treatment of the unstable top resonance and of the interference between $t\bar{t}$ and
1787 tW , and is described in detail in Sec. 6.2. In this work, **bb41** is implemented and
1788 validated for the first time in the CMS simulation setup. The comparison is done
1789 at the generator level, i.e. including parton showering and hadronization but not
1790 detector simulation and experimental reconstruction.

1791 The results of this work have been published in a CMS public note as Ref. [6].
1792 Since the publication of this note, a new version of **bb41** has been made avail-
1793 able [147], leading to small differences as discussed below. In this thesis, updated
1794 results including both versions will be shown.

1795 6.2 The Monte Carlo generator **bb41**

1796 **bb41** [7, 147] is a full NLO+PS MC generator for the process $pp \rightarrow b\bar{b}\ell^+\ell^-\nu_\ell\bar{\nu}_\ell$,
1797 including all off-shell contributions. This includes the dilepton decay channel of
1798 both $t\bar{t}$ and tW production, as well as non-resonant contributions involving Z or
1799 Higgs bosons, as shown in Fig. 6.1. Since these processes all lead to the same
1800 final state at NLO in QCD, they interfere with each other and can not be easily
1801 separated. **bb41** includes this interference by construction since it computes the full
1802 amplitude including all diagrams at once.

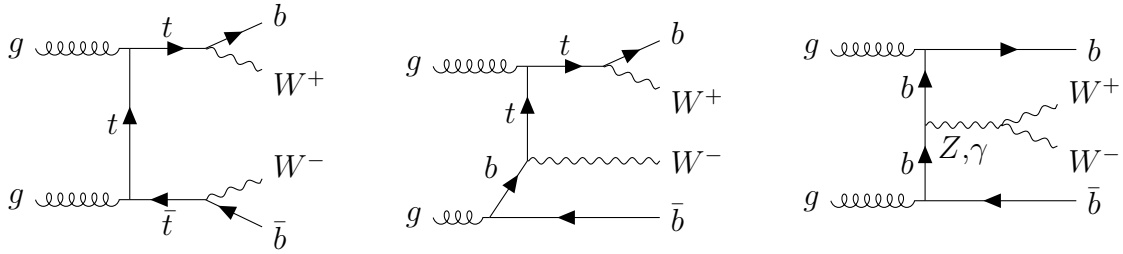


Figure 6.1: **Feynman diagrams for bb41.** Examples of Feynman diagrams for the $pp \rightarrow b\bar{b}W^+W^-$ process as described by bb41, including double-resonant (left), single-resonant (center) and non-resonant contributions (right). The decay of the W bosons into leptons is not shown for brevity.

1803 In addition, by considering the full amplitude instead of splitting it into production
 1804 and decay parts, bb41 fully treats the top quark as an unstable resonance without
 1805 approximations. It is implemented in the “resonance-aware” version of POWHEG,
 1806 called POWHEG vRES [148], which includes hard QCD radiation also for unstable
 1807 resonances - such as top quarks - in addition to the initial state radiation always
 1808 provided by POWHEG. As a result, an event generated by bb41 can have up to
 1809 three hard emissions at matrix element level. The correct description of these FSR
 1810 emissions is relevant e.g. for observables related to the mass of the top quark, and
 1811 can be challenging for parton showers, leading to large uncertainties.

1812 This work investigates two different versions of bb41. The first version is the one
 1813 originally published in Ref. [7] and publically available on the POWHEG website [149].
 1814 In the following, it will be referred to as bb41 v1.

1815 The second version of bb41 was recently published in Ref. [147]. Its most promi-
 1816 nent feature compared to the previous version is the addition of the lepton+jets
 1817 decay channel of $t\bar{t}$, i.e. the $b\bar{b}\ell\nu_\ell q\bar{q}'$ final state. In addition, it includes several
 1818 improvements to the dilepton final state, such as avoidance of spurious finite width
 1819 effects and improved resonance history projectors (see Ref. [147] for details). At the
 1820 time of writing this thesis, the new code is not publically available. A preview ver-
 1821 sion was made available to the CMS collaboration by the authors, and the dilepton
 1822 final state of this version - referred to as bb41 v2 - is shown in this work. The lep-
 1823 ton+jets final state, on the other hand, was not ready for validation in the preview
 1824 version, and so could not be included.

1825 6.3 Other $t\bar{t}$ Monte Carlo generators

1826 The distributions predicted by bb41 are compared to three other MC generators
 1827 for the $t\bar{t}/tW$ final state, which are briefly presented in this section. All of these
 1828 are implemented in POWHEG v2, and as such do not contain explicit treatment of

1829 radiation in unstable resonances.

1830 6.3.1 **hvq**

1831 **hvq** [70], standing for *heavy quark*, is the standard code used, at the time of writing,
1832 by both the ATLAS and CMS collaborations for producing $t\bar{t}$ MC events. It
1833 applies the narrow-width approximation (NWA) to generate stable $t\bar{t}$ pairs at NLO
1834 in QCD, with up to one additional ISR emission. The top quarks are then ran-
1835 domly smeared according to the top quark width, giving an approximate treatment
1836 of finite-width effects. Following this, the top quarks are decayed - in this case, in
1837 the dilepton channel for all lepton flavors - using internal POWHEG routines [150].
1838 These routines work at tree level with NLO matrix element corrections and preserve
1839 spin correlations. Further ISR emissions as well as all FSR emissions are handled
1840 by the matching to the parton shower.

1841 6.3.2 **ST_wtch**

1842 Since **hvq** generates only the double-resonant $t\bar{t}$ amplitude, a second generator has to
1843 be used alongside it for the single-resonant tW and $t\bar{t}/tW$ interference contributions.
1844 Here, **ST_wtch** [151] is used for this purpose. It works very similar to **hvq**, also
1845 generating a stable tW pair in the NWA, smearing with the top width and decaying
1846 the particles using the same routines.

1847 However, in order to at least approximately recover the full $b\bar{b}W^+W^-$ amplitude,
1848 it is necessary to select a scheme for the treatment of the $t\bar{t}/tW$ interference to
1849 prevent double-counting. Since the separation between $t\bar{t}$ and tW is not well defined
1850 at NLO, such schemes will to some degree always be ad-hoc and ambiguous. Two
1851 such schemes are implemented for **ST_wtch**, and both are compared in this work:
1852 in the first, called diagram removal (DR), all terms involving the square of double-
1853 resonant diagrams are simply removed from the squared amplitude. This is the
1854 most intuitive choice, but has the disadvantage of not being gauge invariant [152].
1855 The second method, diagram subtraction (DS), keeps double-resonant diagrams in
1856 the squared amplitude, and subtracts a gauge invariant counter-term to remove the
1857 double counting [151–153]. For both schemes, the prediction of **ST_wtch** is added
1858 to the one of **hvq** (together called $t\bar{t} + tW$) to produce distributions that can be
1859 compared to **bb41**.

1860 6.3.3 **ttb_NLO_dec**

1861 The generator **ttb_NLO_dec** [154], similar to **hvq**, works in the NWA and thus
1862 generates stable $t\bar{t}$ pairs with ad-hoc smearing. However, unlike **hvq**, it is fully
1863 NLO-accurate not only in the production, but also in the decay of the top quarks.

Parameter	Value
POWHEG settings	
Top quark mass	172.5 GeV
Top quark width	1.33 GeV
h_{damp}	$1.38 m_t$ [132]
PDF set	NNPDF 3.1 [40]
PYTHIA settings	
PYTHIA version	8.307
PYTHIA tune	CP5 [76]
PowhegHooks settings [72]	
POWHEG:veto	on
POWHEG:pThard	0
POWHEG:pTdef	1

Table 6.1: **Generator settings.** An overview of the settings for POWHEG and PYTHIA, as well as the matching between them, for all considered generators.

1864 This means that, like `bb41`, it generates up to one hard FSR emission per decaying
 1865 top quark, leading to up to three hard emissions in the final state.

1866 It also provides an LO-accurate treatment of the $t\bar{t}/tW$ interference by reweighting
 1867 the generated $t\bar{t}$ events to the full off-shell LO amplitude. Thus, like `bb41`, it can
 1868 be used on its own and does not need to be added together with e.g. `ST_wtch`, but
 1869 is expected to work at a lower accuracy since it includes more approximations.

1870 6.4 Technical setup

1871 For all generators, LHE events were generated and then showered and hadronized
 1872 with the multi-purpose generator PYTHIA. Wherever possible, the same settings
 1873 were used for the different generators, an overview of which can be found in Tab. 6.1.
 1874 They are mostly identical to the default settings used by CMS for MC generation,
 1875 as discussed in Ref. [76].

1876 6.4.1 Parton shower matching

1877 Special care has to be taken regarding the matching of the POWHEG ME gener-
 1878 ators to the parton shower as provided by PYTHIA. For `hvq` and `ST_wtch`, this
 1879 is accomplished here using a shower veto as described in Sec. 3.2, and technically
 1880 implemented using the PowhegHooks module of PYTHIA. By default, this module
 1881 can only handle one ISR emission at matrix element level, and thus needs to be
 1882 extended for `bb41` and `ttb_NLO_dec`, which also contain FSR emissions in the top

decay. This was implemented by the **bb41** authors in the **PowhegHooksBB4L** module as described in detail in Ref. [155]. A updated form of this module compatible with **bb41** v2 is used here. Similarly to the ISR case, it is possible to directly start the shower at the energy scale of the POWHEG emission, or alternatively employ a veto for emissions above this scale. The latter is used as the default option, and compared to the former in Sec. 6.5.2.

6.4.2 Same-flavor leptons

By default, both versions of **bb41** generate only dilepton final states with opposite-flavor leptons (electrons, muons or τ leptons). This is because, in principle, there are additional diagrams contributing to the $b\bar{b}\ell^+\ell^-\nu_\ell\bar{\nu}_\ell$ amplitude for same-flavor leptons, such as $b\bar{b}ZZ$ with $ZZ \rightarrow \ell^+\ell^-\nu_\ell\bar{\nu}_\ell$, that are not included in **bb41**.

In practice, the effect of these diagrams will be small, especially in experimental analyses where a cut is applied to reject resonant same-flavor lepton pairs close to the Z boson mass (compare Sec. 5.2.3). To make sure that **bb41** can be used in CMS for experimental analyses involving all lepton flavors, a relabeling procedure already included in **bb41** is extended to also produce same-flavor lepton final states, neglecting the aforementioned diagrams. This procedure is used for all **bb41** distributions shown in this chapter.

6.5 Results

6.5.1 Comparison between generators

In this section, the two **bb41** versions are compared against each other, as well as to the alternative generators introduced in Sec. 6.3, for different observables. All of these comparisons are done after parton showering and hadronization, but without any detector simulation.

The package **RIVET** [156] was used to analyze the events. For some observables, publically available analysis packages were employed, which is stated in the captions of the figures where applicable. Furthermore, some observables include distributions at the jet level, which are obtained by running an anti- k_T algorithm with distance parameter $\Delta R = 0.4$ (AK4) [106].

Lepton observables To begin the comparison, events with at least two leptons of opposite sign satisfying $p_T > 20$ GeV and $|\eta| < 2.4$ are selected. Photons surrounding the leptons in a small cone of $\Delta R < 0.1$, originating from photon radiation, are clustered together with the leptons (“dressed leptons”). The p_T distributions of the leading and subleading of these two leptons are shown in Fig. 6.2. They show

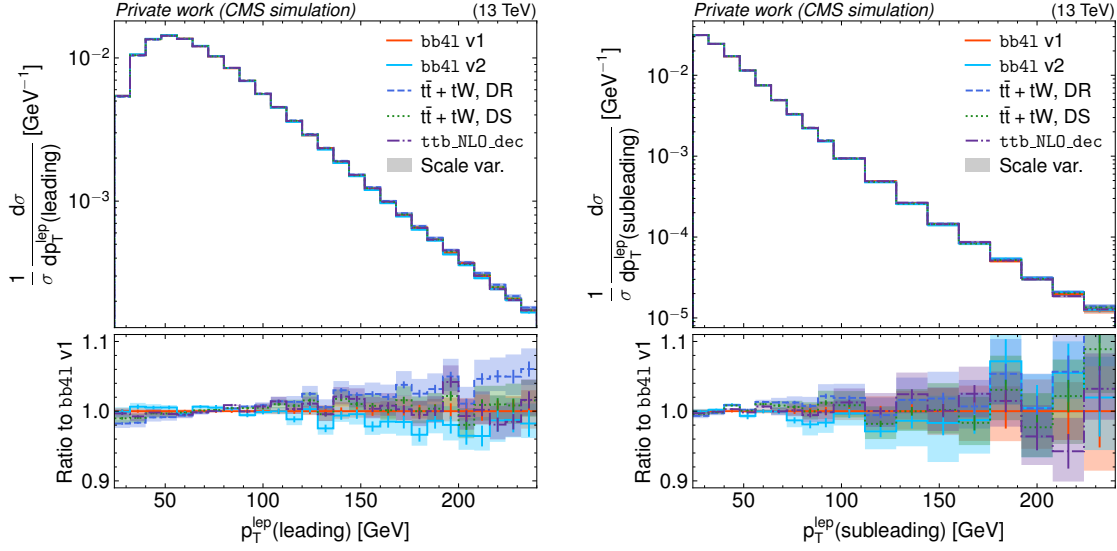


Figure 6.2: **Distributions of lepton p_T** of the leading (left) and subleading (right) lepton for bb41 v1 (red), v2 (aqua), $t\bar{t} + tW$ with the DR (blue) and DS scheme (green), as well as ttb_NLO_dec (magenta). The shaded bands show the uncertainty due to scale variations, while the error bars show the statistical uncertainty.

good agreement between the generators within the scale uncertainties, with $t\bar{t} + tW$ predicting a slightly harder lepton spectrum than the others.

The same trend can be seen in Fig. 6.3 for the invariant lepton mass $m_{\ell\ell}$, both inclusively and split by lepton flavor channels. The per-channel distributions are all comparable within statistical uncertainties, which validates the extension to same-flavor leptons for bb41 presented in Sec. 6.4.2.

Jet observables Next, some selected AK4 jet observables are compared. Jets containing a B hadron are identified as b jets using a ghost association technique [157, 158].

Fig. 6.4 shows the inclusive number of jets and the p_T of the leading b jet for the different cases. Several differences are observable here both between the two versions of bb41 and between bb41 and the other generators. For the number of jets, these are mostly covered by the scale uncertainties, while for the b jet p_T , there is an uncovered discrepancy at very low p_T . It is interesting to note that the number of jets agrees well between $t\bar{t} + tW$ and bb41 v2, while bb41 v1 and ttb_NLO_dec disagree and predict a larger number of jets. The origin of these discrepancies, especially between the bb41 versions, is not yet understood.

Next, Fig. 6.5 shows the b quark fragmentation, defined as the fraction of energy of the central B hadron in a jet compared to the total jet energy, as well as the average

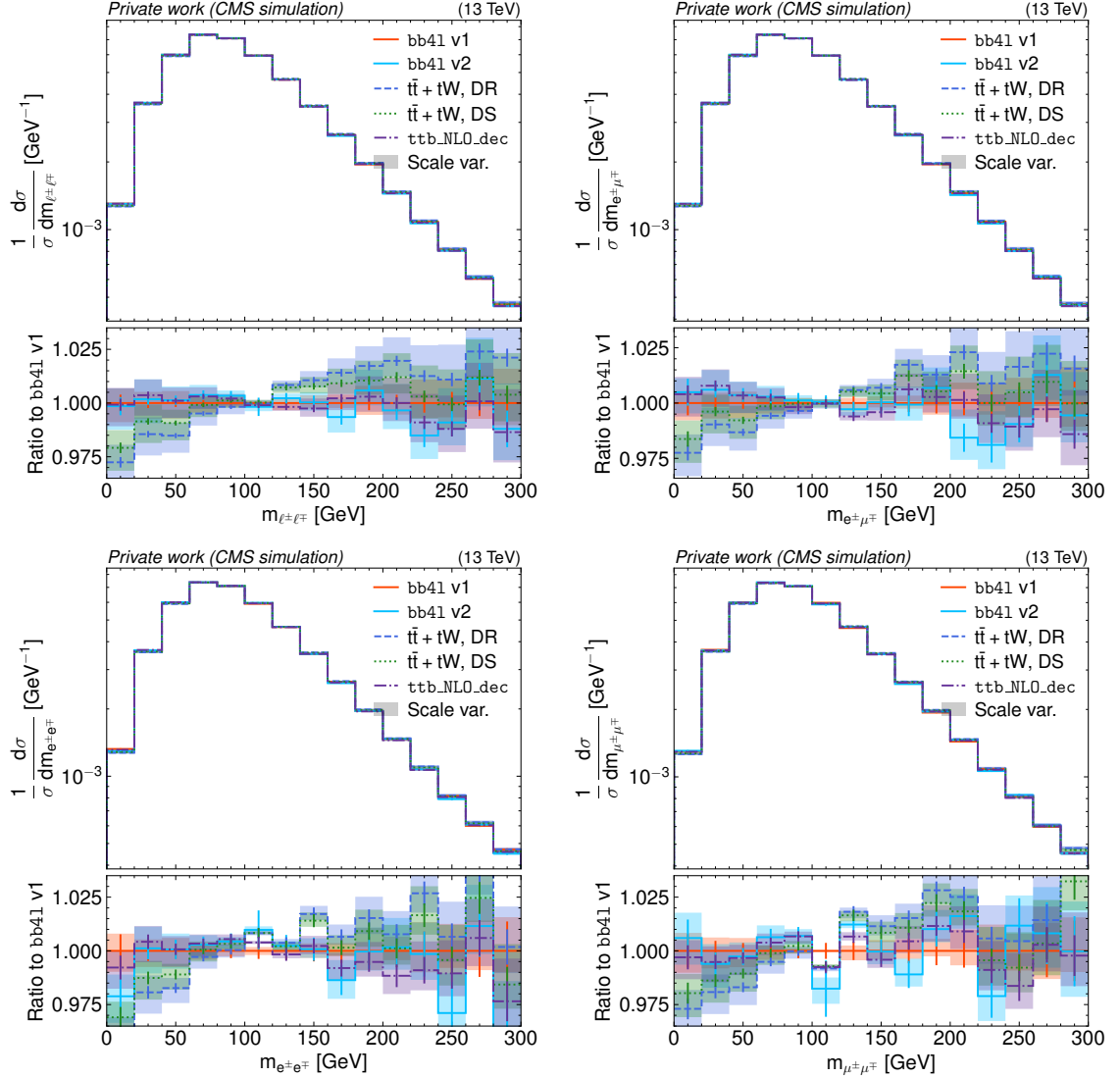


Figure 6.3: **Distributions of m_{ll}** for all lepton flavors combined (upper left) as well as in the $e\mu$ (upper right), ee (lower left) and $\mu\mu$ channels (lower right), shown in the same manner as in Fig. 6.2.

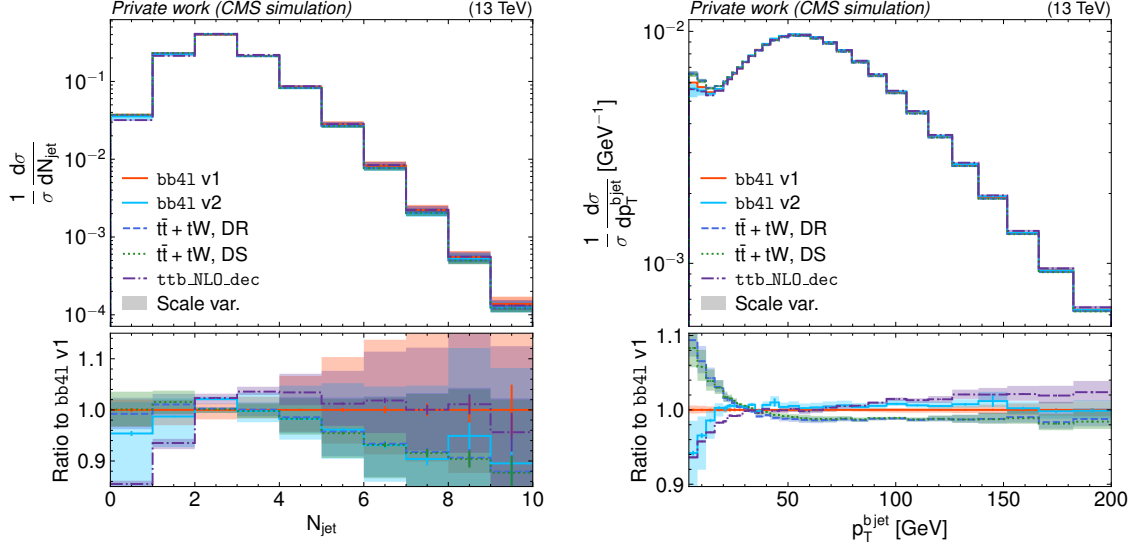


Figure 6.4: **Number of jets and b jet p_T .** Distributions of the inclusive number of AK4 jets (left) and the p_T of the leading b jet (right, RIVET analysis MC_HF JETS), shown in the same manner as in Fig. 6.2.

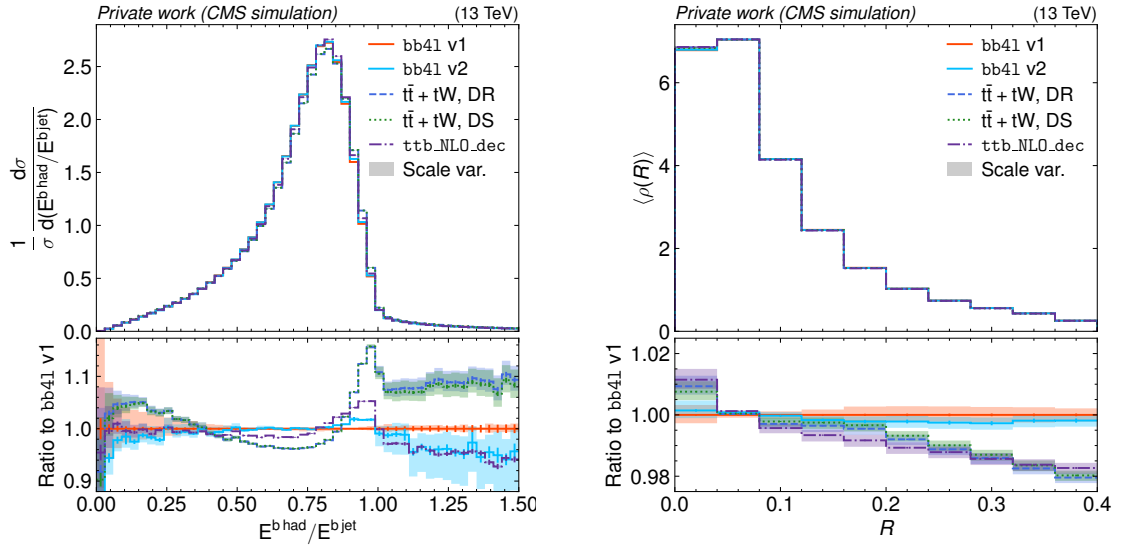


Figure 6.5: **b fragmentation and jet shape.** Distributions of the b quark fragmentation (left, RIVET analysis MC_HFJETS) and the average differential b jet shape (right, RIVET analysis MC_HFDECAYS), shown in the same manner as in Fig. 6.2.

1936 differential b jet shape $\langle \rho(R) \rangle$, which is the density of particles making up the b
 1937 jet as a function of its radius R . Both of these variables are sensitive to final-state
 1938 radiation from the top decay, and are thus expected to be affected by the full NLO
 1939 calculation performed by **bb41**. It can be seen that both versions of **bb41** predict
 1940 softer b jet spectra and wider jets than both $t\bar{t} + tW$ and **ttb_NLO_dec**, which can
 1941 be interpreted as more FSR emissions being generated. Notably, this effect cannot
 1942 be solely due to the inclusion of hard FSR emissions in **bb41** since these are also
 1943 present in **ttb_NLO_dec**.

1944 In general, all of these trends for **bb41** (softer lepton and b jet spectra as well
 1945 as wider jets) agree with what was observed in Refs. [155, 159], but differ from the
 1946 results initially reported in Ref. [7].

1947 **Invariant $b\ell$ mass** A common proxy observable to use for measurements of the
 1948 top quark mass in dilepton events is the invariant mass $m_{b\ell}$ of a b jet and a lepton.
 1949 To do so, a procedure is needed to unambiguously assign the leptons and b jets (of
 1950 which there might be varying numbers per event depending on the event selection)
 1951 to each other. Here, exactly two b jets per event are required, and the so-called
 1952 minimax mass is used, defined as

$$m_{b\ell}^{\text{minimax}} = \min [\max(m_{b_1\ell_1}, m_{b_2\ell_2}), \max(m_{b_1\ell_2}, m_{b_2\ell_1})]. \quad (6.1)$$

1953 This prescription amounts to maximizing over the two $b\ell$ pairs in the event,
 1954 and then minimizing over the two possible assignments of b jets and leptons. It
 1955 is notable in that, for double-resonant $t\bar{t}$ events, it shows a kinematic cutoff at a
 1956 value of $\sqrt{m_t^2 - m_W^2} \approx 150$ GeV. As a result, the tail above this cutoff is sensitive to
 1957 single-resonant tW events as well as $t\bar{t}/tW$ interference and thus to the top quark
 1958 width.

1959 Fig. 6.6 shows the distribution of $m_{b\ell}^{\text{minimax}}$, again for all considered cases. It can
 1960 be seen that both versions of **bb41** are in good agreement with each other, and are also
 1961 in agreement with **ttb_NLO_dec** except for the lowest bin. Unfolded ATLAS data
 1962 taken from Ref. [146] is overlaid on top of the predictions, and shows good agreement
 1963 for both **bb41** and **ttb_NLO_dec**. In the tail, the two interference handling schemes
 1964 for $t\bar{t} + tW$ show significant differences as expected, with **bb41** and **ttb_NLO_dec**
 1965 lying between them. Since **bb41** is expected to provide a more accurate prediction
 1966 of the interference than either scheme, this validates that using the difference of
 1967 the schemes as an uncertainty covers the true values, as is done in many CMS and
 1968 ATLAS measurements. Going forward, such uncertainties could be dropped from
 1969 future measurements by using **bb41** predictions directly.

1970 **Top quark reconstruction** Finally, in order to directly study the effects on top
 1971 quark observables, a simple generator-level top quark reconstruction is performed.
 1972 To do so, two dressed leptons and two b jets are selected as before, while the two

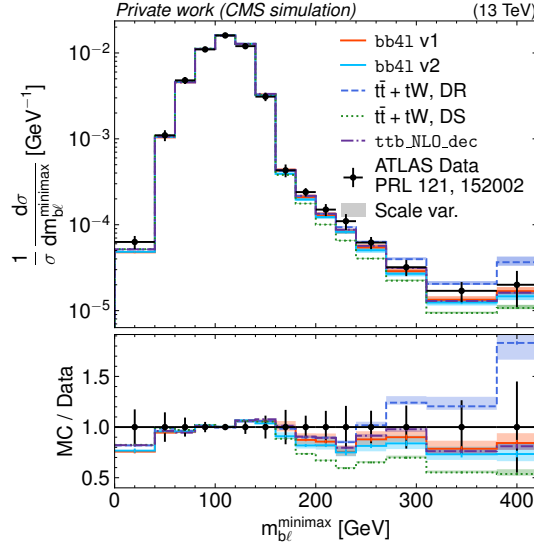


Figure 6.6: **Distribution of $m_{b\ell}^{\text{minimax}}$** , shown in the same manner as in Fig. 6.2. ATLAS data from Ref. [146] is overlaid as black dots, and the RIVET routine from said reference was used to obtain the distributions.

neutrinos in the dileptonic top decay are taken from truth-level information. The W bosons are reconstructed from the neutrinos and charged leptons according to the lepton charge, and then combined with the b jets to form two possible assignments of b-W pairs, which are taken as top quark and antiquark candidates again depending on the lepton charge. The ambiguity in assignments is resolved by choosing the pairs for which the difference Δm_t between the invariant masses is minimized.

This reconstruction procedure is not equivalent to a full experimental reconstruction, in which the neutrinos are only measured as missing transverse momentum and can thus not be directly assigned to the leptons. It also does not include any detector resolution effects. However, it does take into account the effects of FSR in the top decay by considering the full b jets instead of parton-level b quarks, which is why it was chosen for the comparison.

Fig. 6.7 shows the resulting distributions for the top quark mass and p_T . It can be seen that the different generators show different lineshapes for the top quark mass: `bb41` predicts a small shift towards lower values compared to $t\bar{t} + tW$ for both interference handling schemes as well as `ttb_NLO_dec`, and also predicts significantly lower amounts of off-shell tops with masses below the pole mass compared to $t\bar{t} + tW$. Both of these facts are important for precision top mass measurements, in which such shifts can influence the final fit results. The presence of these differences is expected: due to the use of the NWA for both $t\bar{t} + tW$ and `ttb_NLO_dec`, the top lineshape can only be modeled approximately in these generators, while `bb41` provides a true NLO-accurate description. It can furthermore be seen that the two

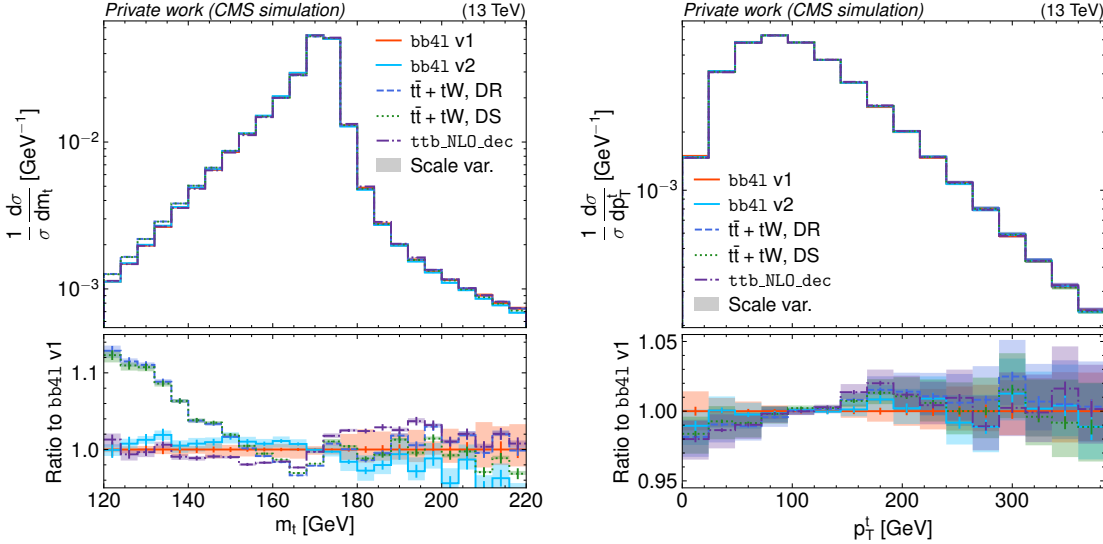


Figure 6.7: **Top quark lineshape and p_T .** Distributions of the reconstructed top quark mass (left) and p_T (right), summed for both top quark and antiquark, shown in the same manner as in Fig. 6.2.

1995 bb41 versions are not in perfect agreement with each other, though the difference is
1996 within the scale uncertainties by 1 standard deviation.

1997 For the top quark p_T , on the other hand, any trend in the comparison between the
1998 generators is covered by the scale uncertainties, though bb41 does seem to again pre-
1999 dict softer p_T spectra than the other generators, consistent with the trends observed
2000 for the lepton p_T and $m_{\ell\ell}$.

2001 Lastly, the invariant mass and p_T distributions of the $t\bar{t}$ system as a whole are
2002 shown in Fig. 6.8. For $m_{t\bar{t}}$, no clear trend can be seen for any of the considered
2003 generators. The p_T of the $t\bar{t}$ system, on the other hand, shows significant differences
2004 both between the two bb41 versions and between bb41 and the other generators
2005 (which agree with each other). It should be noted that, since the initial state of
2006 the $pp \rightarrow t\bar{t}$ process has negligible p_T , this variable is exactly zero at LO in QCD,
2007 and consequently determined only by emissions at NLO and beyond. As a result,
2008 it is expected to be sensitive to the NLO calculation and matching between matrix
2009 element and parton shower.

2010 6.5.2 Comparison of FSR matching settings

2011 Complementary to the previous generator comparisons, this section investigates the
2012 effect of the matching between matrix element and parton shower for FSR in bb41.
2013 As explained in Sec. 6.4.1, two principal options are available to match bb41 to
2014 PYTHIA in the used module PowhegHooksBB4L: In the first and nominal approach

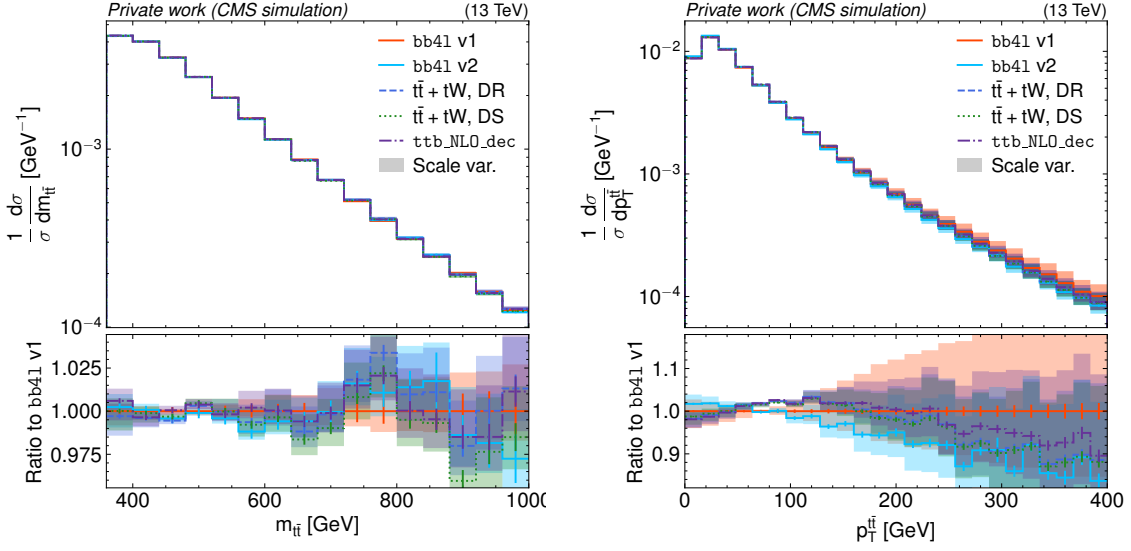


Figure 6.8: **Kinematics of the $t\bar{t}$ system.** Distributions of the reconstructed invariant mass (left) and p_T (right) of the $t\bar{t}$ system, shown in the same manner as in Fig. 6.2.

(denoted “FSR veto”), the parton shower is started at the kinematic limit, and FSR emissions that lie above the POWHEG energy scale of the relevant emission from the top decay as generated by POWHEG are vetoed. In the second approach (“Res. scale”), the shower is directly started at the energy scale of the FSR emission, neglecting the mismatch between scale definitions in POWHEG and PYTHIA.

In order to demonstrate the importance of correct parton shower matching, a third case (“Kin. limit”) is considered, in which the parton shower for FSR emissions is started naively at the kinematic limit without any veto procedure specifically directed at bb41. This approach is thus expected to double-count FSR emissions.

The comparison in this section has been performed with bb41 v1. The matching for ISR emissions, done by PowhegHooks, is left identical between the three cases, as given in Tab. 6.1.

Fig. 6.9 shows the distributions of the top quark mass, reconstructed the same as before, and the b fragmentation for the different matching choices. Both of these observables were chosen for their sensitivity to FSR effects. It can be seen that the options “FSR veto” and “Res. scale” agree reasonably well with each other, with the top mass lineshape showing a small shift between them within the scale uncertainties. This implies that the mismatch between the POWHEG and PYTHIA energy scale definitions has a subleading effect in practice. On the other hand, the naive “Kin. limit” approach shows a large discrepancy due to its double-counting of FSR emissions, highlighting the importance of correct matching FSR matching

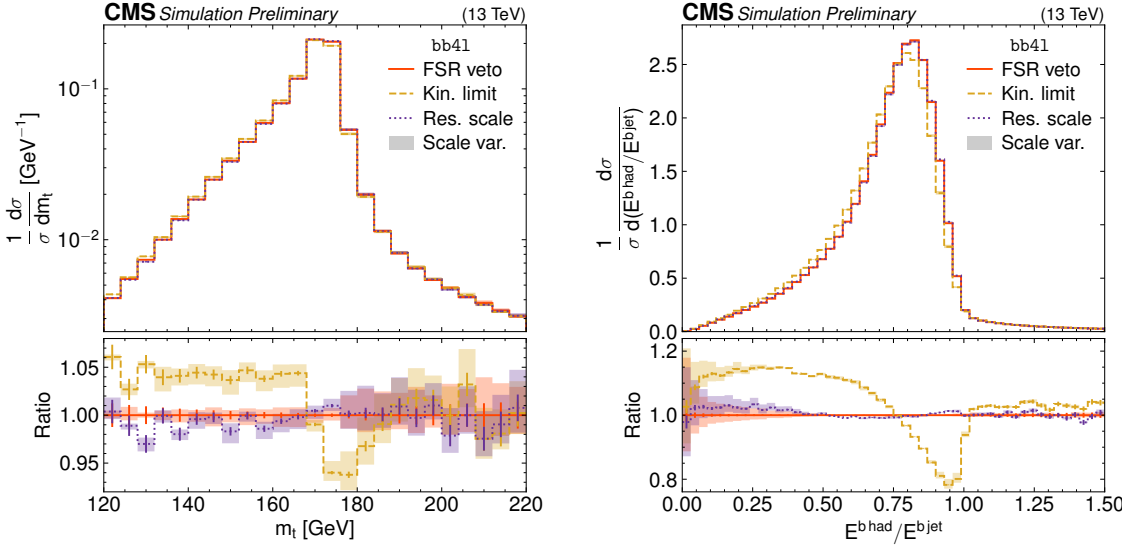


Figure 6.9: **Comparison of FSR matching settings.** Distributions of the reconstructed top quark mass (left, same as in Fig. 6.7) and the b quark fragmentation (right, same as in Fig. 6.5), for **bb41** with different FSR matching settings as explained in the text (Sec. 6.5.2). The shaded bands show scale uncertainties.

procedures for NLO generators.

6.5.3 Recoil in top decay

In the simple parton shower in PYTHIA, there is a well-known problem affecting the virtualities of heavy unstable colored resonances, such as the top quark, in the treatment of FSR emissions in the resonance decay [160]. In particular, when performing a gluon emission off the decaying top quark and thus changing a $t \rightarrow Wb$ configuration to $t \rightarrow Wbg$, there is an ambiguity on how to distribute the recoil imposed by the gluon between the top decay products (W and b quark) such that the four-momentum of the Wbg system is conserved.

PYTHIA 8.307, which is the version used for the previous studies in this chapter, offers two different treatments for this problem, which amount to assigning the recoil to only the W (“recoil to W”) or only to the b quark (“recoil to b”). Both of these are approximations, since a true treatment would distribute the recoil between the W and b quark in some form. CMS, and thus the studies previously shown in this chapter, use the “recoil to b” option.

Since PYTHIA 8.310, a third option (“recoil to top”) has been made available via the setting `TimeShower:recoilStrategyRF`. For this option, the W is chosen as the recoil at first, but the emissions are then reweighted according to the ra-

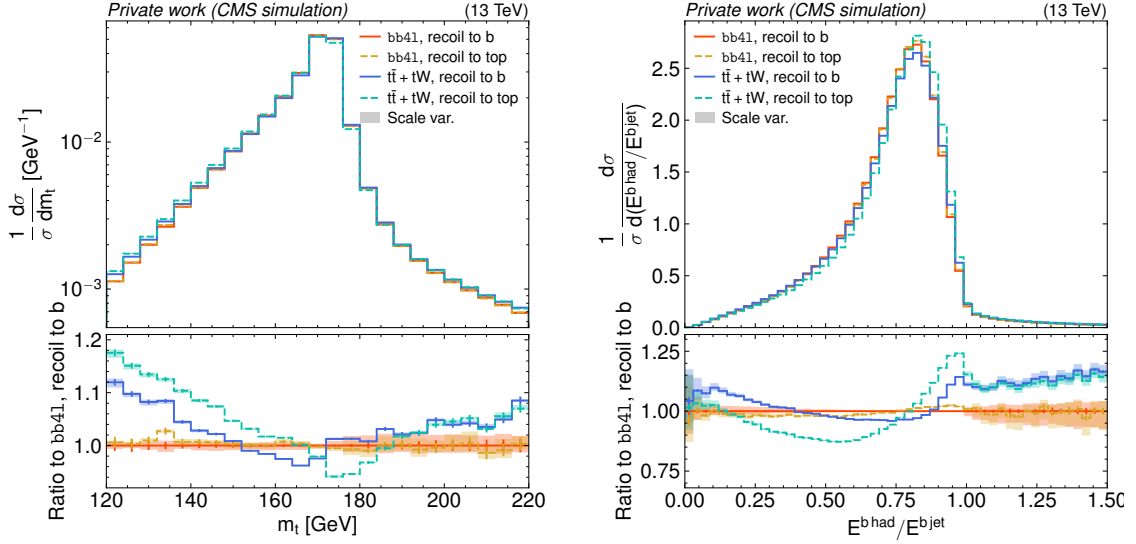


Figure 6.10: **Comparison of top recoil strategies.** Distributions of the reconstructed top quark mass (left, same as in Fig. 6.7) and the b quark fragmentation (right, same as in Fig. 6.5), for bb41 and $t\bar{t} + tW$ with two different recoil treatments, as defined in the text (Sec. 6.5.3). The shaded bands show scale uncertainties.

2055 tios of eikonal radiation factors to approximate the radiation pattern expected in a
 2056 resonance-aware shower [160]. It has been found in Ref. [161] that the difference be-
 2057 tween this improved method and the old ones can have a substantial impact on top
 2058 mass proxy observables and consequently measured top mass values, and it has been
 2059 discussed whether such a difference should be included as a systematic uncertainty.

2060 This problem, in its core, is an issue of the parton shower and not the ME gen-
 2061 erator. Nonetheless, bb41 is expected to alleviate some of the ambiguities since it
 2062 always includes the hardest gluon emission in each top decay at the ME level, where
 2063 no question of assigning the recoil is raised. For subsequent and thus subleading
 2064 emissions, the issue in principle still persists.

2065 To estimate the effect of the top recoil in bb41 and compare it to $t\bar{t} + tW$, events
 2066 from both generators are re-showered in PYTHIA 8.310 with the two choices of setting

```
TimeShower:recoilStrategyRF = 1 ("recoil to b") and
TimeShower:recoilStrategyRF = 2 ("recoil to top").
```

2067 bb41 v2 is used for this comparison, and all other settings are kept at the nominal.
 2068 For $t\bar{t} + tW$, only the DR scheme is considered for the interference handling.

2069 The results are shown in Fig. 6.10 for the reconstructed top mass and the b
 2070 quark fragmentation. Large differences are visible between the two recoil strategies

for $t\bar{t} + tW$, as expected from Refs. [160, 161]. For **bb41**, on the other hand, the differences are almost invisible, and lie within the scale uncertainties for the top quark mass. This implies that the effect of the recoil in subleading emissions is negligible in **bb41** for the shown observables. As a result, **bb41** fully circumvents the problem of top recoil that can otherwise be significant for $t\bar{t}$ analyses.

6.6 Summary and Outlook

In this chapter, several generator-level studies of the MC generator **bb41**, which generates the full $b\bar{b}\ell^+\ell^-\nu_\ell\bar{\nu}_\ell$ final state including $t\bar{t}/tW$ interference and off-shell top effects at NLO in QCD, have been presented. **bb41** has been compared to other common $t\bar{t}$ generators, namely **hvq**, **ST_wtch** (with two interference handling schemes) and **ttb_NLO_dec**, for different lepton, (b) jet and reconstructed top quark observables. For $m_{b\ell}^{\text{minimax}}$, **bb41** agrees well with ATLAS data from Ref. [146], improving greatly upon the two interference handling schemes DR and DS for $t\bar{t} + tW$. For the reconstructed top quark mass, **bb41** shows a significant shift compared to $t\bar{t} + tW$. In addition, two different **bb41** versions have been compared, with no significant differences found outside of scale uncertainties, and the matching of ME and parton shower as well as the treatment of the recoil in **bb41** have been studied further.

These studies represent valuable information for the choice of $t\bar{t}$ MC generator in upcoming CMS measurements. For analyses in which $t\bar{t}$ and tW are major backgrounds, **bb41** can help reduce uncertainties originating in the $t\bar{t}/tW$ interference treatment, and provide a more accurate description when off-shell regions of phase space are probed. This is briefly explored in Sec. 7.5.4 in the context of a search for $t\bar{t}$ bound state effects, which are naturally located in an off-shell-region. Furthermore, **bb41** will be of use when the $pp \rightarrow t\bar{t}$ process is instead the signal of a measurement. In particular, for future work it would be interesting to perform a simultaneous top mass and width measurement using MC templates generated with **bb41**, as originally proposed in Ref. [155], in CMS, or alternatively perform an differential $t\bar{t} + tW$ cross section measurement, where **bb41** could be used to unfold the data to generator level.

2100 **7 Search for heavy scalar or pseudoscalar**
2101 **bosons in $t\bar{t}$ final states**

2102 **7.1 Introduction**

2103 Additional spin-0 particles are predicted in many attractive extensions of the Stan-
2104 dard Model, and can be searched for in $t\bar{t}$ final states at the LHC if the new states are
2105 heavy (i.e. have a mass larger than $2m_t$), electrically neutral, and exhibit Yukawa-
2106 like couplings to fermions (see Sec. 2.3.1). A generic model for such states with either
2107 pseudoscalar (A) or scalar (H) couplings to top quarks was given in Eq. (2.18).

2108 In addition, $t\bar{t}$ bound state effects are expected in the SM in several calculations,
2109 with a pseudoscalar component dominating at the LHC as discussed in Sec. 2.2.3.
2110 Since the experimental invariant mass resolution for the $t\bar{t}$ final state is rather coarse,
2111 additional BSM particles and bound state effects are expected to lead to similar
2112 experimental signatures, and it thus makes sense to search for them for using the
2113 same methods.

2114 This chapter presents such a search for new spin-0 states with either scalar or
2115 pseudoscalar interactions with the top quark, using the full Run 2 dataset with an
2116 integrated luminosity of 138 fb^{-1} at the CMS experiment. It follows up on a similar
2117 search done using only 35.9 fb^{-1} of data taken in 2016 [16]. Similar searches have
2118 also been published by ATLAS, one with 20.3 fb^{-1} of data taken at $\sqrt{s} = 8 \text{ TeV}$ [162]
2119 and one with 140 fb^{-1} of data taken at $\sqrt{s} = 13 \text{ TeV}$ [163].

2120 The work done as part of this thesis focused on the dilepton decay channel of $t\bar{t}$,
2121 which is thus described in detail in Secs. 7.2 to 7.6. A significant excess of events
2122 is observed at invariant masses close to the $t\bar{t}$ threshold, which is interpreted either
2123 as a pseudoscalar $t\bar{t}$ bound state (Secs. 7.7.1 to 7.7.3) or as an additional scalar
2124 or pseudoscalar boson (Sec. 7.7.4). For the latter interpretation, exclusion limits
2125 for a large mass range are also presented in Sec. 7.8. Following this, the dilepton
2126 channel is combined with a similar analysis of the $\ell+\text{jets}$ decay channel, which is
2127 discussed in Sec. 7.9, and exclusion regions are provided for the presence of either
2128 one or two additional bosons. Finally, the results of this work are briefly compared
2129 in Sec. 7.10 to those of Ref. [163], in which no excess was observed, as well as to
2130 other $t\bar{t}$ measurements, and a summary and outlook are given in Sec. 7.11.

2131 The results presented here were first made public as a Physics Analysis Sum-
2132 mary [8], and later submitted to *Reports on Progress in Physics* in an updated form
2133 focusing solely on the interpretation of a $t\bar{t}$ bound state [9]. A further submission

focusing on the interpretation in terms of additional bosons is in preparation. They are the continuation of a previous PhD thesis [164], in which the analysis strategy of the dilepton channels as well as the procedure of obtaining exclusion limits for additional bosons was designed. Following up on this, the contribution of the work at hand consists of the implementation of matrix element reweighting for the signal simulation (Sec. 7.4), the simulation of the $t\bar{t}$ bound state signal (Sec. 2.2.3), the interpretation of the observed excess in terms of $t\bar{t}$ bound states or additional bosons including all corresponding cross-checks (Sec. 7.7), the comparison to other results (Sec. 7.10), and the preparation of the results for publication in Refs. [8] and [9].

7.2 Analysis setup

This section describes the analysis strategy in the dilepton channels, consisting of the considered datasets, object definitions, event selection criteria, corrections and reconstruction algorithms.

7.2.1 Datasets

Experimental data The analysis is performed using the full CMS Run 2 ultra-legacy (UL) dataset, which is the final, re-reconstructed and recalibrated dataset recommended by CMS for physics analyses. It is split into the three datataking years of Run 2: 2016, 2017 and 2018, where 2016 is further split into two parts, denoted “2016pre” and “2016post”, because of a modification of the APV readout chip settings that affects the efficiency of the track hit reconstruction during the 2016 data-taking period [165].

A similar combination of dilepton and single-lepton triggers as in Sec. 5.2.1 is used for all years, with the p_T thresholds varying slightly between datataking eras, as shown in Tab. 7.1.

Background simulation Since the final state of the signals considered in this analysis are the same as in the SM $t\bar{t}$ background, it is clear that a large irreducible background is expected. As a result, it is essential that the SM Monte Carlo simulation is as both theoretically precise and has sufficient statistics, and that any remaining imprecisions are covered by the systematic uncertainty model.

The SM $t\bar{t}$ background is again simulated at NLO in QCD with the `hvq` process from the MC generator package `POWHEG v2` and interfaced to `PYTHIA 8` for showering. Similar settings as in Sec. 5.2.1 have been used. To achieve the necessary precision, the NLO simulation is reweighted to higher orders in both QCD and electroweak (EW) processes, which is described in Sec. 7.3.

In addition, several minor backgrounds are included, a summary of which can be found in Tab. 7.2. Of note here is the Z+jets background, which is simulated at

Trigger	Year	Lepton p_T requirement
single-e	2016	e ($p_T > 27 \text{ GeV}$)
	2017	e ($p_T > 35 \text{ GeV}$)
	2018	e ($p_T > 32 \text{ GeV}$)
single- μ	2016	μ ($p_T > 24 \text{ GeV}$)
	2017	μ ($p_T > 27 \text{ GeV}$)
	2018	μ ($p_T > 24 \text{ GeV}$)
e μ	all	e ($p_T > 12 \text{ GeV}$) and μ ($p_T > 23 \text{ GeV}$) or e ($p_T > 23 \text{ GeV}$) and μ ($p_T > 8 \text{ GeV}$)
ee	all	e ₁ ($p_T > 23 \text{ GeV}$) and e ₂ ($p_T > 12 \text{ GeV}$)
$\mu\mu$	all	μ_1 ($p_T > 17 \text{ GeV}$) and μ_2 ($p_T > 8 \text{ GeV}$)

Table 7.1: **Trigger p_T thresholds.** Overview of the used triggers in the three datataking years, as well as their lepton p_T thresholds.

NNLO in QCD using the MiNNLO method in POWHEG v2. It was found here that the higher-order corrections are relevant to the analysis especially for low values of the invariant dilepton mass $m_{\ell\ell}$. Most processes are normalized to cross sections predicted at higher orders of QCD where available, which can be found in Tab. 7.3.

Signal simulation The signal for the general A/H model described in Sec. 7.1 is generated at LO in QCD using MADGRAPH 5 with a custom Universal FeynRules Output (UFO) model. The $pp \rightarrow A/H \rightarrow t\bar{t}$ resonance and the A/H-SM interference are simulated separately, and both are again showered with PYTHIA 8. In order to cover the phase space of the A/H model, the signals are generated for all combinations of the following values of the A/H masses and widths:

$$\begin{aligned} m_{A/H} &\in \{365, 400, 500, 600, 800, 1000\} \text{ GeV} \\ \Gamma_{A/H}/m_{A/H} &\in \{2.5, (5), 10, 25\} \% \end{aligned} \quad (7.1)$$

Samples with a width of 5% were generated only for a mass of 400 GeV, which leads to 38 signal points total. In addition, samples for the pseudoscalar case only were generated with

$$m_A \in \{450, 550, 700, 900\} \text{ GeV}, \quad \Gamma_A/m_A = 9\%. \quad (7.2)$$

All of these samples were combined and used reweighted at matrix element level to obtain also phase space points between these mass and width values, as described further in Sec. 7.4.

Furthermore, signal samples for possible $t\bar{t}$ bound state effects are generated using the color-singlet η_t and χ_t models as defined in Sec. 2.2.3, using custom UFO models

Process	QCD order	ME Generator
$t\bar{t}$	NLO	POWHEG v2 (hvq)
tW	NLO	POWHEG v2 (ST_wtch)
$Z/\gamma^* + \text{jets}$	NNLO	POWHEG v2 (Zj MiNNLO)
t -channel single top	NLO	POWHEG v2 (ST_tch) + MADSPIN
s -channel single top	NLO	MG5_AMC@NLO
$t\bar{t}W$	NLO	MG5_AMC@NLO
$t\bar{t}Z$	NLO	MG5_AMC@NLO
WW, WZ & ZZ	LO	PYTHIA 8.2
A/H signal	LO	MG5_AMC@NLO
η_t signal	LO	MG5_AMC@NLO

Table 7.2: **Simulated background and signal samples.** An overview of the different background and signal processes considered, as well as the theoretical order in QCD and the ME generator used to simulate them. For all samples, PYTHIA 8.2 is used for showering and hadronization.

Process	Cross section (pb)	Order	Program / reference
$t\bar{t}$	833.9	NNLO+NNLL	Top++ [119]
tW	71.7	NNLO (approx.)	[123]
t -channel single top	217.0	NLO	Hathor [166, 167]
s -channel single top	10.3	NLO	Hathor [166, 167]
$t\bar{t}W$	0.64	NLO	MG5_AMC@NLO
$t\bar{t}Z$	0.75	NLO	MG5_AMC@NLO
$Z/\gamma^* + \text{jets} \rightarrow \ell\ell,$ $m_{\ell\ell} > 10 \text{ GeV}$	24.7×10^3	NNLO	FEWZ [168, 169]
WW	118.7	NNLO	[170]
WZ	471.3	NLO	MCFM [171]
ZZ	165.2	NLO	MCFM [171]

Table 7.3: **Cross sections for background processes.** The cross sections used for the normalization of background processes relevant for this search, as well as the orders in QCD at which they were computed.

2188 implemented in MADGRAPH 5 and again showered with PYTHIA.

2189 For all signal and background samples, the detector response is simulated with
2190 GEANT 4 and the full CMS simulation and reconstruction chain as described in
2191 Sec. 3.6 is performed.

2192 7.2.2 Object definition

2193 **Leptons** All electrons and muons are required to have $p_T > 20 \text{ GeV}$ and $|\eta| < 2.4$
2194 to be considered for the analysis. Similar to Sec. 5.2.2, electrons in the transition
2195 region between barrel and endcaps in the ECAL are removed, and additional ID
2196 criteria are applied for both types of leptons.

2197 For electrons, the multivariate classifier (MVA)-based ID described in Ref. [95] is
2198 used at a working point giving 90 % background rejection. This ID already includes
2199 an isolation requirement as part of the MVA training, and no further requirement
2200 is applied.

2201 For muons, the same cut-based ID from Ref. [124] as in Sec. 5.2.2, also at the tight
2202 working point, is used, and the same I_{rel} requirement using a cone size of $\Delta R < 0.4$
2203 is applied in addition.

2204 **Jets** Jets are again reconstructed using the anti- k_T algorithm [106] with a distance
2205 parameter of 0.4. They are required to fulfill $p_T > 20 \text{ GeV}$, $|\eta| < 2.4$, and have a
2206 minimum distance of $\Delta R > 0.4$ from all leptons passing the above criteria in the
2207 event.

2208 The DEEPJET algorithm [107], same as in Sec. 5.2.2, is used to identify jets
2209 originating from the showering and hadronization of b quarks. The medium working
2210 point of DEEPJET in CMS, corresponding to an identification efficiency of 77 % is
2211 chosen [125].

2212 **Missing transverse momentum** In the dileptonic decay of $t\bar{t}$, the two neutrinos
2213 can not be measured experimentally, and escape the detector unseen. However, their
2214 presence can be inferred from momentum conservation: In a proton-proton collision,
2215 the longitudinal component of the incoming partons in the hard scattering process is
2216 unknown, while the transverse component can be assumed to be close to zero. Thus,
2217 the missing transverse momentum \vec{p}_T^{miss} can be inferred as the negative vectorial sum
2218 of all reconstructed objects (jets, leptons and photons) [108]. Along with the leptons
2219 and jets, it will be used to reconstruct the $t\bar{t}$ system.

2220 7.2.3 Event selection

2221 Events are selected with exactly two leptons of opposite electric charge and sorted
2222 into three channels (ee, e μ and $\mu\mu$) by lepton flavor, similar to Sec. 5.2.3. The two

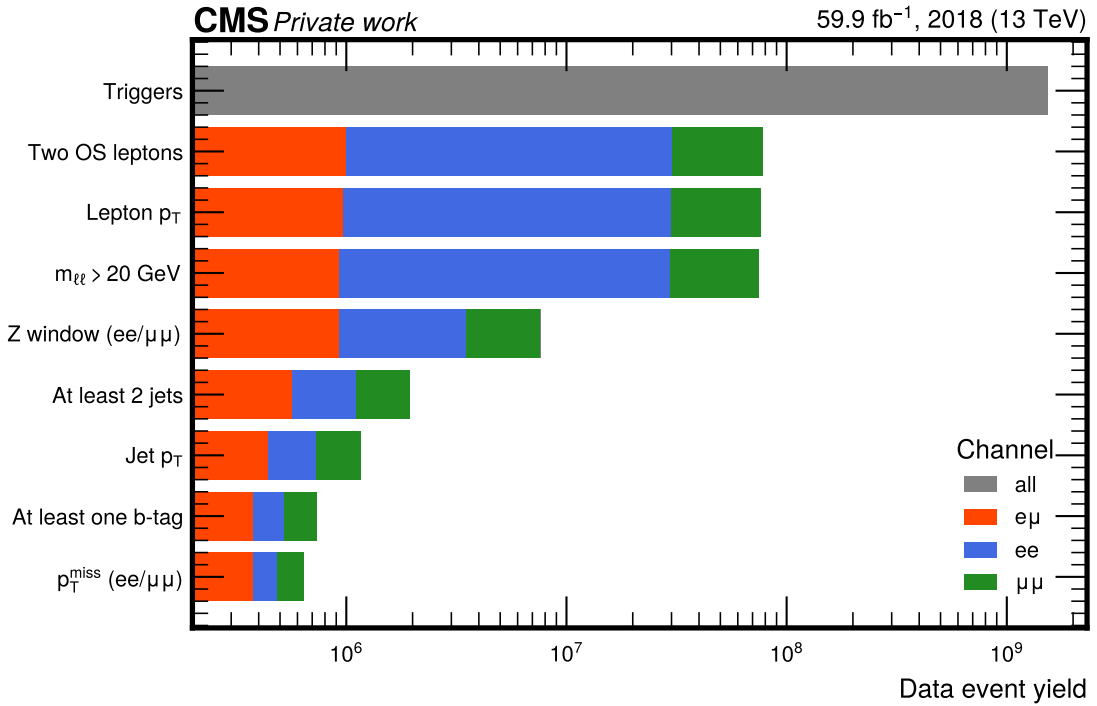


Figure 7.1: **Selection cuts.** Shown is the data yield in 2018 (corresponding to $L_{\text{int}} = 59.9 \text{ fb}^{-1}$) after successively applying all selection cuts. Starting with the requirement of two opposite-sign leptons, the three channels are marked with different colors.

leptons need to fulfill $p_T > 25 \text{ GeV}$ and $p_T > 20 \text{ GeV}$ for the leading and subleading lepton, respectively, and their invariant mass is required to be $m_{ll} > 20 \text{ GeV}$ in order to reject background from $\gamma^* + \text{jets}$ production and low-mass resonances.

In all channels, at least two jets with $p_T > 30 \text{ GeV}$ are required, of which at least one needs to be b-tagged. Furthermore, in the same-flavor lepton channels (ee and $\mu\mu$), additional cuts are applied to reject $Z + \text{jets}$ background: Events with $|m_{ll} - m_Z| < 15 \text{ GeV}$, i.e. close to the Z boson mass peak, are discarded (again just as in Sec. 5.2.3), and the magnitude of the missing transverse momentum is required to be $p_T^{\text{miss}} > 40 \text{ GeV}$.

The effect of all selection cuts can be seen in Fig. 7.1.

7.2.4 Experimental corrections

Similar as in Sec. 5.3, several corrections are applied to the MC simulation in order to achieve good agreement with the data. In contrast to the $t\bar{t}$ cross section measurement, where most of these corrections were derived as part of this work, many

of the experimental corrections used in this chapter were provided centrally by the CMS collaboration. These will only be described very briefly; more details can be found in the associated references.

Trigger scale factors The selection efficiency of the triggers from Tab. 7.1 needs to be corrected in simulation to the one measured in data. This is done via scale factors, which were centrally derived as a function of the p_T of the two leptons using the so-called cross-trigger method: Events are selected using a different set of triggers - here, a combination of jet and p_T^{miss} triggers - which is assumed to be fully orthogonal to the lepton triggers used for the main selection. Thus, the event sample is unbiased with respect to the lepton triggers, and the lepton trigger efficiency can be measured as the fraction of these events who pass the lepton triggers in addition to the jet/ p_T^{miss} triggers. This is done independently for all datataking years, and the resulting scale factor differs from unity by less than 1 % in most cases.

Lepton scale factors Differences in the efficiency for a lepton to pass the identification and isolation criteria as defined in Sec. 7.2.2 are measured using the tag-and-probe method, as in Sec. 5.3, and applied to simulation using scale factors binned in p_T and $|\eta|$ of the lepton. The scale factor typically differs from unity by about 1-5 %, with the magnitude increasing for high $|\eta|$. For more details on this method see Refs. [95, 124].

Pileup reweighting In contrast to the data-driven reweighting method used for the inclusive $t\bar{t}$ cross section measurement (Sec. 5.3), the mean number of pileup interactions per bunch crossing in simulation is reweighted to year-dependant distributions provided centrally by CMS. These have been derived from measurements of the instantaneous luminosity combined with a total inelastic proton-proton cross section of $69.2 \text{ mb} \pm 4.6\%$ at $\sqrt{s} = 13 \text{ TeV}$ [82].

Jet energy corrections The difference in the jet energy response of the detector as well as the jet energy resolution in data and simulation was corrected in the same way as described in Sec. 5.3, using centrally derived jet energy corrections (JECs) as described in Ref. [126].

b-tagging scale factors The identification efficiency of the DEEPJET b-tagging algorithm was calibrated on events with jets containing a muon, which are likely to result from the semileptonic decay of a B hadron, using the methodology described in Ref. [125]. Note that, unlike most CMS analyses using b-tagging, the calibration done on dileptonic $t\bar{t}$ events presented in the same reference is not used as an input here, since it was derived in part on the same dataset as used for this search, and would thus lead to double-counting. However, similar to the discussion in Sec. 5.6,

	2016pre	2016post	2017	2018
ee	0.96 ± 0.010	0.97 ± 0.008	0.87 ± 0.006	0.88 ± 0.005
e μ	0.96 ± 0.007	0.97 ± 0.005	0.88 ± 0.004	0.89 ± 0.003
$\mu\mu$	0.96 ± 0.009	0.97 ± 0.006	0.90 ± 0.005	0.90 ± 0.004

Table 7.4: **Z+jets scale factors.** Ratio of the Z+jets event yields estimated in data using the method described in Sec. 5.3.2 to the prediction by the MC simulation for the four data-taking periods. The results in the e μ channel are the geometric means of those in the ee and $\mu\mu$ channels. Uncertainties are statistical only.

it is expected that the b-tagging efficiency will be constrained from the data during the likelihood fit.

ECAL L1 pre-firing In the 2016 and 2017 data-taking years, the L1 trigger of the electromagnetic calorimeter was affected by a gradual shift in the timing of the inputs in the forward region ($|\eta| > 2.0$) [101]. This effect, called L1 pre-firing, is corrected for using simulation scale factors computed from data.

Z+jets background normalization In the same-flavor lepton channels (ee and $\mu\mu$), Z+jets events again constitute a minor but important background. Since this analysis is sensitive to small shape effects, it is necessary to precisely model this background both in shape and normalization. An NNLO Monte Carlo simulation (see Tab. 7.2) is used for this purpose, which generates up to two partons (including b quarks) in the final state, as required by the event selection of at least two jets and at least one b tag. Still, in order to be certain of the Z+jets rate, the same data-driven estimation as presented in Sec. 5.3.2, using a control region with $|m_{\ell\ell} - m_Z| < 15$ GeV and a sideband with zero b-tagged jets, is performed. The resulting ratios of Z+jets yields compared to the prediction of the original simulation can be found in Tab. 7.4.

7.2.5 Reconstruction of the $t\bar{t}$ system

Having identified the relevant objects - leptons, jets and \vec{p}_T^{miss} - in an event, the next step consists of reconstructing the $t\bar{t}$ system, i.e. the four-momenta of the top and antitop quark. Due to the presence of the two neutrinos in the dileptonic $t\bar{t}$ decay, which escape the detector unobserved except for \vec{p}_T^{miss} and thus represent a loss of information, this is a non-trivial procedure which requires several assumptions on the kinematic properties. In this work, a variation of the algorithm first presented in Ref. [172] is used, which is briefly outlined in this section.

The algorithm works in two steps, starting with the assignment of jets to the b and \bar{b} quarks originating from the $t\bar{t}$ decay. To do so, pairs of jets are selected from

2299 all jets in the event (passing the requirements outlined in Sec. 7.2.2) depending on
 2300 the number n_b of b-tagged jets: For events with $n_b \geq 2$, all (ordered) combinations
 2301 of two b-tagged jets each are considered as candidate pairs, while for events with
 2302 $n_b = 1$, the candidate pairs are formed by pairing the single b-tagged jet with all
 2303 other jets in the event.

2304 From these candidates, the best pair is now chosen based on the invariant masses
 2305 $m_{\ell+b}$ and $m_{\ell-\bar{b}}$ of the b/ \bar{b} candidate and the corresponding (anti)lepton. In each
 2306 event, the candidate pair is chosen that maximizes the product of the truth-level
 2307 likelihoods, as evaluated from MC events, to obtain the measured values of $m_{\ell+b}$
 2308 and $m_{\ell-\bar{b}}$. This pair is then used for the remainder of the reconstruction.

2309 Next, the four-momenta of the top and antitop quark are reconstructed using the
 2310 momentum conservation equations. That is, one demands

$$\begin{aligned} p_t &= p_{W^+} + p_b = p_{\ell^+} + p_{\nu_\ell} + p_b \\ p_{\bar{t}} &= p_{W^-} + p_{\bar{b}} = p_{\ell^-} + p_{\bar{\nu}_\ell} + p_{\bar{b}} \end{aligned} \quad (7.3)$$

2311 where all variables are understood as four-momenta. The lepton and b-quark
 2312 momenta are experimentally measured, while the neutrino momenta are unknowns.
 2313 Demanding them to be massless, i.e. $p_{\nu_\ell}^2 = p_{\bar{\nu}_\ell}^2 = 0$, yields the six components of the
 2314 two neutrino three-momenta as free parameters.

2315 To resolve the ambiguities, several assumptions need to be made. First, it is
 2316 assumed that all of the missing transverse momentum in the event stems from the
 2317 neutrinos, i.e.

$$p_{\nu_\ell,x} + p_{\bar{\nu}_\ell,x} = p_x^{\text{miss}}, \quad p_{\nu_\ell,y} + p_{\bar{\nu}_\ell,y} = p_y^{\text{miss}} \quad (7.4)$$

2318 Additionally, it is assumed that both the top quarks and W bosons are exactly
 2319 on-shell, that is

$$p_{W^+}^2 = m_W^2, \quad p_{W^-}^2 = m_W^2 \quad (7.5)$$

2320 and

$$p_t^2 = m_t^2, \quad p_{\bar{t}}^2 = m_t^2 \quad (7.6)$$

2321 where m_t and m_W are the pole masses of the top quark and W boson, respectively.
 2322 Applying these six constraints leads to a system of quartic equations for the neutrino
 2323 three-momenta \vec{p}_{ν_ℓ} and $\vec{p}_{\bar{\nu}_\ell}$, which was solved in Ref. [173]. From these, the top and
 2324 antitop quark four-momenta can then be calculated. Since the quartic equation
 2325 can in general have up to four solutions, the solution with the lowest value of the
 2326 invariant $t\bar{t}$ mass $m_{t\bar{t}}$ is chosen. This was found in Ref. [174] to minimize the bias
 2327 in $m_{t\bar{t}}$ especially for low- $m_{t\bar{t}}$ events.

2328 In practice, however, this method will not give a real solution even for those $b\bar{b}$

pair candidates which are correctly assigned to the truth-level b quarks. This is because the experimental inputs to the method - the jet and lepton four-momenta as well as \vec{p}_T^{miss} - will deviate from their truth-level values within the experimental resolution of the detectors and object reconstruction. In addition, the constraints will not be fulfilled exactly: There might be additional p_T^{miss} in the event because of e.g. neutrinos produced in τ lepton or B hadron decays, and the W bosons and top quarks might be off-shell with respect to their pole masses by their respective widths.

To alleviate this, several of the input variables are randomly smeared to model the experimental resolution. For both the b jets and leptons, the energies are varied while keeping their masses constant, and the directions of their three-momenta are varied in a uniformly random direction. For both of these cases, the variations are randomly sampled from a distribution obtained by comparing the reconstructed and truth four-momentum in the nominal $t\bar{t}$ MC simulation, as shown in Ref. [164]. Additionally, the values of m_W used for the constraints on p_{W+} and p_{W-} are randomly sampled from a relativistic Breit-Wigner distribution corresponding to the W boson width Γ_W . This smearing procedure is repeated 100 times per event with different random values, resulting in up to 100 reconstructed $t\bar{t}$ systems per event, depending on the number of cases where there is no real solution.

Finally, one unambiguous solution per event is constructed by again using the invariant lepton-b quark masses and their truth-level likelihoods. For each iteration of the smearing procedure that yielded a real solution, a weight is defined as the product of the likelihoods for obtaining the smeared values of $m_{\ell+b}$ and $m_{\ell-\bar{b}}$, i.e.

$$w = \mathcal{P}(m_{\ell+b}) \cdot \mathcal{P}(m_{\ell-\bar{b}}) \quad (7.7)$$

The final solution for the reconstructed top and antitop four-momenta is defined as the weighted average over all real solutions, using the weight as given in Eq. (7.7).

For $t\bar{t} \rightarrow b\bar{b}\ell\ell\nu\nu$ events passing all previous selection steps, the efficiency of the full reconstruction algorithm is ca. 90%, as evaluated in MC simulation. To assess the accuracy of the reconstruction relative to the truth-level top quarks, defined after parton showering, a per-event relative deviation is defined as

$$\Delta m_{t\bar{t}} = \frac{m_{t\bar{t}}^{\text{reco}} - m_{t\bar{t}}^{\text{gen}}}{m_{t\bar{t}}^{\text{gen}}}, \quad (7.8)$$

where $m_{t\bar{t}}^{\text{reco}}$ and $m_{t\bar{t}}^{\text{gen}}$ stand for the reconstructed and truth-level $m_{t\bar{t}}$, respectively. The mean and standard deviation of $\Delta m_{t\bar{t}}$ are then the relative bias and resolution of the reconstruction algorithm. They are evaluated in simulation of dileptonic $t\bar{t}$ and shown in Fig. 7.2 as a function of truth-level $m_{t\bar{t}}$. The method shows a bias towards high $m_{t\bar{t}}$ for events with $m_{t\bar{t}}^{\text{gen}} \lesssim 600$ GeV and towards low $m_{t\bar{t}}$ for $m_{t\bar{t}}^{\text{gen}} \gtrsim 600$ GeV, with resolutions in the range of 17 – 25%. It should be noted here that this bias relative to the truth level is by itself not problematic for this analysis,

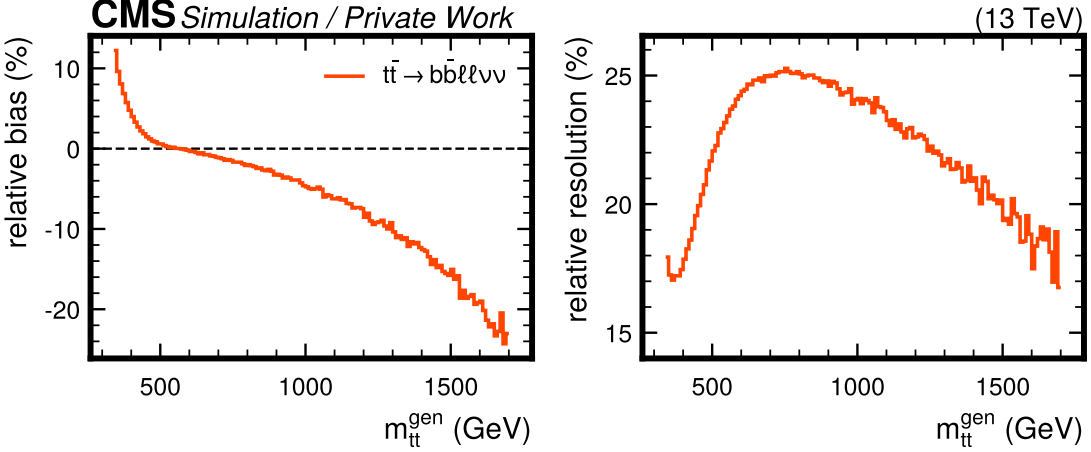


Figure 7.2: **Bias and resolution of $m_{t\bar{t}}$.** Relative bias and resolution of the $t\bar{t}$ reconstruction algorithm, defined in Eq. (7.8), as a function of truth-level $m_{t\bar{t}}$ and evaluated in MC simulation of dileptonic $t\bar{t}$.

since it is expected to be the same in both simulation and data and no unfolding of the reconstructed distributions to the truth level is attempted here.

7.2.6 Sensitive observables

To extract the A/H and η_t signals from the background, three sensitive observables are considered. The first is simply the invariant $t\bar{t}$ mass $m_{t\bar{t}}$, defined with the reconstruction procedure as explained in the last section. As shown in Fig. 2.7, an A/H signal is expected to result in a peak-dip structure in $m_{t\bar{t}}$ around the SM background, where the zero crossing between peak and dip should be in the vicinity of the A/H mass, and the magnitude as well as ratio of the peak and the dip depends non-linearly on the coupling modifier. The η_t signal, on the other hand, is expected to peak slightly below the $t\bar{t}$ production threshold at $m_{t\bar{t}} \simeq 2m_t - 2$ GeV as shown in Fig. 2.5. In practice, due to the limited detector resolution, the exact position of this peak will not be observable, and the signal will result in a generic enhancement of the yield for very low values of $m_{t\bar{t}}$.

In addition, the two spin correlation observables c_{hel} and c_{han} , as defined in Eq. (2.4) and Eq. (2.10), are used to gain further sensitivity. Both variables are again defined using the $t\bar{t}$ system reconstruction as described in the previous section. As discussed in Sec. 2.2.2, they are ideal for separating spin-singlet and spin-triplet states, respectively. Thus, A and η_t signals, producing singlet states, will have enhanced contributions at high values of c_{hel} , while H signals, producing triplet states, will be enhanced at low values of c_{han} . This allows not only for better discrimination between signal and background, but also to distinguish whether a possible observed

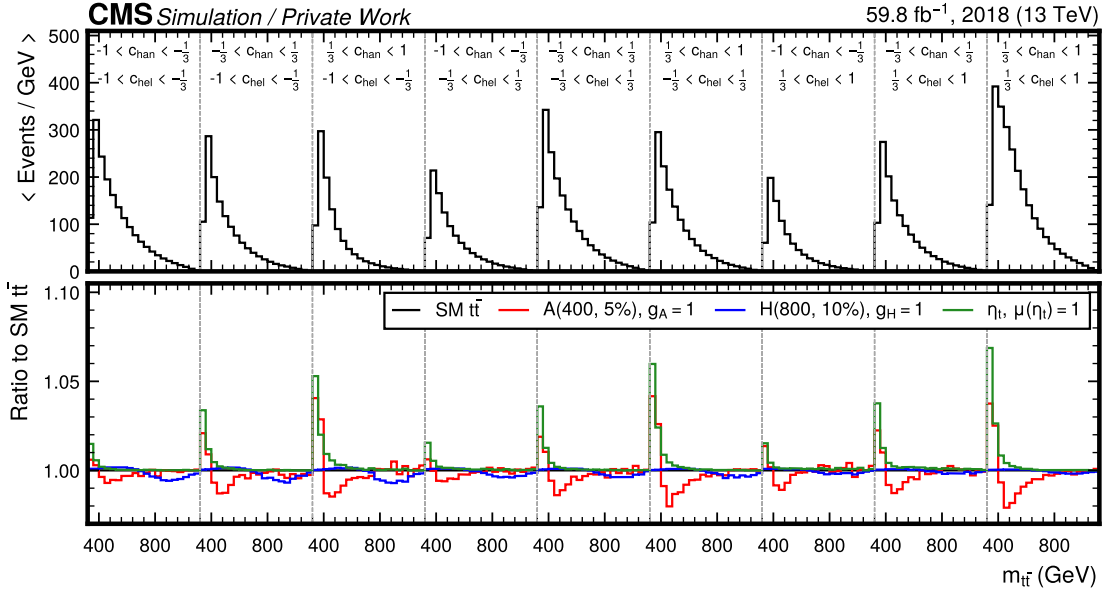


Figure 7.3: **3D template for $m_{t\bar{t}} \times c_{\text{hel}} \times c_{\text{han}}$** for SM $t\bar{t}$ (top) as well as three different example signals (bottom, shown as the ratio to SM $t\bar{t}$), corresponding to the luminosity taken in 2018 only.

signal is scalar or pseudoscalar in nature.

To combine all three variables, three-dimensional templates are created with $20 \times 3 \times 3$ bins in the three observables $m_{t\bar{t}}$, c_{hel} and c_{han} . For $m_{t\bar{t}}$, an irregular binning is chosen to account for the decrease in production cross section at high values. An example can be seen in Fig. 7.3 for SM $t\bar{t}$ and three different signals (A, H and η_t).

7.3 Higher-order corrections in $t\bar{t}$

In this analysis, the SM $t\bar{t}$ background is irreducible - after all, it leads to the exact same final state as the signal. As a result, it is crucial to model it as precisely as possible: a mismodeling of the $t\bar{t}$ kinematic distribution, especially in $m_{t\bar{t}}$, might otherwise be confused for a signal and lead to bias.

The MC simulation used for the SM $t\bar{t}$ background is performed at NLO in QCD using the POWHEG v2 subprocess hvq, as studied also in Chapter 6. On top of this, two different sets of corrections are applied to include missing higher orders, namely NNLO QCD and NLO electroweak (EW) corrections. Both of these are estimated by comparing the MC simulation, which is matched to a parton shower, to fixed-order predictions. The simulation is then reweighted using scale factors binned two-dimensionally in $m_{t\bar{t}}$ and $\cos\theta_t^*$, where the latter is the cosine of the scattering angle of the top quark to the beam axis in the $t\bar{t}$ rest frame. In the SM,

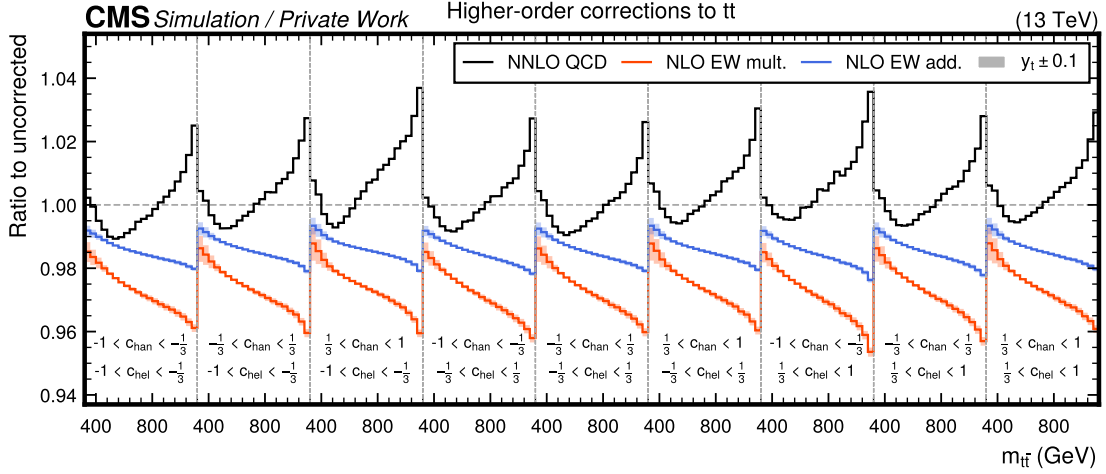


Figure 7.4: **Effect of NNLO QCD and NLO EW corrections** on the 3D $m_{t\bar{t}} \times c_{\text{hel}} \times c_{\text{han}}$ distribution after reconstruction in the form of ratios to the uncorrected distributions. The NNLO QCD corrections are shown as the solid black line, while the NLO EW corrections are shown in orange for the multiplicative scheme and in blue for the additive scheme. The effect of varying y_t by ± 0.1 in the NLO EW corrections is shown as the shaded bands.

2405 this variable is strongly correlated with the observables c_{hel} and c_{han} , and is thus used
 2406 in their place since spin correlation observables cannot be defined in calculations at
 2407 stable top level.

2408 7.3.1 NNLO QCD corrections

2409 The NNLO QCD predictions are obtained with the program MATRIX [122]. They
 2410 are computed at the level of stable top quarks with a dynamic scale choice of
 2411 $\sqrt{m_t^2 + p_{T,t}^2}$, where $p_{T,t}$ is the top quark transverse momentum. Fig. 7.4 shows the
 2412 resulting effect on the 3D $m_{t\bar{t}} \times c_{\text{hel}} \times c_{\text{han}}$ distribution at the detector level as the
 2413 black line. They are on the order of 1 – 2%.

2414 7.3.2 NLO EW corrections

2415 The NLO corrections in the electroweak coupling α_{EW} are computed with the
 2416 HATHOR code [166, 175–177] using the same nominal scale choices. Of partic-
 2417 ular interest here is a class of diagrams which contain an exchange of a virtual SM
 2418 Higgs boson, an example of which is seen in Fig. 7.5. The matrix element for this
 2419 diagram is proportional to the square of the SM Higgs-top Yukawa coupling y_t ,
 2420 giving a y_t^2 -dependent correction to $t\bar{t}$ distributions from the interference with LO

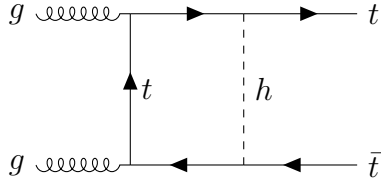


Figure 7.5: **EW correction involving a SM Higgs boson.** An example Feynman diagram for NLO EW corrections to $t\bar{t}$ production involving the exchange of a virtual SM Higgs boson h .

diagrams. This correction is sizeable mostly for low $m_{t\bar{t}}$ values, and is important for this analysis because the SM Higgs exchange might change the $t\bar{t}$ spin state and thus c_{hel} and c_{han} . To accurately account for this, the correction is derived separately for the different initial states (gg , $q\bar{q}$ and gq) of $t\bar{t}$ production.

The results obtained with HATHOR are accurate only to LO in α_S , i.e. $\mathcal{O}(\alpha_S^2)$, and as of the time of writing no full calculation including both NLO QCD and EW effects exists. Thus, there is an ambiguity on how the NLO-accurate (in QCD) MC simulation and the NNLO-accurate corrections presented in the previous section should be combined with the EW corrections.

Formally, the differential cross section as predicted by Powheg can be decomposed as

$$d\sigma_{\text{POWHEG}} = \alpha_S^2 d\sigma_{\text{LO}} + \alpha_S^3 d\sigma_{\text{NLO}} \quad (7.9)$$

where additional terms beyond $\mathcal{O}(\alpha_S^3)$ due to additional radiation in Powheg and Pythia are not written for simplicity. On the other hand, HATHOR predicts

$$d\sigma_{\text{HATHOR}} = \alpha_S^2 d\sigma_{\text{LO}} + \alpha_S^2 \alpha_{\text{EW}} d\sigma_{\text{EW}}. \quad (7.10)$$

One possible way to combine the calculations is the additive scheme, given by

$$\begin{aligned} d\sigma_{\text{add.}} &= d\sigma_{\text{POWHEG}} + d\sigma_{\text{HATHOR}} - \alpha_S^2 d\sigma_{\text{LO}} \\ &= \alpha_S^2 d\sigma_{\text{LO}} + \alpha_S^3 d\sigma_{\text{NLO}} + \alpha_S^2 \alpha_{\text{EW}} d\sigma_{\text{EW}} \end{aligned} \quad (7.11)$$

which is formally accurate to $\mathcal{O}(\alpha_S^3)$ and $\mathcal{O}(\alpha_S^2 \alpha_{\text{EW}})$. This approach does not include any cross terms of order $\mathcal{O}(\alpha_S^3 \alpha_{\text{EW}})$, which are not fully calculated by either Powheg or HATHOR. However, it is reasonable to assume that these cross terms factorize approximately, leading to the alternative multiplicative scheme [177]

$$\begin{aligned}
 d\sigma_{\text{mult.}} &= d\sigma_{\text{POWHEG}} \times \frac{d\sigma_{\text{HATHOR}}}{\alpha_S^2 d\sigma_{\text{LO}}} \\
 &= \alpha_S^2 d\sigma_{\text{LO}} + \alpha_S^3 d\sigma_{\text{NLO}} + \alpha_S^2 \alpha_{\text{EW}} d\sigma_{\text{EW}} + \alpha_S^3 \alpha_{\text{EW}} \frac{d\sigma_{\text{NLO}} d\sigma_{\text{EW}}}{d\sigma_{\text{LO}}}
 \end{aligned} \tag{7.12}$$

2439 The difference between the two schemes is in the last term of order $\mathcal{O}(\alpha_S^3 \alpha_{\text{EW}})$,
 2440 which is an approximation to the QCD-EW cross terms. In this work, the multi-
 2441 plicative approach is used for all nominal results, while the difference to the additive
 2442 approach is included as a systematic uncertainty. In both cases, the needed term
 2443 $\alpha_S^2 d\sigma_{\text{LO}}$ is computed with MADGRAPH 5.

2444 The effect of both approaches on the 3D $m_{t\bar{t}} \times c_{\text{hel}} \times c_{\text{han}}$ distribution at the
 2445 detector level after parton showering can be seen in Fig. 7.4 for different values of
 2446 y_t . The multiplicative scheme leads to a larger correction of roughly 2 – 4%, while
 2447 the additive scheme only gives 1 – 2%. Notably, the effect of varying y_t modifies not
 2448 only the $m_{t\bar{t}}$ distribution close to the $t\bar{t}$ threshold, but also the distribution of c_{hel} .
 2449 As a result, such a variation in data could potentially be confused for a pseudoscalar
 2450 signal. It is thus important to include it as a systematic uncertainty, as described
 2451 in Sec. 7.5.

2452 7.4 Matrix element reweighting for A/H signals

2453 In order to probe the full phase space of the generic A/H model as described in
 2454 Sec. 7.1, predictions at different A/H masses and widths with a sufficiently small
 2455 spacing are required so that interpolation between the points is possible. However,
 2456 generating a separate MC sample for each mass and width point is computationally
 2457 very expensive.

2458 7.4.1 Principle of the method

2459 As an alternative, it is possible to re-use existing samples for different mass and
 2460 width points via matrix element reweighting. This method works by noting that a
 2461 given MC sample can be seen as a random sample, drawn from a PDF of the form

$$\mathcal{P}(x_i^{\text{ME}}, x_j^{\text{reco}}) = \mathcal{P}^{\text{ME}}(x_i^{\text{ME}}) \cdot \mathcal{P}^{\text{rem}}(x_j^{\text{reco}} | x_i^{\text{ME}}) \tag{7.13}$$

2462 Here, x_i^{ME} are all variables defining the event at the matrix element (ME) level,
 2463 i.e. at the level of the hard interaction, and x_j^{reco} are all variables after detector
 2464 simulation and object reconstruction. For the case of the A/H signals, which are
 2465 generated at LO in QCD, x_i^{ME} is given fully by the four-momenta and helicities of
 2466 the final-state particles (leptons, neutrinos and b quarks) in the hard process. The

²⁴⁶⁷ x_j^{reco} consist of all possible reconstruction-level variables that are relevant to the
²⁴⁶⁸ analysis, such as e.g. jet and lepton four-momenta, lepton identification criteria or
²⁴⁶⁹ $\vec{p}_{\text{T}}^{\text{miss}}$.

²⁴⁷⁰ $\mathcal{P}^{\text{ME}}(x_i^{\text{ME}})$ refers to the probability density of the ME-level variables as predicted
²⁴⁷¹ by the ME generator, which will be proportional to the absolute square of the matrix
²⁴⁷² element. This function will depend on the chosen scenario of the A/H model, i.e.
²⁴⁷³ $m_{\text{A}/\text{H}}$ and $\Gamma_{\text{A}/\text{H}}$. Meanwhile, the conditional probability density $\mathcal{P}^{\text{rem}}(x_j^{\text{reco}}|x_i^{\text{ME}})$
²⁴⁷⁴ encodes the effects of all other components of the simulation chain, such as the
²⁴⁷⁵ parton shower, hadronization, detector simulation and reconstruction. It gives the
²⁴⁷⁶ probability to observe reconstruction-level variables x_j^{reco} for an event with ME-level
²⁴⁷⁷ variables x_i^{ME} .

²⁴⁷⁸ The principal assumption of the method is now that \mathcal{P}^{rem} , and thus the whole
²⁴⁷⁹ simulation chain except for the matrix element, is independent of the underlying
²⁴⁸⁰ A/H signal scenario ($m_{\text{A}/\text{H}}$ and $\Gamma_{\text{A}/\text{H}}$). This assumption is certainly true for the
²⁴⁸¹ detector simulation and reconstruction, while care must be taken for the parton
²⁴⁸² shower, which in general needs to be matched to the matrix element and can this
²⁴⁸³ way have a residual dependence. The validity of the assumption will be discussed
²⁴⁸⁴ in more detail below.

²⁴⁸⁵ If the assumption is fulfilled, a given A/H MC sample generated with parameters
²⁴⁸⁶ $m_{\text{A}/\text{H}}^0$ and $\Gamma_{\text{A}/\text{H}}^0$ can now be reweighted to a different A/H scenario with parameters
²⁴⁸⁷ $\hat{m}_{\text{A}/\text{H}}$ and $\hat{\Gamma}_{\text{A}/\text{H}}$ by applying to each event i a weight

$$w_i = \frac{\mathcal{P}^{\text{ME}}(x_i^{\text{ME}}|\hat{m}_{\text{A}/\text{H}}, \hat{\Gamma}_{\text{A}/\text{H}})}{\mathcal{P}^{\text{ME}}(x_i^{\text{ME}}|m_{\text{A}/\text{H}}^0, \Gamma_{\text{A}/\text{H}}^0)} \quad (7.14)$$

²⁴⁸⁸ The quantities in the denominator and nominator are the ME-level probability
²⁴⁸⁹ densities for each event, evaluated at the original and target A/H parameters, respec-
²⁴⁹⁰ tively. When this weight is inserted into Eq. (7.13), the original probability cancels,
²⁴⁹¹ giving the correct probability density for the target scenario $\hat{m}_{\text{A}/\text{H}}$ and $\hat{\Gamma}_{\text{A}/\text{H}}$.

²⁴⁹² In practice, this method will only work if the MC sample used for the reweighting
²⁴⁹³ has sufficient phase space overlap with the target A/H scenario, i.e. if the two
²⁴⁹⁴ probabilities in Eq. (7.14) are not too different from each other for the majority of
²⁴⁹⁵ the events. Otherwise, the weights will become very small in some regions of the
²⁴⁹⁶ phase space and very large in others, resulting in poor statistics for the reweighted
²⁴⁹⁷ sample.

²⁴⁹⁸ The method was implemented by directly evaluating the squared matrix elements
²⁴⁹⁹ for the different A/H hypotheses, using the standalone reweighting interface pro-
²⁵⁰⁰ vided by MADGRAPH 5 and the same UFO model as for the signal generation.

2501 7.4.2 Combination of multiple origin samples

2502 For the purpose of this analysis, a set of signal samples for different A/H scenarios
 2503 (as given in Sec. 7.2.1) was already available at the time of starting these studies.
 2504 These samples were used as origin samples for the reweighting. In order to maximize
 2505 the statistics achieved after reweighting for each target A/H scenario, and mitigate
 2506 problems from poor phase space overlap, a subset of the available samples were
 2507 combined after reweighting for each target scenario.

2508 This procedure works as follows: First, a set of several origin samples j with
 2509 different parameters $m_{A/H}$ and $\Gamma_{A/H}$ are all reweighted separately to the same target
 2510 parameters $\hat{m}_{A/H}$ and $\hat{\Gamma}_{A/H}$ with per-event weights $w_{i,j}$ as given in Eq. (7.14). Then,
 2511 the different samples are again weighted with a per-sample weight v_j proportional
 2512 to

$$v_j \propto \langle w_{i,j} \rangle^{-1} = \frac{\sum_i w_{i,j}}{\sum_i w_{i,j}^2} \quad (7.15)$$

2513 where the sums run over all events i in the considered sample j . This expression is
 2514 the inverse of the average ME weight for sample j . It is chosen such that samples
 2515 with large phase space overlap with the target A/H scenario - and thus small ME
 2516 weights $w_{i,j}$ - are assigned a large weight v_j in the combination of samples. Similarly,
 2517 samples with poor phase space overlap, and thus large average ME weights, get
 2518 assigned small weights and contribute less strongly to the combined sample. Finally,
 2519 the total combined sample is normalized to the expected cross section for the target
 2520 scenario, which is calculated independently. It can be shown that this procedure
 2521 minimizes the total statistical error of the combined sample.

2522 In practice, all available masses and parities (A and H) are combined for each
 2523 target A/H mass. Resonance and interference contributions are treated separately
 2524 from each other. Furthermore, it was found that, for the resonance contribution only,
 2525 it is necessary to split the combination of different A/H widths into two halves:
 2526 those with $\Gamma_{A/H}/m_{A/H}$ less or greater than 10%. This is due to an interplay of
 2527 MADGRAPH 5 and the PYTHIA shower leading to a dependency on the A/H width
 2528 in the matrix element, which is not taken into account in the reweighting. For
 2529 $\Gamma_{A/H}/m_{A/H} < 10\%$ (narrow resonance), MADGRAPH 5 includes the intermediate
 2530 A/H particle in the event record, which is then treated by PYTHIA as a unstable
 2531 resonance and its virtuality as predicted by the matrix element is preserved. For
 2532 $\Gamma_{A/H}/m_{A/H} \geq 10\%$ (broad resonance), the A/H particle is not included in the event
 2533 record, and its virtuality is thus not preserved. This leads to slight differences in
 2534 distributions affected by the parton showering. The choice of 10% for the transition
 2535 between the two modes is an arbitrary parameter, and thus not necessarily physical.
 2536 Nonetheless, it was decided in this analysis to not mix the two width ranges in the
 2537 reweighting in order to obtain full closure with a standalone generation.

2538 7.4.3 Validation

2539 The combined reweighting is validated for three masses of $m_{A/H} = 400, 600$ and 800
2540 GeV as well as widths of 2.5 and 10% . For each of these points, the reweighting is
2541 performed as stated above, but leaving out A/H scenarios with the same mass from
2542 the combination of origin samples since otherwise the weights would be trivially
2543 one. The reweighted $m_{t\bar{t}}$ distributions at generator level are then compared to the
2544 standalone samples at the same $m_{A/H}$ and $\Gamma_{A/H}$.

2545 The resulting comparisons and residuals can be seen in Figs. 7.6 and 7.7 for A and
2546 H, respectively, separated into the resonance and interference contributions. It can
2547 be seen that the closure between reweighting and standalone generation is excellent
2548 within the statistical uncertainties.

2549 7.5 Systematic uncertainties

2550 Similar to Sec. 5.5, systematic uncertainties affect the distributions of both SM
2551 background and signal processes. They are listed in this section, split into theory
2552 (Sec. 7.5.1) and experimental uncertainties (Sec. 7.5.2).

2553 7.5.1 Theory uncertainties

2554 **Scale uncertainties** Uncertainties due to missing higher orders in the matrix element
2555 as well as the parton shower are included separately for the SM $t\bar{t}$, tW , and
2556 $Z/\gamma^* + \text{jets}$ backgrounds as well as all considered signals by varying the associated
2557 scales by a factor 2 up and down independently, same as in Sec. 5.5. For A and
2558 H, the uncertainties are considered uncorrelated between the resonance and inter-
2559 ference components, which is found to be conservative. For η_t , the renormalization
2560 scale uncertainty is not included since the considered model does not encode any
2561 dependence on either μ_R or α_S .

2562 **PDF uncertainties** For the SM $t\bar{t}$ background, the uncertainty due to the PDF is
2563 again included based on the 100 provided eigenvalues of the used NNPDF 3.1 PDF
2564 set. However, it is not considered sufficient to simply take the envelope of these
2565 variations since this would distort possible shape variations. Instead, a principal
2566 component analysis (PCA) is performed on the final 3D $m_{t\bar{t}} \times c_{\text{hel}} \times c_{\text{han}}$ templates
2567 obtained from the different eigenvalues, thus finding those linear combinations that
2568 have a noticeable shape effect. It is found that only the first eigenvector (correspond-
2569 ing to the largest eigenvalue) is non-negligible, and this variation is considered as
2570 the PDF uncertainty. Independently of this, another uncertainty based on the value
2571 of α_S in the PDF is considered similarly to Sec. 5.5.

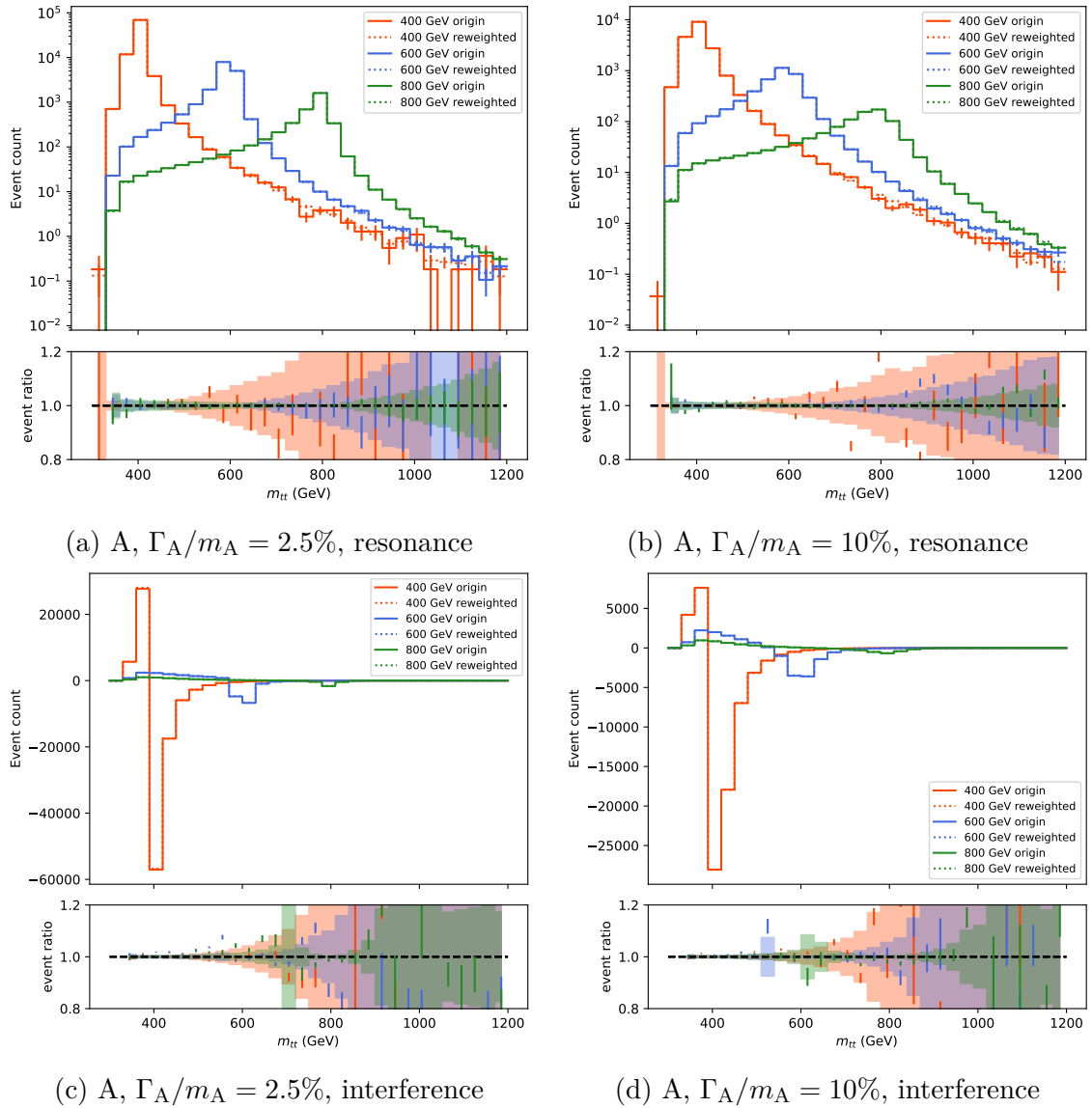


Figure 7.6: **Validation of the ME reweighting for A.** Comparison of standalone generated (solid) and reweighted (dashed) $m_{t\bar{t}}$ distributions for different values of m_A . The lower panel shows the ratio of reweighted and standalone distributions. The error bars and colored areas give the statistical uncertainty of the reweighted and standalone sample, respectively.

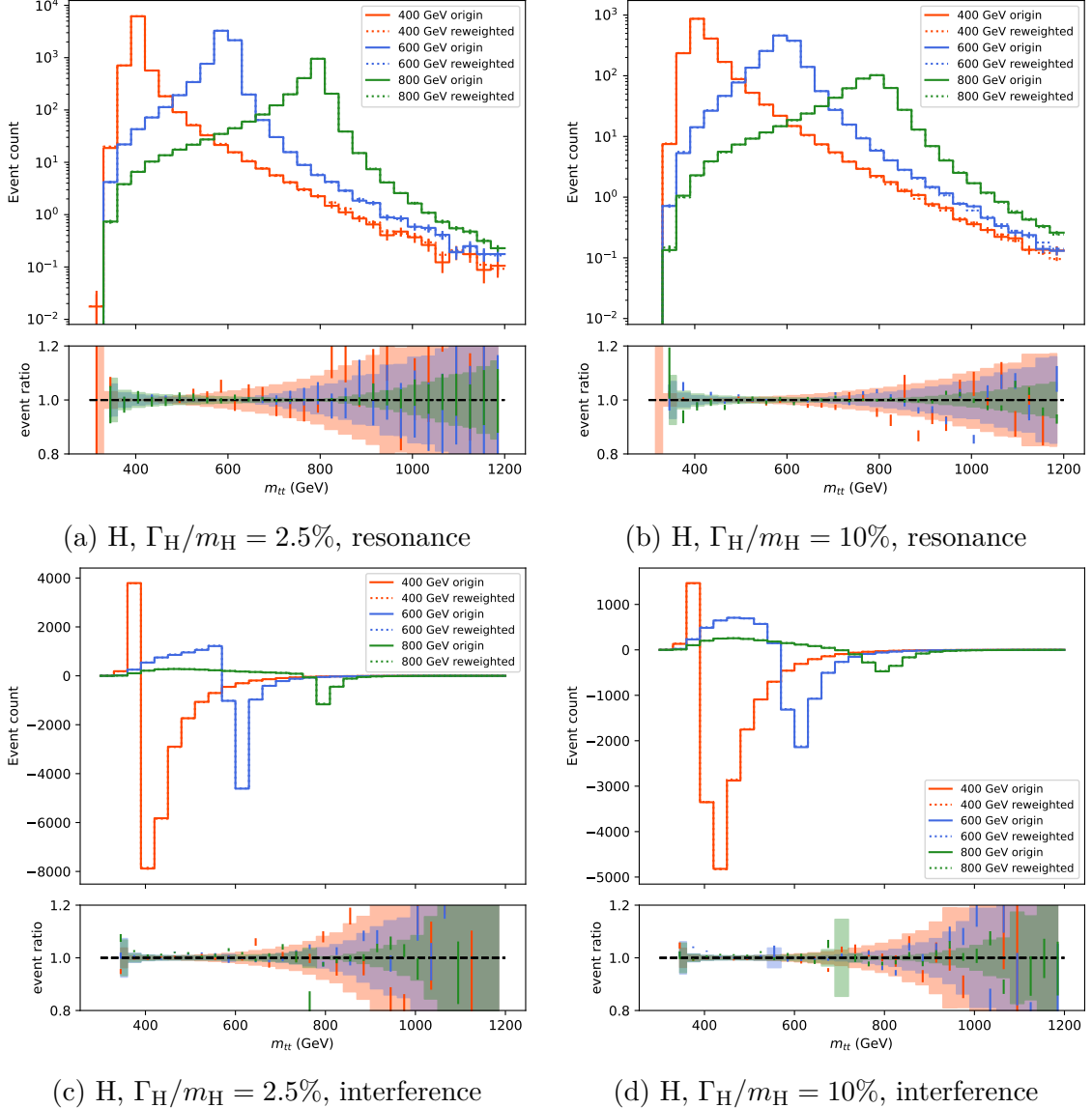


Figure 7.7: **Validation of the ME reweighting for H .** Comparison of standalone generated and reweighted $m_{t\bar{t}}$ distributions for different values of m_H , similar to Fig. 7.6.

2572 **EW correction uncertainties** As described in Sec. 7.3.2, two independent un-
2573 certainties are attached to the NLO electroweak correction of SM $t\bar{t}$: First, the
2574 value of the SM top-Higgs Yukawa coupling is allowed to vary in the range $y_t =$
2575 $1.00^{+0.11}_{-0.11}$, with the range given by the uncertainty of the experimental measurement
2576 in Ref. [178]. Second, the difference between the additive and multiplicative appli-
2577 cation scheme (Eqs. (7.11) and (7.12)) is considered as a separate uncertainty, as
2578 recommended in Ref. [177], and symmetrized around the nominal.

2579 **Top quark mass uncertainty** The top quark mass uncertainty in SM $t\bar{t}$ is es-
2580 timated by varying it from its nominal value of $m_t = 172.5 \text{ GeV}$ by $\pm 3 \text{ GeV}$ in
2581 the POWHEG simulation, and then scaling down the resulting relative deviation by
2582 a factor $1/3$, leading to a $\pm 1 \text{ GeV}$ uncertainty. This is done since the variation,
2583 obtained from an independent MC sample, is otherwise plagued by large statisti-
2584 cal uncertainties. Furthermore, the top mass is also varied in all considered signal
2585 samples directly by $\pm 1 \text{ GeV}$ through an ME reweighting method similar to Sec. 7.4.
2586 The top mass uncertainties between background and signals are considered as fully
2587 correlated.

2588 **Further uncertainties in SM $t\bar{t}$** Additionally, separate SM $t\bar{t}$ samples are used
2589 to evaluate uncertainties due to ME/PS matching (same as in Sec. 5.5), the under-
2590 lying event tune [76], and the color reconnection model in PYTHIA [80, 179]. All of
2591 these effects are found to be small in the channels considered here.

2592 **Background cross section uncertainties** For the SM $t\bar{t}$ background, instead of
2593 including an explicit cross section uncertainty, the shift in the predicted NNLO+NNLL
2594 $t\bar{t}$ cross section due to the ME scales and the top quark mass is correlated with the
2595 respective uncertainties. For minor backgrounds, explicit uncertainties of 15% for
2596 tW and t-channel single top, 30% for diboson and $t\bar{t} + X$, and 5% for the data-driven
2597 Z/γ^* + jets normalization are considered.

2598 **Background statistical uncertainties** Again similar to Sec. 5.5, per-bin back-
2599 ground statistical uncertainties for all simulated processes are included following
2600 Ref. [133].

2601 7.5.2 Experimental uncertainties

2602 **Jet and p_T^{miss} uncertainties** The uncertainty on the calibration of the jet p_T
2603 detector response is split into five subsources, of which three are considered uncor-
2604 related between years and two (related to the response to jets of different flavor)
2605 are correlated. Further subsources as provided by CMS are found to be negligible
2606 for this analysis. Furthermore, the uncertainty in the jet p_T resolution is considered

separately, again uncorrelated between years. All jet uncertainties are fully propagated to the calculation of p_T^{miss} , and an additional p_T^{miss} uncertainty based on soft, unclustered hadronic activity is also considered.

b tagging uncertainties Similarly, the uncertainty on the b tagging efficiency is split into 17 subsources, corresponding e.g. to different parton shower modeling, the treatment of leptons in the jet, or the propagation of the jet p_T scale uncertainties. One component represents the statistical uncertainty and is thus considered uncorrelated, while all others are correlated among years. Moreover, an uncertainty on mistagging of light-flavor jets is included, also split into a statistical and a systematic component.

Lepton and trigger uncertainties Uncertainties on the lepton reconstruction, identification, and isolation efficiencies, as measured centrally in CMS using the tag-and-probe method, are considered separately for muons and electrons [95, 124]. For the muons, the uncertainty is split into a statistical component (uncorrelated between the analysis years) and a systematic component (correlated). Similarly, the dilepton trigger efficiency uncertainties are considered uncorrelated between years and lepton flavor channels. Finally, in data taken in 2016 or 2017, an additional uncertainty is assigned due to an inefficiency in the ECAL L1 trigger [101], as described in Sec. 7.2.4.

Luminosity uncertainty The uncertainty on the total integrated luminosity is included following Refs. [82, 180, 181], leading to a total luminosity uncertainty of 1.6%, split into a total of seven components with different correlations between the years.

Pileup uncertainty To estimate the uncertainty on the amount of pileup per pp bunch crossing, the effective inelastic proton-proton cross section used for pileup reweighting in the simulation is varied by 4.6% from its nominal value.

7.5.3 Uncertainty smoothing

Several of the considered uncertainty sources, e.g. the top quark mass in SM $t\bar{t}$, are estimated by either comparing to separate MC samples, which causes the relative deviation due to the source to be affected by large statistical noise. A similar problem appears for uncertainties which effectively vary the cuts applied on MC events, such as e.g. the jet p_T scale uncertainties by way of jet acceptances. If left untreated, fitting these noisy shape templates to the data could lead to erroneous constraints in the likelihood fit. To prevent this, the smoothing algorithm LOWESS [182, 183] is applied to the relative deviations for these sources, with the bandwidth used for

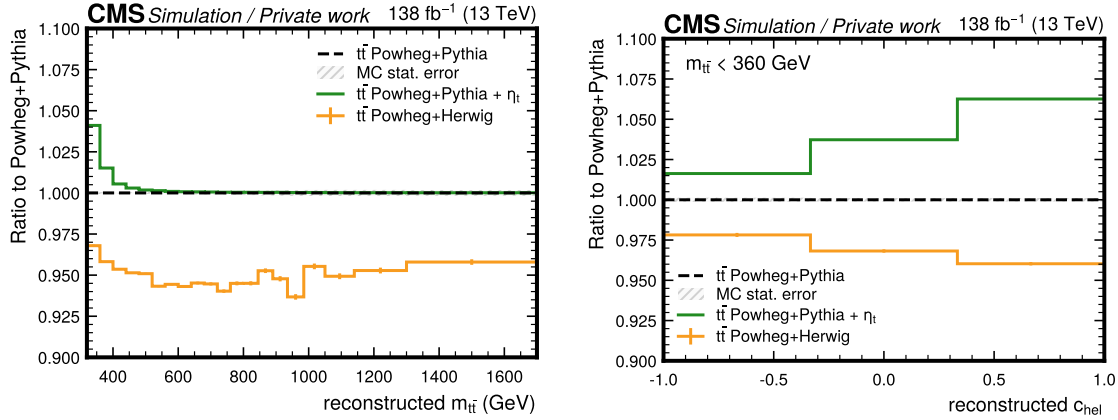


Figure 7.8: Comparison of Herwig and Pythia. The ratio of the predictions of POWHEG hvq $t\bar{t}$ matched to HERWIG and to PYTHIA for the inclusive reconstructed $m_{t\bar{t}}$ distribution (left) and the reconstructed c_{hel} distribution, restricted to $m_{t\bar{t}} < 360 \text{ GeV}$ (right). The effect of the η_t signal is also shown for comparison.

the smoothing determined separately through cross-validation for each source. For more details on the procedure, see Ref. [26].

7.5.4 Differences between MC generators

It has been observed in previous analyses that the theoretical uncertainties collected in Sec. 7.5.1 do not necessarily cover the differences in the predictions of different MC generators for $t\bar{t}$ [24, 25, 146, 184]. To assess the size of these effects, the standard $t\bar{t}$ prediction as computed using POWHEG hvq matched to PYTHIA is compared to alternate generator setups.

The first of these is the same POWHEG hvq matrix element matched to the multi-purpose event generator HERWIG instead of PYTHIA. The angular-ordered parton shower in HERWIG is used (as opposed to the p_T -ordered dipole shower in PYTHIA) together with the CMS CH3 tune [185]. Furthermore, HERWIG uses a cluster hadronization model [186] instead of the string hadronization model of PYTHIA as described in Sec. 3.4.

Figure 7.8 shows the ratios of the predictions from HERWIG and PYTHIA for the reconstructed $m_{t\bar{t}}$ distribution, as well as for the c_{hel} distribution close to the $t\bar{t}$ threshold (i.e. where the η_t signal is located). Besides a significantly lower $t\bar{t}$ acceptance, HERWIG predicts an increase of events at the $t\bar{t}$ threshold similar to η_t . This appears concerning at first glance since, should the data follow the prediction from HERWIG instead of PYTHIA, this enhancement could be confused with an η_t signal if PYTHIA is used as the baseline prediction. However, as seen in Fig. 7.8

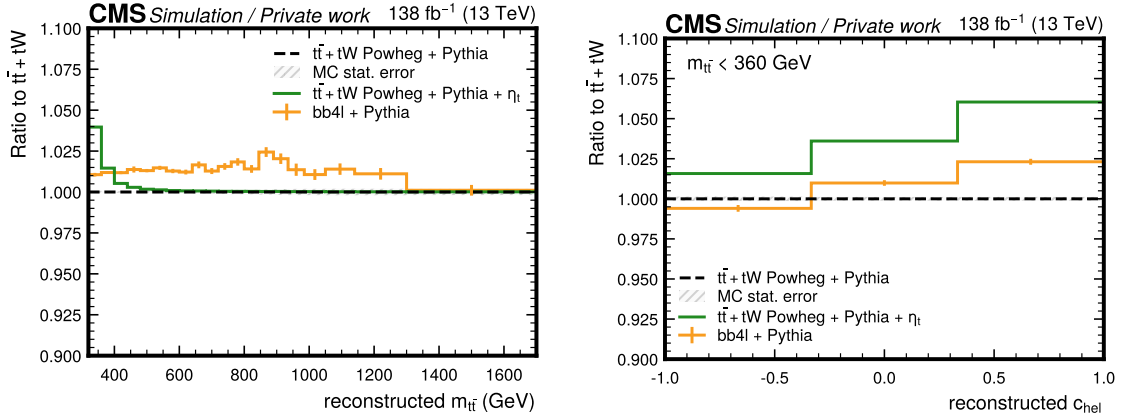


Figure 7.9: **Comparison of Powheg $t\bar{t} + tW$ and bb4l.** The ratio of the predictions of the sum of POWHEG hvq $t\bar{t}$ and tW to bb4l (all matched to PYTHIA) for the inclusive reconstructed $m_{t\bar{t}}$ distribution (left) and the reconstructed c_{hel} distribution, restricted to $m_{t\bar{t}} < 360$ GeV (right). The effect of the η_t signal is also shown for comparison.

on the right, HERWIG at the same predicts a flatter slope in c_{hel} than PYTHIA, equivalent to less $t\bar{t}$ spin correlation¹. This is in contrast to the η_t signal, in which the $t\bar{t}$ spins are maximally anticorrelated. The inclusion of the spin correlation variable c_{hel} in the analysis thus makes it possible to separate the differences between POWHEG and HERWIG with respect to η_t .

The second alternative generator is bb4l matched to PYTHIA, as studied extensively in Chapter 6. Here, particularly the off-shell effects included in bb4l might be of interest for the extraction of η_t since the latter is located below the $t\bar{t}$ threshold. The setup denoted as “bb4l v2” in Sec. 6.2, corresponding to Ref. [147], is used, and compared to the sum of the POWHEG hvq $t\bar{t}$ and tW predictions for consistency.

A caveat here is presented by the corrections to NNLO QCD and NLO EW as described in Sec. 7.3. These are derived from fixed-order corrections assuming stable top quarks, and are not available for the full $b\bar{b}\ell\bar{\ell}\nu\nu$ final state. To still be able to apply them to bb4l predictions, the bb4l sample is split into a $t\bar{t}$ and a tW part in an ad-hoc way by using the matrix element history projectors implemented in bb4l v2 [147]. The corrections are then applied to the $t\bar{t}$ part only, in the same manner as to POWHEG hvq.

The ratios of the predictions are shown in Fig. 7.9 in the same manner as before. It can be seen that bb4l does not predict major differences in the reconstructed $m_{t\bar{t}}$ spectrum even at its lower edge. However, it results in a significantly steeper slope in reconstructed c_{hel} close to the threshold. This increase in slope is of similar magnitude as the effect expected due to η_t .

¹This effect was also seen in the context of Ref. [25].

The source of this difference is not yet fully understood. bb41 contains NLO QCD corrections to the top decay which are not present in hvq (though they are approximated through the matrix element corrections in PYTHIA). However, NLO corrections to spin correlations are expected to not only be small, but reduce the spin correlation instead of enhancing it [17]. It is possible that the effect instead originates in the $t\bar{t}/tW$ interference: The tW contribution on its own is expected to have approximately flat c_{hel} since one of the leptons is not actually the decay product of a top quark, and the interference between $t\bar{t}$ and tW is destructive in large parts of the phase space. If the interference in bb41 is now larger than in $t\bar{t} + tW$, it could thus reduce the contribution from tW , effectively enhancing the c_{hel} slope. Since $t\bar{t}$ and tW are not cleanly separable in bb41, however, this hypothesis is difficult to confirm, and such studies are beyond the scope of this analysis.

A third alternative prediction is provided by $t\bar{t} + \text{jets}$ production simulated with MG5_AMC@NLO, matched to PYTHIA with the FxFx scheme [187]. While this prediction is formally also NLO-accurate in QCD in the NWA, and thus comparable to POWHEG hvq, it has been observed in past measurements that MG5_AMC@NLO does not agree as well with data as POWHEG for $t\bar{t}$ production. As a result, MG5_AMC@NLO is given less focus compared to the other two predictions in this work.

In this work, POWHEG hvq + PYTHIA is considered for the nominal background prediction in all cases. A comparison to POWHEG hvq + HERWIG, MG5_AMC@NLO + PYTHIA, and bb41 + PYTHIA is shown in Sec. 7.7.3 in the context of measuring the η_t cross section. Furthermore, the effect of including the differences to POWHEG hvq + HERWIG and bb41 + PYTHIA as two additional shape-based nuisance parameters in the fit is similarly given in Sec. 7.7.3. Note that in Ref. [9], these nuisance parameters were considered as part of the main result in order to be conservative with respect to the total uncertainty.

7.6 Pre-fit distributions

The agreement between the total MC prediction, including all corrections described in Secs. 7.2.4 and 7.3, and the observed data are presented in this section. Shown observables are lepton p_T , η , and $\Delta\phi_{\ell\ell}$ (Fig. 7.10); jet p_T , η , and number of jets (Fig. 7.11); as well as p_T^{miss} , the invariant mass of the two leptons $m_{\ell\ell}$, and the invariant mass of the two leptons and two b-tagged jets $m_{b\bar{b}\ell\ell}$ (Fig. 7.12). All of them are shown after all lepton, jet, b tag and p_T^{miss} requirements, but before the $t\bar{t}$ reconstruction, summed over all analysis years, and separately for the same-flavor (ee and $\mu\mu$) and opposite-flavor ($e\mu$) channels, since the latter have different backgrounds and cuts.

It can be seen that there is a slight but consistent overprediction of the background normalization compared to the data in almost all distributions. Furthermore, there

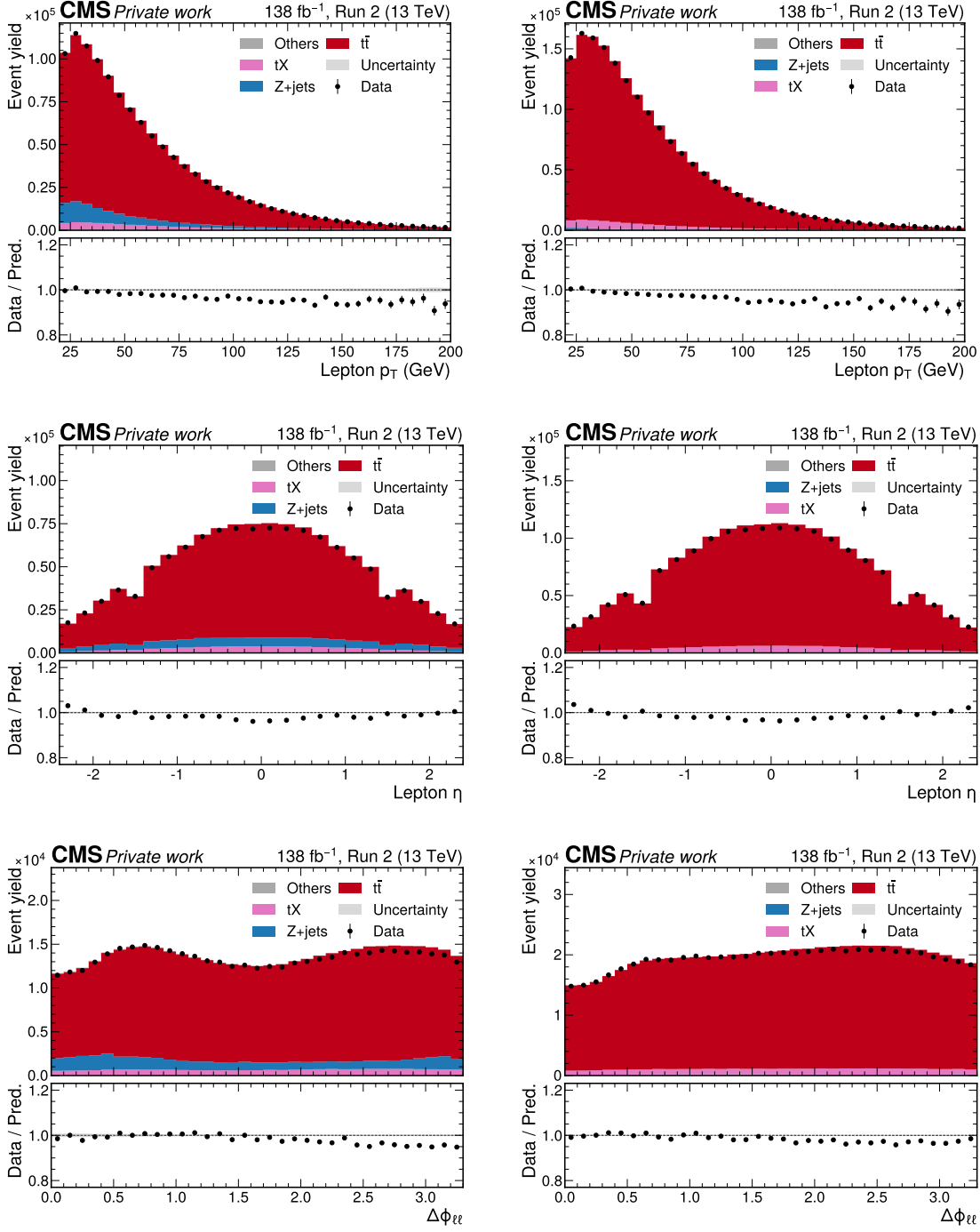


Figure 7.10: Control distributions. Shown are the distributions of p_T of both leptons (top), η of both leptons (center), and the azimuthal angle $\Delta\phi_{ll}$ between the leptons (bottom) in the ee/ $\mu\mu$ (left) and e μ channels (right). All figures show both data (black dots) and different simulated background processes (colored bars), as well as the statistical uncertainty only.

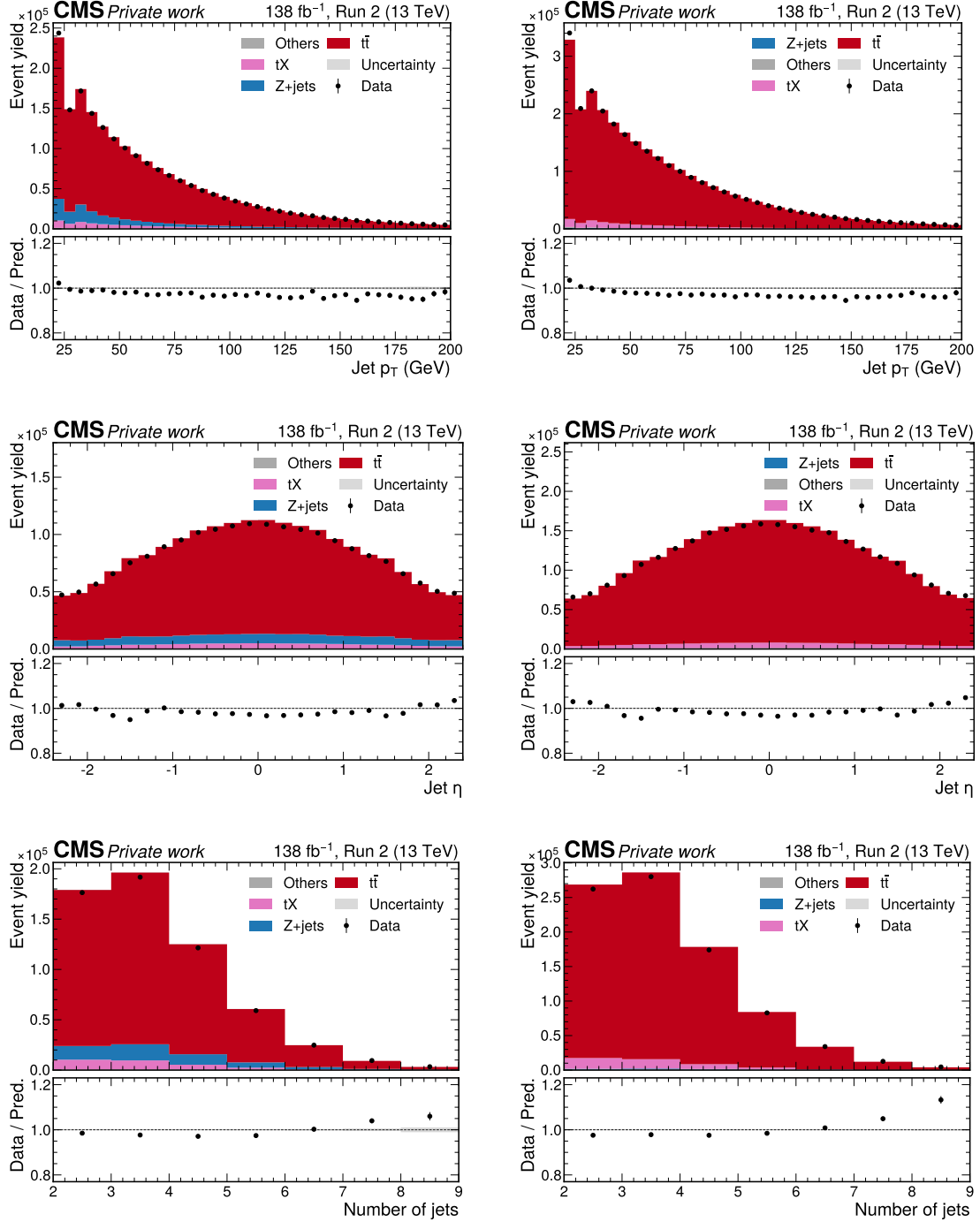


Figure 7.11: **Control distributions.** Shown are the distributions of p_T of all jets (top), η of all jets (center), and the number of jets (bottom) in the ee/ $\mu\mu$ (left) and e μ channels (right). All figures show both data (black dots) and different simulated background processes (colored bars), as well as the statistical uncertainty only.

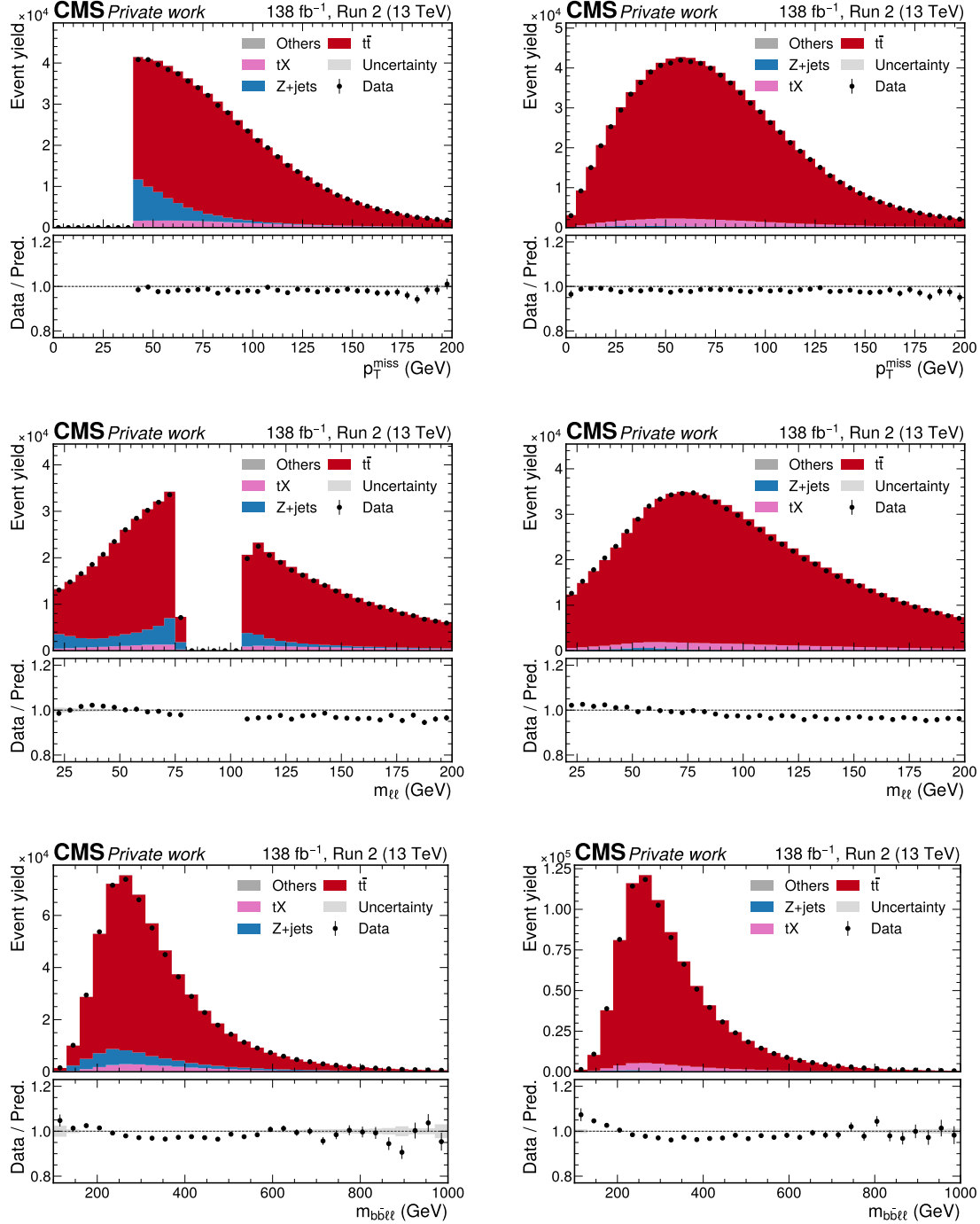


Figure 7.12: Control distributions. Shown are the distributions of p_T^{miss} (top), $m_{\ell\ell}$ (center), and the invariant mass $m_{bb\bar{b}\ell\ell}$ of both b candidates and both leptons (bottom) in the ee/ $\mu\mu$ (left) and e μ channels (right). All figures show both data (black dots) and different simulated background processes (colored bars), as well as the statistical uncertainty only.

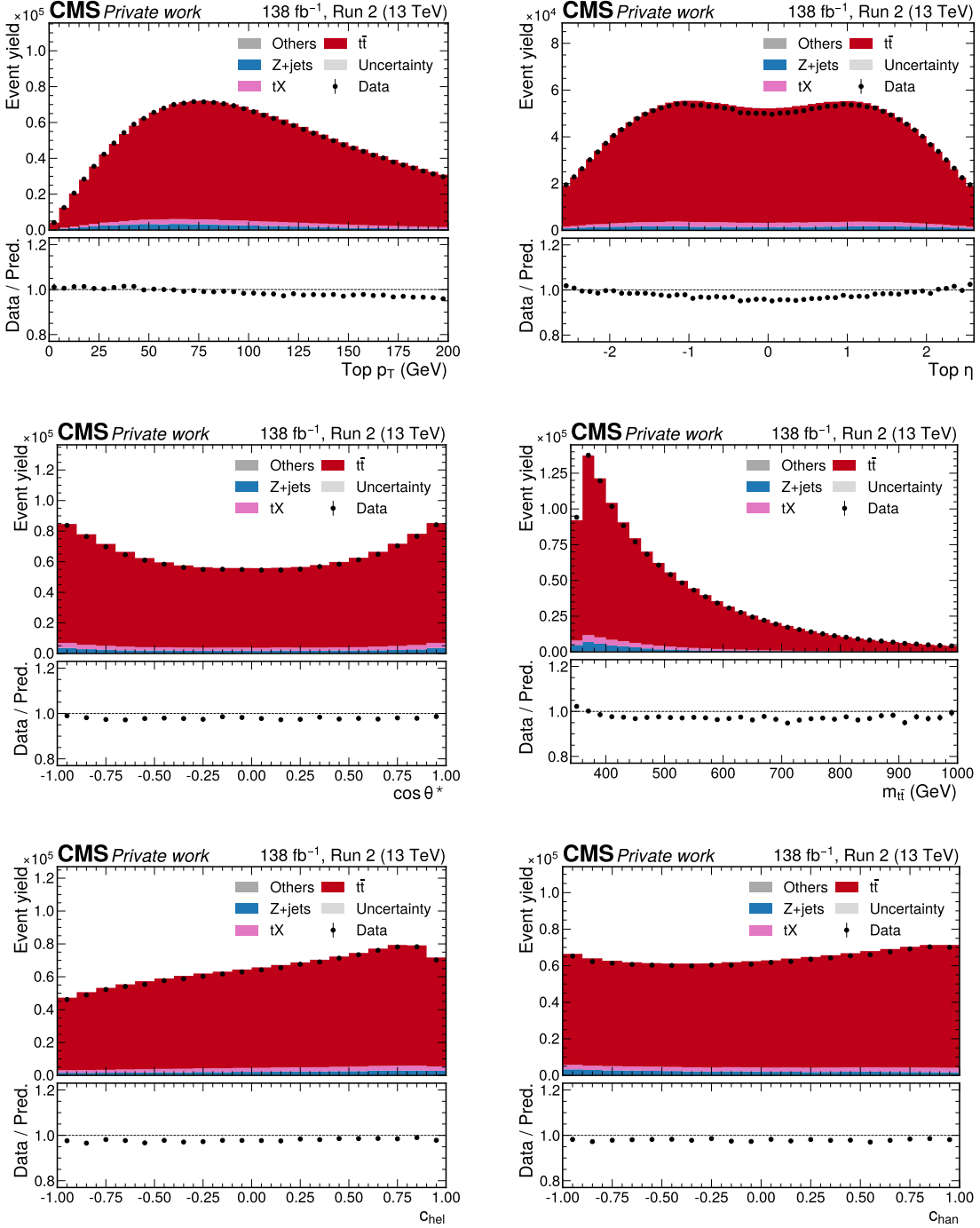


Figure 7.13: **Control distributions after $t\bar{t}$ reconstruction.** Shown are (from top left to bottom right) the distributions of the top quark p_T , top quark η , $m_{t\bar{t}}$, $\cos \theta^*$, c_{hel} and c_{han} for the sum of all dilepton channels. All figures show both data (black dots) and different simulated background processes (colored bars), as well as the statistical uncertainty only.

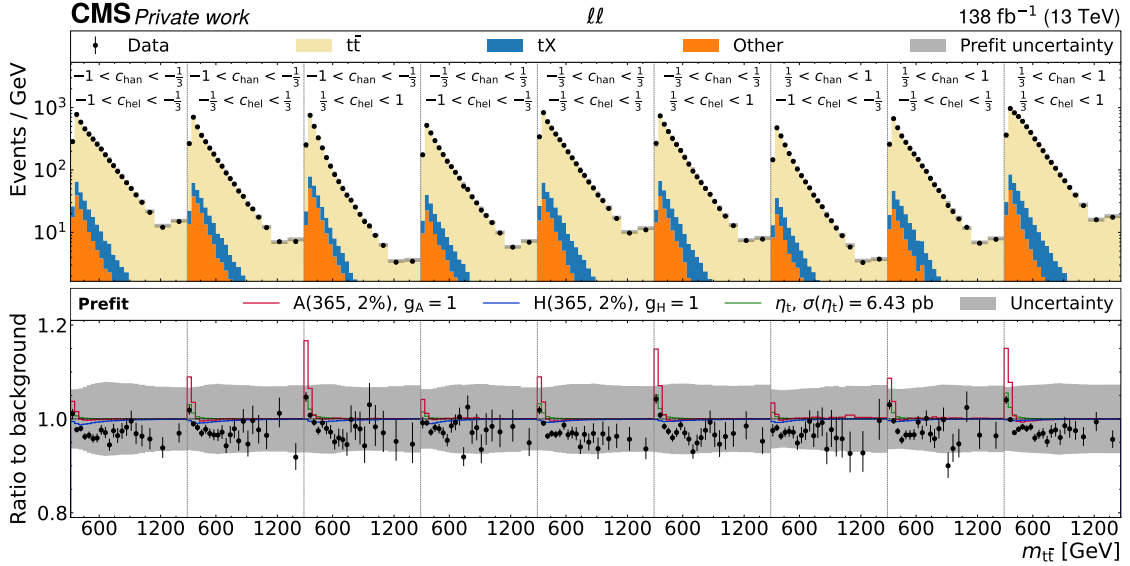


Figure 7.14: **Prefit distributions of $m_{t\bar{t}} \times c_{\text{hel}} \times c_{\text{han}}$.** The unrolled three-dimensional distribution in $m_{t\bar{t}}$, c_{hel} and c_{han} as used for statistical analysis before the fit to the data, summed over all years and lepton flavors. The upper panel shows the sum of the background simulation (colored bars) and the observed data (black dots), while the lower panel shows the ratio of the data to the prediction, with different signals overlaid: A (red) and H (blue), both for $m_{A/H} = 365$ GeV and $\Gamma_{A/H}/m_{A/H} = 2\%$, and η_t (green).

is a slight slope in the ratio of data and simulation yields in some energy-related observables like lepton or jet p_T . Both of these discrepancies are well covered by systematic uncertainties **TODO reproduce plots with syst uncs and make sure this is the case.**

Furthermore, different distributions resulting from the $t\bar{t}$ reconstruction are shown in Fig. 7.13, this time summed also over lepton flavor. They consist of top quark p_T , η , and scattering angle $\cos\theta^*$, as well as the three observables used for the fit $m_{t\bar{t}}$, c_{hel} , and c_{han} .

Finally, the three-dimensional $m_{t\bar{t}} \times c_{\text{hel}} \times c_{\text{han}}$ distribution used for the statistical analysis is shown before the fit, including all systematic uncertainties, in Fig. 7.14. A notable excess of the data compared to the prediction is observed for low values of $m_{t\bar{t}}$, consistent with the excess seen in the one-dimensional $m_{t\bar{t}}$ distribution (Fig. 7.13) and in the related observables $m_{\ell\ell}$ and $m_{b\bar{b}\ell\ell}$ (Fig. 7.12). The excess is stronger for large values of c_{hel} as seen from the multi-dimensional binning, while no trend can be seen by eye regarding c_{han} .

2739 7.7 Interpretation of the excess

2740 7.7.1 Extraction of $t\bar{t}$ bound state effects

2741 The prefit excess visible in Fig. 7.14 is interpreted in terms of a pseudoscalar $t\bar{t}$
 2742 bound state by performing a signal+background fit with η_t as the signal, as defined
 2743 in Sec. 2.2.3. The POI in the fit is $\sigma(\eta_t)$, the cross section of the η_t model, which can
 2744 be understood as the difference between the data and the fixed-order perturbative
 2745 QCD (FO pQCD) background prediction. It is measured to be

$$\sigma(\eta_t) = 8.7 \pm 0.5(\text{stat}) \pm 1.0(\text{syst}) \text{ pb} = 8.7 \pm 1.1 \text{ pb}. \quad (7.16)$$

2746 The statistical and systematic component of the uncertainty are estimated as
 2747 described in Sec. 4.4. The significance of the result compared to a background-only
 2748 hypothesis, i.e. without a bound state, is more than five standard deviations.

2749 The result is of a similar order of magnitude as the prediction of 6.43 pb given in
 2750 Ref. [35], obtained by fitting the results of an NRQCD calculation from Ref. [31],
 2751 though this result is not one-to-one comparable since it considers only the range of
 2752 $m_{t\bar{t}} \in [338, 350] \text{ GeV}$.

2753 The postfit $m_{t\bar{t}} \times c_{\text{hel}} \times c_{\text{han}}$ distribution can be seen in Fig. 7.15. The data,
 2754 including the excess at low $m_{t\bar{t}}$, is described well by the η_t model combined with the
 2755 FO pQCD background. To illustrate this further, one-dimensional projections of the
 2756 $m_{t\bar{t}} \times c_{\text{hel}} \times c_{\text{han}}$ template into inclusive $m_{t\bar{t}}$, as well as into c_{hel} for both low and high
 2757 $m_{t\bar{t}}$, are shown in Fig. 7.16. One can clearly see that the data at the $t\bar{t}$ threshold
 2758 shows a stronger slope in data than in the FO pQCD prediction, consistent with the
 2759 η_t signal, while no such slope is seen at high $m_{t\bar{t}}$, i.e. in the $t\bar{t}$ continuum.

2760 7.7.2 Parity of the excess

2761 To investigate whether the observed excess is \mathcal{CP} -odd (pseudoscalar) or \mathcal{CP} -even
 2762 (scalar) in nature, a simultaneous fit is performed with both η_t and χ_t , as defined in
 2763 Sec. 2.2.3, as freely floating signals. These correspond to pure 1S_0 and 3P_0 $t\bar{t}$ states,
 2764 respectively, both localized at the $t\bar{t}$ threshold.

2765 The result is shown in Fig. 7.17 in the form of exclusion contours. Consistent
 2766 with the result of the η_t -only fit, a non-zero η_t contribution is preferred by the fit by
 2767 more than 5 standard deviations. By contrast, the measured χ_t cross section, which
 2768 can be seen as the 3P_0 component of the excess, is compatible with zero within
 2769 one standard deviation. Based on this, it can be said that the observed excess is
 2770 dominated by a pseudoscalar or 1S_0 spin state.

2771 7.7.3 Checks of the result

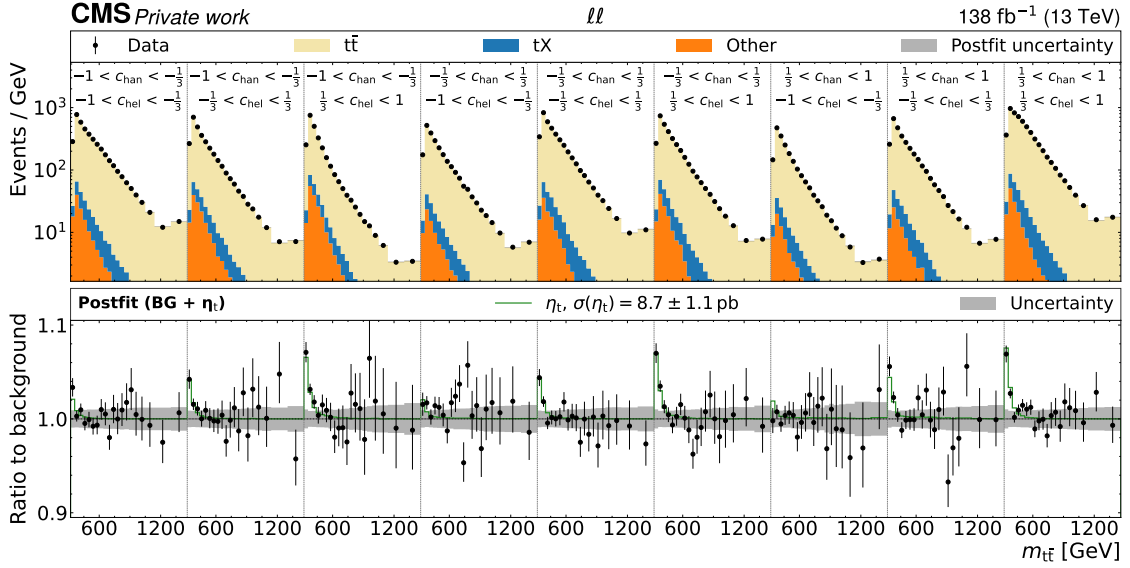


Figure 7.15: **Postfit distributions of $m_{t\bar{t}} \times c_{\text{hel}} \times c_{\text{han}}$ for the η_t fit.** The unrolled three-dimensional distribution in $m_{t\bar{t}}$, c_{hel} and c_{han} as after the fit to data with η_t as the signal, summed over all years and lepton flavors. The upper panel shows the sum of the background simulation (colored bars) and the observed data (black dots), while the lower panel shows the ratio of the data to the prediction with the postfit η_t signal overlaid.

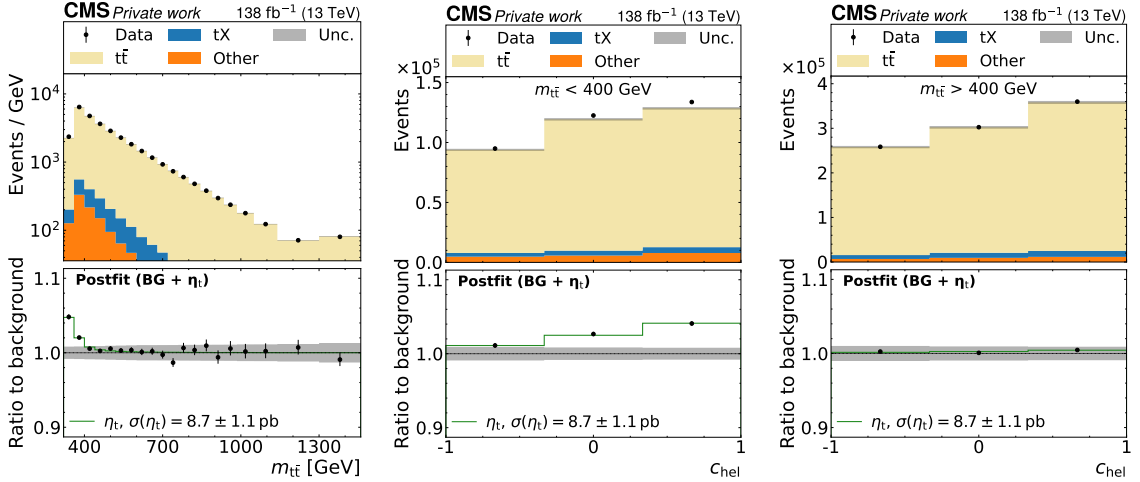


Figure 7.16: **Postfit distributions of $m_{t\bar{t}}$ and c_{hel} for the η_t fit.** One-dimensional distributions of inclusive $m_{t\bar{t}}$ (left), c_{hel} for $m_{t\bar{t}} < 400$ GeV (center), and c_{hel} for $m_{t\bar{t}} > 400$ GeV (right), projected from the $m_{t\bar{t}} \times c_{\text{hel}} \times c_{\text{han}}$ template in Fig. 7.15 with the same notations.

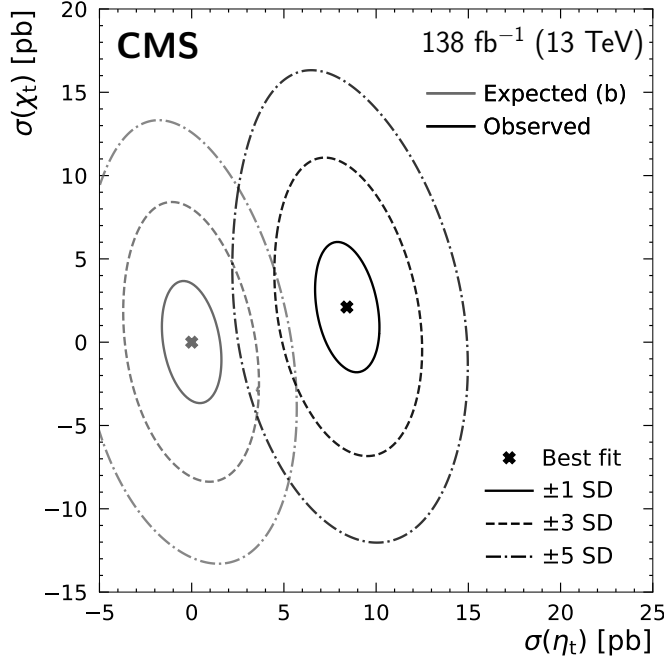


Figure 7.17: **Parity of the excess.** Expected and observed exclusion contours in a simultaneous fit of η_t (corresponding to 1S_0) and χ_t (corresponding to 3P_0). **TODO update colors**

2772 **Nuisance parameter pulls and impacts** In Fig. 7.18, nuisance parameter pulls,
2773 constraints and impacts for the η_t extraction fit are presented, following the definitions
2774 in Sec. 4.4. The most impactful nuisances are all related to the modeling of
2775 the $t\bar{t}$ background. In particular, the value of the top Yukawa coupling y_t in the EW
2776 corrections is the leading uncertainty. This is notably one of the few uncertainties
2777 which can lead to a steeper c_{hel} slope in the $t\bar{t}$ prediction and could thus to some
2778 degree be confused for η_t , as discussed in Sec. 7.3.2. Further important modeling
2779 uncertainties are the FSR scales in the $t\bar{t}$ parton shower as well as the top quark
2780 mass.

2781 On the other hand, experimental nuisances which influence mostly $m_{t\bar{t}}$ like the jet
2782 energy scales do not have a large impact on the POI. Regardless, no pulls larger than
2783 one prefit standard deviation are observed, indicating that the uncertainty model
2784 accommodates the data well.

2785 **Fit using $m_{b\bar{b}\ell\ell}$ instead of $m_{t\bar{t}}$** The three observables $m_{t\bar{t}}$, c_{hel} and c_{han} are
2786 all obtained from the kinematic reconstruction as described in Sec. 7.2.5. This
2787 procedure assumes, among others, that the top quarks are exactly on-shell with
2788 a fixed mass of 172.5 GeV. For η_t , which is located below the $t\bar{t}$ threshold, this
2789 assumption is clearly violated. Since the same kinematic reconstruction procedure

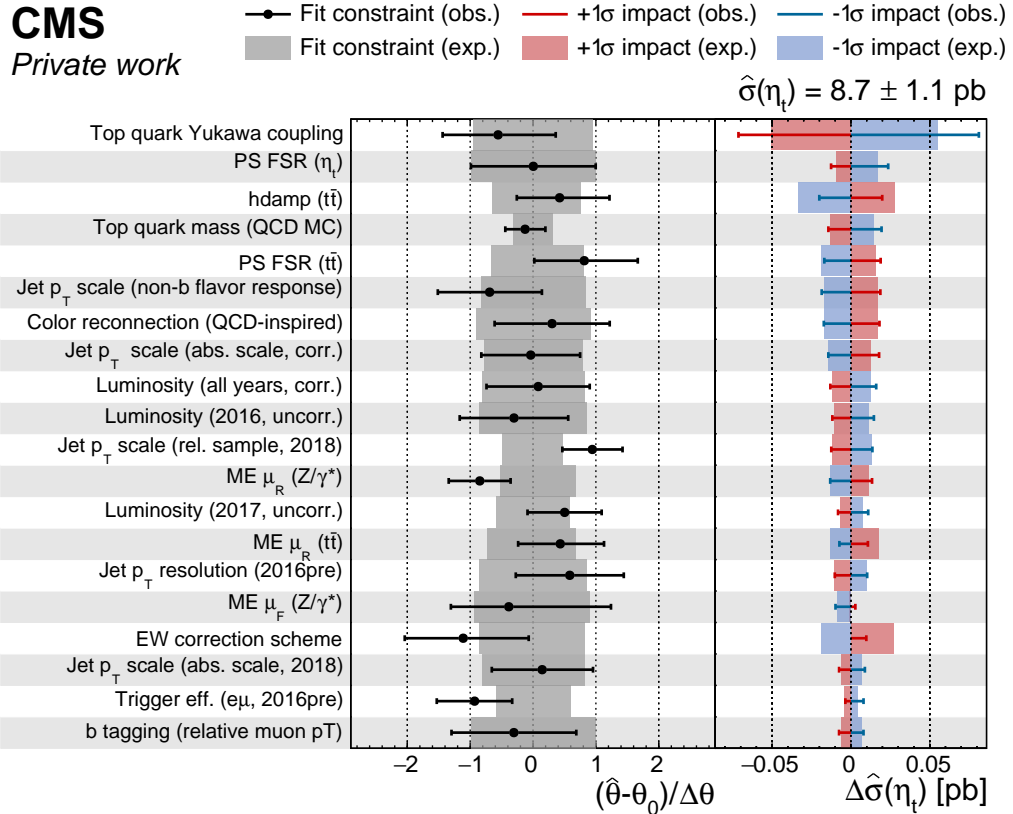


Figure 7.18: **Nuisance parameter pulls and impacts.** Expected and observed pulls, constraints, and impacts on the η_t cross section for the most impactful nuisance parameters in the η_t -only fit.

is applied to simulation and data, this is in principle not a problem as long as the virtuality of the top quarks is well described by simulation. However, since the modeling of η_t in particular is rather uncertain, it is still important to check whether this assumption in the kinematic reconstruction introduces any bias.

This is done by repeating the fit with the observable $m_{t\bar{t}}$ replaced by $m_{b\bar{b}\ell\ell}$ (as shown also in Fig. 7.12), thus removing kinematic information obtained via the reconstruction from the fit. The kinematic reconstruction is still performed, however, to obtain c_{hel} and c_{han} ².

The resulting $m_{b\bar{b}\ell\ell} \times c_{\text{hel}} \times c_{\text{han}}$ postfit distribution can be found in Figs. 7.19 and 7.20. It can be seen that the excess is still clearly present, though with a wider spread due to the coarser resolution of $m_{b\bar{b}\ell\ell}$ compared to $m_{t\bar{t}}$. An η_t cross section of $\sigma(\eta_t) = 7.5 \pm 1.8 \text{ pb}$ is extracted, which is in agreement with the nominal result

²It has separately been checked that the requirement for events to pass the kinematic reconstruction does not bias the result, either.

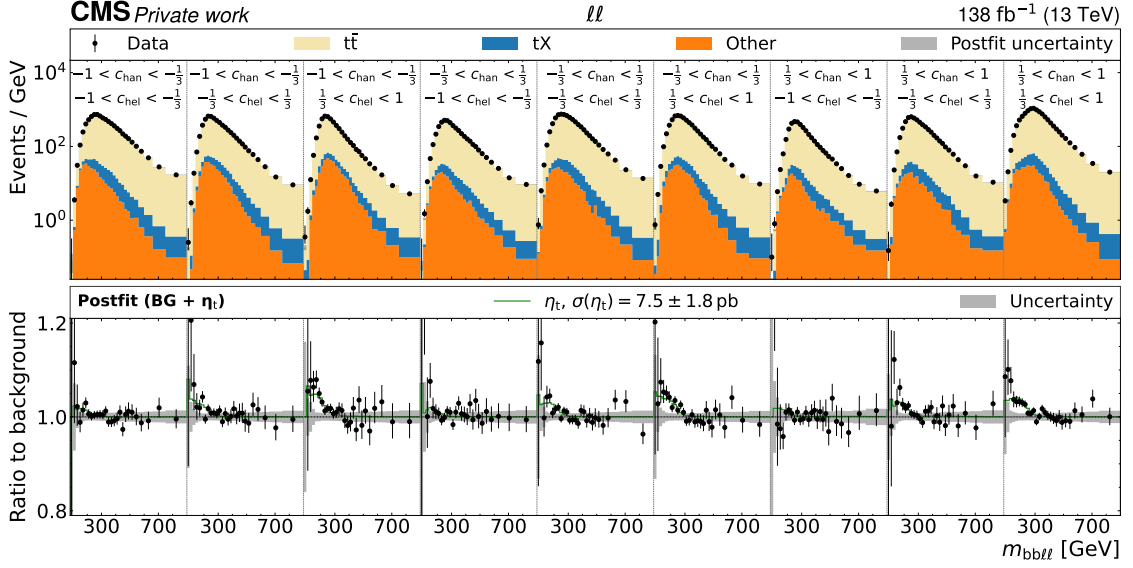


Figure 7.19: **Postfit distributions of $m_{bb\ell\ell} \times c_{hel} \times c_{chan}$ for the η_t fit.** The unrolled three-dimensional distribution in $m_{bb\ell\ell}$, c_{hel} and c_{chan} after the fit to data with η_t as the signal using $m_{bb\ell\ell}$ instead of $m_{t\bar{t}}$, summed over all years and lepton flavors. The first $m_{bb\ell\ell}$ bin in each $c_{hel} \times c_{chan}$ slice is an underflow bin containing events with $m_{bb\ell\ell} < 180$ GeV. Otherwise, notations are as in Fig. 7.15.

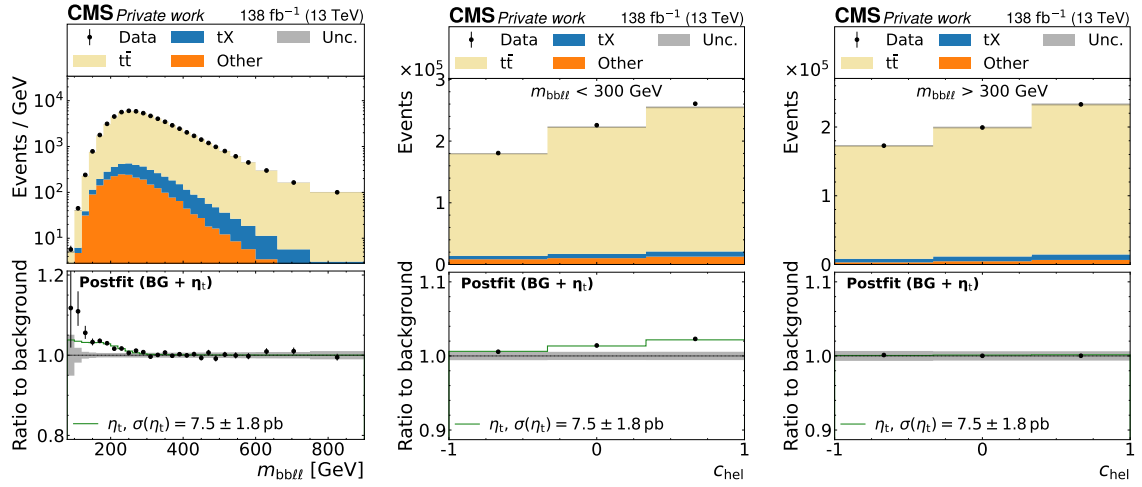


Figure 7.20: **Postfit distributions of $m_{bb\ell\ell}$ and c_{hel} for the η_t fit.** One-dimensional distributions of inclusive $m_{bb\ell\ell}$ (left), c_{hel} for $m_{bb\ell\ell} < 300$ GeV (center), and c_{hel} for $m_{bb\ell\ell} > 300$ GeV (right), projected from a 3D template of $m_{bb\ell\ell} \times c_{hel} \times c_{chan}$. The first $m_{bb\ell\ell}$ bin in the left figure is an underflow bin containing events with $m_{bb\ell\ell} < 180$ GeV. Otherwise, notations are as in Fig. 7.15.

2802 within one standard deviation.

2803 **Alternate generator setups** The influence of the choice of generator setup for
 2804 the $t\bar{t}$ prediction is further quantified by repeating the η_t extraction fit with alternate
 2805 setups. Besides the nominal setup from POWHEG hvq matched to PYTHIA, the three
 2806 setups introduced in Sec. 7.5.4 are considered: POWHEG hvq matched to HERWIG,
 2807 MG5_AMC@NLO matched to PYTHIA with the FxFx scheme, and bb41 matched
 2808 to PYTHIA.

Generator setup	$\sigma(\eta_t)$ [pb]
POWHEG hvq + PYTHIA (nominal)	8.7 ± 1.1
POWHEG hvq + HERWIG	8.6 ± 1.1
MG5_AMC@NLO FxFx + PYTHIA	9.8 ± 1.3
POWHEG bb41 + PYTHIA	6.6 ± 1.4

Table 7.5: **Results for alternate generators.** Results for $\sigma(\eta_t)$ obtained with different simulated event samples for the FO pQCD $t\bar{t}+tW$ prediction.

2809 The results can be found in Tab. 7.5. The results from PYTHIA and HERWIG are
 2810 fully in agreement with each other, while MG5_AMC@NLO results in a higher η_t
 2811 cross section by about one standard deviation, and bb41 results in a lower η_t cross
 2812 section by about ~ 1.5 standard deviations.

2813 As an additional check, the differences between the predictions from POWHEG hvq
 2814 + HERWIG and POWHEG hvq + PYTHIA as well as between bb41 and $t\bar{t} + tW$ are
 2815 included in the fit as additional nuisance parameters. In both cases, the POWHEG
 2816 hvq + PYTHIA prediction is considered the nominal, and the alternate prediction
 2817 is considered the $+1\sigma$ template. The -1σ template is constructed by symmetrizing
 2818 the relative difference around the nominal, and intermediate values are obtained by
 2819 interpolation as usual.

2820 The resulting η_t cross section with these nuisance parameters included is $\sigma(\eta_t) =$
 2821 $8.8^{+1.2}_{-1.4}$ pb³. This figure is fully compatible with the nominal result with an asymmet-
 2822 rically increased uncertainty. The reason for the increase can be seen in Fig. 7.21,
 2823 showing the nuisance parameter pulls and impacts: The nuisance parameter encod-
 2824 ing the difference between bb41 and $t\bar{t} + tW$ represents the leading impact on the
 2825 η_t cross section and is asymmetric. This is understandable from the steeper slope
 2826 in c_{hel} for bb41 as seen in Fig. 7.9, which is similar to the η_t signal, and is also in
 2827 agreement with the reduced η_t cross section for a bb41 background prediction shown
 2828 in Tab. 7.5. It is furthermore significantly constrained towards zero, i.e. towards the
 2829 default $t\bar{t} + tW$ prediction, implying that the data prefers the NWA approach over
 2830 the *a priori* superior bb41 prediction. The reason for this is not readily apparent.

³This figure is considered the nominal result in Ref. [9]

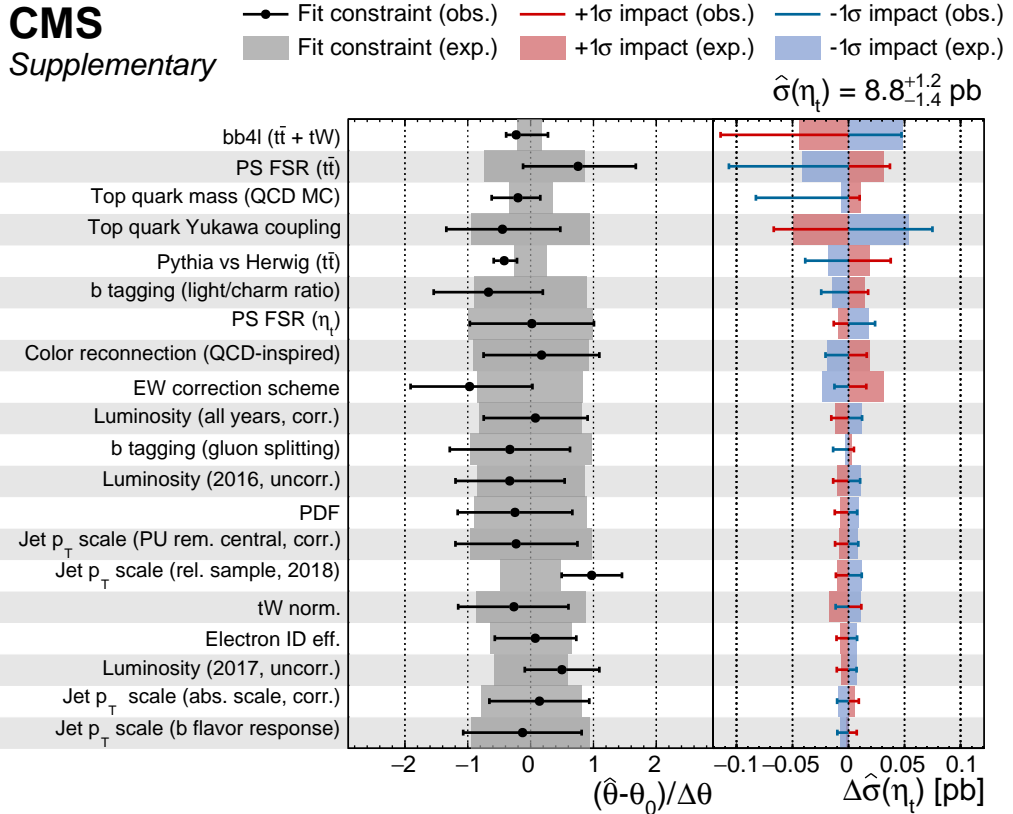


Figure 7.21: **Nuisance parameter pulls and impacts including alternate generators.** Expected and observed pulls, constraints, and impacts on the η_t cross section for the most impactful nuisance parameters in the η_t -only fit where the differences between the predictions from POWHEG hvq + HERWIG and bb4l + PYTHIA compared to POWHEG hvq + PYTHIA are included as additional nuisance parameters.

2831 One possible cause could be the fact that the NLO EW and NNLO QCD correc-
 2832 tions are applied to bb4l in a necessarily ad-hoc manner, and might thus spoil the
 2833 agreement with the data (cf. Sec. 7.5.4). However, in the scope of this work, this
 2834 remains speculation.

2835 On the other hand, the nuisance parameter encoding the difference of PYTHIA
 2836 and HERWIG is less impactful, consistent with the results for HERWIG in Tab. 7.5,
 2837 and similarly strongly constrained. This is likely because the difference between
 2838 PYTHIA and HERWIG can be distinguished from η_t based on the combination of $m_{t\bar{t}}$
 2839 and c_{hel} information, as expanded upon in Sec. 7.5.4.

2840 7.7.4 Interpretation in terms of A and H

2841 While a $t\bar{t}$ bound state is the conceptually simplest explanation of the enhancement
2842 at the $t\bar{t}$ threshold in the sense that it is predicted in the SM and does not invoke any
2843 further (BSM) degrees of freedom, it is also possible to perform an interpretation
2844 in terms of the generic spin-0 bosons A and H as introduced in Sec. 2.3.1. For this
2845 purpose, fits allowing the presence of both A and H at the same time are performed.
2846 The two independent POIs are the A/H-top coupling modifiers $g_{At\bar{t}}$ and $g_{Ht\bar{t}}$, and
2847 the interference with the SM is fully taken into account through a parametrization in
2848 terms of $g_{A/Ht\bar{t}}^2$ and $g_{A/Ht\bar{t}}^4$ (cf. Eq. (2.19)), thus allowing negative A/H contributions
2849 with respect to the SM.

2850 A scan is performed over all pairs of considered A/H masses and widths (see
2851 Sec. 7.2.1), and the pair with the largest difference in logarithmic likelihood $\Delta \ln L$
2852 is identified as the best-fit point. This results in $m_A = 365$ GeV, $\Gamma_A/m_A = 2\%$ for
2853 A and $m_H = 925$ GeV, $\Gamma_H/m_H = 3\%$ for H. It should be noted here that 365 GeV is
2854 the lowest mass point considered in the available signals for A and H, while η_t and
2855 χ_t are located at a lower value of 343 GeV. It is possible that considering a lower
2856 value of m_A would lead to an even better fit; however, close to the $t\bar{t}$ threshold,
2857 modeling the interference with the SM might be difficult due to large corrections at
2858 higher orders in QCD [188, 189].

2859 Figure 7.22 shows the postfit $m_{t\bar{t}} \times c_{hel} \times c_{han}$ distribution, and Fig. 7.23 shows
2860 the allowed region for the two couplings $g_{At\bar{t}}$ and $g_{Ht\bar{t}}$ as obtained from a likelihood
2861 scan. From the latter, the best-fit values and total ranges for the coupling modifiers
2862 are found to be

$$g_{At\bar{t}} = 0.79^{+0.04}_{-0.05} \quad \text{and} \quad g_{Ht\bar{t}} = 1.47^{+0.17}_{-0.30}. \quad (7.17)$$

2863 The same excess close to the $t\bar{t}$ threshold already seen in Sec. 7.7.1 manifests as
2864 of a non-zero value of $g_{At\bar{t}}$, which Fig. 7.23 shows is preferred by more than five
2865 standard deviations, similar as for the interpretation in terms of η_t . In addition,
2866 there is also a preference for a non-zero value of $g_{Ht\bar{t}}$, though this is significant only
2867 at about 2 standard deviations and could thus be a simple statistical fluctuation.
2868 It should be noted that both of these values are local significances, i.e. they do not
2869 account for the look-elsewhere effect. The source of this preference is again evident
2870 from Fig. 7.22: it is due to a mild, broad excess in events compared to the prediction
2871 around $m_{t\bar{t}} \approx 900$ GeV, which is more pronounced in the low c_{han} bins compared to
2872 the others as would be expected for a scalar particle H.

2873 It is important to stress that these results do not constitute any observation of a
2874 new BSM particle. Given the experimental resolution in $m_{t\bar{t}}$, as well as the signal
2875 mass points available, the $t\bar{t}$ bound state η_t and a BSM pseudoscalar A cannot be
2876 conclusively distinguished.

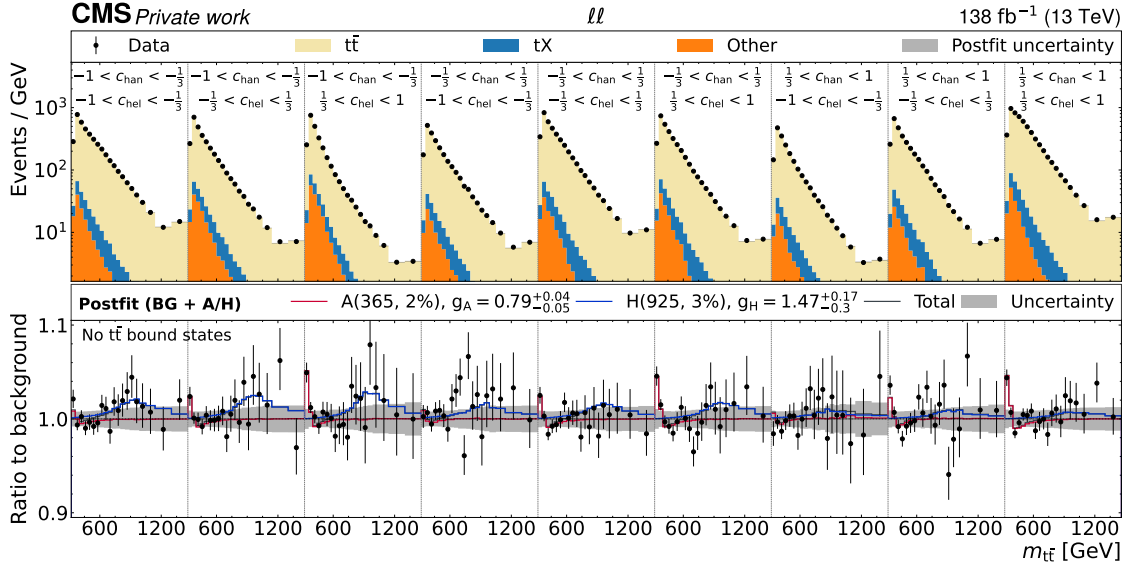


Figure 7.22: **Postfit distributions of $m_{t\bar{t}} \times c_{\text{hel}} \times c_{\text{han}}$ for the A+H fit.** The unrolled three-dimensional distribution in $m_{t\bar{t}}$, c_{hel} and c_{han} as after the fit to data with A and H as signals, summed over all years and lepton flavors. The A/H signals correspond to the best-fit masses and widths of $m_A = 365 \text{ GeV}$, $\Gamma_A/m_A = 2\%$ for A and $m_H = 925 \text{ GeV}$, $\Gamma_H/m_H = 3\%$ for H. The upper panel shows the sum of the background simulation (colored bars) and the observed data (black dots), while the lower panel shows the ratio of the data to the prediction with the postfit A and H signals, as well as their sum, overlaid.

2877 7.8 Limits on A/H bosons

Having discussed the excess seen at the $t\bar{t}$ threshold and its possible interpretations, in this section exclusion limits on A/H bosons in the full considered mass range are presented. This is done for two different scenarios: In the first scenario, denoted “A/H only”, the SM $t\bar{t}$ background is described by the FO pQCD prediction from POWHEG + PYTHIA reweighted to NLO EW and NNLO QCD, same as for the η_t extraction in Sec. 7.7.1 and for the A+H fit in Sec. 7.7.4. The observed excess is thus expected to manifest in the limits in the form of a weaker observed than expected limit for low A/H masses.

In the second scenario, denoted “A/H + η_t ”, the observed excess is assumed to originate solely from a $t\bar{t}$ bound state, which is further assumed to be well described by the η_t model. Under this assumption, the η_t contribution is added to the $t\bar{t}$ background prediction, with a free-floating normalization as an additional nuisance parameter. A and/or H contributions are then considered as signals on top of this background. It should be stressed that, while Fig. 7.15 shows good agreement of the

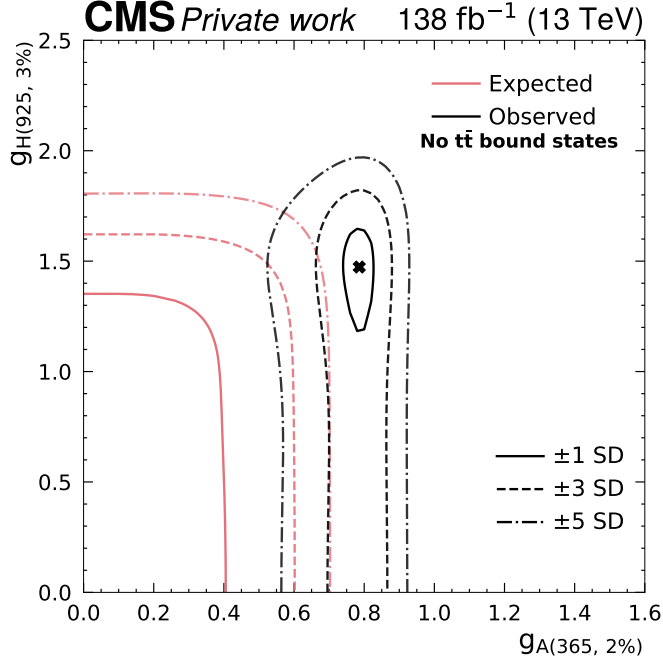


Figure 7.23: **Allowed coupling region in the A+H fit.** The two-dimensional allowed region for the coupling modifiers $g_{A/\bar{t}t}$ and $g_{H/\bar{t}t}$ in the A+H fit, for the best-fit A/H masses and widths of $m_A = 365 \text{ GeV}$, $\Gamma_A/m_A = 2\%$ for A and $m_H = 925 \text{ GeV}$, $\Gamma_H/m_H = 3\%$ for H, obtained through a scan of the profiled likelihood. The observed region is shown in black, while the SM expectation is shown in pink.

²⁸⁹² η_t description with the data, the true cause of the excess can not be fully determined
²⁸⁹³ with the available $m_{t\bar{t}}$ resolution. Thus, all limits shown here should be treated with
²⁸⁹⁴ caution for low values of the A/H mass.

²⁸⁹⁵ In both scenarios, the limits are calculated with the CL_s prescription as introduced
²⁸⁹⁶ in Sec. 4.4. However, a complication is presented by the non-linearity of the A/H
²⁸⁹⁷ signal as a function of $g_{A/\bar{t}t}$, due to which the distribution of the test statistic is
²⁸⁹⁸ not necessarily χ^2 -distributed, and thus the p -values p_{s+b} and p_b cannot be easily
²⁸⁹⁹ computed. To avoid having to perform computationally expensive toy experiments,
²⁹⁰⁰ a *raster scan* method is used in the same way as in Ref. [16]. For a given A/H
²⁹⁰¹ mass and width point, the coupling modifier $g_{A/\bar{t}t}$ is scanned in the range 0–5.
²⁹⁰² For each value of $g_{A/\bar{t}t}$, the total signal contribution is computed as the sum of
²⁹⁰³ the resonant signal, scaling with $g_{A/\bar{t}t}^4$, and the SM-signal interference, scaling with
²⁹⁰⁴ $g_{A/\bar{t}t}^2$. An auxilliary linear signal strength μ is then introduced, so that the total
²⁹⁰⁵ signal contribution becomes

$$s(\mu) = \mu \left(g_{A/\bar{t}t}^4 s_{\text{res}} + g_{A/\bar{t}t}^2 s_{\text{int}} \right) \quad (7.18)$$

where s_{res} and s_{int} are the resonance and interference contributions, respectively, and $g_{A/\text{H}t\bar{t}}$ is held fixed. $\mu = 1$ corresponds to the probed A/H signal, while $\mu = 0$ corresponds to the SM. Intermediate values of μ are in principle unphysical since they do not correspond to any value of $g_{A/\text{H}t\bar{t}}$.

Since the A/H signal now scales linearly with μ , the usual asymptotic approximation can be used to obtain the CL_s value for $\mu = 1$. It has been shown as a part of Ref. [16] that the distribution of the test statistic obtained in this way approximates well the true test statistic for $g_{A/\text{H}t\bar{t}}$ as evaluated using toy experiments. This procedure is repeated for all values of $g_{A/\text{H}t\bar{t}}$, and a value of $g_{A/\text{H}t\bar{t}}$ is, as usual, excluded at 95% confidence level when the CL_s value drops below 0.05.

The resulting observed and expected limits for all considered A and H masses and six representative width choices are shown in Figs. 7.24 and 7.25 for the “A/H only” scenario and in Figs. 7.26 and 7.27 for the “A/H + η_t ” scenario. In the “A/H only” scenario, the excess at the $t\bar{t}$ threshold is visible at low A/H masses as expected. It is stronger for the pseudoscalar A than for the scalar H, consistent with the results in Sec. 7.7.2. In the “A/H + η_t ” scenario, the excess is fully absorbed by the η_t contribution, and the observed and expected limits at low A/H masses agree. It is notable here that the expected limits change only little between the scenarios even though, in the “A/H + η_t ” scenario, the cross section of the η_t contribution is freely floating in the fit. **TODO decide on whether I want to elaborate on this, would need a plot of the signal templates**

Furthermore, the mild excess for H at high masses as seen in Fig. 7.23 is reproduced in the limits on $g_{\text{H}t\bar{t}}$ in both scenarios in the approximate range of $900 < m_H < 1000 \text{ GeV}$.

7.9 Combination with the ℓ +jets channels

So far, all results in this section have covered only the dilepton decay channel of $t\bar{t}$, which was analyzed as part of this thesis. In Ref. [8], the results on A/H bosons are combined with a separate analysis of the ℓ +jets decay channel. The combination (but not the ℓ +jets analysis) was also performed as part of this thesis, and is presented in this chapter. The ℓ +jets analysis strategy is roughly outlined in the following, for a more complete description, see Ref. [8].

7.9.1 Analysis strategy in the ℓ +jets channel

In the ℓ +jets channel, events with exactly one lepton and at least three jets are selected, of which at least two need to be b tagged. In addition to the criteria outlined in Sec. 7.2.2, both the lepton and the jets are required to fulfill $p_T > 30 \text{ GeV}$ to account for the higher single-lepton trigger thresholds. Furthermore, the cut-based identification criteria for electrons, as described in Ref. [95], are applied instead

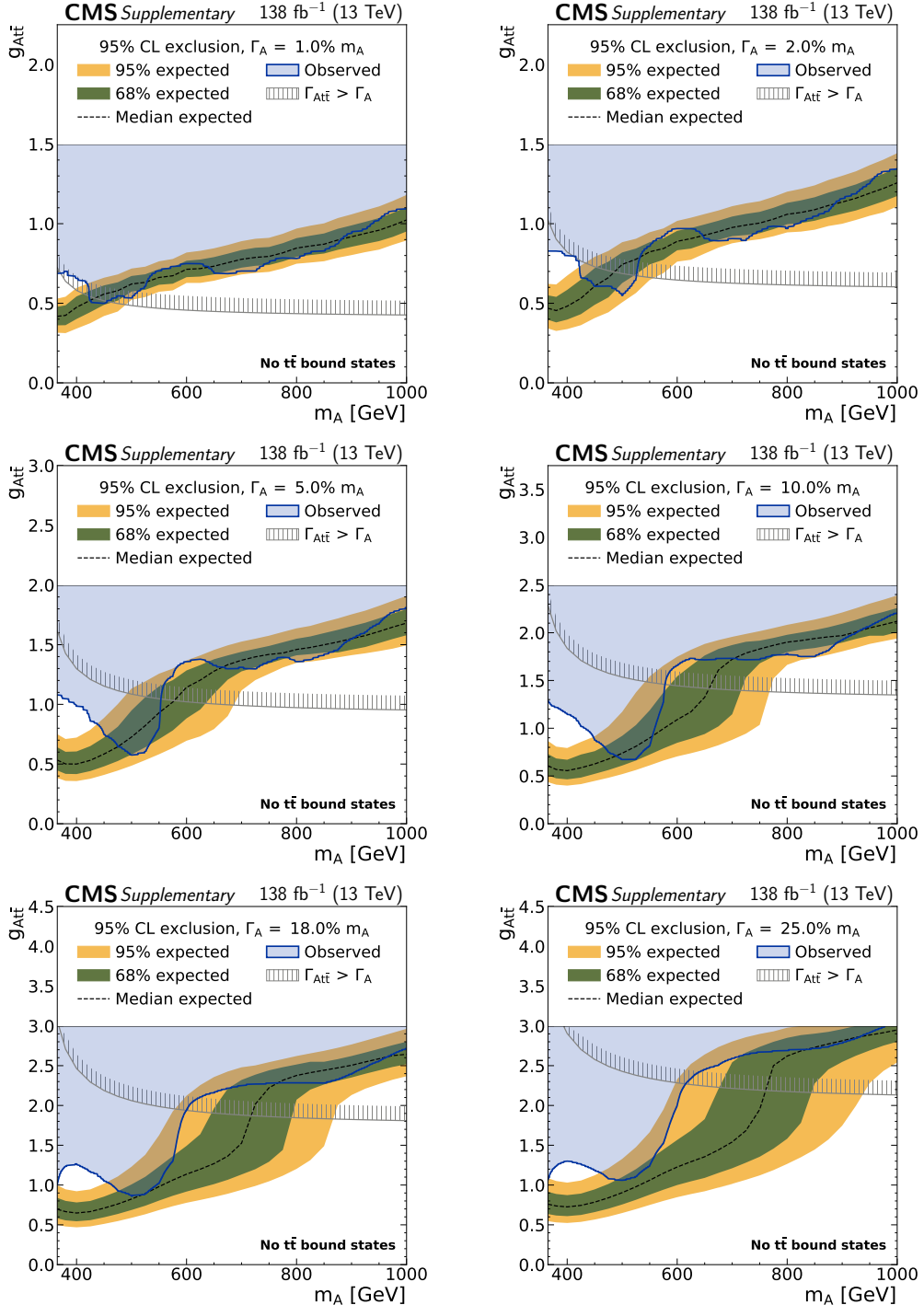


Figure 7.24: **Exclusion limits on $g_{At\bar{t}}$ in the “A only” scenario** in the dilepton channels as a function of the mass of the A boson for relative widths of 1, 2, 5, 10, 18, and 25% (from upper left to lower right). The observed limits are indicated by the blue shaded area, and the inner green band and the outer yellow band indicate the regions containing 68 and 95%, respectively, of the distribution of limits expected under the background-only hypothesis. The unphysical region of phase space in which the partial width $\Gamma_{A \rightarrow t\bar{t}}$ becomes larger than the total width of A is indicated by the hatched line.

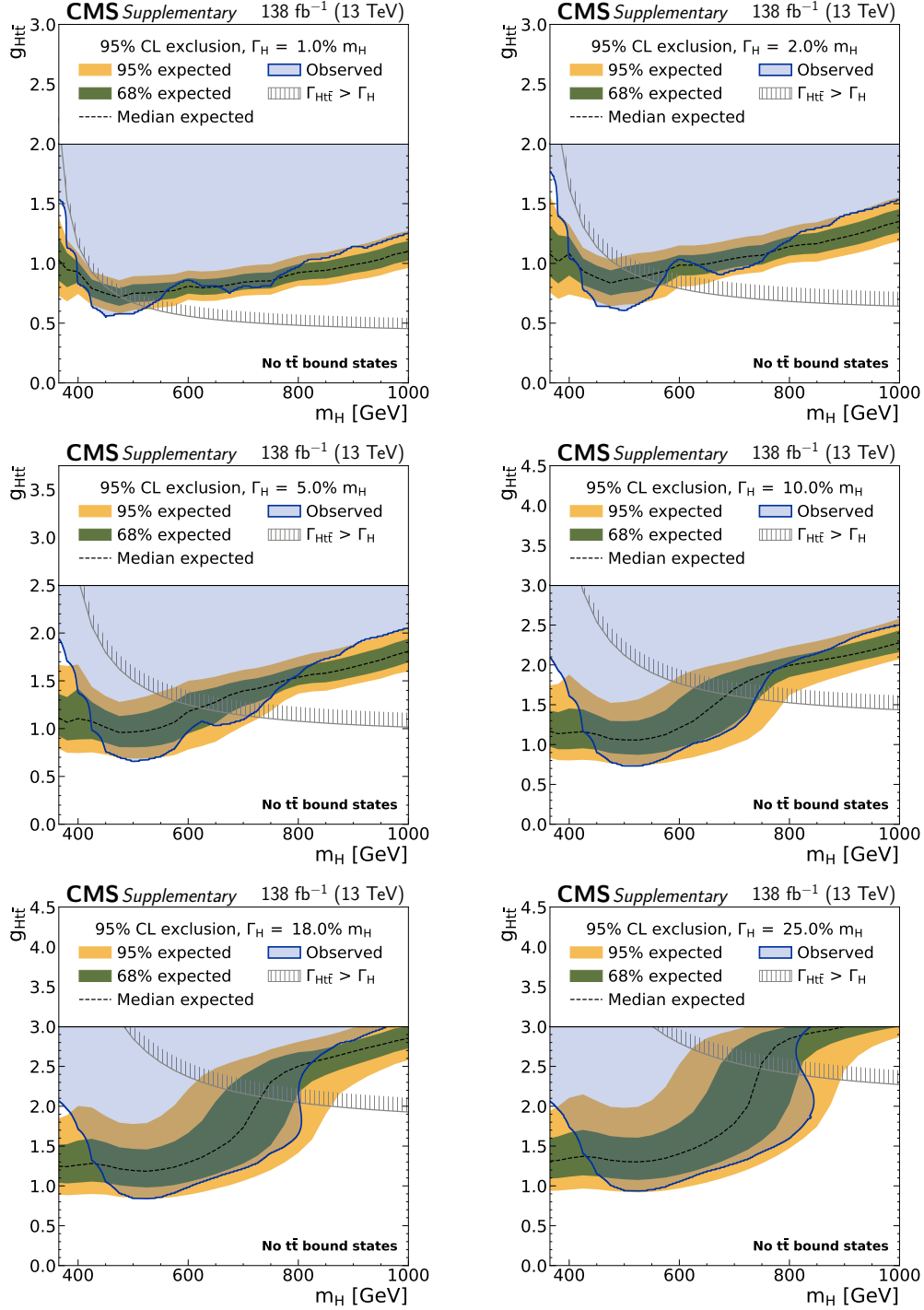


Figure 7.25: **Exclusion limits on g_{Htt} in the “H only” scenario** in the dilepton channels as a function of the mass of the H boson. Notations are equivalent to Fig. 7.24.

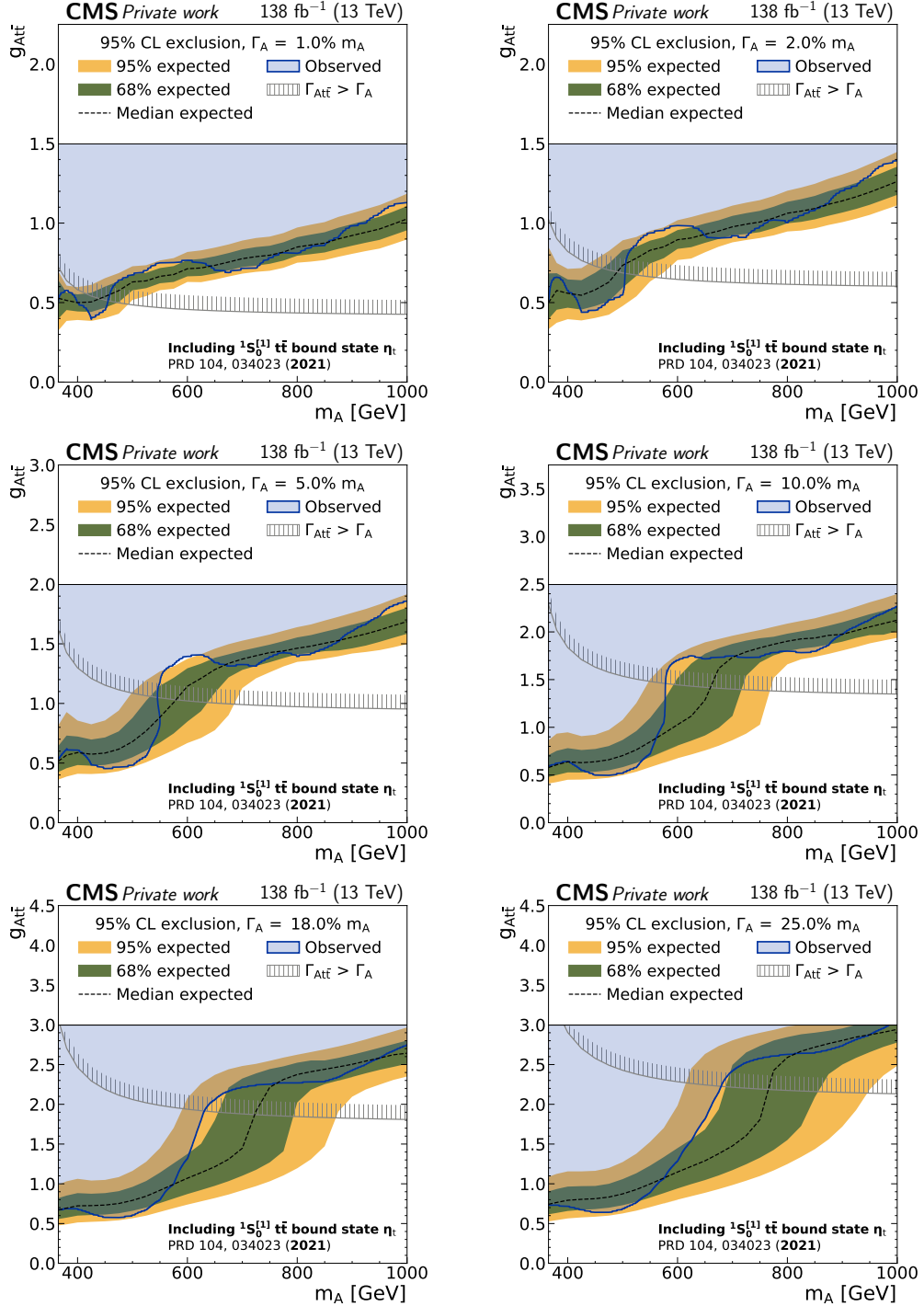


Figure 7.26: **Exclusion limits on $g_{A t\bar{t}}$ in the “A + η_t ” scenario** in the dilepton channels as a function of the mass of the A boson. Notations are equivalent to Fig. 7.24.

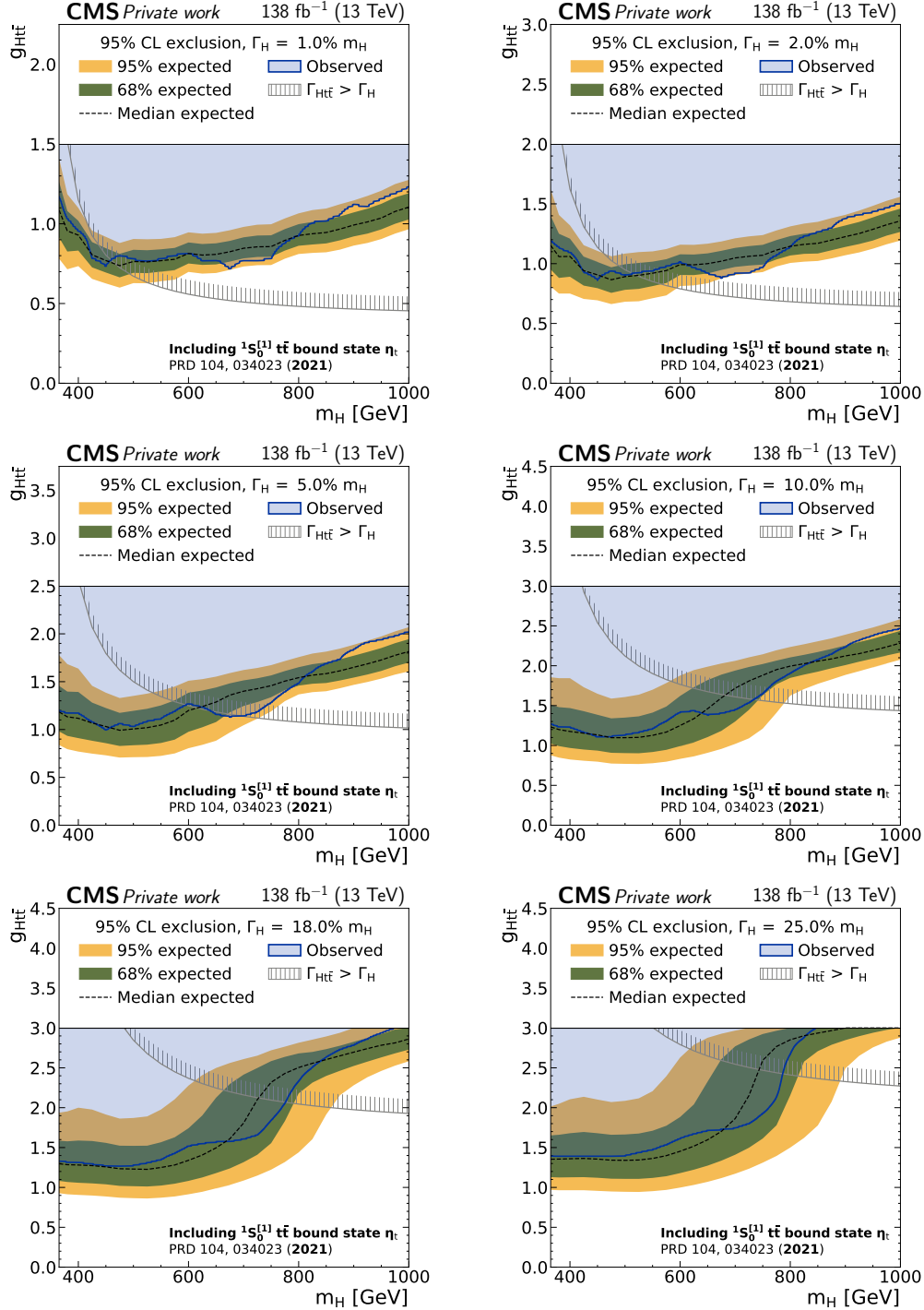


Figure 7.27: **Exclusion limits on $g_{Ht\bar{t}}$ in the “ $H + \eta_t$ ” scenario** in the dilepton channels as a function of the mass of the H boson. Notations are equivalent to Fig. 7.24.

of MVA-based criteria. Similar as in the dilepton channel, the events are categorised by the flavor of the lepton into the e+jets and μ +jets channels.

The algorithm described in Ref. [190] is used to reconstruct the neutrino from the leptonic top decay. It enforces mass constraints on the W boson and leptonically decaying top quark and then minimizes the distance $D_\nu = |p_T^\nu - p_T^{\text{miss}}|$ between the neutrino p_T and the missing transverse momentum. In events with four or more jets, the same distance D_ν is then also used to assign the jets to the b and \bar{b} candidates as well as to the decay products of the hadronically decaying W boson. From this, the $t\bar{t}$ system can then be reconstructed. In events with exactly three jets, where information has been lost due to either an out-of-acceptance jet or the merger of two jets into one, additional steps have to be taken. The procedure described in Ref. [191] is applied to these events, which involves applying an energy correction factor to the four-momentum of the hadronically decaying top quark, depending on its reconstructed mass. Since the resolution of this procedure is necessarily worse than for events where all jets are available, events with three jets and four or more jets are treated as separate categories in the fit.

A two-dimensional template is constructed from the reconstructed value of $m_{t\bar{t}}$ as well as $|\cos \theta_\ell^*|$, where θ_ℓ^* is the scattering angle of the leptonically decaying top quark with respect to the direction of flight of the $t\bar{t}$ system in the laboratory frame. This variable is sensitive to the spin of a possible mediator in $t\bar{t}$ production: For spin-0 mediators like A/H, the top quarks are emitted isotropically in the $t\bar{t}$ rest frame, leading to a flat distribution of $|\cos \theta_\ell^*|$, while in the SM $|\cos \theta_\ell^*|$ peaks at high values. However, it is not sensitive to the \mathcal{CP} structure of the mediator, in contrast to c_{hel} and c_{han} . Furthermore, the SM prediction changes as a function of $m_{t\bar{t}}$; close to the $t\bar{t}$ threshold, the difference to a flat spectrum is rather small, while for high $m_{t\bar{t}}$ the difference is large due to the impact of the $q\bar{q}$ initial state.

The $t\bar{t}$ and tW background predictions as well as the A/H signals are estimated using the same MC simulation as in the dilepton channels. Additionally, there is a significant background contribution from QCD multijet production with a fake or non-prompt lepton as well as EW processes such as W+jets production. These are difficult to model using MC, and are instead estimated together by a data-driven approach (cf. Sec. 5.3.2). A sideband in which the b tagging requirement on the jets is inverted is used for this purpose; details can be found in Ref. [8].

The dilepton and ℓ +jets channels are directly combined by performing a simultaneous likelihood fit to all categories. Systematic uncertainties related to modeling of the $t\bar{t}$ and tW backgrounds are treated as fully correlated, while experimental uncertainties as well as uncertainties of the other minor backgrounds can be correlated or uncorrelated as appropriate. Again, both the “A/H only” and “A/H + η_t ” scenarios are considered. For the latter, the ℓ +jets analysis uses a slightly different η_t model, in which the width of the bound state is set to $\Gamma(\eta_t) = 7 \text{ GeV}$ and a cut on the invariant mass $m_{WWb\bar{b}}$ is applied, as described in Sec. 2.2.3. For the sake of consistency, the same model is also used in the dilepton channels when performing

2985 the combination only. The resulting impact on the limits from the choice of η_t model
2986 is expected to be small.

2987 7.9.2 A/H limits

2988 The resulting observed and expected limits for the combination of both channels
2989 are found in Figs. 7.28 to 7.31 for both scenarios. It can be seen that the large
2990 excess for low A/H masses is still present in the channel combination in the “A/H
2991 only” scenario, and is again stronger for the pseudoscalar A. The mild excess for
2992 the scalar H at $m_H \approx 925$ GeV, on the other hand, is not confirmed in the channel
2993 combination.

2994 To assess the impact of the different channels, the expected limits for the dilepton
2995 and ℓ +jets channels alone are also shown in red and orange, respectively. For most
2996 of the phase space, the ℓ +jets channel leads to stronger limits than the dilepton
2997 channel, which is likely mostly due to the higher branching ratio and thus higher
2998 available statistics as well as the better $m_{t\bar{t}}$ resolution in the ℓ +jets channel especially
2999 at high $m_{t\bar{t}}$. The difference is large at high A and H masses, where the contribution
3000 from the dilepton channels is rather small, while the dilepton channel becomes much
3001 more important for low masses, i.e. close to the $t\bar{t}$ threshold. This could be because
3002 of the lack of sensitivity of $|\cos \theta_\ell^*|$ close to the $t\bar{t}$ threshold, while c_{hel} and c_{han} do
3003 not suffer from such a problem. For H at low masses in particular, the dilepton
3004 channel in fact gives stronger limits than ℓ +jets due to the sensitivity of c_{han} to
3005 scalar mediators.

3006 7.9.3 Simultaneous A+H exclusion contours

3007 In many possible BSM scenarios, multiple additional spin-0 states are expected at
3008 the same time, such as A and H in e.g. the 2HDM (cf. Sec. 2.3.2). Often, the
3009 masses of these scalars are close together since they originate from new physics at
3010 the same energy scale, in which case their signatures would not easily factorize. It
3011 is thus useful for future interpretations of the results to show exclusion contours not
3012 only for either A or H, but for the simultaneous presence of both at the same time.

3013 To do so, simultaneous fits are performed with both A and H as freely floating
3014 signals as in Sec. 7.7.4. Frequentist exclusion contours are set with the Feldman–
3015 Cousins prescription [192, 193], in which the test statistic is numerically evaluated
3016 using toy experiments at each point in the $g_{A\bar{t}\bar{t}}\text{--}g_{H\bar{t}\bar{t}}$ plane. This procedure is
3017 fully correct in the Frequentist sense and does not rely on approximations of the
3018 test statistic, which are not guaranteed to hold for two non-linear signals, but is
3019 computationally expensive.

3020 Due to this, combined with the large four-dimensional phase space of possible
3021 signals, only a few example mass and width points are shown in this work, and only
3022 for the dilepton and ℓ +jets combination in the “A/H + η_t ” scenario. They can be

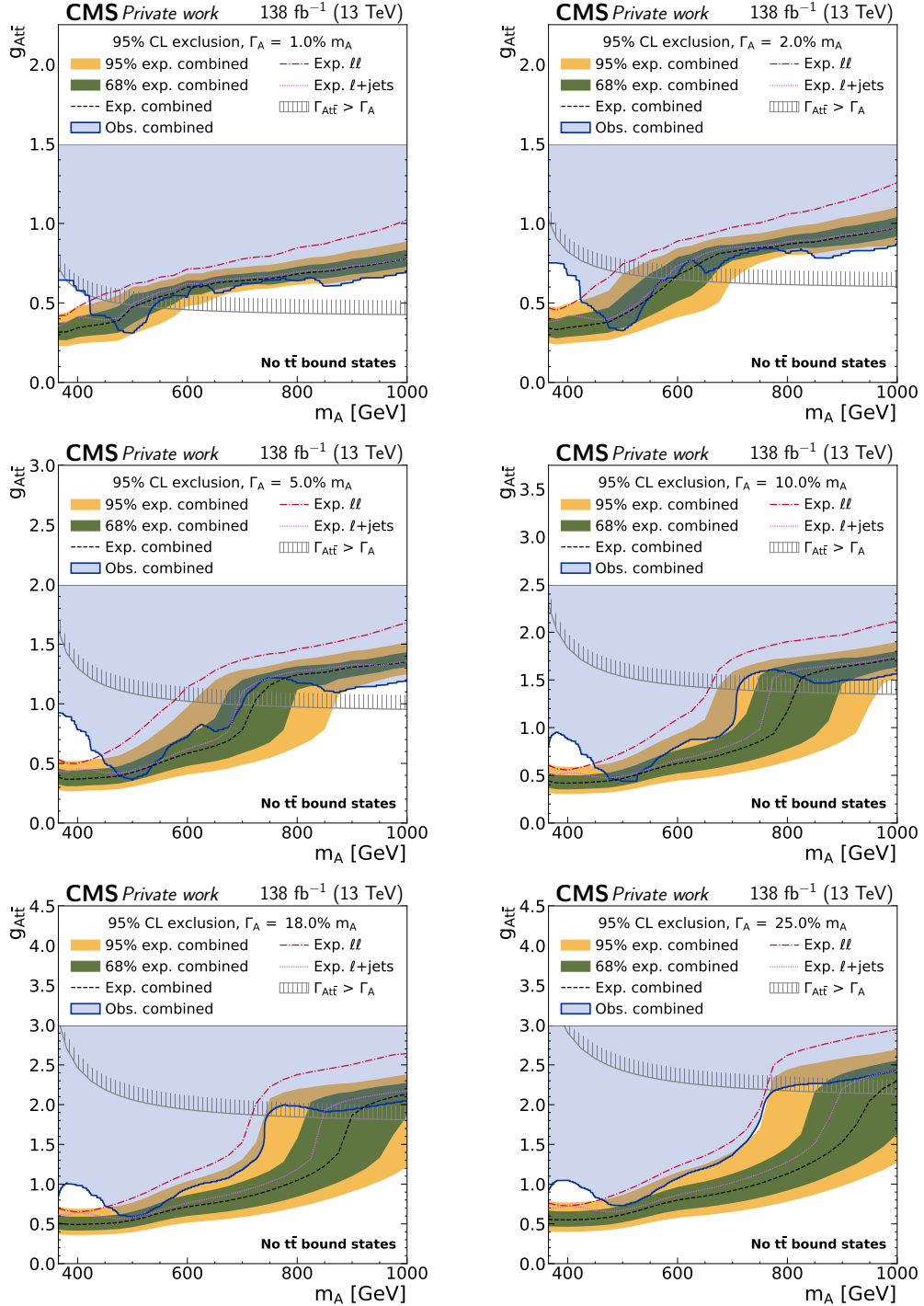


Figure 7.28: **Combined exclusion limits on $g_{At\bar{t}}$ in the “A only” scenario** in the dilepton and $\ell+\text{jets}$ channels as a function of the mass of the A boson. The expected limits in the dilepton and $\ell+\text{jets}$ channels alone are shown as the red and purple lines for comparison. Otherwise, notations are equivalent to Fig. 7.24

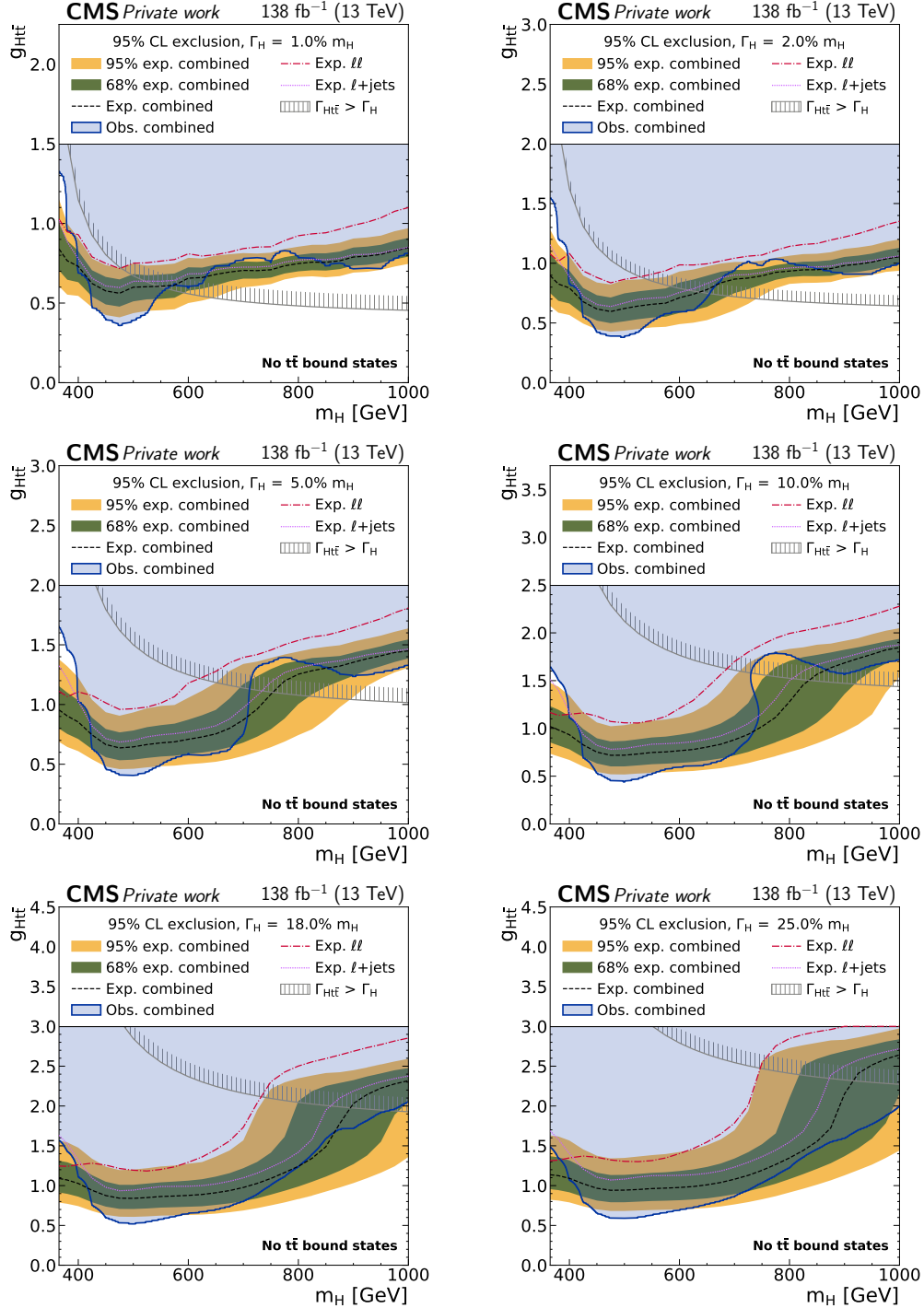


Figure 7.29: Combined exclusion limits on g_{Htt} in the “H only” scenario in the dilepton and ℓ +jets channels as a function of the mass of the H boson. Notations are equivalent to Fig. 7.28.

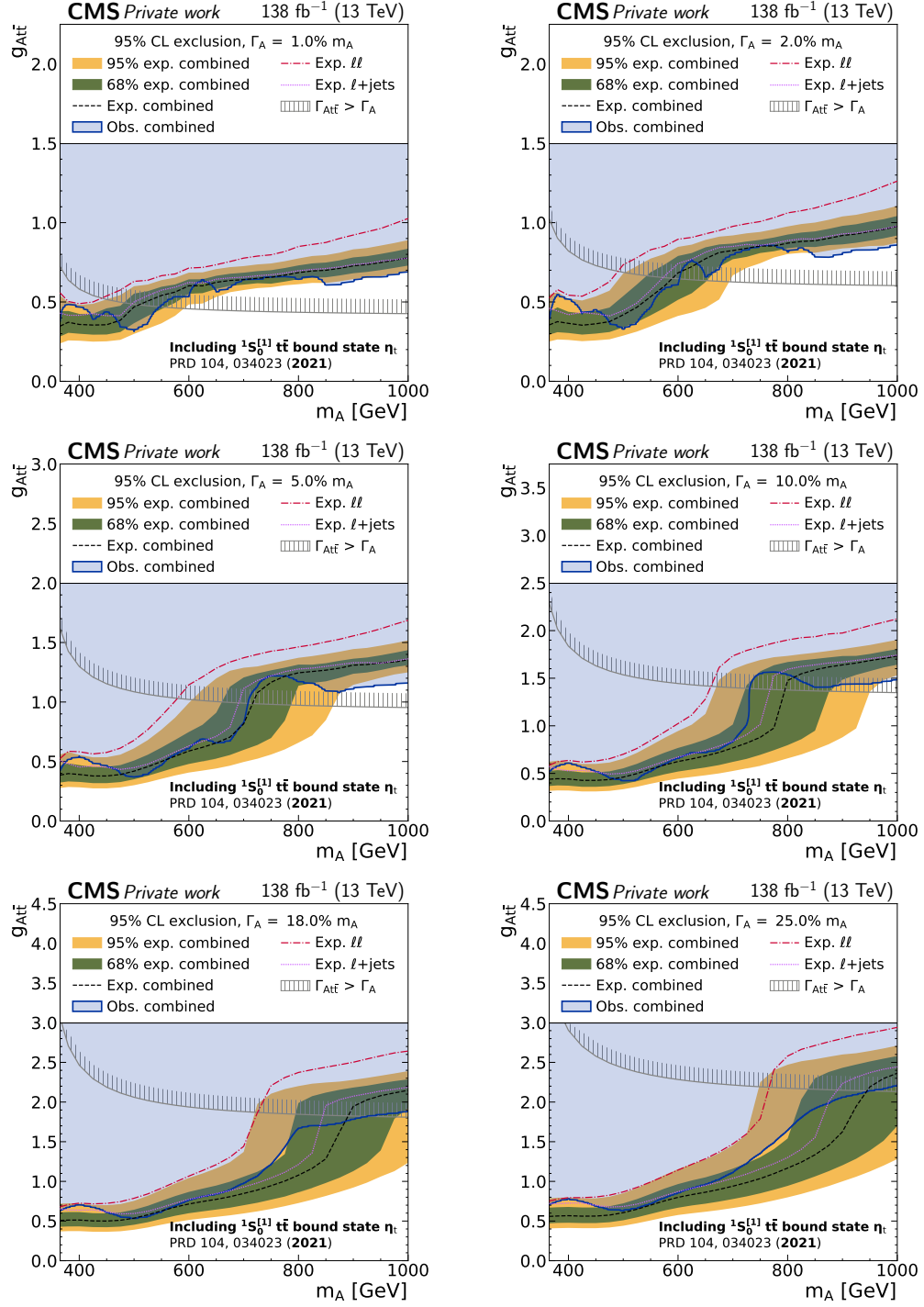


Figure 7.30: **Combined exclusion limits on $g_{A t\bar{t}}$ in the “A + η_t ” scenario** in the dilepton and $\ell + \text{jets}$ channels as a function of the mass of the A boson. Notations are equivalent to Fig. 7.28.

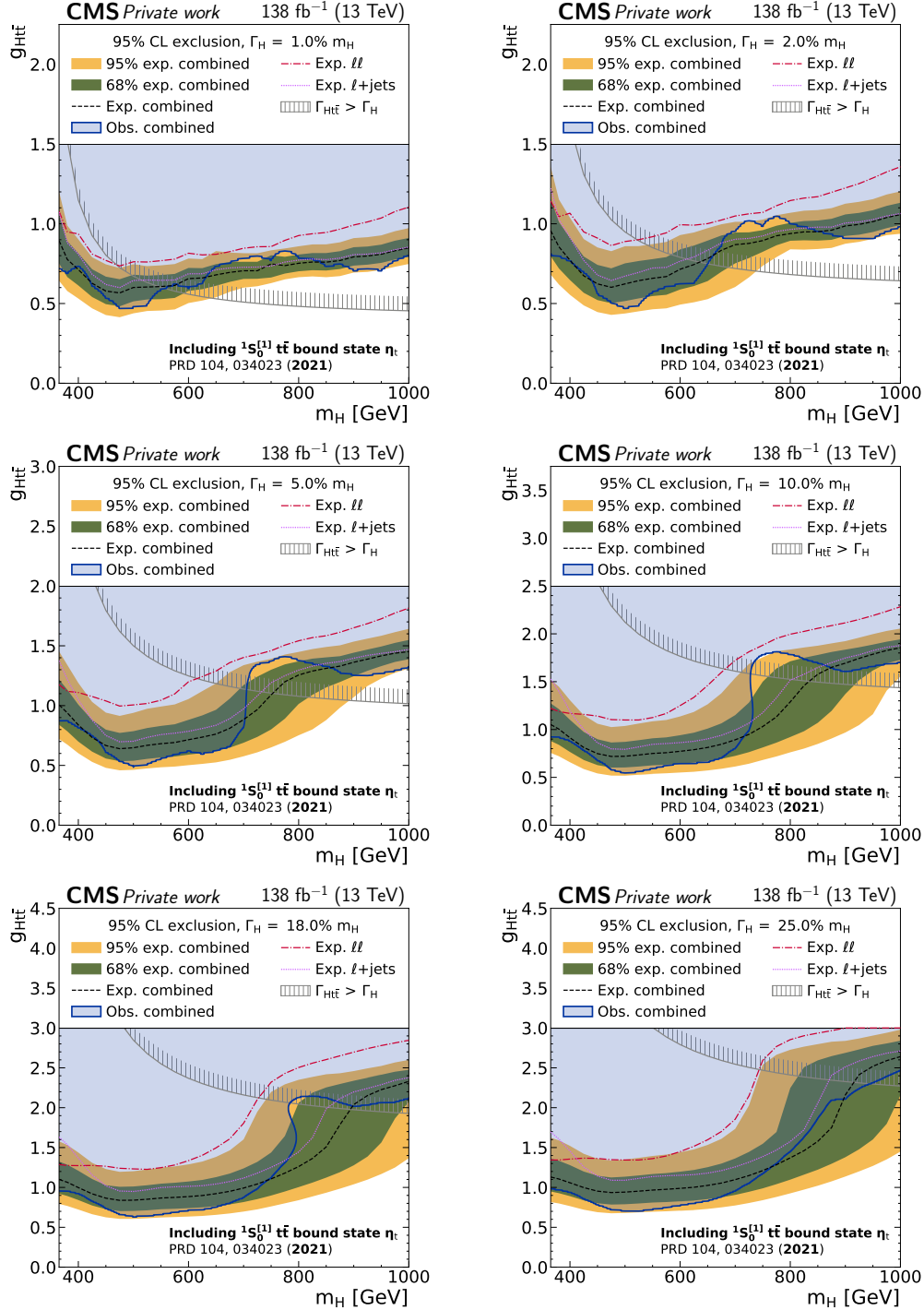


Figure 7.31: Combined exclusion limits on $g_{H\bar{t}\bar{t}}$ in the “H + η_t ” scenario in the dilepton and ℓ +jets channels as a function of the mass of the H boson. Notations are equivalent to Fig. 7.28.

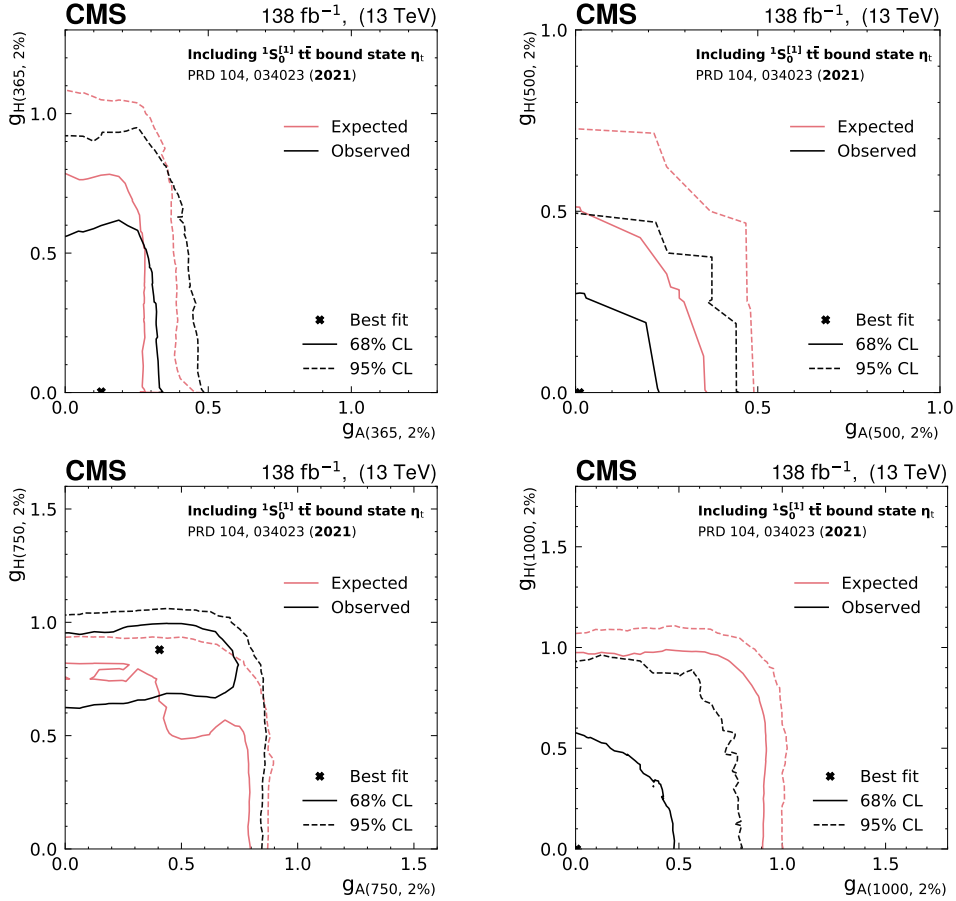


Figure 7.32: **Frequentist 2D exclusion contours for $g_{A t\bar{t}}$ and $g_{H t\bar{t}}$** for four different signal hypotheses with identical A and H masses of 365 GeV (upper left), 500 GeV (upper right), 750 GeV (lower left) and 1000 GeV (lower right), all assuming a width of 2%. In all cases, η_t production is added to the background.

3023 found in Fig. 7.32 for the case of identical A and H masses as well as in Fig. 7.33 for
 3024 differing A and H masses. Alternatively, a coarse scan of the negative log-likelihood
 3025 of the full span is available online as part of the HepData record **TODO ref.**

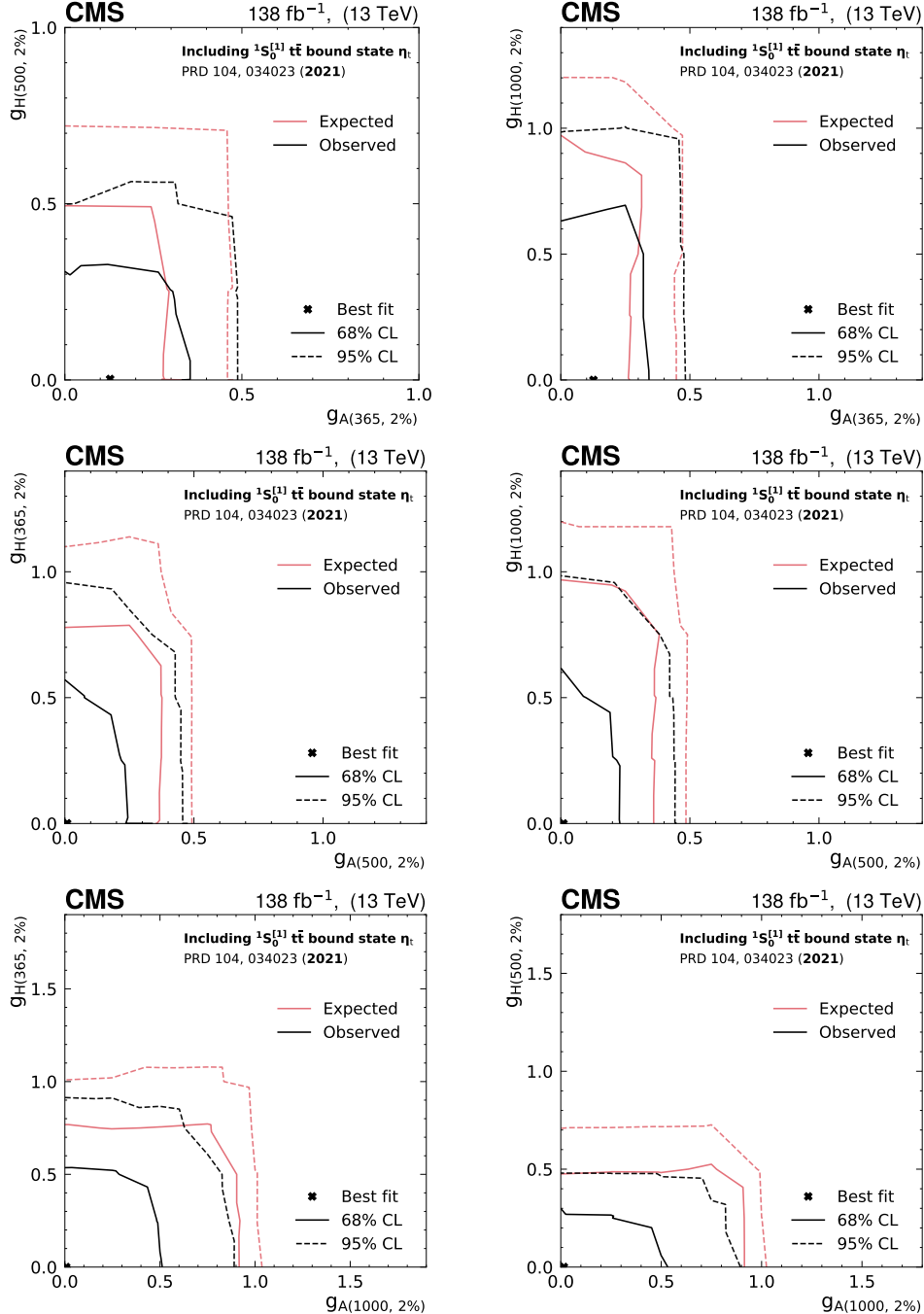


Figure 7.33: **Frequentist 2D exclusion contours for $g_{\text{A}t\bar{t}}$ and $g_{\text{H}t\bar{t}}$** for six different signal hypotheses with differing A and H masses, corresponding to combinations of 365 GeV, 500 GeV and 1000 GeV, all assuming a width of 2%. In all cases, η_t production is added to the background.

3026 7.10 Comparison to other results

3027 7.10.1 ATLAS $A/H \rightarrow t\bar{t}$ search

3028 In Ref. [163], the ATLAS collaboration presented a similar search for heavy pseu-
3029 doscalar or scalar bosons in $t\bar{t}$ events using the full LHC Run 2 dataset, and observed
3030 no excess at the $t\bar{t}$ threshold. To decide whether that result contradicts the one pre-
3031 sented here, it is necessary to understand the differences between the two analyses.

3032 The ATLAS analysis combines the dilepton and $\ell+jets$ decay channels of $t\bar{t}$, sim-
3033 ilar to the combination presented in Sec. 7.9 for A and H , though the definitions of
3034 the channels are different: In the $\ell+jets$ channel, ATLAS does not consider events
3035 with only three jets as described in Sec. 7.9.1, but instead includes events with only
3036 one b tag in addition to events with two or more b tags. Furthermore, ATLAS
3037 defines an additional category with $\ell+jets$ events in which the decay products of the
3038 hadronically decaying top quark are merged, though this is expected to contribute
3039 mostly at high $m_{t\bar{t}}$.

3040 In the dilepton channels, ATLAS uses a fundamentally different strategy than
3041 the one presented in this work. Instead of performing an explicit $t\bar{t}$ reconstruction,
3042 thus giving access to $m_{t\bar{t}}$ and the spin correlation observables c_{hel} and c_{chan} , ATLAS
3043 simply uses the invariant mass $m_{b\bar{b}\ell\ell}$ of the visible decay products as well as $\Delta\phi_{\ell\ell}$,
3044 the azimuthal distance between the two leptons in the laboratory frame. The former
3045 can be considered a proxy for $m_{t\bar{t}}$, though with significant smearing due to the loss
3046 of information from the two neutrinos, as also studied in Sec. 7.7.3. The latter has
3047 indirect sensitivity to the $t\bar{t}$ spin correlation, but this sensitivity is intermixed with
3048 kinematic information due to the boosts of the leptons from their top quark parents.
3049 As a result, it is known to be hard to model accurately and affected by theoretical
3050 uncertainties [22, 194].

3051 Combining these properties, it is expected that the dilepton channels in the AT-
3052 LAS analysis give only subdominant sensitivity compared to the $\ell+jets$ channels. In
3053 this work, while the situation is similar for high $m_{t\bar{t}}$, the dilepton channels contribute
3054 significantly close to the $t\bar{t}$ threshold. Furthermore, the direct use of spin corre-
3055 lation information means that the effect of many systematic uncertainties which only
3056 affect the kinematics is lessened greatly, as elaborated on in Sec. 7.7.3. It has been
3057 checked internally that adopting the strategy employed by ATLAS for the dilepton
3058 channels in this work would lead to a greatly lessened sensitivity at the $t\bar{t}$ threshold,
3059 and likely no claims of a significant excess.

3060 A further cause of differences could be the different treatment of systematic uncer-
3061 tainties. ATLAS considers additional nuisance parameters for the modeling of the $t\bar{t}$
3062 continuum regarding the choice of parton shower (PYTHIA vs. HERWIG), the choice
3063 of calculation for the top quark decay (POWHEG vs. MADSPIN), and the choice
3064 of PDF in the calculation of the NNLO QCD and NLO EW corrections. The first
3065 of these has been studied here in Sec. 7.7.3, and found to not influence the results

3066 strongly in the dilepton channels due to the effect of c_{hel} . However, the important
 3067 uncertainties due to the top quark Yukawa coupling and the EW correction scheme
 3068 are not included in the ATLAS result, since the EW corrections are calculated in a
 3069 different manner. In an effort to be as conservative as possible, ATLAS moreover
 3070 treats several significant uncertainties as decorrelated between different bins of the
 3071 angular variables $\cos \theta^*$ and $\Delta\phi_{\ell\ell}$, which could reduce the sensitivity gained from
 3072 these variables.

3073 Since ATLAS does not consider an explicit signal model for a $t\bar{t}$ bound state,
 3074 the expected sensitivities to η_t cannot be directly compared. Instead, the closest
 3075 considered signal is the generic pseudoscalar A at a mass of 400 GeV, higher than the
 3076 minimum of 365 GeV considered here. Since a non-negligible excess is still present
 3077 at that value in this work both in the dilepton channels alone (Fig. 7.24) and in
 3078 the combination with $\ell+\text{jets}$ (Fig. 7.28), while no such excess is visible in Fig. 15 of
 3079 Ref. [163], the choice of signals is not the cause of the differences on its own. However,
 3080 the shape difference between A at 400 GeV including the SM interference and η_t is
 3081 not negligible. It is thinkable that, if the excess truly originates from a $t\bar{t}$ bound state
 3082 manifesting as a narrow peak at the $t\bar{t}$ threshold, fitting the non-matching A signal
 3083 to the data will worsen the issues due to modeling and systematic uncertainties as
 3084 described in the previous paragraphs, though this is partly speculation.

3085 Even with all this information, it is not fully clear whether the result of this work
 3086 and the ATLAS result in Ref. [163] should be considered in conflict with each other
 3087 or not. Together with the cross-checks performed in Sec. 7.7.3, it seems likely that
 3088 the $t\bar{t}$ kinematic reconstruction in the dilepton channels, in particular the access to
 3089 spin correlation, is the most important difference. To decisively answer the question
 3090 of consistency, it would be desirable for ATLAS to repeat their analysis with a
 3091 similar strategy in the dilepton channels, as well as with a dedicated signal model
 3092 for a $t\bar{t}$ bound state.

3093 7.10.2 Other $t\bar{t}$ measurements

3094 While this work constitutes the first time that an excess consistent with a $t\bar{t}$ bound
 3095 state has been observed with a large significance, there have been hints for such
 3096 an effect in other $t\bar{t}$ measurements. First, several measurements of unfolded $t\bar{t}$
 3097 differential cross sections have observed excesses in data compared to MC predictions
 3098 of the $t\bar{t}$ continuum at low invariant masses, such as $m_{t\bar{t}}$ in dilepton events [195],
 3099 $m_{\ell\ell}$ in $e\mu$ events [196], and $m_{t\bar{t}}$ in $\ell+\text{jets}$ events [184]. The significances of these
 3100 excesses vary depending on the MC generator the data is compared to, and are also
 3101 strongly influenced by systematic uncertainties for the two $m_{t\bar{t}}$ measurements.

3102 Secondly, the measurements of quantum entanglement in $t\bar{t}$ pairs in the dilepton
 3103 channel presented in Refs. [24, 25] measure as a sensitive observable the value of
 3104 D , i.e. the slope of c_{hel} (cf. Sec. 2.2.1), for low $m_{t\bar{t}}$ events. This is very similar
 3105 in spirit to the observables $m_{t\bar{t}}$ and c_{hel} used in the dilepton channel of this work,

3106 though the measurement is only performed one-dimensionally in c_{hel} instead of the
 3107 3D $m_{t\bar{t}} \times c_{\text{hel}} \times c_{\text{han}}$ template used here. In both Refs. [24, 25], a smaller (i.e. more
 3108 negative) value of D is observed in data compared to MC $t\bar{t}$ continuum predictions,
 3109 though the significance is only at the level of one SD. This can be interpreted as
 3110 a hint for the presence of an additional pseudoscalar contribution from a $t\bar{t}$ bound
 3111 state, consistent with the results of this work.

3112 7.11 Summary and Outlook

3113 In this chapter, a generic search for spin-0 states in $t\bar{t}$ events with the full data of
 3114 LHC Run 2 was presented, targeting the dilepton decay channel of $t\bar{t}$. In addition
 3115 to the invariant mass $m_{t\bar{t}}$, it uses the spin correlation variables c_{hel} and c_{han} to probe
 3116 the spin and \mathcal{CP} structure of $t\bar{t}$ and possible new particles.

3117 A statistically significant excess was observed in data for low $m_{t\bar{t}}$ events, close
 3118 to the $t\bar{t}$ production threshold, showing spin correlations consistent with a pseu-
 3119 doscalar state. This excess is interpreted as a pseudoscalar $t\bar{t}$ quasi-bound state η_t ,
 3120 which is expected to be present in the SM according to NRQCD calculations. A
 3121 simplified model for the production of η_t is used to measure its cross section, yielding
 3122 $\sigma(\eta_t) = 8.7 \pm 1.1 \text{ pb}$. Several cross-checks of this result, relaxing assumptions on the
 3123 $t\bar{t}$ kinematic reconstruction as well as considering alternate MC generator setups,
 3124 validate the observed excess. This result represents the first observation of η_t .

3125 Alternatively, the excess could be interpreted as an additional pseudoscalar boson
 3126 A , with mass close to the $t\bar{t}$ threshold. While the explanation as a $t\bar{t}$ bound state
 3127 might be favored *a priori* as it is part of the SM and does not invoke any new
 3128 physics, experimentally the two interpretations cannot be distinguished with the
 3129 current resolution. In addition to the interpretation of the excess, exclusion limits
 3130 are set on new pseudoscalar or scalar bosons A/H through their coupling strengths
 3131 to the top quark, allowing for either one or both of these bosons simultaneously.
 3132 They are presented for two scenarios, where the observed excess is either assumed
 3133 to be fully described by the bound state η_t or fully by the new boson A . These limits
 3134 are further combined with a separate analysis targeting the $\ell+\text{jets}$ decay channel of
 3135 $t\bar{t}$.

3136 It is clear that much remains to be studied about the excess observed in this
 3137 work. Firstly, the interpretation in terms of η_t presented here is performed only
 3138 in the dilepton channels. In the preliminary results of Ref. [8], the combination
 3139 with the $\ell+\text{jets}$ channels was also performed for the measurement of the η_t cross
 3140 section; however, since the $\ell+\text{jets}$ analysis used was not optimized for signals at the
 3141 $t\bar{t}$ threshold, little sensitivity could be gained compared to the dilepton channels
 3142 alone. Instead, a separate $\ell+\text{jets}$ analysis optimized for a $t\bar{t}$ bound state should be
 3143 performed in the future. In particular, spin correlation variables analogous to c_{hel}
 3144 and c_{han} could be defined also in the $\ell+\text{jets}$ channel, as has already been done in

3145 Ref. [23] through ML-based identification of the decay products of the hadronically
 3146 decaying top quark.

3147 By contrast, in the dilepton channel, the most pressing targets of improvement
 3148 are the kinematic reconstruction and the $t\bar{t}$ modeling uncertainties. For the for-
 3149 mer, it would again be useful to investigate ML-based reconstruction techniques,
 3150 for which several proof-of-concept studies have already been performed [164, 197].
 3151 For the latter, the differences between different generator setups, as briefly studied
 3152 in Sec. 7.5.4, needs to be understood more deeply. It would be ideal to cover the
 3153 difference between predictions by a set of well-motivated nuisance parameters with
 3154 clear physical meaning, as has been recently used by CMS in the measurement of
 3155 the W boson mass [198, 199]. Extending this approach to the $t\bar{t}$ process however
 3156 requires many theoretical advancements, and is likely to lie far in the future for now.
 3157 In a similar fashion, it will be required to obtain a more precise prediction for the $t\bar{t}$
 3158 bound state itself. A possible approach here, involving the reweighting of $t\bar{t}$ events
 3159 by the ratio of Green’s functions, is presented in Ref. [37], though this remains to
 3160 be validated.

3161 To sidestep the issue of imperfect modeling of both η_t and the $t\bar{t}$ continuum,
 3162 one could attempt to observe the $t\bar{t}$ bound state in other decay channels, the most
 3163 promising being the decay $\eta_t \rightarrow \gamma\gamma$ to two photons. This final state is experimentally
 3164 extremely clean and does not require MC modeling of the $\gamma\gamma$ background. Instead,
 3165 a possible signal could be extracted using a parametric fit of a peak over a falling
 3166 background, similar to the measurement of the SM Higgs boson in the $h \rightarrow \gamma\gamma$
 3167 channel. The most important obstacle in such a project would be the branching ratio
 3168 of η_t to $\gamma\gamma$, which is very uncertain. Extrapolations of the partial width to $\gamma\gamma$ from
 3169 $b\bar{b}$ and $c\bar{c}$ bound states [200], combined with an expected total width of $\Gamma(\eta_t) \approx 2m_t$,
 3170 predict a branching ratio of $\approx 2 \times 10^{-5}$, though this is a rough estimate that could
 3171 be wrong by as much as an order of magnitude. If this prediction holds, it might
 3172 be possible to observe this decay channel with the full statistics collected in Runs 2
 3173 and 3 of the LHC. Moreover, a measurement of the ratio of branching fractions to
 3174 $\gamma\gamma$ and $t\bar{t}$ could help distinguish a bound state from possible BSM scenarios.

3175 It is further necessary, of course, to repeat the analysis presented here with the
 3176 data of LHC Run 3, ideally combining the results. While the η_t cross section, and
 3177 similarly A/H limits at low masses, are dominated by systematic effects, especially
 3178 the sensitivity at high A and H masses is limited by the statistics of the data. The
 3179 increase in center-of-mass energy from 13 to 13.6 TeV will also help increase the
 3180 cross section of high-mass signals, together making it possible to extend the probed
 3181 A/H mass range to higher values.

3182 Furthermore, concerning the limits on A and H derived here, the next step is
 3183 to include these generic exclusion limits into concrete bounds on BSM models of
 3184 interest. A particular such model, the production of heavy Axion-Like Particles
 3185 coupling to top quarks, is studied on a phenomenological basis in the following
 3186 chapter.

3187 **8 Investigation of Axion-Like Particles**
3188 **decaying to $t\bar{t}$**

3189 **8.1 Introduction**

3190 Following the results of Chapter 7 including the interpretations as generic scalar or
3191 pseudoscalar bosons and $t\bar{t}$ bound states, this chapter is dedicated to Axion-Like
3192 Particles decaying to $t\bar{t}$. As explained in Sec. 2.3.3, the coupling structure of ALPs
3193 to top quarks is identical to those of the generic pseudoscalar A, such as e.g. in
3194 the 2HDM, if the basis for the ALP is chosen appropriately (cf. Eq. (2.23)). The
3195 difference comes from the gluon interaction term, which is absent for the model used
3196 for A in Chapter 7, and which results in an additional diagram where the ALP is
3197 produced through a contact interaction with the gluons.

3198 If the coefficient $c_{\tilde{G}}$ of the ALP-gluon interaction term in Eq. (2.23) vanishes, the
3199 forms of the Lagrangians for ALP and A become identical, and the limits for A
3200 shown in Chapter 7 can be directly recasted. This is done in Sec. 8.2. If on the
3201 other hand $c_{\tilde{G}} \neq 0$, the kinematic distributions of the ALP will differ from those of
3202 A, and the experimental results are not easily translatable. This case is addressed in
3203 the scope of this work through an phenomenological study on simulation only. The
3204 technical setup of this study is described in Sec. 8.3, after which the distributions
3205 of ALP and A are compared for different benchmark points in Sec. 8.4. Projected
3206 exclusion limits for the $c_{\tilde{G}} \neq 0$ case are presented in Sec. 8.5, and a short summary
3207 is given in Sec. 8.6.

3208 The results of this chapter have been originally published in *JHEP* as Ref. [10].
3209 Since the results of Chapter 7 (Refs. [8, 9]) were not yet public at the time, the
3210 previous CMS result from Ref. [16] was used as a baseline. For this thesis, the
3211 translation of limits in Sec. 8.2 has been updated to reflect the results of Chapter 7.

3212 All results presented in this chapter have been obtained as part of this thesis,
3213 except for the comparison to other final states in Sec. 8.5, which was performed by
3214 the coauthors of Ref. [10] as indicated.

3215 **8.2 Translation of experimental limits**

3216 In the basis of Eq. (2.23), the ALP Lagrangian is identical in form to the Lagrangian
3217 of the generic pseudoscalar A given in Eq. (2.18) as long as the gluon interaction

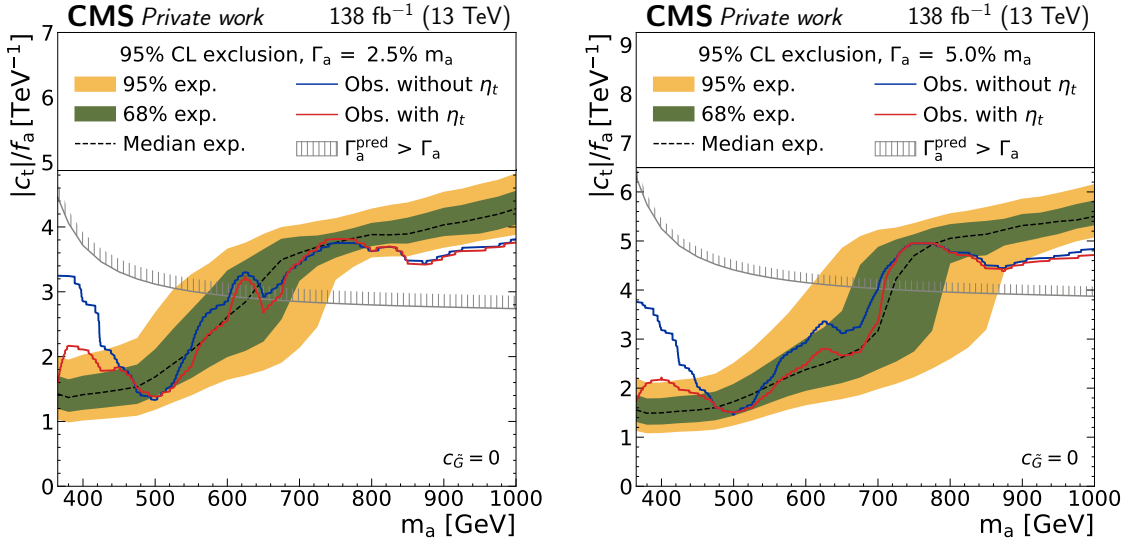


Figure 8.1: **ALP limits for $c_{\tilde{G}} = 0$.** Expected and observed limits on the ALP-top coupling c_t/f_a as a function of the ALP mass for the case $c_{\tilde{G}} = 0$ for the combined dilepton and $\ell+\text{jets}$ decay channels, translated from the results of Chapter 7. The expected limit (black line) is shown without contribution from $t\bar{t}$ bound states in the background modeling, while the observed limit is shown both without $t\bar{t}$ bound states (blue) and with η_t included in the background (red).

3218 coefficient $c_{\tilde{G}}$ vanishes. For this case, one finds by comparing the coefficients that
3219 the phenomenology will be identical if

$$\frac{c_t}{f_a} = \frac{g_{A t\bar{t}}}{v} \quad (8.1)$$

3220 where $v = 246$ GeV is the SM Higgs vacuum expectation value. Thus, the experi-
3221 mental results of Chapter 7, particularly the limits on $g_{A t\bar{t}}$ from the combination of
3222 dilepton and $\ell+\text{jets}$ decay channels as presented in Sec. 7.9.2, can be recasted into
3223 limits on the ALP coupling c_t/f_a for the case $c_{\tilde{G}} = 0$. This is shown in Fig. 8.1 for
3224 two different (fixed) ALP widths. The observed limits are shown with and without
3225 a $t\bar{t}$ bound state contribution as modeled by η_t in the background modeling, corre-
3226 sponding to the two scenarios in Fig. 7.28 and Fig. 7.30, and the same excess as in
3227 Chapter 7 is seen for at low ALP masses when the η_t contribution is not included.

3228 In a similar fashion, the best-fit point for A as presented in Eq. (7.17) can be
3229 translated to an ALP for the case of $c_{\tilde{G}} = 0$, giving

$$m_a = 365 \text{ GeV}, \quad \Gamma_a/m_a = 2\%, \quad \text{and} \quad \frac{c_t}{f_a} = 3.2 \pm 0.2 \text{ TeV}^{-1}.$$

This represents a third alternative interpretation of the excess besides a $t\bar{t}$ bound state or a generic pseudoscalar A. The same caveats as for the A interpretation, as outlined in Sec. 7.7.4, apply; in particular, the mass of 365 GeV is the lowest mass point considered in the signal samples, and it is possible that lower masses closer to the $t\bar{t}$ threshold would result in a better fit.

8.3 Phenomenological setup

The remainder of this chapter is dedicated to exploring an ALP decaying to $t\bar{t}$ for the case $c_{\tilde{G}} \neq 0$, for which the results of Chapter 7 are not easily translatable since the distributions are expected to differ in shape. Due to time constraints, it was not possible as part of this work to investigate this case experimentally in the same fashion as done in Chapter 7. Instead, a phenomenological study is performed on MC simulation only, using a setup that approximates the workflow in Chapter 7.

To do so, MC samples for the signal are generated at LO in QCD with MADGRAPH 5 for two different ALP masses (400 GeV and 800 GeV). For the ALP, an UFO model taken from Ref. [201] is used and modified to include the top quark loop form factor including finite mass effects, according to the expressions given in Ref. [202]. Both possible production diagrams, as shown in Fig. 2.8, as well as their interference with the SM are considered. A similar ME reweighting technique as in Sec. 7.4 is used to obtain samples for different widths and $c_{\tilde{G}}$ values. For the generic pseudoscalar A as well as the SM $t\bar{t}$ background, the same generators as in Sec. 7.2.1 are used (MADGRAPH 5 and POWHEG v2 hvq, respectively). For all samples, the NNPDF 3.1 PDF set [40] is used, and PYTHIA 8.2 is used to simulate initial and final state radiation [71].

Only the dilepton decay channel of $t\bar{t}$ is considered, and no detector simulation is performed. Instead, the truth-level top quarks and leptons after parton showering are used, and a Gaussian smearing is applied to $m_{t\bar{t}}$ randomly on a per-event basis, the standard deviation of which is chosen so that the resolution of the resulting distribution matches that observed in full detector simulation. Since this study was performed before the results of Chapter 7 were public, its predecessor Ref. [16] is used to extract the resolution by fitting to the $m_{t\bar{t}}$ distributions displayed therein. The result is $\sigma(m_{t\bar{t}})/m_{t\bar{t}} = 15\%$, which is somewhat lower than the widths found using the full detector simulation in Sec. 7.2.5 (c.f. Fig. 7.2). However, it should be cautioned that since the true $m_{t\bar{t}}$ smearing in the full detector simulation is not perfectly Gaussian, the results are not one-to-one comparable.

The experimental acceptance and efficiency, defined as the fraction of $t\bar{t} \rightarrow \ell\ell$ (ℓ being electrons, muons or leptonically decaying taus) events to survive all trigger and selection requirements, is estimated to be 10.6% for both signal and $t\bar{t}$ background, also based on Ref. [16]. This is lower compared to the updated analysis presented in Chapter 7, where values of 15–16% are achieved, varying slightly with the data-

3269 taking period. Thus, the projections in this chapter should be considered somewhat
 3270 conservative.

3271 Since the ALP always has a \mathcal{CP} -odd coupling to top quarks (cf. Eq. (2.23)), it
 3272 is expected to decay to a $t\bar{t}$ system in the 1S_0 state, identically to A. This is true
 3273 irrespective of the gluon coupling $c_{\tilde{G}}$ since the latter only affects the production, not
 3274 the decay, and the ALP as a colorless, spinless particle has no internal degrees of
 3275 freedom. Thus, $m_{t\bar{t}}$ and c_{hel} are good discriminating variables, again similar to A,
 3276 while c_{han} (optimal for \mathcal{CP} -even couplings) does not offer much additional discrim-
 3277 ination and is not considered here. For simplicity, instead of a multi-dimensional
 3278 binning in $m_{t\bar{t}}$ and c_{hel} like in Chapter 7, a one-dimensional binning in $m_{t\bar{t}}$ only is
 3279 used, and events are required to have $c_{\text{hel}} > 0.6$ to enhance the ALP signal over the
 3280 background.

3281 A simplified version of the likelihood model from Chapter 7 is used, implemented
 3282 in `pyhf` [116], in order to estimate projected significances and limits. Only sources
 3283 of systematic uncertainty arising from theory are considered, namely:

- 3284 • Missing higher orders in the matrix element, estimated from varying renor-
 3285 malization and factorization scale by factors of 2,
- 3286 • The PDF uncertainty, estimated as the envelope of 100 pseudo-Hessian NNPDF 3.1
 3287 replicas [40],
- 3288 • The total $t\bar{t}$ background production cross section, taken as a log-normal un-
 3289 certainty of 6% following Ref. [16],
- 3290 • The top quark mass in the $t\bar{t}$ background, varied in the range $m_t = 172.5 \pm$
 3291 1 GeV.

3292 It is clear that this simple treatment of systematic uncertainties can only give a
 3293 rough estimate of the full likelihood as used in Chapter 7, which is sensitive mostly to
 3294 the differences in shapes induced by the various systematic sources. In particular,
 3295 like in the experimental result, the variation in the top quark mass is important
 3296 especially for ALPs with masses close to the $t\bar{t}$ threshold.

3297 To illustrate the dependence on the likelihood model, the significances in the fol-
 3298 lowing results will be quoted for three different setups including different systematic
 3299 uncertainties, namely all of the above, all of the above except for the top quark
 3300 mass, and statistical uncertainties only. By comparing to the expected significance
 3301 given in Ref. [16] for the best-fit point of the pseudoscalar A, it is found that the
 3302 full setup overestimates the uncertainty, while the setup without the top quark mass
 3303 slightly underestimates it.

c_t/f_a [TeV $^{-1}$]	$c_{\tilde{G}}/f_a$ [TeV $^{-1}$]	A	$(\sigma^{\text{tot}} - \sigma^{\text{SM}})$ [pb]
3.0	+0.015	0.95	+6.7
3.0	-0.015	0.43	-2.7
1.0	+0.025	0.75	-1.7
1.0	-0.025	0.87	+2.0

Table 8.1: **Benchmark points for comparing ALP and A.** In addition to the ALP couplings c_t/f_a and $c_{\tilde{G}}/f_a$ for the benchmark points, also the difference in integrated cross section to the SM is shown, as well as a value of $g_{A\bar{t}\bar{t}}$ corresponding to a generic pseudoscalar A with the same integrated cross section.

8.4 Comparison of ALP and A

To investigate the differences and possible discrimination between ALP and A, four different ALP benchmark points with $c_{\tilde{G}} \neq 0$ are defined for a mass of 400 GeV and a width of 2.5%. Each of the benchmarks is compared to a generic pseudoscalar A with its coupling $g_{A\bar{t}\bar{t}}$ chosen such that the total integrated cross section of ALP and A are identical, i.e. that they can not be distinguished by cross section information alone. The chosen couplings and resulting cross sections can be found in Tab. 8.1.

The expected $m_{t\bar{t}}$ distributions, including the smearing and acceptance described in Sec. 8.3, for the four benchmark points are shown in Fig. 8.2, together with the expected statistical uncertainty for both Run 2 and the HL-LHC.

It can be seen that the shapes of the distributions differ qualitatively for the different benchmarks: For example, the case $c_t/f_a = 3.0$ TeV $^{-1}$ and $c_{\tilde{G}}/f_a = 0.015$ TeV $^{-1}$ (top left) shows a clear peak-dip structure similar to the A case, and as a result will likely not be distinguishable from it. In contrast, e.g. the case $c_t/f_a = 1.0$ TeV $^{-1}$ and $c_{\tilde{G}}/f_a = -0.025$ TeV $^{-1}$ (bottom right) shows a dip-peak structure instead, which cannot be reproduced by the A. This is possible because of the relative sign of the two couplings in this case, i.e. $c_t c_{\tilde{G}} < 0$, which flips the sign of the interference between the gluon interaction diagram in Fig. 2.8 and the SM.

By comparing the distributions to the expected statistical uncertainty, one can already estimate roughly whether discrimination of the signals with respect to the SM or with respect to each other is possible. To quantify this further, the expected significance to reject the SM-only hypothesis under the benchmark scenarios are reported in Tab. 8.2. They are computed with the likelihood model as defined in Sec. 8.3, and quoted both for the three different described uncertainty setups as well as for three different eras of the LHC, corresponding to different (expected) integrated luminosities: full Run 2 (138 fb $^{-1}$), Run 2+3 (300 fb $^{-1}$), and the HL-LHC (3 ab $^{-1}$). For the latter case, all systematic uncertainties are halved to account

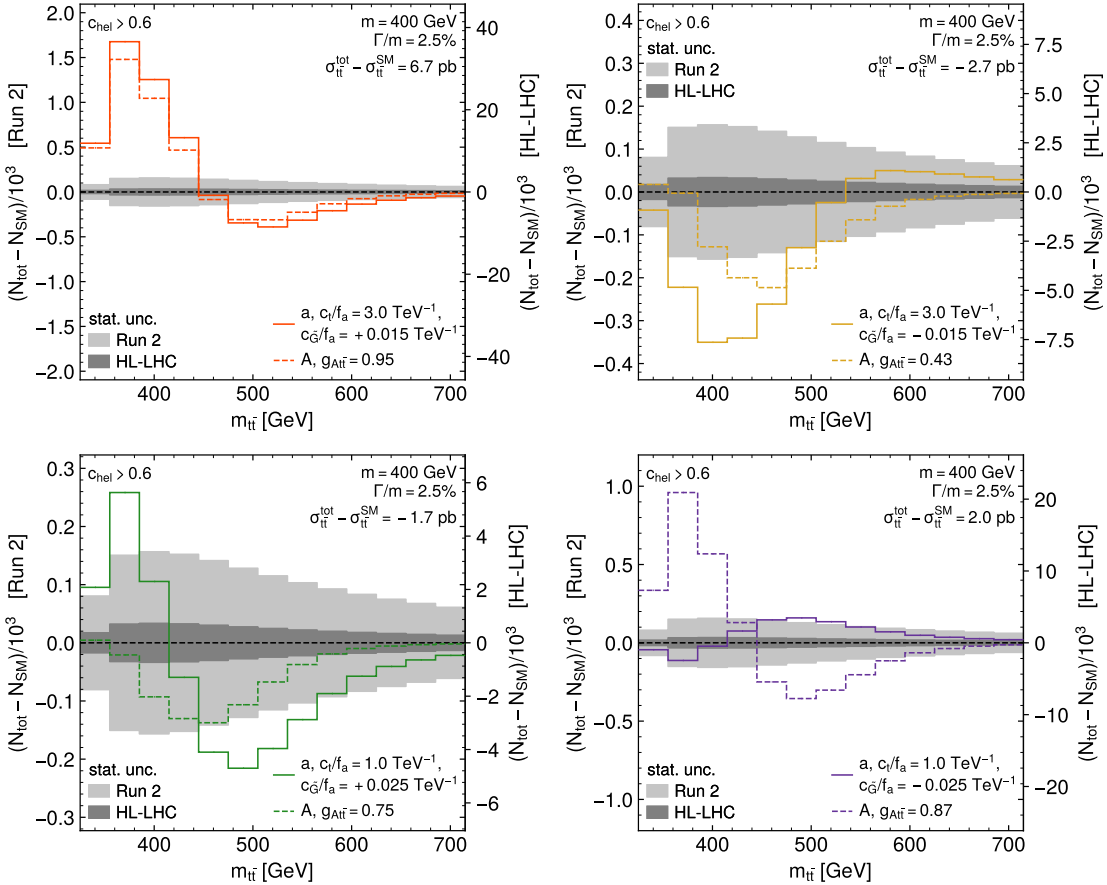


Figure 8.2: **Expected $m_{t\bar{t}}$ distributions for $pp \rightarrow a/A \rightarrow t\bar{t}$.** Shown are both ALP and A at a mass of 400 GeV for four benchmark points, with the SM subtracted. The couplings for A and a are adjusted such that the inclusive cross section is identical. The grey bands show the expected statistical uncertainty for Run 2 and HL-LHC.

for the expected increase in data reconstruction quality and reduction in theoretical uncertainty.

Tab. 8.2 shows that all considered benchmark scenarios can be expected to be distinguished from the SM with $> 5\sigma$ significance if the top quark mass uncertainty is not considered in the model, that is, if experimentally it can be significantly reduced from the estimate used in this study.

If one such signal would be discovered in the future, it would be important to ascertain the particle it originates from. The $m_{t\bar{t}}$ distribution could then be used to distinguish between an ALP, exhibiting both couplings to top quarks and gluons, and the more restrictive case of A, in which only a top quark coupling is allowed. To quantify this, Tab. 8.3 now shows, for the four benchmark points, the expected

c_t/f_a [TeV $^{-1}$]	$c_{\tilde{G}}/f_a$ [TeV $^{-1}$]	a	Luminosity	Significance (a vs. SM)		
				all syst.	no m_t	stats only
3.0	+0.015		Run 2	3.9	> 10	> 10
			Run 2+3	5.2	> 10	> 10
			HL-LHC	> 10	> 10	> 10
3.0	-0.015		Run 2	2.1	2.2	4.4
			Run 2+3	3.0	3.0	6.5
			HL-LHC	8.7	8.8	> 10
1.0	+0.025		Run 2	1.1	2.6	4.0
			Run 2+3	1.4	3.2	5.9
			HL-LHC	3.9	8.2	> 10
1.0	-0.025		Run 2	0.7	1.7	2.8
			Run 2+3	0.9	2.2	4.1
			HL-LHC	2.3	5.5	> 10

Table 8.2: **Significances for detecting an ALP** with a mass of 400 GeV and a width of 2.5% for the benchmark scenarios considered in Fig. 8.2. Three different treatments of the uncertainties as defined in Sec. 8.3 are shown. For the HL-LHC projection, all systematic uncertainties are scaled by a factor of 0.5.

significances for rejecting the A hypothesis assuming that the corresponding ALP model is realized in nature. Again, the three different uncertainty models and three LHC eras are shown in the same fashion. It can be seen that for all benchmarks, the HL-LHC data would make it possible to distinguish the two scenarios with $> 5\sigma$ significance in the case of an observation.

8.5 Projected limits for ALPs

In case that no (additional) signal is seen in either Run 3 or at the HL-LHC, one would quantify the exclusion of ALP models based on limits in the plane of c_t/f_a and $c_{\tilde{G}}/f_a$. Projections for such expected 95% exclusion limits are presented in Fig. 8.3 for the three different considered luminosities as well as for ALP masses of 400 and 800 GeV, again computed with the same likelihood model. All systematic uncertainties save for the top quark mass are considered here, same as in the “no m_t ” column in Tabs. 8.2 and 8.3.

The figures show that strong limits can be set for values of $|c_{\tilde{G}}|/f_a \gtrsim 0.05$ TeV $^{-1}$ where the gluon-ALP interaction dominates and leads to signals with large cross sections, while the limits are weaker close to $c_{\tilde{G}} = 0$. Notably, the smallest signals are obtained for slightly negative values of $c_{\tilde{G}}/f_a$ due to destructive interference between the two production diagrams, leading to a slight tilt of the curve in the

c_t/f_a [TeV $^{-1}$]	$c_{\tilde{G}}/f_a$ [TeV $^{-1}$]	a	A	Luminosity	Significance (a vs. A)		
					all syst.	no m_t	stats only
3.0	+0.015	0.95	$g_{A t \bar{t}}$	Run 2	1.3	1.9	3.3
				Run 2+3	1.8	2.3	4.9
				HL-LHC	5.3	5.7	> 10
3.0	−0.015	0.43	$g_{A t \bar{t}}$	Run 2	1.2	1.9	3.3
				Run 2+3	1.7	2.4	4.9
				HL-LHC	5.0	6.0	> 10
1.0	+0.025	0.75	$g_{A t \bar{t}}$	Run 2	1.5	2.3	2.7
				Run 2+3	2.0	3.1	3.9
				HL-LHC	5.8	8.8	> 10
1.0	−0.025	0.87	$g_{A t \bar{t}}$	Run 2	3.7	9.0	> 10
				Run 2+3	4.6	> 10	> 10
				HL-LHC	> 10	> 10	> 10

Table 8.3: **Significances for the discrimination of an ALP and A** for the benchmark scenarios considered in Fig. 8.2. The uncertainties are treated as in Tab. 8.2.

left panel of Fig. 8.3. Of the four considered benchmark points for a 400 GeV ALP, all can be safely expected to be excluded with HL-LHC data, while those with $c_t/f_a = 3$ TeV $^{-1}$ might already be excluded by the combination of Run 2 and 3.

As part of the work of the coauthors in Ref. [10], the projected limits for Run 2 were compared with limits derived from existing analyses in other search channels, using the tool `HiggsTools` [203]. These are reproduced briefly in the following in order to provide a point of reference; details can be found in Ref. [10]. The following search channels were found to be of relevance:

- $pp \rightarrow a \rightarrow \gamma\gamma$, from a generic narrow-resonance search in ATLAS [204],
- $pp \rightarrow a \rightarrow Zh$, from a search for pseudoscalars decaying into a Z boson and a SM Higgs boson in ATLAS [205],
- $pp \rightarrow t\bar{t}a \rightarrow t\bar{t}t\bar{t}$, from the CMS measurement of the four-top production cross section [206],
- interference effects between the ALP effective Lagrangian and SM Effective Field Theory (SMEFT), which would induce non-zero Wilson coefficients of SMEFT operators in electroweak precision observables such as e.g. the W boson mass, leading to indirect limits [207].

The comparison of all these limits to the projected limits from $pp \rightarrow a \rightarrow t\bar{t}$ derived in this work is shown in Fig. 8.4 in the c_t - $c_{\tilde{G}}$ plane for a 400 GeV ALP.

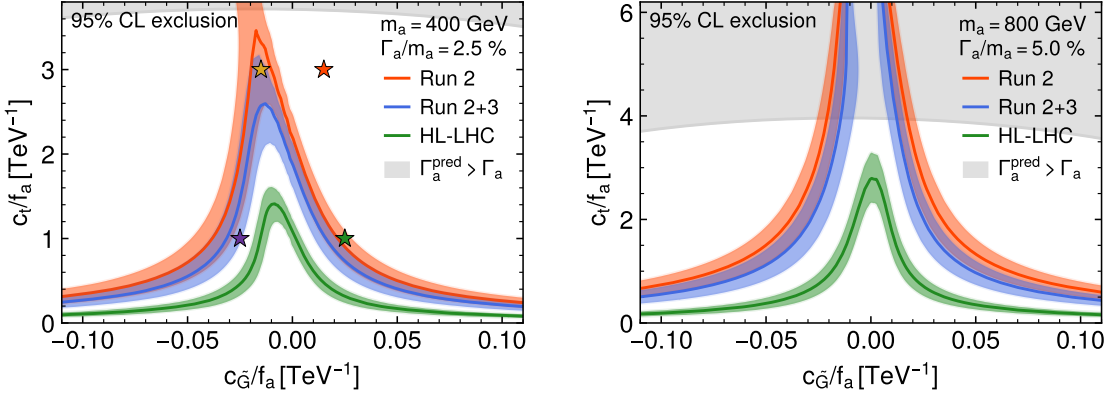


Figure 8.3: **Projected ALP limits.** Projected 95% exclusion limits in the plane of $c_{\tilde{G}}/f_a$ and c_t/f_a for a mass of 400 GeV and a width of 2.5% (left) as well as 800 GeV and 5.0% (right). The limits are shown for three different integrated luminosities, corresponding to Run 2, Run 2+3, and the HL-LHC, where for the latter the systematic uncertainties are halved.

3379 For almost all points, $pp \rightarrow a \rightarrow t\bar{t}$ leads to stronger limits than all other direct
 3380 search channels. Furthermore, for $|c_{\tilde{G}}|/f_a \gtrsim 0.03 \text{ TeV}^{-1}$ the projected limits are also
 3381 stronger than the indirect ones from ALP-SMEFT interference, while this is not the
 3382 case for smaller $|c_{\tilde{G}}|/f_a$. It should however be noted here that the indirect limits are
 3383 subject to more assumptions, in particular, that the ALP is the only new physics
 3384 contribution at the ALP scale ($\approx f_a$). For a more detailed discussion, see again
 3385 Ref. [10].

3386 8.6 Summary and Outlook

3387 In this chapter, the $t\bar{t}$ final state is found to be an excellent channel for searching
 3388 for heavy ALPs coupling to top quarks. Depending on the value of the explicit
 3389 gluon-ALP coupling $c_{\tilde{G}}$, two scenarios are considered. For $c_{\tilde{G}} = 0$, the results of
 3390 the experimental search for a generic pseudoscalar presented in Chapter 7 of this
 3391 work, including the excess observed there, are directly translated into limits on the
 3392 ALP-top coupling c_t/f_a .

3393 For $c_{\tilde{G}} \neq 0$, on the other hand, a phenomenological study targeting the dilepton
 3394 decay channel of $t\bar{t}$ is performed on simulation only, comparing ALPs to a generic
 3395 pseudoscalar A which does not couple directly to gluons. It is found that ALP
 3396 and A can lead to drastically different $m_{t\bar{t}}$ distributions depending on the coupling
 3397 values, and could possibly be distinguished at the HL-LHC if a signal is observed.
 3398 Furthermore, projected expected limits in the plane of the ALP couplings c_t/f_a and
 3399 $c_{\tilde{G}}/f_a$ are set for different integrated luminosities. They are more sensitive than

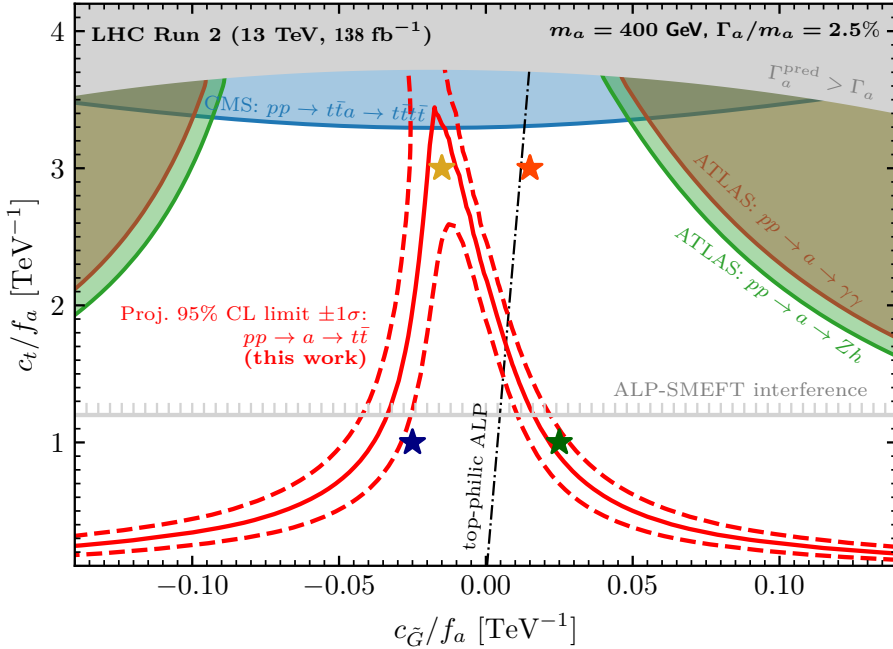


Figure 8.4: **Comparison of limits from different search channels.** 95% exclusion limits in the plane of $c_{\tilde{G}}/f_a$ and c_t/f_a for a mass of 400 GeV and a width of 2.5% (left) from different search channels. The projected limits from this work are overlaid in red.

3400 other possible direct search channels in almost the whole parameter space.

3401 The obvious continuation of this work would be to include the ALP signals, par-
 3402 ticularly the $c_{\tilde{G}} \neq 0$ case, into an experimental search like the one performed in
 3403 Chapter 7. For the purpose of this thesis, this was not possible within the time
 3404 constraints, and needs to be postponed to the future. Alternatively, one could in-
 3405 vestigate how the parameter space considered in this work - in particular, the very
 3406 large ALP mass and comparatively strong top coupling - match to possible UV com-
 3407 pletions of the ALP effective Lagrangian and, if such models exist, whether they can
 3408 still solve the strong \mathcal{CP} problem.

₃₄₀₉ **9 Summary and Conclusions**

3410 A Bibliography

- 3411 [1] G. Aad et al., “Observation of a new particle in the search for the standard
3412 model Higgs boson with the ATLAS detector at the LHC”, *Phys. Lett. B*,
3413 vol. 716, p. 1, 2012. DOI: 10.1016/j.physletb.2012.08.020. arXiv:
3414 1207.7214 [hep-ex].
- 3415 [2] S. Chatrchyan et al., “Observation of a new boson at a mass of 125 GeV with
3416 the CMS experiment at the LHC”, *Phys. Lett. B*, vol. 716, p. 30, 2012. DOI:
3417 10.1016/j.physletb.2012.08.021. arXiv: 1207.7235 [hep-ex].
- 3418 [3] S. Chatrchyan et al., “Observation of a new boson with mass near 125 GeV
3419 in pp collisions at $\sqrt{s} = 7$ and 8 TeV”, *JHEP*, vol. 06, p. 081, 2013. DOI:
3420 10.1007/JHEP06(2013)081. arXiv: 1303.4571 [hep-ex].
- 3421 [4] S. Chatrchyan et al., “The CMS Experiment at the CERN LHC”, *JINST*,
3422 vol. 3, S08004, 2008. DOI: 10.1088/1748-0221/3/08/S08004.
- 3423 [5] A. Tumasyan et al., “First measurement of the top quark pair production
3424 cross section in proton-proton collisions at $\sqrt{s} = 13.6$ TeV”, *JHEP*, vol. 08,
3425 p. 204, 2023. DOI: 10.1007/JHEP08(2023)204. arXiv: 2303.10680 [hep-ex].
- 3426 [6] C. Collaboration, “Simulation of on- and off-shell $t\bar{t}$ production with the
3427 Monte Carlo generator b_bbar_4l at CMS”, CERN, Geneva, Tech. Rep.,
3428 2023. [Online]. Available: <https://cds.cern.ch/record/2884265>.
- 3429 [7] T. Ježo, J. M. Lindert, P. Nason, C. Oleari, and S. Pozzorini, “An NLO+PS
3430 generator for $t\bar{t}$ and Wt production and decay including non-resonant and
3431 interference effects”, *Eur. Phys. J. C*, vol. 76, p. 691, 2016. DOI: 10.1140/
3432 epjc/s10052-016-4538-2. arXiv: 1607.04538 [hep-ph].
- 3433 [8] CMS Collaboration, “Search for heavy pseudoscalar and scalar bosons de-
3434 caying to top quark pairs in proton-proton collisions at $\sqrt{s} = 13$ TeV”, CMS
3435 Physics Analysis Summary CMS-PAS-HIG-22-013, 2024. [Online]. Available:
3436 <https://cds.cern.ch/record/2911775>.
- 3437 [9] A. Tumasyan et al., “Observation of a pseudoscalar excess at the top quark
3438 pair production threshold”, 2025. arXiv: 2503.22382 [hep-ex].
- 3439 [10] A. Anuar et al., “ALP-ine quests at the LHC: hunting axion-like particles
3440 via peaks and dips in $t\bar{t}$ production”, *JHEP*, vol. 24, p. 197, 2024. DOI: 10.
3441 1007/JHEP12(2024)197. arXiv: 2404.19014 [hep-ph].
- 3442 [11] R. L. Workman et al., “Review of Particle Physics”, *PTEP*, vol. 2022, p. 083C01,
3443 2022. DOI: 10.1093/ptep/ptac097.

- [3444] [12] P. W. Higgs, “Broken symmetries, massless particles and gauge fields”, *Phys. Lett.*, vol. 12, pp. 132–133, 1964. DOI: [10.1016/0031-9163\(64\)91136-9](https://doi.org/10.1016/0031-9163(64)91136-9).
- [3445]
- [3446] [13] F. Englert and R. Brout, “Broken Symmetry and the Mass of Gauge Vector Mesons”, *Phys. Rev. Lett.*, vol. 13, J. C. Taylor, Ed., pp. 321–323, 1964. DOI: [10.1103/PhysRevLett.13.321](https://doi.org/10.1103/PhysRevLett.13.321).
- [3447]
- [3448]
- [3449] [14] F. Abe et al., “Observation of top quark production in $\bar{p}p$ collisions”, *Phys. Rev. Lett.*, vol. 74, pp. 2626–2631, 1995. DOI: [10.1103/PhysRevLett.74.2626](https://doi.org/10.1103/PhysRevLett.74.2626). arXiv: [hep-ex/9503002](https://arxiv.org/abs/hep-ex/9503002).
- [3450]
- [3451]
- [3452] [15] S. Abachi et al., “Observation of the top quark”, *Phys. Rev. Lett.*, vol. 74, pp. 2632–2637, 1995. DOI: [10.1103/PhysRevLett.74.2632](https://doi.org/10.1103/PhysRevLett.74.2632). arXiv: [hep-ex/9503003](https://arxiv.org/abs/hep-ex/9503003).
- [3453]
- [3454]
- [3455] [16] A. M. Sirunyan et al., “Search for heavy Higgs bosons decaying to a top quark pair in proton-proton collisions at $\sqrt{s} = 13$ TeV”, *JHEP*, vol. 04, p. 171, 2020, [Erratum: *JHEP* 03, 187 (2022)]. DOI: [10.1007/JHEP04\(2020\)171](https://doi.org/10.1007/JHEP04(2020)171). arXiv: [1908.01115 \[hep-ex\]](https://arxiv.org/abs/1908.01115).
- [3456]
- [3457]
- [3458]
- [3459] [17] W. Bernreuther, A. Brandenburg, Z. G. Si, and P. Uwer, “Top quark pair production and decay at hadron colliders”, *Nucl. Phys. B*, vol. 690, pp. 81–137, 2004. DOI: [10.1016/j.nuclphysb.2004.04.019](https://doi.org/10.1016/j.nuclphysb.2004.04.019). arXiv: [hep-ph/0403035](https://arxiv.org/abs/hep-ph/0403035).
- [3460]
- [3461]
- [3462]
- [3463] [18] F. Maltoni, C. Severi, S. Tentori, and E. Vryonidou, “Quantum detection of new physics in top-quark pair production at the LHC”, *JHEP*, vol. 03, p. 099, 2024. DOI: [10.1007/JHEP03\(2024\)099](https://doi.org/10.1007/JHEP03(2024)099). arXiv: [2401.08751 \[hep-ph\]](https://arxiv.org/abs/2401.08751).
- [3464]
- [3465]
- [3466] [19] A. Czarnecki, M. Jezabek, and J. H. Kuhn, “Lepton Spectra From Decays of Polarized Top Quarks”, *Nucl. Phys. B*, vol. 351, pp. 70–80, 1991. DOI: [10.1016/0550-3213\(91\)90082-9](https://doi.org/10.1016/0550-3213(91)90082-9).
- [3467]
- [3468]
- [3469] [20] W. Bernreuther, A. Brandenburg, Z. G. Si, and P. Uwer, “Spin properties of top quark pairs produced at hadron colliders”, *Acta Phys. Polon. B*, vol. 34, K. Fialkowski, M. Jezabek, and M. Rozanska, Eds., pp. 4477–4490, 2003. arXiv: [hep-ph/0304244](https://arxiv.org/abs/hep-ph/0304244).
- [3470]
- [3471]
- [3472]
- [3473] [21] V. Khachatryan et al., “Measurements of $t\bar{t}$ spin correlations and top quark polarization using dilepton final states in pp collisions at $\sqrt{s} = 8$ TeV”, *Phys. Rev. D*, vol. 93, no. 5, p. 052007, 2016. DOI: [10.1103/PhysRevD.93.052007](https://doi.org/10.1103/PhysRevD.93.052007). arXiv: [1601.01107 \[hep-ex\]](https://arxiv.org/abs/1601.01107).
- [3474]
- [3475]
- [3476]
- [3477] [22] A. M. Sirunyan et al., “Measurement of the top quark polarization and $t\bar{t}$ spin correlations using dilepton final states in proton-proton collisions at $\sqrt{s} = 13$ TeV”, *Phys. Rev. D*, vol. 100, no. 7, p. 072002, 2019. DOI: [10.1103/PhysRevD.100.072002](https://doi.org/10.1103/PhysRevD.100.072002). arXiv: [1907.03729 \[hep-ex\]](https://arxiv.org/abs/1907.03729).
- [3478]
- [3479]
- [3480]

- 3481 [23] A. Hayrapetyan et al., “Measurements of polarization and spin correlation
3482 and observation of entanglement in top quark pairs using lepton+jets events
3483 from proton-proton collisions at $\sqrt{s} = 13$ TeV”, *Phys. Rev. D*, vol. 110, no. 11,
3484 p. 112016, 2024. DOI: [10.1103/PhysRevD.110.112016](https://doi.org/10.1103/PhysRevD.110.112016). arXiv: [2409.11067](https://arxiv.org/abs/2409.11067)
3485 [hep-ex].
- 3486 [24] A. Hayrapetyan et al., “Observation of quantum entanglement in top quark
3487 pair production in proton–proton collisions at $\sqrt{s} = 13$ TeV”, *Rept. Prog.
3488 Phys.*, vol. 87, no. 11, p. 117801, 2024. DOI: [10.1088/1361-6633/ad7e4d](https://doi.org/10.1088/1361-6633/ad7e4d).
3489 arXiv: [2406.03976](https://arxiv.org/abs/2406.03976) [hep-ex].
- 3490 [25] G. Aad et al., “Observation of quantum entanglement with top quarks at
3491 the ATLAS detector”, *Nature*, vol. 633, no. 8030, pp. 542–547, 2024. DOI:
3492 [10.1038/s41586-024-07824-z](https://doi.org/10.1038/s41586-024-07824-z). arXiv: [2311.07288](https://arxiv.org/abs/2311.07288) [hep-ex].
- 3493 [26] A. A. Anuar, “Top Quark Spin and Polarization Properties in Searches for
3494 New Phenomena with the CMS Detector at the LHC”, PhD thesis, DESY,
3495 Hamburg, 2019.
- 3496 [27] W. Bernreuther, P. Galler, Z.-G. Si, and P. Uwer, “Production of heavy Higgs
3497 bosons and decay into top quarks at the LHC. II: Top-quark polarization and
3498 spin correlation effects”, *Phys. Rev. D*, vol. 95, no. 9, p. 095012, 2017. DOI:
3499 [10.1103/PhysRevD.95.095012](https://doi.org/10.1103/PhysRevD.95.095012). arXiv: [1702.06063](https://arxiv.org/abs/1702.06063) [hep-ph].
- 3500 [28] W. Bernreuther, D. Heisler, and Z.-G. Si, “A set of top quark spin correlation
3501 and polarization observables for the LHC: Standard Model predictions and
3502 new physics contributions”, *JHEP*, vol. 12, p. 026, 2015. DOI: [10.1007/JHEP12\(2015\)026](https://doi.org/10.1007/JHEP12(2015)026). arXiv: [1508.05271](https://arxiv.org/abs/1508.05271) [hep-ph].
- 3504 [29] V. S. Fadin, V. A. Khoze, and T. Sjöstrand, “On the threshold behaviour
3505 of heavy top production”, *Z. Phys. C*, vol. 48, p. 613, 1990. DOI: [10.1007/BF01614696](https://doi.org/10.1007/BF01614696).
- 3507 [30] Y. Kiyo, J. H. Kuhn, S. Moch, M. Steinhauser, and P. Uwer, “Top-quark
3508 pair production near threshold at LHC”, *Eur. Phys. J. C*, vol. 60, pp. 375–
3509 386, 2009. DOI: [10.1140/epjc/s10052-009-0892-7](https://doi.org/10.1140/epjc/s10052-009-0892-7). arXiv: [0812.0919](https://arxiv.org/abs/0812.0919)
3510 [hep-ph].
- 3511 [31] Y. Sumino and H. Yokoya, “Bound-state effects on kinematical distributions
3512 of top quarks at hadron colliders”, *JHEP*, vol. 09, p. 034, 2010, [Erratum:
3513 *JHEP* 06, 037 (2016)]. DOI: [10.1007/JHEP09\(2010\)034](https://doi.org/10.1007/JHEP09(2010)034). arXiv: [1007.0075](https://arxiv.org/abs/1007.0075)
3514 [hep-ph].
- 3515 [32] W.-L. Ju, G. Wang, X. Wang, X. Xu, Y. Xu, and L. L. Yang, “Top quark
3516 pair production near threshold: single/double distributions and mass deter-
3517 mination”, *JHEP*, vol. 06, p. 158, 2020. DOI: [10.1007/JHEP06\(2020\)158](https://doi.org/10.1007/JHEP06(2020)158).
3518 arXiv: [2004.03088](https://arxiv.org/abs/2004.03088) [hep-ph].

- [33] M. V. Garzelli, G. Limatola, S. .-. Moch, M. Steinhauser, and O. Zenaiev, “Updated predictions for toponium production at the LHC”, Dec. 2024. arXiv: 2412.16685 [hep-ph].
- [34] F. Maltoni, C. Severi, S. Tentori, and E. Vryonidou, “Quantum tops at circular lepton colliders”, *JHEP*, vol. 09, p. 001, 2024. DOI: 10.1007/JHEP09(2024)001. arXiv: 2404.08049 [hep-ph].
- [35] B. Fuks, K. Hagiwara, K. Ma, and Y.-J. Zheng, “Signatures of toponium formation in LHC run 2 data”, *Phys. Rev. D*, vol. 104, no. 3, p. 034023, 2021. DOI: 10.1103/PhysRevD.104.034023. arXiv: 2102.11281 [hep-ph].
- [36] J. A. Aguilar-Saavedra, “Toponium hunter’s guide”, *Phys. Rev. D*, vol. 110, no. 5, p. 054032, 2024. DOI: 10.1103/PhysRevD.110.054032. arXiv: 2407.20330 [hep-ph].
- [37] B. Fuks, K. Hagiwara, K. Ma, and Y.-J. Zheng, “Simulating toponium formation signals at the LHC”, *Eur. Phys. J. C*, vol. 85, no. 2, p. 157, 2025. DOI: 10.1140/epjc/s10052-025-13853-3. arXiv: 2411.18962 [hep-ph].
- [38] CMS Collaboration, “Search for dark matter produced in association with a single top quark or a top quark pair in proton-proton collisions at $\sqrt{s} = 13$ TeV”, CERN, Geneva, Tech. Rep., 2024. [Online]. Available: <https://cds.cern.ch/record/2895470>.
- [39] W. Bernreuther, P. Galler, C. Mellein, Z. G. Si, and P. Uwer, “Production of heavy Higgs bosons and decay into top quarks at the LHC”, *Phys. Rev. D*, vol. 93, no. 3, p. 034032, 2016. DOI: 10.1103/PhysRevD.93.034032. arXiv: 1511.05584 [hep-ph].
- [40] R. D. Ball et al., “Parton distributions from high-precision collider data”, *Eur. Phys. J. C*, vol. 77, p. 663, 2017. DOI: 10.1140/epjc/s10052-017-5199-5. arXiv: 1706.00428 [hep-ph].
- [41] T. D. Lee, “A Theory of Spontaneous T Violation”, *Phys. Rev. D*, vol. 8, G. Feinberg, Ed., pp. 1226–1239, 1973. DOI: 10.1103/PhysRevD.8.1226.
- [42] G. C. Branco, P. M. Ferreira, L. Lavoura, M. N. Rebelo, M. Sher, and J. P. Silva, “Theory and phenomenology of two-Higgs-doublet models”, *Phys. Rept.*, vol. 516, pp. 1–102, 2012. DOI: 10.1016/j.physrep.2012.02.002. arXiv: 1106.0034 [hep-ph].
- [43] H. E. Haber and G. L. Kane, “The Search for Supersymmetry: Probing Physics Beyond the Standard Model”, *Phys. Rept.*, vol. 117, pp. 75–263, 1985. DOI: 10.1016/0370-1573(85)90051-1.
- [44] J. E. Kim, “Light Pseudoscalars, Particle Physics and Cosmology”, *Phys. Rept.*, vol. 150, pp. 1–177, 1987. DOI: 10.1016/0370-1573(87)90017-2.

- 3556 [45] R. D. Peccei and H. R. Quinn, “CP Conservation in the Presence of In-
 3557 instantons”, *Phys. Rev. Lett.*, vol. 38, pp. 1440–1443, 1977. DOI: 10.1103/
 3558 PhysRevLett.38.1440.
- 3559 [46] R. D. Peccei and H. R. Quinn, “Constraints Imposed by CP Conservation in
 3560 the Presence of Instantons”, *Phys. Rev. D*, vol. 16, pp. 1791–1797, 1977. DOI:
 3561 10.1103/PhysRevD.16.1791.
- 3562 [47] S. Weinberg, “A New Light Boson?”, *Phys. Rev. Lett.*, vol. 40, pp. 223–226,
 3563 1978. DOI: 10.1103/PhysRevLett.40.223.
- 3564 [48] F. Wilczek, “Problem of Strong P and T Invariance in the Presence of
 3565 Instantons”, *Phys. Rev. Lett.*, vol. 40, pp. 279–282, 1978. DOI: 10.1103/
 3566 PhysRevLett.40.279.
- 3567 [49] L. Di Luzio, M. Giannotti, E. Nardi, and L. Visinelli, “The landscape of
 3568 QCD axion models”, *Phys. Rept.*, vol. 870, pp. 1–117, 2020. DOI: 10.1016/
 3569 j.physrep.2020.06.002. arXiv: 2003.01100 [hep-ph].
- 3570 [50] J. E. Kim, “Weak Interaction Singlet and Strong CP Invariance”, *Phys. Rev.
 3571 Lett.*, vol. 43, p. 103, 1979. DOI: 10.1103/PhysRevLett.43.103.
- 3572 [51] M. A. Shifman, A. I. Vainshtein, and V. I. Zakharov, “Can Confinement En-
 3573 sure Natural CP Invariance of Strong Interactions?”, *Nucl. Phys. B*, vol. 166,
 3574 pp. 493–506, 1980. DOI: 10.1016/0550-3213(80)90209-6.
- 3575 [52] M. Dine, W. Fischler, and M. Srednicki, “A Simple Solution to the Strong
 3576 CP Problem with a Harmless Axion”, *Phys. Lett. B*, vol. 104, pp. 199–202,
 3577 1981. DOI: 10.1016/0370-2693(81)90590-6.
- 3578 [53] A. R. Zhitnitsky, “On Possible Suppression of the Axion Hadron Interac-
 3579 tions”, *Sov. J. Nucl. Phys.*, vol. 31, p. 260, 1980.
- 3580 [54] H. Georgi, D. B. Kaplan, and L. Randall, “Manifesting the Invisible Axion at
 3581 Low-energies”, *Phys. Lett. B*, vol. 169, pp. 73–78, 1986. DOI: 10.1016/0370-
 3582 2693(86)90688-X.
- 3583 [55] V. A. Rubakov, “Grand unification and heavy axion”, *JETP Lett.*, vol. 65,
 3584 pp. 621–624, 1997. DOI: 10.1134/1.567390. arXiv: hep-ph/9703409.
- 3585 [56] B. Holdom and M. E. Peskin, “Raising the Axion Mass”, *Nucl. Phys. B*,
 3586 vol. 208, pp. 397–412, 1982. DOI: 10.1016/0550-3213(82)90228-0.
- 3587 [57] S. Dimopoulos, A. Hook, J. Huang, and G. Marques-Tavares, “A collider ob-
 3588 servable QCD axion”, *JHEP*, vol. 11, p. 052, 2016. DOI: 10.1007/JHEP11(2016)
 3589 052. arXiv: 1606.03097 [hep-ph].
- 3590 [58] T. Gherghetta, N. Nagata, and M. Shifman, “A Visible QCD Axion from an
 3591 Enlarged Color Group”, *Phys. Rev. D*, vol. 93, no. 11, p. 115010, 2016. DOI:
 3592 10.1103/PhysRevD.93.115010. arXiv: 1604.01127 [hep-ph].

- 3593 [59] M. E. Peskin and D. V. Schroeder, *An Introduction to quantum field theory*.
3594 Reading, USA: Addison-Wesley, 1995, ISBN: 978-0-201-50397-5, 978-0-429-
3595 50355-9, 978-0-429-49417-8. DOI: [10.1201/9780429503559](https://doi.org/10.1201/9780429503559).
- 3596 [60] G. Altarelli and G. Parisi, “Asymptotic Freedom in Parton Language”, *Nucl.*
3597 *Phys. B*, vol. 126, pp. 298–318, 1977. DOI: [10.1016/0550-3213\(77\)90384-4](https://doi.org/10.1016/0550-3213(77)90384-4).
- 3598 [61] P. Skands, “Introduction to QCD”, in *Theoretical Advanced Study Institute*
3599 *in Elementary Particle Physics: Searching for New Physics at Small and*
3600 *Large Scales*, 2013, pp. 341–420. DOI: [10.1142/9789814525220_0008](https://doi.org/10.1142/9789814525220_0008). arXiv:
3601 [1207.2389 \[hep-ph\]](https://arxiv.org/abs/1207.2389).
- 3602 [62] F. Maltoni and T. Stelzer, “MadEvent: Automatic event generation with
3603 MadGraph”, *JHEP*, vol. 02, p. 027, 2003. DOI: [10.1088/1126-6708/2003/02/027](https://doi.org/10.1088/1126-6708/2003/02/027). arXiv: [hep-ph/0208156](https://arxiv.org/abs/hep-ph/0208156).
- 3605 [63] M. D. Schwartz, *Quantum Field Theory and the Standard Model*. Cambridge
3606 University Press, Mar. 2014, ISBN: 978-1-107-03473-0, 978-1-107-03473-0.
- 3607 [64] P. Nason and B. Webber, “Next-to-Leading-Order Event Generators”, *Ann.*
3608 *Rev. Nucl. Part. Sci.*, vol. 62, pp. 187–213, 2012. DOI: [10.1146/annurev-nucl-102711-094928](https://doi.org/10.1146/annurev-nucl-102711-094928). arXiv: [1202.1251 \[hep-ph\]](https://arxiv.org/abs/1202.1251).
- 3610 [65] J. Alwall et al., “The automated computation of tree-level and next-to-
3611 leading order differential cross sections, and their matching to parton shower
3612 simulations”, *JHEP*, vol. 07, p. 079, 2014. DOI: [10.1007/JHEP07\(2014\)079](https://doi.org/10.1007/JHEP07(2014)079).
3613 arXiv: [1405.0301 \[hep-ph\]](https://arxiv.org/abs/1405.0301).
- 3614 [66] C. Degrande, C. Duhr, B. Fuks, D. Grellscheid, O. Mattelaer, and T. Re-
3615 iter, “UFO - The Universal FeynRules Output”, *Comput. Phys. Commun.*,
3616 vol. 183, pp. 1201–1214, 2012. DOI: [10.1016/j.cpc.2012.01.022](https://doi.org/10.1016/j.cpc.2012.01.022). arXiv:
3617 [1108.2040 \[hep-ph\]](https://arxiv.org/abs/1108.2040).
- 3618 [67] P. Nason, “A new method for combining NLO QCD with shower Monte Carlo
3619 algorithms”, *JHEP*, vol. 11, p. 040, 2004. DOI: [10.1088/1126-6708/2004/11/040](https://doi.org/10.1088/1126-6708/2004/11/040). arXiv: [hep-ph/0409146](https://arxiv.org/abs/hep-ph/0409146).
- 3621 [68] S. Frixione, P. Nason, and C. Oleari, “Matching NLO QCD computations
3622 with parton shower simulations: The POWHEG method”, *JHEP*, vol. 11,
3623 p. 070, 2007. DOI: [10.1088/1126-6708/2007/11/070](https://doi.org/10.1088/1126-6708/2007/11/070). arXiv: [0709.2092](https://arxiv.org/abs/0709.2092)
3624 [hep-ph].
- 3625 [69] S. Alioli, P. Nason, C. Oleari, and E. Re, “A general framework for imple-
3626 menting NLO calculations in shower Monte Carlo programs: The POWHEG
3627 BOX”, *JHEP*, vol. 06, p. 043, 2010. DOI: [10.1007/JHEP06\(2010\)043](https://doi.org/10.1007/JHEP06(2010)043). arXiv:
3628 [1002.2581 \[hep-ph\]](https://arxiv.org/abs/1002.2581).

- 3629 [70] S. Frixione, G. Ridolfi, and P. Nason, “A positive-weight next-to-leading-
 3630 order Monte Carlo for heavy flavour hadroproduction”, *JHEP*, vol. 09, p. 126,
 3631 2007. DOI: 10.1088/1126-6708/2007/09/126. arXiv: 0707.3088 [hep-ph].
- 3632 [71] T. Sjöstrand et al., “An introduction to PYTHIA8.2”, *Comput. Phys. Commun.*, vol. 191, p. 159, 2015. DOI: 10.1016/j.cpc.2015.01.024. arXiv:
 3633 1410.3012 [hep-ph].
- 3635 [72] C. Bierlich et al., “A comprehensive guide to the physics and usage of PYTHIA
 3636 8.3”, *SciPost Phys. Codeb.*, vol. 2022, p. 8, 2022. DOI: 10.21468/SciPostPhysCodeb.
 3637 8. arXiv: 2203.11601 [hep-ph].
- 3638 [73] J. Bellm et al., “HERWIG7.0/HERWIG++3.0 release note”, *Eur. Phys. J. C*, vol. 76, p. 196, 2016. DOI: 10.1140/epjc/s10052-016-4018-8. arXiv:
 3639 1512.01178 [hep-ph].
- 3641 [74] M. Bähr et al., “HERWIG++ physics and manual”, *Eur. Phys. J. C*, vol. 58,
 3642 p. 639, 2008. DOI: 10.1140/epjc/s10052-008-0798-9. arXiv: 0803.0883
 3643 [hep-ph].
- 3644 [75] P. Skands, S. Carrazza, and J. Rojo, “Tuning PYTHIA 8.1: the Monash 2013
 3645 Tune”, *Eur. Phys. J. C*, vol. 74, no. 8, p. 3024, 2014. DOI: 10.1140/epjc/
 3646 s10052-014-3024-y. arXiv: 1404.5630 [hep-ph].
- 3647 [76] A. M. Sirunyan et al., “Extraction and validation of a new set of CMS Pythia
 3648 8 tunes from underlying-event measurements”, *Eur. Phys. J. C*, vol. 80, p. 4,
 3649 2020. DOI: 10.1140/epjc/s10052-019-7499-4. arXiv: 1903.12179 [hep-
 3650 ex].
- 3651 [77] B. Andersson, G. Gustafson, G. Ingelman, and T. Sjostrand, “Parton Frag-
 3652 mentation and String Dynamics”, *Phys. Rept.*, vol. 97, pp. 31–145, 1983. DOI:
 3653 10.1016/0370-1573(83)90080-7.
- 3654 [78] T. Sjostrand, “Jet Fragmentation of Nearby Partons”, *Nucl. Phys. B*, vol. 248,
 3655 pp. 469–502, 1984. DOI: 10.1016/0550-3213(84)90607-2.
- 3656 [79] S. Argyropoulos and T. Sjöstrand, “Effects of color reconnection on $t\bar{t}$ final
 3657 states at the LHC”, *JHEP*, vol. 11, p. 043, 2014. DOI: 10.1007/JHEP11(2014)
 3658 043. arXiv: 1407.6653 [hep-ph].
- 3659 [80] J. R. Christiansen and P. Z. Skands, “String Formation Beyond Leading
 3660 Colour”, *JHEP*, vol. 08, p. 003, 2015. DOI: 10.1007/JHEP08(2015)003.
 3661 arXiv: 1505.01681 [hep-ph].
- 3662 [81] A. M. Sirunyan et al., “Pileup mitigation at CMS in 13 TeV data”, *JINST*,
 3663 vol. 15, no. 09, P09018, 2020. DOI: 10.1088/1748-0221/15/09/P09018.
 3664 arXiv: 2003.00503 [hep-ex].

- [82] A. M. Sirunyan et al., “Precision luminosity measurement in proton-proton collisions at $\sqrt{s} = 13$ TeV in 2015 and 2016 at CMS”, *Eur. Phys. J. C*, vol. 81, no. 9, p. 800, 2021. DOI: 10.1140/epjc/s10052-021-09538-2. arXiv: 2104.01927 [hep-ex].
- [83] S. Agostinelli et al., “GEANT4 — a simulation toolkit”, *Nucl. Instrum. Meth. A*, vol. 506, p. 250, 2003. DOI: 10.1016/S0168-9002(03)01368-8.
- [84] “LHC Design Report Vol.1: The LHC Main Ring”, O. S. Bruning et al., Eds., Jun. 2004. DOI: 10.5170/CERN-2004-003-V-1.
- [85] G. Aad et al., “The ATLAS Experiment at the CERN Large Hadron Collider”, *JINST*, vol. 3, S08003, 2008. DOI: 10.1088/1748-0221/3/08/S08003.
- [86] A. A. Alves Jr. et al., “The LHCb Detector at the LHC”, *JINST*, vol. 3, S08005, 2008. DOI: 10.1088/1748-0221/3/08/S08005.
- [87] K. Aamodt et al., “The ALICE experiment at the CERN LHC”, *JINST*, vol. 3, S08002, 2008. DOI: 10.1088/1748-0221/3/08/S08002.
- [88] I. Zurbano Fernandez et al., “High-Luminosity Large Hadron Collider (HL-LHC): Technical design report”, vol. 10/2020, I. Béjar Alonso, O. Brüning, P. Fessia, L. Rossi, L. Tavian, and M. Zerlauth, Eds., Dec. 2020. DOI: 10.23731/CYRM-2020-0010.
- [89] CMS Collaboration, “Technical Proposal for the Phase-II Upgrade of the CMS Detector”, Geneva, Tech. Rep., 2015. DOI: 10.17181/CERN.VU8I.D59J. [Online]. Available: <https://cds.cern.ch/record/2020886>.
- [90] A. Hayrapetyan et al., “Development of the CMS detector for the CERN LHC Run 3”, *JINST*, vol. 19, P05064, 2024. DOI: 10.1088/1748-0221/19/05/P05064. arXiv: 2309.05466 [physics.ins-det].
- [91] D. Barney, *CMS Detector Slice*, 2016. [Online]. Available: <https://cds.cern.ch/record/2120661>.
- [92] S. Chatrchyan et al., “Description and performance of track and primary-vertex reconstruction with the CMS tracker”, *JINST*, vol. 9, P10009, 2014. DOI: 10.1088/1748-0221/9/10/P10009. arXiv: 1405.6569 [physics.ins-det].
- [93] W. Adam et al., “The CMS Phase-1 Pixel Detector Upgrade”, *JINST*, vol. 16, no. 02, P02027, 2021. DOI: 10.1088/1748-0221/16/02/P02027. arXiv: 2012.14304 [physics.ins-det].
- [94] “The CMS electromagnetic calorimeter project: Technical Design Report”, Tech. Rep., 1997.

- 3700 [95] A. M. Sirunyan et al., “Electron and photon reconstruction and identifica-
3701 tion with the CMS experiment at the CERN LHC”, *JINST*, vol. 16, no. 05,
3702 P05014, 2021. DOI: 10.1088/1748-0221/16/05/P05014. arXiv: 2012.06888
3703 [[hep-ex](#)].
- 3704 [96] “The CMS hadron calorimeter project: Technical Design Report”, Tech. Rep.,
3705 1997.
- 3706 [97] “CMS Technical Design Report for the Phase 1 Upgrade of the Hadron
3707 Calorimeter”, Tech. Rep., Sep. 2012. DOI: 10.2172/1151651.
- 3708 [98] “The CMS muon project: Technical Design Report”, Tech. Rep., 1997.
- 3709 [99] N. Pozzobon, “The CMS Muon System performance during the LHC Run-2”,
3710 CERN, Geneva, Tech. Rep., 2019. DOI: 10.1088/1748-0221/14/11/C11031.
3711 [Online]. Available: <https://cds.cern.ch/record/2701333>.
- 3712 [100] V. Khachatryan et al., “The CMS trigger system”, *JINST*, vol. 12, no. 01,
3713 P01020, 2017. DOI: 10.1088/1748-0221/12/01/P01020. arXiv: 1609.02366
3714 [[physics.ins-det](#)].
- 3715 [101] A. M. Sirunyan et al., “Performance of the CMS Level-1 trigger in proton-
3716 proton collisions at $\sqrt{s} = 13$ TeV”, *JINST*, vol. 15, no. 10, P10017, 2020.
3717 DOI: 10.1088/1748-0221/15/10/P10017. arXiv: 2006.10165 [[hep-ex](#)].
- 3718 [102] W. Adam et al., “The CMS high level trigger”, *Eur. Phys. J. C*, vol. 46,
3719 pp. 605–667, 2006. DOI: 10.1140/epjc/s2006-02495-8. arXiv: [hep-ex/0512077](#).
- 3721 [103] S. Varghese, “CMS High Level Trigger Performance for Run 3”, *PoS*, vol. EPS-
3722 HEP2023, p. 517, 2023. DOI: 10.22323/1.449.0517.
- 3723 [104] A. M. Sirunyan et al., “Particle-flow reconstruction and global event descrip-
3724 tion with the CMS detector”, *JINST*, vol. 12, P10003, 2017. DOI: 10.1088/
3725 1748-0221/12/10/P10003. arXiv: 1706.04965 [[physics.ins-det](#)].
- 3726 [105] D. Bertolini, P. Harris, M. Low, and N. Tran, “Pileup Per Particle Identifica-
3727 tion”, *JHEP*, vol. 10, p. 059, 2014. DOI: 10.1007/JHEP10(2014)059. arXiv:
3728 1407.6013 [[hep-ph](#)].
- 3729 [106] M. Cacciari, G. P. Salam, and G. Soyez, “The anti- k_t jet clustering algo-
3730 rithm”, *JHEP*, vol. 04, p. 063, 2008. DOI: 10.1088/1126-6708/2008/04/063.
3731 arXiv: 0802.1189 [[hep-ph](#)].
- 3732 [107] E. Bols, J. Kieseler, M. Verzetti, M. Stoye, and A. Stakia, “Jet Flavour
3733 Classification Using DeepJet”, *JINST*, vol. 15, no. 12, P12012, 2020. DOI:
3734 10.1088/1748-0221/15/12/P12012. arXiv: 2008.10519 [[hep-ex](#)].

- 3735 [108] A. M. Sirunyan et al., “Performance of missing transverse momentum re-
3736 construction in proton-proton collisions at $\sqrt{s} = 13$ TeV using the CMS
3737 detector”, *JINST*, vol. 14, no. 07, P07004, 2019. DOI: 10.1088/1748-0221/
3738 14/07/P07004. arXiv: 1903.06078 [hep-ex].
- 3739 [109] G. Cowan, K. Cranmer, E. Gross, and O. Vitells, “Asymptotic formulae for
3740 likelihood-based tests of new physics”, *Eur. Phys. J. C*, vol. 71, p. 1554, 2011,
3741 [Erratum: Eur.Phys.J.C 73, 2501 (2013)]. DOI: 10.1140/epjc/s10052-011-
3742 1554-0. arXiv: 1007.1727 [physics.data-an].
- 3743 [110] S. S. Wilks, “The large-sample distribution of the likelihood ratio for testing
3744 composite hypotheses”, *Annals Math. Statist.*, vol. 9, no. 1, pp. 60–62, 1938.
3745 DOI: 10.1214/aoms/1177732360.
- 3746 [111] A. Wald, “Tests of statistical hypotheses concerning several parameters when
3747 the number of observations is large”, *Trans. Am. Math. Soc.*, vol. 54, no. 3,
3748 pp. 462–482, 1942. DOI: 10.1090/S0002-9947-1943-0012401-3.
- 3749 [112] T. Junk, “Confidence level computation for combining searches with small
3750 statistics”, *Nucl. Instrum. Meth. A*, vol. 434, p. 435, 1999. DOI: 10.1016/
3751 S0168-9002(99)00498-2. arXiv: hep-ex/9902006.
- 3752 [113] A. L. Read, “Presentation of search results: The CL_s technique”, *J. Phys. G*,
3753 vol. 28, p. 2693, 2002. DOI: 10.1088/0954-3899/28/10/313.
- 3754 [114] A. Hayrapetyan et al., “The CMS Statistical Analysis and Combination Tool:
3755 Combine”, *Comput. Softw. Big Sci.*, vol. 8, no. 1, p. 19, 2024. DOI: 10.1007/
3756 s41781-024-00121-4. arXiv: 2404.06614 [physics.data-an].
- 3757 [115] L. Heinrich, M. Feickert, and G. Stark, *pyhf: v0.7.4*, version 0.7.4, <https://github.com/scikit-hep/pyhf/releases/tag/v0.7.4>. DOI: 10.5281/zenodo.1169739. [Online].
3758 Available: <https://doi.org/10.5281/zenodo.1169739>.
- 3760 [116] L. Heinrich, M. Feickert, G. Stark, and K. Cranmer, “Pyhf: Pure-Python
3761 implementation of HistFactory statistical models”, *Journal of Open Source
3762 Software*, vol. 6, no. 58, p. 2823, 2021. DOI: 10.21105/joss.02823. [Online].
3763 Available: <https://doi.org/10.21105/joss.02823>.
- 3764 [117] CMS Collaboration, “First measurement of the top quark pair production
3765 cross section in proton-proton collisions at $\sqrt{s} = 13.6$ TeV”, CMS Physics
3766 Analysis Summary CMS-PAS-TOP-22-012, 2022. [Online]. Available: <https://cds.cern.ch/record/2834110>.
- 3768 [118] G. Aad et al., “Measurement of the $t\bar{t}$ cross section and its ratio to the
3769 Z production cross section using pp collisions at $\sqrt{s} = 13.6$ TeV with the
3770 ATLAS detector”, *Phys. Lett. B*, vol. 848, p. 138376, 2024. DOI: 10.1016/
3771 j.physletb.2023.138376. arXiv: 2308.09529 [hep-ex].

- [119] M. Czakon and A. Mitov, “TOP++: A program for the calculation of the top-pair cross-section at hadron colliders”, *Comput. Phys. Commun.*, vol. 185, p. 2930, 2014. DOI: 10.1016/j.cpc.2014.06.021. arXiv: 1112.5675 [hep-ph].
- [120] J. Campbell, T. Neumann, and Z. Sullivan, “Single-top-quark production in the t -channel at NNLO”, *JHEP*, vol. 02, p. 040, 2021. DOI: 10.1007/JHEP02(2021)040. arXiv: 2012.01574 [hep-ph].
- [121] S. Camarda et al., “DYTURBO: Fast predictions for Drell–Yan processes”, *Eur. Phys. J. C*, vol. 80, p. 251, 2020. DOI: 10.1140/epjc/s10052-020-7757-5. arXiv: 1910.07049 [hep-ph].
- [122] M. Grazzini, S. Kallweit, and M. Wiesemann, “Fully differential NNLO computations with MATRIX”, *Eur. Phys. J. C*, vol. 78, p. 537, 2018. DOI: 10.1140/epjc/s10052-018-5771-7. arXiv: 1711.06631 [hep-ph].
- [123] N. Kidonakis and N. Yamanaka, “Higher-order corrections for tW production at high-energy hadron colliders”, *JHEP*, vol. 05, p. 278, 2021. DOI: 10.1007/JHEP05(2021)278. arXiv: 2102.11300 [hep-ph].
- [124] A. M. Sirunyan et al., “Performance of the CMS muon detector and muon reconstruction with proton-proton collisions at $\sqrt{s} = 13$ TeV”, *JINST*, vol. 13, no. 06, P06015, 2018. DOI: 10.1088/1748-0221/13/06/P06015. arXiv: 1804.04528 [physics.ins-det].
- [125] A. M. Sirunyan et al., “Identification of heavy-flavour jets with the CMS detector in pp collisions at 13 TeV”, *JINST*, vol. 13, no. 05, P05011, 2018. DOI: 10.1088/1748-0221/13/05/P05011. arXiv: 1712.07158 [physics.ins-det].
- [126] CMS Collaboration, “Jet energy scale and resolution in the CMS experiment in pp collisions at 8 TeV”, *JINST*, vol. 12, P02014, 2017. DOI: 10.1088/1748-0221/12/02/P02014. arXiv: 1607.03663 [hep-ex].
- [127] A. M. Sirunyan et al., “Search for dark matter particles produced in association with a top quark pair at $\sqrt{s} = 13$ TeV”, *Phys. Rev. Lett.*, vol. 122, no. 1, p. 011803, 2019. DOI: 10.1103/PhysRevLett.122.011803. arXiv: 1807.06522 [hep-ex].
- [128] CMS Collaboration, “Luminosity monitoring with z counting in early 2022 data”, CMS Detector Performance Note CMS-DP-2023-003, 2023. [Online]. Available: <https://cds.cern.ch/record/2851655>.
- [129] CMS Collaboration, “Luminosity measurement in proton-proton collisions at 13.6 TeV in 2022 at CMS”, CERN, Geneva, CMS Physics Analysis Summary, 2024. [Online]. Available: <http://cds.cern.ch/record/2890833>.

- [3809] [130] M. Cacciari, S. Frixione, M. L. Mangano, P. Nason, and G. Ridolfi, “The $t\bar{t}$ cross-section at 1.8 and 1.96 TeV: A study of the systematics due to parton densities and scale dependence”, *JHEP*, vol. 04, p. 068, 2004. doi: 10.1088/1126-6708/2004/04/068. arXiv: hep-ph/0303085.
- [3810]
- [3811]
- [3812]
- [3813] [131] J. Butterworth et al., “PDF4LHC recommendations for LHC Run II”, *J. Phys. G*, vol. 43, p. 023001, 2016. doi: 10.1088/0954-3899/43/2/023001. arXiv: 1510.03865 [hep-ph].
- [3814]
- [3815]
- [3816] [132] CMS Collaboration, “Investigations of the impact of the parton shower tuning in PYTHIA 8 in the modelling of $t\bar{t}$ at $\sqrt{s} = 8$ and 13 TeV”, CMS Physics Analysis Summary CMS-PAS-TOP-16-021, 2016. [Online]. Available: <https://cds.cern.ch/record/2235192>.
- [3817]
- [3818]
- [3819]
- [3820] [133] R. Barlow and C. Beeston, “Fitting using finite Monte Carlo samples”, *Comput. Phys. Commun.*, vol. 77, p. 219, 1993. doi: 10.1016/0010-4655(93)90005-W.
- [3821]
- [3822]
- [3823] [134] S. Chatrchyan et al., “Measurement of the $t\bar{t}$ production cross section in the all-jet final state in pp collisions at $\sqrt{s} = 7$ TeV”, *JHEP*, vol. 05, p. 065, 2013. doi: 10.1007/JHEP05(2013)065. arXiv: 1302.0508 [hep-ex].
- [3824]
- [3825]
- [3826] [135] V. Khachatryan et al., “Measurement of the $t\bar{t}$ production cross section in the all-jets final state in pp collisions at $\sqrt{s} = 8$ TeV”, *Eur. Phys. J. C*, vol. 76, p. 128, 2016. doi: 10.1140/epjc/s10052-016-3956-5. arXiv: 1509.06076 [hep-ex].
- [3827]
- [3828]
- [3829]
- [3830] [136] V. Khachatryan et al., “Measurements of the $t\bar{t}$ production cross section in lepton+jets final states in pp collisions at 8 TeV and ratio of 8 to 7 TeV cross sections”, *Eur. Phys. J. C*, vol. 77, p. 15, 2017. doi: 10.1140/epjc/s10052-016-4504-z. arXiv: 1602.09024 [hep-ex].
- [3831]
- [3832]
- [3833]
- [3834] [137] V. Khachatryan et al., “Measurement of the $t\bar{t}$ production cross section in the $e\mu$ channel in proton-proton collisions at $\sqrt{s} = 7$ and 8 TeV”, *JHEP*, vol. 08, p. 029, 2016. doi: 10.1007/JHEP08(2016)029. arXiv: 1603.02303 [hep-ex].
- [3835]
- [3836]
- [3837]
- [3838] [138] A. M. Sirunyan et al., “Measurement of the $t\bar{t}$ production cross section, the top quark mass, and the strong coupling constant using dilepton events in pp collisions at $\sqrt{s} = 13$ TeV”, *Eur. Phys. J. C*, vol. 79, p. 368, 2019. doi: 10.1140/epjc/s10052-019-6863-8. arXiv: 1812.10505 [hep-ex].
- [3839]
- [3840]
- [3841]
- [3842] [139] A. M. Sirunyan et al., “Measurement of the top quark pair production cross section in dilepton final states containing one τ lepton in pp collisions at $\sqrt{s} = 13$ TeV”, *JHEP*, vol. 02, p. 191, 2020. doi: 10.1007/JHEP02(2020)191. arXiv: 1911.13204 [hep-ex].
- [3843]
- [3844]
- [3845]

- 3846 [140] A. Tumasyan et al., “Measurement of differential $t\bar{t}$ production cross sections
 3847 in the full kinematic range using lepton+jets events from proton-proton col-
 3848 lisions at $\sqrt{s} = 13$ TeV”, *Phys. Rev. D*, vol. 104, p. 092013, 2021. DOI:
 3849 10.1103/PhysRevD.104.092013. arXiv: 2108.02803 [hep-ex].
- 3850 [141] A. Tumasyan et al., “Measurement of the inclusive $t\bar{t}$ production cross section
 3851 in proton-proton collisions at $\sqrt{s} = 5.02$ TeV”, *JHEP*, vol. 04, p. 144, 2022.
 3852 DOI: 10.1007/JHEP04(2022)144. arXiv: 2112.09114 [hep-ex].
- 3853 [142] M. Czakon, P. Fiedler, and A. Mitov, “Total top-quark pair-production cross
 3854 section at hadron colliders through $\mathcal{O}(\alpha_S^4)$ ”, *Phys. Rev. Lett.*, vol. 110,
 3855 p. 252004, 2013. DOI: 10.1103/PhysRevLett.110.252004. arXiv: 1303.
 3856 6254 [hep-ph].
- 3857 [143] R. Tarrach, “The Pole Mass in Perturbative QCD”, *Nucl. Phys. B*, vol. 183,
 3858 pp. 384–396, 1981. DOI: 10.1016/0550-3213(81)90140-1.
- 3859 [144] M. C. Smith and S. S. Willenbrock, “Top quark pole mass”, *Phys. Rev. Lett.*,
 3860 vol. 79, pp. 3825–3828, 1997. DOI: 10.1103/PhysRevLett.79.3825. arXiv:
 3861 hep-ph/9612329.
- 3862 [145] A. H. Hoang, “What is the Top Quark Mass?”, *Ann. Rev. Nucl. Part. Sci.*,
 3863 vol. 70, pp. 225–255, 2020. DOI: 10.1146/annurev-nucl-101918-023530.
 3864 arXiv: 2004.12915 [hep-ph].
- 3865 [146] M. Aaboud et al., “Probing the quantum interference between singly and
 3866 doubly resonant top-quark production in pp collisions at $\sqrt{s} = 13$ TeV with
 3867 the ATLAS detector”, *Phys. Rev. Lett.*, vol. 121, p. 152002, 2018. DOI: 10.
 3868 1103/PhysRevLett.121.152002. arXiv: 1806.04667 [hep-ex].
- 3869 [147] T. Ježo, J. M. Lindert, and S. Pozzorini, “Resonance-aware NLOPS matching
 3870 for off-shell $t\bar{t} + tW$ production with semileptonic decays”, *JHEP*, vol. 10,
 3871 p. 008, 2023. DOI: 10.1007/JHEP10(2023)008. arXiv: 2307.15653 [hep-ph].
- 3872 [148] T. Ježo and P. Nason, “On the treatment of resonances in next-to-leading
 3873 order calculations matched to a parton shower”, *JHEP*, vol. 12, p. 065, 2015.
 3874 DOI: 10.1007/JHEP12(2015)065. arXiv: 1509.09071 [hep-ph].
- 3875 [149] <https://powhegbox.mib.infn.it>.
- 3876 [150] S. Frixione, E. Laenen, P. Motylinski, and B. R. Webber, “Angular corre-
 3877 lations of lepton pairs from vector boson and top quark decays in Monte Carlo
 3878 simulations”, *JHEP*, vol. 04, p. 081, 2007. DOI: 10.1088/1126-6708/2007/
 3879 04/081. arXiv: hep-ph/0702198.
- 3880 [151] E. Re, “Single-top Wt -channel production matched with parton showers us-
 3881 ing the powheg method”, *Eur. Phys. J. C*, vol. 71, p. 1547, 2011. DOI: 10.
 3882 1140/epjc/s10052-011-1547-z. arXiv: 1009.2450 [hep-ph].

- 3883 [152] S. Frixione, E. Laenen, P. Motylinski, B. R. Webber, and C. D. White,
3884 “Single-top hadroproduction in association with a W boson”, *JHEP*, vol. 07,
3885 p. 029, 2008. DOI: 10.1088/1126-6708/2008/07/029. arXiv: 0805.3067
3886 [hep-ph].
- 3887 [153] T. M. P. Tait, “The tW^- mode of single top production”, *Phys. Rev. D*,
3888 vol. 61, p. 034001, 1999. DOI: 10.1103/PhysRevD.61.034001. arXiv: hep-
3889 ph/9909352.
- 3890 [154] J. M. Campbell, R. K. Ellis, P. Nason, and E. Re, “Top-pair production and
3891 decay at NLO matched with parton showers”, *JHEP*, vol. 04, p. 114, 2015.
3892 DOI: 10.1007/JHEP04(2015)114. arXiv: 1412.1828 [hep-ph].
- 3893 [155] S. Ferrario Ravasio, T. Ježo, P. Nason, and C. Oleari, “A theoretical study of
3894 top-mass measurements at the LHC using NLO+PS generators of increasing
3895 accuracy”, *Eur. Phys. J. C*, vol. 78, p. 458, 2018. DOI: 10.1140/epjc/s10052-018-5909-7. arXiv: 1906.09166 [hep-ph].
- 3896 [156] C. Bierlich et al., “Robust independent validation of experiment and theory:
3897 Rivet version 3”, *SciPost Phys.*, vol. 8, p. 026, 2020. DOI: 10.21468/
3898 SciPostPhys.8.2.026. arXiv: 1912.05451 [hep-ph].
- 3900 [157] M. Cacciari and G. P. Salam, “Pileup subtraction using jet areas”, *Phys. Lett.*
3901 *B*, vol. 659, pp. 119–126, 2008. DOI: 10.1016/j.physletb.2007.09.077.
3902 arXiv: 0707.1378 [hep-ph].
- 3903 [158] M. Cacciari, G. P. Salam, and G. Soyez, “The Catchment Area of Jets”,
3904 *JHEP*, vol. 04, p. 005, 2008. DOI: 10.1088/1126-6708/2008/04/005. arXiv:
3905 0802.1188 [hep-ph].
- 3906 [159] ATLAS Collaboration, “Studies of $t\bar{t}/tW$ interference effects in $b\bar{b}\ell^+\ell^-\nu\bar{\nu}$
3907 final states with POWHEG and MG5_AMC@NLO setups”, ATLAS PUB
3908 Note ATL-PHYS-PUB-2021-042, 2021. [Online]. Available: <https://cds.cern.ch/record/2792254>.
- 3910 [160] H. Brooks and P. Skands, “Coherent showers in decays of colored resonances”,
3911 *Phys. Rev. D*, vol. 100, no. 7, p. 076006, 2019. DOI: 10.1103/PhysRevD.100.
3912 076006. arXiv: 1907.08980 [hep-ph].
- 3913 [161] G. Aad et al., “Measurement of the top-quark mass using a leptonic invariant
3914 mass in pp collisions at $\sqrt{s} = 13$ TeV with the ATLAS detector”, *JHEP*,
3915 vol. 06, p. 019, 2023. DOI: 10.1007/JHEP06(2023)019. arXiv: 2209.00583
3916 [hep-ex].
- 3917 [162] M. Aaboud et al., “Search for Heavy Higgs Bosons A/H Decaying to a Top
3918 Quark Pair in pp Collisions at $\sqrt{s} = 8$ TeV with the ATLAS Detector”, *Phys.*
3919 *Rev. Lett.*, vol. 119, no. 19, p. 191803, 2017. DOI: 10.1103/PhysRevLett.
3920 119.191803. arXiv: 1707.06025 [hep-ex].

- 3921 [163] G. Aad et al., “Search for heavy neutral Higgs bosons decaying into a top
 3922 quark pair in 140 fb^{-1} of proton-proton collision data at $\sqrt{s} = 13 \text{ TeV}$ with the
 3923 ATLAS detector”, *JHEP*, vol. 08, p. 013, 2024. DOI: 10.1007/JHEP08(2024)
 3924 013. arXiv: 2404.18986 [hep-ex].
- 3925 [164] J. Rübenach, “Search for Heavy Higgs Bosons in Conjunction with Neural-
 3926 Network-Driven Reconstruction and Upgrade of the Fast Beam Condition
 3927 Monitor at the CMS Experiment”, PhD thesis, DESY, Hamburg, May 2023.
- 3928 [165] CMS Collaboration, “Simulation of the silicon strip tracker pre-amplifier in
 3929 early 2016 data”, CMS Detector Performance Note CMS-DP-2020-045, 2020.
 3930 [Online]. Available: <https://cds.cern.ch/record/2740688>.
- 3931 [166] M. Aliev, H. Lacker, U. Langenfeld, S. Moch, P. Uwer, and M. Wiedermann,
 3932 “HATHOR: Hadronic top and heavy quarks cross section calculator”, *Comput.
 3933 Phys. Commun.*, vol. 182, p. 1034, 2011. DOI: 10.1016/j.cpc.2010.12.040.
 3934 arXiv: 1007.1327 [hep-ph].
- 3935 [167] P. Kant et al., “HatHor for single top-quark production: Updated predictions
 3936 and uncertainty estimates for single top-quark production in hadronic col-
 3937 lisions”, *Comput. Phys. Commun.*, vol. 191, pp. 74–89, 2015. DOI: 10.1016/
 3938 j.cpc.2015.02.001. arXiv: 1406.4403 [hep-ph].
- 3939 [168] K. Melnikov and F. Petriello, “Electroweak gauge boson production at hadron
 3940 colliders through $\mathcal{O}(\alpha_S^2)$ ”, *Phys. Rev. D*, vol. 74, p. 114017, 2006. DOI: 10.
 3941 1103/PhysRevD.74.114017. arXiv: hep-ph/0609070.
- 3942 [169] Y. Li and F. Petriello, “Combining QCD and electroweak corrections to dilep-
 3943 ton production in FEWZ”, *Phys. Rev. D*, vol. 86, p. 094034, 2012. DOI:
 3944 10.1103/PhysRevD.86.094034. arXiv: 1208.5967 [hep-ph].
- 3945 [170] T. Gehrmann et al., “ W^+W^- Production at Hadron Colliders in Next to Next
 3946 to Leading Order QCD”, *Phys. Rev. Lett.*, vol. 113, no. 21, p. 212001, 2014.
 3947 DOI: 10.1103/PhysRevLett.113.212001. arXiv: 1408.5243 [hep-ph].
- 3948 [171] J. M. Campbell and R. K. Ellis, “MCFM for the Tevatron and the LHC”,
 3949 *Nucl. Phys. B Proc. Suppl.*, vol. 205–206, J. Blümlein, S.-O. Moch, and T.
 3950 Riemann, Eds., pp. 10–15, 2010. DOI: 10.1016/j.nuclphysbps.2010.08.
 3951 011. arXiv: 1007.3492 [hep-ph].
- 3952 [172] V. Khachatryan et al., “Measurement of the differential cross section for top
 3953 quark pair production in pp collisions at $\sqrt{s} = 8 \text{ TeV}$ ”, *Eur. Phys. J. C*,
 3954 vol. 75, no. 11, p. 542, 2015. DOI: 10.1140/epjc/s10052-015-3709-x.
 3955 arXiv: 1505.04480 [hep-ex].
- 3956 [173] L. Sonnenschein, “Analytical solution of ttbar dilepton equations”, *Phys. Rev.
 3957 D*, vol. 73, p. 054015, 2006, [Erratum: Phys.Rev.D 78, 079902 (2008)]. DOI:
 3958 10.1103/PhysRevD.78.079902. arXiv: hep-ph/0603011.

- 3959 [174] I. Korol, “Measurement of double differential $t\bar{t}$ production cross sections with
3960 the CMS detector”, CERN-THESIS-2016-060, DESY-THESIS-2016-011, Ph.D.
3961 dissertation, Universität Hamburg, 2016. DOI: 10.3204/DESY-THESIS-2016-
3962 011.
- 3963 [175] J. H. Kühn, A. Scharf, and P. Uwer, “Electroweak corrections to top-quark
3964 pair production in quark-antiquark annihilation”, *Eur. Phys. J. C*, vol. 45,
3965 p. 139, 2006. DOI: 10.1140/epjc/s2005-02423-6. arXiv: hep-ph/0508092.
- 3966 [176] J. H. Kühn, A. Scharf, and P. Uwer, “Electroweak effects in top-quark pair
3967 production at hadron colliders”, *Eur. Phys. J. C*, vol. 51, p. 37, 2007. DOI:
3968 10.1140/epjc/s10052-007-0275-x. arXiv: hep-ph/0610335.
- 3969 [177] J. H. Kühn, A. Scharf, and P. Uwer, “Weak interactions in top-quark pair
3970 production at hadron colliders: An update”, *Phys. Rev. D*, vol. 91, p. 014020,
3971 2015. DOI: 10.1103/PhysRevD.91.014020. arXiv: 1305.5773 [hep-ph].
- 3972 [178] CMS Collaboration, “Combined measurements of Higgs boson couplings in
3973 proton–proton collisions at $\sqrt{s} = 13 \text{ TeV}$ ”, *Eur. Phys. J. C*, vol. 79, no. 5,
3974 p. 421, 2019. DOI: 10.1140/epjc/s10052-019-6909-y. arXiv: 1809.10733
3975 [hep-ex].
- 3976 [179] CMS Collaboration, “CMS pythia 8 colour reconnection tunes based on
3977 underlying-event data”, *Eur. Phys. J. C*, vol. 83, no. 7, p. 587, 2023. DOI:
3978 10.1140/epjc/s10052-023-11630-8. arXiv: 2205.02905 [hep-ex].
- 3979 [180] CMS Collaboration, “CMS luminosity measurement for the 2017 data-taking
3980 period at $\sqrt{s} = 13 \text{ TeV}$ ”, CMS Physics Analysis Summary CMS-PAS-LUM-
3981 17-004, 2018. [Online]. Available: <https://cds.cern.ch/record/2621960>.
- 3982 [181] CMS Collaboration, “CMS luminosity measurement for the 2018 data-taking
3983 period at $\sqrt{s} = 13 \text{ TeV}$ ”, CMS Physics Analysis Summary CMS-PAS-LUM-
3984 18-002, 2019. [Online]. Available: <https://cds.cern.ch/record/2676164>.
- 3985 [182] W. S. Cleveland, “Robust locally weighted regression and smoothing scat-
3986 terplots”, *Journal of the American Statistical Association*, vol. 74, no. 368,
3987 pp. 829–836, 1979. DOI: 10.1080/01621459.1979.10481038.
- 3988 [183] W. S. Cleveland and S. J. Devlin, “Locally weighted regression: An approach
3989 to regression analysis by local fitting”, *Journal of the American Statistical
3990 Association*, vol. 83, no. 403, pp. 596–610, 1988. DOI: 10.1080/01621459.
3991 1988.10478639.
- 3992 [184] A. M. Sirunyan et al., “Measurement of differential cross sections for the
3993 production of top quark pairs and of additional jets in lepton+jets events
3994 from pp collisions at $\sqrt{s} = 13 \text{ TeV}$ ”, *Phys. Rev. D*, vol. 97, no. 11, p. 112003,
3995 2018. DOI: 10.1103/PhysRevD.97.112003. arXiv: 1803.08856 [hep-ex].

- 3996 [185] A. M. Sirunyan et al., “Development and validation of HERWIG 7 tunes
 3997 from CMS underlying-event measurements”, *Eur. Phys. J. C*, vol. 81, no. 4,
 3998 p. 312, 2021. DOI: 10.1140/epjc/s10052-021-08949-5. arXiv: 2011.03422
 3999 [hep-ex].
- 4000 [186] B. R. Webber, “A QCD Model for Jet Fragmentation Including Soft Gluon
 4001 Interference”, *Nucl. Phys. B*, vol. 238, pp. 492–528, 1984. DOI: 10.1016/
 4002 0550-3213(84)90333-X.
- 4003 [187] R. Frederix and S. Frixione, “Merging meets matching in MC@NLO”, *JHEP*,
 4004 vol. 12, p. 061, 2012. DOI: 10.1007/JHEP12(2012)061. arXiv: 1209.6215
 4005 [hep-ph].
- 4006 [188] A. Djouadi, J. Ellis, A. Popov, and J. Quevillon, “Interference effects in $t\bar{t}$
 4007 production at the LHC as a window on new physics”, *JHEP*, vol. 03, p. 119,
 4008 2019. DOI: 10.1007/JHEP03(2019)119. arXiv: 1901.03417 [hep-ph].
- 4009 [189] A. Djouadi, J. Ellis, and J. Quevillon, “Discriminating between Pseudoscalar
 4010 Higgs and Toponium States at the LHC and Beyond”, Dec. 2024. arXiv:
 4011 2412.15138 [hep-ph].
- 4012 [190] B. A. Betchart, R. Demina, and A. Harel, “Analytic solutions for neutrino
 4013 momenta in decay of top quarks”, *Nucl. Instrum. Meth. A*, vol. 736, p. 169,
 4014 2014. DOI: 10.1016/j.nima.2013.10.039. arXiv: 1305.1878 [hep-ph].
- 4015 [191] R. Demina, A. Harel, and D. Orbaker, “Reconstructing $t\bar{t}$ events with one
 4016 lost jet”, *Nucl. Instrum. Meth. A*, vol. 788, p. 128, 2015. DOI: 10.1016/j.
 4017 nima.2015.03.069. arXiv: 1310.3263 [hep-ex].
- 4018 [192] G. J. Feldman and R. D. Cousins, “Unified approach to the classical statistical
 4019 analysis of small signals”, *Phys. Rev. D*, vol. 57, p. 3873, 1998. DOI: 10.1103/
 4020 PhysRevD.57.3873. arXiv: physics/9711021.
- 4021 [193] R. D. Cousins and V. L. Highland, “Incorporating systematic uncertainties
 4022 into an upper limit”, *Nucl. Instrum. Meth. A*, vol. 320, pp. 331–335, 1992.
 4023 DOI: 10.1016/0168-9002(92)90794-5.
- 4024 [194] G. Aad et al., “Measurement of the $t\bar{t}$ production cross-section and lepton
 4025 differential distributions in $e\mu$ dilepton events from pp collisions at $\sqrt{s} =$
 4026 13 TeV with the ATLAS detector”, *Eur. Phys. J. C*, vol. 80, no. 6, p. 528,
 4027 2020. DOI: 10.1140/epjc/s10052-020-7907-9. arXiv: 1910.08819 [hep-
 4028 ex].
- 4029 [195] A. Tumasyan et al., “Differential cross section measurements for the produc-
 4030 tion of top quark pairs and of additional jets using dilepton events from pp
 4031 collisions at $\sqrt{s} = 13$ TeV”, *JHEP*, vol. 02, p. 064, 2025. DOI: 10.1007/
 4032 JHEP02(2025)064. arXiv: 2402.08486 [hep-ex].

- 4033 [196] G. Aad et al., “Inclusive and differential cross-sections for dilepton $t\bar{t}$ production measured in $\sqrt{s} = 13$ TeV pp collisions with the ATLAS detector”, *JHEP*, vol. 07, p. 141, 2023. DOI: 10.1007/JHEP07(2023)141. arXiv: 2303.15340 [hep-ex].
- 4034
4035
4036
- 4037 [197] J. A. Raine, M. Leigh, K. Zoch, and T. Golling, “Fast and improved neutrino reconstruction in multineutrino final states with conditional normalizing flows”, *Phys. Rev. D*, vol. 109, no. 1, p. 012 005, 2024. DOI: 10.1103/PhysRevD.109.012005. arXiv: 2307.02405 [hep-ph].
- 4038
4039
4040
- 4041 [198] V. Chekhovsky et al., “High-precision measurement of the W boson mass with the CMS experiment at the LHC”, Dec. 2024. arXiv: 2412.13872 [hep-ex].
- 4042
- 4043 [199] F. J. Tackmann, “Beyond Scale Variations: Perturbative Theory Uncertainties from Nuisance Parameters”, Nov. 2024. arXiv: 2411.18606 [hep-ph].
- 4044
- 4045 [200] S.-J. Jiang, B.-Q. Li, G.-Z. Xu, and K.-Y. Liu, “Study on Toponium: Spectrum and Associated Processes”, Dec. 2024. arXiv: 2412.18527 [hep-ph].
- 4046
- 4047 [201] I. Brivio et al., “ALPs Effective Field Theory and Collider Signatures”, *Eur. Phys. J. C*, vol. 77, no. 8, p. 572, 2017. DOI: 10.1140/epjc/s10052-017-5111-3. arXiv: 1701.05379 [hep-ph].
- 4048
4049
- 4050 [202] J. Bonilla, I. Brivio, M. B. Gavela, and V. Sanz, “One-loop corrections to ALP couplings”, *JHEP*, vol. 11, p. 168, 2021. DOI: 10.1007/JHEP11(2021)168. arXiv: 2107.11392 [hep-ph].
- 4051
4052
- 4053 [203] H. Bahl et al., “HiggsTools: BSM scalar phenomenology with new versions of HiggsBounds and HiggsSignals”, *Comput. Phys. Commun.*, vol. 291, p. 108 803, 2023. DOI: 10.1016/j.cpc.2023.108803. arXiv: 2210.09332 [hep-ph].
- 4054
4055
- 4056 [204] G. Aad et al., “Search for resonances decaying into photon pairs in 139 fb^{-1} of pp collisions at $\sqrt{s}=13$ TeV with the ATLAS detector”, *Phys. Lett. B*, vol. 822, p. 136 651, 2021. DOI: 10.1016/j.physletb.2021.136651. arXiv: 2102.13405 [hep-ex].
- 4057
4058
4059
- 4060 [205] G. Aad et al., “Search for heavy resonances decaying into a Z or W boson and a Higgs boson in final states with leptons and b -jets in 139 fb^{-1} of pp collisions at $\sqrt{s} = 13$ TeV with the ATLAS detector”, *JHEP*, vol. 06, p. 016, 2023. DOI: 10.1007/JHEP06(2023)016. arXiv: 2207.00230 [hep-ex].
- 4061
4062
4063
- 4064 [206] A. Hayrapetyan et al., “Observation of four top quark production in proton-proton collisions at $s=13\text{TeV}$ ”, *Phys. Lett. B*, vol. 847, p. 138 290, 2023. DOI: 10.1016/j.physletb.2023.138290. arXiv: 2305.13439 [hep-ex].
- 4065
4066
- 4067 [207] A. Biekötter, J. Fuentes-Martín, A. M. Galda, and M. Neubert, “A global analysis of axion-like particle interactions using SMEFT fits”, *JHEP*, vol. 09, p. 120, 2023. DOI: 10.1007/JHEP09(2023)120. arXiv: 2307.10372 [hep-ph].
- 4068
4069